HAL
open science

Scaling laws and electron properties in Hall effect thrusters

Käthe Dannenmayer

To cite this version:

Käthe Dannenmayer. Scaling laws and electron properties in Hall effect thrusters. Other. Université d'Orléans, 2012. English. NNT : 2012ORLE2033 . tel-00797732

HAL Id: tel-00797732

https://theses.hal.science/tel-00797732

Submitted on 7 Mar 2013

HAL is a multi-disciplinary open access archive for the deposit and dissemination of scientific research documents, whether they are published or not. The documents may come from teaching and research institutions in France or abroad, or from public or private research centers.

L'archive ouverte pluridisciplinaire **HAL**, est destinée au dépôt et à la diffusion de documents scientifiques de niveau recherche, publiés ou non, émanant des établissements d'enseignement et de recherche français ou étrangers, des laboratoires publics ou privés.

UNIVERSITÉ D'ORLÉANS

ÉCOLE DOCTORALE SCIENCES ET TECHNOLOGIES

Institut de Combustion Aérothermique Réactivité et Environnement,
CNRS Orléans

THÈSE présentée par :

Käthe DANNENMAYER

soutenue le : **04 octobre 2012**

pour obtenir le grade de : **Docteur de l'université d'Orléans**

Discipline : Physique

Scaling laws and electron properties in Hall effect thrusters

THÈSE dirigée par :

Stéphane MAZOUFFRE	Chargé de recherche, ICARE, CNRS Orléans

RAPPORTEURS :

Eduardo AHEDO	Professeur, EP2, Universidad Poytécnica de Madrid
Stéphane BECHU	Chargé de recherche, CRPMN, CNRS-LPSC Grenoble

---

JURY:

Thierry DUDOK DE WIT	Professeur, LPC2E, Université d'Orléans, Président du jury
Eduardo AHEDO	Professeur, EP2, Universidad Polytécnica de Madrid
Stéphane BECHU	Chargé de recherche, CRPMN, CNRS-LPSC Grenoble
Stéphane MAZOUFFRE	Chargé de recherche, ICARE, CNRS Orléans
Milan TICHY	Professeur, Charles University Prague
Nicolas ARCIS	Docteur, CNES, invité
Georg HERDRICH	Docteur, Universität Stuttgart, invité
Stephan ZURBACH	Docteur, Snecma, invité

Acknowledgements

The present dissertation is the result of over 3 years of research work in the field of Hall thrusters. Although obtaining a PhD requires a complete independent work, it can never be successfully accomplished without the help and support of an entire network of people. I would like to take this opportunity to thank and acknowledge all the people that have helped along the way.

First of all, I would like to thank my advisor, Stéphane Mazouffre for his unfailing support, the confidence he has shown in me and his guidance through the successes and setbacks. From my first internship 7 years ago, it has always been a real pleasure to work with you. I owe you the discovery of this fascinating area of electric propulsion. I will never forget the endless hours we spent discussing physics but also just about life. I am looking forward to continue working with you in the future.

I would also like to thank my two referees, Eduardo Ahedo and Stéphane Béchu, who have taken the time to carefully read my manuscript. I appreciate the time you devoted to the careful reading of my manuscript and the insightful comments to improve the quality of my work. Furthermore, I would also like to thank the other members of my committee, Thierry Dudok de Wit, Milan Tichý, Stéphan Zurbach, Denis Arrat and Georg Herdrich for their interest in my work.

I have also to express my sincere gratitude to Milan Tichý and Pavel Kudrna. I owe you almost everything I know about electrostatic probes. It has always been a great pleasure to spend some days with you in the lab and I could not have done all the interesting experiments without your help. Thank you also for the fantastic days in Prague. I hope we will continue to cooperate in the future because I still have so much to learn from you.

The research presented in this work was made possible by the doctoral scholarship provided by CNES and Snecma and the financial support of the joint research program GdR 3161 entitled "*Propulsion par plasma dans l'espace*". I also want to thank all the member of the GdR for the fruitful discussions.

I have had the pleasure to work with great people during the past three years in the electric propulsion team at the ICARE laboratory in Orléans. Thanks to Sedina, Aurélien, Mihaela, Julien, Friederieke and Stéphane for the countless discussions about physics and life, the help and the pleasant atmosphere in the team. Special thanks to Guillaume for sharing the office, numerous hours of experiments and all the ups and downs of this 3-year adventure. I would also like to thank the administration and technical staff of the ICARE laboratory for the all the help: A big thanks to Murielle, Corinne and Vincent for guiding me through bureaucracy and administration; to Nicolas, Jacques and Fabrice for your help with all electronics problems; to Laurent and Eric for machining all the necessary parts to built up a new experiment. I would also like to thank the PIVOINE team, Pascal, Sisouk and the two Guillaumes for all their help with the experiments. Thanks also to the $lunch - team$, I will always remember all the funny moments during our well-deserved lunch break.

During the last 3 years I had the chance to collaborate with many great people in the electric propulsion community. I would like to thank the whole PEPL crew for two amazing and instructive months at the University of Michigan, the staff from the ESA Propulsion Laboratory at ESTEC in Noordwijk for a successful month of experiments and Mario from Universidad

Polytécnica de Madrid for the pleasant cooperation on the comparison of experimental data and numerical plume models.
In my personal life, I want to thank my family and my close friends that have supported me long before I started this thesis and that will always be there for me. I would not be where I am today without the love and the encouragement of my parents. Mum and Dad, thank you for all you have done and continue to do for me. I am also thankful for my brother and my friend in Germany that have always been there for me despite being hundreds of kilometres away. Danke: Bastian, Julia, Matze, Marc, Hanna, Kathrin, Markus, David und Angel. I also want to thank my friends here in France, it has been a really cool time with you. Merci à Florie, Laure, Valerio, Roman, Vladeta and David. Finally, my deepest thanks belongs to Stéphane ♡. Merci pour ton amour et ton soutient depuis 7 ans.

Contents

Acknowledgements **i**

List of Figures **xiii**

List of Tables **xv**

1 General introduction **1**

2 Electric Propulsion **5**
2.1 Fundamentals of space propulsion 5
2.2 Electric propulsion versus chemical propulsion 5
2.3 Methods of electric propulsion 6
2.4 Hall thrusters 7
2.5 Description of different test benches 9
2.5.1 PIVOINE-2g 9
2.5.2 NExET 10
2.5.3 CORONA 10
2.6 Description of different types of Hall thrusters 10
2.6.1 PPS®100-ML 11
2.6.2 PPS®1350-ML 11
2.6.3 PPI 11

3 Scaling laws **15**
3.1 Introduction 15
3.2 Review of previous works 16
3.3 Set of governing relations and scaling 18
3.3.1 Ionization and plasma containment 18
3.3.2 Relationship between performances and dimensions 20
3.4 Performance and geometry data 24
3.4.1 Description of the database 24
3.4.2 Dimensional trends in the data 25
3.5 Scaling relations in the case of high assumptions 28
3.5.1 List of high simplifying assumptions 28
3.5.2 Set of scaling relations 29
3.5.3 Magnetic field 29
3.5.4 Assessment of proportionality coefficients 30
3.6 Sizing of high-power Hall thrusters 31
3.6.1 Sizing methodology 31
3.6.2 Thermal load 31
3.6.3 Design of a 20 kW Hall thruster 32

3.7 Scaling relations with low assumptions . . . 33
3.7.1 List of low assumptions . . . 33
3.7.2 Available data and scaling relations . . . 33
3.7.3 Sizing of a 20 kW Hall thruster . . . 35
3.7.4 Comparison between the two approaches . . . 37
3.8 Comparison with the 20 kW-class thruster PPS-20k ML . . . 38
3.9 Conclusion . . . 38

4 Influence of the channel width 41
4.1 Introduction . . . 41
4.2 PPI thruster with variable channel width . . . 42
4.3 PPI thruster operating with xenon . . . 42
4.3.1 Discharge current waveform . . . 43
4.3.2 Operating envelope . . . 43
4.3.3 Ionization efficiency . . . 45
4.3.4 Ion velocity . . . 49
4.3.5 Ion energy . . . 50
4.3.6 Thrust . . . 53
4.3.7 Anode efficiency . . . 54
4.3.8 Plasma wall interactions . . . 54
4.4 Discussion . . . 58
4.5 PPI thruster operating with krypton . . . 59
4.5.1 Ionisation efficiency . . . 59
4.5.2 Ion energy . . . 62
4.5.3 Performances: thrust and anode efficiency . . . 63
4.6 Comparison between xenon and krypton . . . 66
4.7 Conclusion . . . 67

5 Time-averaged electron properties 69
5.1 Introduction . . . 69
5.2 Probes . . . 70
5.2.1 Langmuir probe . . . 70
5.2.2 Emissive probe . . . 70
5.3 Time-averaged measurements in the far-field plume of the PPS®100-ML . . . 72
5.3.1 Complete map of the far-field plume . . . 74
5.3.2 Influence of the discharge voltage . . . 76
5.3.3 Influence of the anode mass flow rate . . . 78
5.3.4 Influence of the cathode mass flow rate . . . 78
5.3.5 Influence of the magnetic field strength . . . 81
5.3.6 Comparison between Langmuir and emissive probe . . . 84
5.4 Fast-moving probe system . . . 87
5.4.1 Introduction . . . 87
5.4.2 Description system . . . 88
5.4.3 First results . . . 89

5.5 Conclusion 93

6 Time-resolved electron properties 95
6.1 Introduction 95
6.2 Review of previous works 96
6.3 Time-resolved measurement technique 97
6.4 Time-resolved measurements in the far-field plume of the PPI thruster 99
6.4.1 PPI thruster operated with xenon 99
6.4.2 Comparison between xenon and krypton 117
6.5 Time-resolved measurements in the far-field plume of the PPS®1350-ML 121
6.5.1 Influence of the keeper modulation on the discharge behavior 121
6.5.2 Time evolution of the plasma parameters 122
6.6 Conclusion 125

7 General conclusion and perspectives 127

Bibliography 133

A List of publications 141

B Version française 145
B.1 Introduction 145
B.2 Chapitre 2: Propulsion électrique 147
B.3 Chapitre 3: Lois d'échelle 148
B.4 Chapitre 4: Influence de la géométrie 149
B.5 Chapitre 5: Propriétés électronique moyennées dans le temps 150
B.6 Chapitre 6: Propriétés électronique résolues en temps 150
B.7 Conclusion 151

List of Figures

2.1 The consumed propellant mass plotted as a function of the propellant ejection speed for two types of missions in case of a 5 ton spacecraft. 7
2.2 Schematic of a Hall thruster. 9
2.3 Typical Hall thruster radial magnetic field (red line) and axial electric field (blue line) along the channel length. 9
2.4 Picture of the PPS®100-ML. 11
2.5 Picture of the PPS®1350. 11
2.6 Picture of the low-power permanent magnet PPI Hall thruster. 12
2.7 Temperatures of the 200 W-class PPI Hall thruster (S_0 configuration) operating at 200 V and 1.0 mg/s in the NExET test bench. 12
2.8 The 200 W-class PPI Hall thruster (S_0 configuration) operating at 200 V and 1.0 mg/s in the NExET test bench (front view). 13
2.9 The 200 W-class PPI Hall thruster ($2S_0$ configuration) operating at 200 V and 1.0 mg/s in the NExET test bench (side view). 13

3.1 Cross-section view of a Hall thruster showing the main components. The three characteristic dimensions L, h and d are also indicated. 18
3.2 Thrust as a function of the discharge voltage for seven different Hall thrusters: micro-thruster (0.2 mg/s), SPT20 (0.472 mg/s), SPT50 (1.0 mg/s), PPS®1350 (3.5 mg/s), PPS®X000 (5.0 mg/s), T220 (19.4 mg/s) and NASA-457M (35.2 mg/s). 26
3.3 Upper graph: Specific impulse as a function of the discharge voltage for seven different Hall thrusters. Lower graph: Anode thrust efficiency as a function of discharge voltage. The xenon mass flow rate is: micro-thruster (0.2 mg/s), SPT20 (0.472 mg/s), SPT50 (1.0 mg/s), PPS®1350 (3.5 mg/s), PPS®X000 (5.0 mg/s), T220 (19.4 mg/s) and NASA-457M (35.2 mg/s). 27
3.4 Channel width h as a function of the channel mean diameter d for a variety of Hall thrusters (sizes are in arbitrary units). The two dimensions d and h are proportional. . 28
3.5 Normalized ratio of the channel mean diameter to the channel width as a function of the thruster input power. 28
3.6 Thrust as function of $\mathrm{d}^2\mathrm{U}_d^{0.5}$ and the linear fit for different Hall thrusters (dashed line). For each thruster, some thrust values are chosen around the point of normal operation. 30
3.7 The maximum electron temperature T_e as a function of the discharge voltage for different Hall thrusters. The equation for the linear fit is: $T_e = 0.12\,U_d$. 34
3.8 Voltage losses for the SPT100 and the PPS®X000-ML measured by RPA and LIF as a function of the discharge voltage. PPS®X000-ML LIF[1] operates at a constant mass flow rate ($\dot{m} = 6\,mg/s$), whereas PPS®X000-ML LIF[2] operates at a constant discharge voltage ($U_d = 300\,V$). 35
3.9 Fraction of doubly charged ions as a function of the discharge voltage for the NASA-173Mv2 at a mass flow rate of 10 mg/s 36

3.10 Thrust as function of $\gamma\,\theta_d\,1/\mathrm{U}_d^{0.5}\,(\mathrm{U}_d\text{ - }\Delta)^{0.5}\,\mathrm{d}^2/\mathrm{L}$ and the linear fit for different Hall thrusters (dashed line). For each thruster, some thrust values are chosen around the point of normal operation. The NASA-457M thruster is represented by the asterisk-symbol. 36
3.11 Picture of the 20 kW-class PPS-20k ML Hall thruster with the cathode mounted in the center of the thruster. 38
3.12 Photograph of the 20 kW-class PPS-20k ML Hall thruster operating with xenon in the PIVOINE-2g test bench. From left to right: low power, 15 kW and 23.5 kW. 38

4.1 Channel width h against mean diameter d for different Hall thrusters [48]. Star symbols show the three different PPI configurations. 42
4.2 Schematic of the thruster acceleration channel showing the three geometries. A sketch of the magnetic field strength along the channel radius is also shown. . . 42
4.3 Waveform of the anode current and the associated power spectrum density for various operating conditions in the case of the S_0 configuration of the PPI thruster. 44
4.4 Influence of the channel geometry upon the mass flow rate-voltage envelope. . . 45
4.5 Discharge current as a function of the discharge voltage for 3 anode mass flow rates and the 3 PPI configurations 45
4.6 Plume ion current density angular profile for the PPI Hall thruster in the S_0 configuration for several discharge voltages (0.8 mg/s). The 0° angle corresponds to the thruster axis. 46
4.7 Plume ion current density profile of the PPI thruster (S_0 geometry, 300 V, 0.8 mg/s) and associated Gaussian fit (line). Corrected data removes the tails for angles larger than 30°. 47
4.8 Reconstructed 3D ion current density distribution in the plume of the PPI thruster (S_0 geometry, 300 V, 0.8 mg/s). 47
4.9 Total ion current as a function of the discharge voltage for the three different channel geometries. 48
4.10 Beam current efficiency as a function of the discharge voltage for the three different channel geometries. 48
4.11 Anode propellant utilization as a function of the discharge voltage for the three channel configurations. 49
4.12 Influence of the channel width on Xe^+ ion axial velocity. The PPI thruster is operated at 200 V and 1 mg/s for the 3 configurations. The position $x = 0$ mm refers to the channel exit plane. 50
4.13 Schematic view of a RPA. Also shown in the polarization of the grids, where 0 corresponds to the ground. 51
4.14 RPA current trace (circle) and corresponding ion energy distribution function (blue line). Measurements were performed in the plume at $x = 70$ cm ($3S_0$, 250 V, 1.2 mg/s). 51
4.15 Most probable (open symbols) and mean ion energy (full symbols) measured with the RPA as a function of the discharge voltage for the three PPI thruster channel configurations. 53

4.16 Full width at half maximum (open symbols) and standard deviation (full symbols) of the IEDF as a function of the discharge voltage for the three PPI thruster channel configurations. 53
4.17 Computed thrust level as a function of the input power for the three PPI thruster channel configurations. 54
4.18 Anode efficiency η_a as a function of the input power for the three channel geometries. The triangle symbols correspond to thrust measurements carried out in 2008 in the PIVOINE test bench with a different version of the PPI thruster in the S_0 configuration [16]. 54
4.19 Calibrated infrared image of the low-power permanent magnet PPI Hall thruster operating at 200 V and 1.1 A (front view, $3S_0$ configuration)). 55
4.20 Simplified thermal enclosure with radiative heat exchanges of the PPI thruster. Plasma-wall interactions are characterized by the energy flux q_p. 56
4.21 Calulated channel wall temperatures assuming a constant loss term q_p for the three geometries 56
4.22 Plume ion current density angular profile of the $3S_0$ configuration of the PPI thruster operated at 250 V and 1.0 mg/s. The associated Gaussian fit (solid line) removes the tails at angles larger than 30°. 60
4.23 Total ion current as a function of the discharge voltage at a constant anode mass flow rate of 1.0 mg/s (Kr) for the 3 PPI configurations. 61
4.24 Total ion current as a function of the anode mass flow rate at a constant discharge voltage of 250 V for the 3 PPI configurations. 61
4.25 Beam current efficiency as a function of the input power for the 3 PPI configurations. 62
4.26 Anode propellant utilization as a function of the input power for the 3 PPI configurations. 62
4.27 Most probable ion energy as a function of the discharge voltage for the 3 PPI configurations. 63
4.28 Most probable ion energy as a function of the anode mass flow rate for the 3 PPI configurations. 63
4.29 Energy conversion efficiency ξ as a function of the discharge voltage for the 3 PPI configurations. 64
4.30 Energy conversion efficiency ξ as a function of the anode mass flow rate for the 3 PPI configurations. 64
4.31 Full width at half maximum as a function of the discharge voltage for the 3 PPI configurations. 64
4.32 Full width at half maximum as a function of the anode mass flow rate for the 3 PPI configurations. 64
4.33 Thrust as a function of the input power for the 3 PPI configurations. 65
4.34 Anode efficiency as a function of the input power for the 3 PPI configurations. . 65
4.35 Thrust as a function of the input power for the 3 PPI configurations. 66
4.36 Anode efficiency as a function of the input power for the 3 PPI configurations. . 66

5.1 Example of a current-voltage characteristic recorded at a discharge voltage of 200 V and a mass flow rate of 4.0 mg/s. The probe was located at 300 mm downstream the thruster exit plane on the thruster axis. 71
5.2 Picture of the emissive probe. Also shown are all the different elements necessary to built the probe. 72
5.3 Emissive probe potential against the heating current in the far-field plume of the PPS®100-ML thruster. 72
5.4 Schematic view of the Hall thruster and probe positioning system. 73
5.5 Schematic view of the different measurement positions in the far-field plume of the PPS®100-ML thruster. 73
5.6 Complete map of the plasma parameters (V_p, T_e and n_e) in the far-field plume for $U_d = 300$ V, $\dot{m}_a = 4.0$ mg/s. 75
5.7 Electron temperature as a function of the electron density in the far-field plume of the PPS®100-ML operating at 300 V and 4.0 mg. The isentropic fit is also shown (dashed line). 77
5.8 Electron density (log scale) as a function of the V_p / T_e ratio in the far-field plume of the PPS®100-ML operating at 300 V and 4.0 mg. 77
5.9 Plasma potential as a function of the electron density in the far-field plume of the PPS®100-ML operating at 300 V and 4.0 mg. The corresponding fit is also shown (dashed line). 77
5.10 Electron temperature as a function of the plasma potential in the far-field plume of the PPS®100-ML operating at 300 V and 4.0 mg. 77
5.11 Influence of the discharge voltage on the plasma parameters for $\dot{m}_a = 4.0$ mg/s and $\dot{m}_c = 0.42$ mg/s. 79
5.12 Influence of the anode mass flow rate on the plasma parameters for $U_d = 200$ V, $\dot{m}_c = 0.42$ mg/s. 80
5.13 Influence of the cathode mass flow rate on V_p, T_e and n_e for $U_d = 300$ V, $\dot{m}_a = 4.0$ mg/s. 82
5.14 Influence of CRP and cathode mass flow rate on V_p, T_e and n_e. The PPI thruster is operated at 200 V and 1.0 mg/s (full symbols) as well as at 250 V and 0.8 mg/s (open symbols). 83
5.15 Influence of the coil current on the plasma parameters for $U_d = 200$ V, $\dot{m}_a = 2.5$ mg/s and $\dot{m}_c = 0.42$ mg/s. 85
5.16 Plasma potential measured with an emissive probe in the far-field plume of the PPS®100-ML with permanent magnets at $U_d = 200$ V and $\dot{m}_a = 4.0$ mg/s. . . . 86
5.17 Fractional difference of plasma potential D_{V_p} measured with an emissive probe (EP) and a Langmuir probe (LP) for the PPS®100-ML operating at $U_d = 200$ V and $\dot{m}_a = 4.0$ mg/s. 86
5.18 Electron temperature measured with an emissive probe (EP) for the PPS®100-ML operating at $U_d = 200$ V and $\dot{m}_a = 4.0$ mg/s. 87
5.19 Fractional difference of electron temperature D_{T_e} measured with an emissive probe (EP) and a Langmuir probe (LP) for the PPS®100-ML operating at $U_d = 200$ V and $\dot{m}_a = 4.0$ mg/s. 87
5.20 Picture of the ultrasonic piezo PILine® Linear Motor Stage M664K018. 88

5.21 Motion profile of the fast reciprocating probe for the measurement of the plasma parameters in the near-field plume. 89
5.22 Schematic view of the setup (not at scale). The blue arrows show the implementations of the first and second measurement series. 90
5.23 Picture of the PPI thruster and the high-speed reciprocating probe system (side-view). 91
5.24 Picture of the PPI thruster and the high-speed reciprocating probe system (topview). 91
5.25 Discharge current and plasma potential time series measured by means of a current probe and a heated emissive probe during probe sweep. 91
5.26 Cathode-to-ground potential and plasma potential time series measured by means of a voltage probe and a heated emissive probe during probe sweep. 91
5.27 Axial profile of V_p measured with the emissive probe in the near-field plume along axial direction 5 mm away from the channel centerline of the PPI thruster operating at 200 V and 1.0 mg/s. 92
5.28 Radial profile of V_p measured with the emissive probe in the near-field plume 20 mm downstream the channel exit plane of the PPI thruster operating at 200 V and 1.0 mg/s. 92

6.1 Schematic view of the electrical set-up of the keeper electrode modulation. . . . 98
6.2 Modulation signal applied between the keeper and the negative pole of the cathode heating circuit. 98
6.3 Schematic view of the amplifier of the keeper electrode modulation. 99
6.4 Schematic view of the different measurement positions in the far-field plume of the PPI thruster. 100
6.5 Influence of the keeper modulation on I_d, CRP and V_p for the PPI thruster operating at $U_d = 200$ V, $\dot{m}_a = 1.0$ mg/s (Xe). The solid black line represents the modulation signal. 101
6.6 Power spectrum of the discharge current and the plasma potential without modulation and for the 2 modulation frequencies. 102
6.7 Influence of the modulation on the Xe^+ ion velocity distribution measured by means of LIF at two different positions along the channel centerline. 103
6.8 Time evolution of the plasma potential V_p, the electron temperature T_e and the electron density n_e measured by means of a Langmuir probe at x = 100 mm and y = 0 mm in the plasma plume of the PPI operating at $U_d = 200$ V, $\dot{m}_a = 1.0$ mg/s (Xe). The discharge current I_d time series is shown in solid line 104
6.9 Evolution in time and space (radial direction) of V_p, T_e and n_e for the two different frequencies at 100 mm downstream thruster exit plane. The thruster is operated at $U_d = 200$ V, $\dot{m}_a = 1.0$ mg/s (Xe). 106
6.10 Comparison of V_p, T_e and n_e obtained from time-resolved and time-averaged measurements with a Langmuir probe at 100 mm downstream the thruster exit plane in the far-field plume of the PPI thruster ($3S_0$ configuration) operating with Xe at $U_d = 200$ V, $\dot{m}_a = 1.0$ mg/s. 108

6.11 Comparison of the plasma potential measured with an emissive (green line) and a Langmuir (purple symbols) probe in the far-field plume of the PPI thruster operating at $U_d = 200\,\mathrm{V}$, $\dot{m}_a = 1.0\,\mathrm{mg/s}$ (Xe). 109

6.12 Operating conditions of the PPI thruster for the investigation of the influence of the average on plasma parameters. 111

6.13 Influence average on the plasma parameters for two different operating conditions of the PPI thruster. 112

6.14 Comparison operating conditions (I_d and V_p) of the PPI thruster operating at $U_d = 200\,\mathrm{V}$, $\dot{m}_a = 1.0\,\mathrm{mg/s}$ for two different channel widths ($2S_0$ and $3S_0$). The plasma potential is measured with an emissive probe 100 mm downstream the thruster exit plane on the thruster axis. 113

6.15 Influence of the channel width on the time evolution of V_p measured with a Langmuir probe at three different axial positions on the axis of PPI thruster operating at $U_d = 200\,\mathrm{V}$, $\dot{m}_a = 1.0\,\mathrm{mg/s}$ (Xe). The $2S_0$ and the $3S_0$ configuration are compared. 114

6.16 Influence of the channel width on the time evolution of T_e measured with a Langmuir probe at three different axial positions on the axis of PPI thruster operating at $U_d = 200\,\mathrm{V}$, $\dot{m}_a = 1.0\,\mathrm{mg/s}$ (Xe). The $2S_0$ and the $3S_0$ configuration are compared. 115

6.17 Influence of the channel width on the time evolution of n_e measured with a Langmuir probe at three different axial positions on the axis of PPI thruster operating at $U_d = 200\,\mathrm{V}$, $\dot{m}_a = 1.0\,\mathrm{mg/s}$ (Xe). The $2S_0$ and the $3S_0$ configuration are compared. 116

6.18 Influence of the keeper modulation on I_d, CRP and V_p for the PPI thruster operating at $U_d = 200\,\mathrm{V}$, $\dot{m}_a = 1.0\,\mathrm{mg/s}$ (Kr). The solid black line represents the modulation signal. 117

6.19 Comparison of the time evolution over one period of V_p, T_e and n_e for Xe and Kr for the two different frequencies at 100 mm downstream thruster exit plane on the thruster axis. 119

6.20 Comparison of the mean values of V_p, T_e and n_e measured with a Langmuir probe in the far-field plume of the PPI thruster operating with Xe (purple symbol) and Kr (blue symbol) at $U_d = 200\,\mathrm{V}$, $\dot{m}_a = 1.0\,\mathrm{mg/s}$. 120

6.21 Influence of the keeper modulation on I_d, CRP and V_p for the PPS®1350-ML thruster operating at $U_d = 250\,\mathrm{V}$, $\dot{m}_a = 3.0\,\mathrm{mg/s}$ (Xe). The solid black line represents the modulation signal. 122

6.22 Power spectrum of the discharge current and the plasma potential without modulation and for the 2 modulation frequencies. 123

6.23 Time evolution of the plasma potential V_p, the electron temperature T_e and the electron density n_e measured by means of a Langmuir probe at 250 mm downstream the thruster exit plane on the thruster axis in the plasma plume of the PPS®1350-ML operating at $U_d = 250\,\mathrm{V}$, $\dot{m}_a = 3.0\,\mathrm{mg/s}$ (Xe). 124

7.1 Electron energy distribution function (EEDF) measured with a single cylindrical Langmuir probe in the far-field plume of two different Hall thrusters (PPS®1350-ML and PPI). 131

B.1 Fonction de distribution en énergie des électrons (FDEE) meaurée avec une sonde de Langmuir dans la plume de deux propulseurs de Hall différents (PPS®1350-ML et PPI). 156

List of Tables

2.1 Comparison between chemical and electric propulsion. 6

3.1 Computed dimensions, parameters and performances evaluated from scaling relations for a 20 kW thruster delivering 1 N of thrust in the case of high hypothesis. The magnetic field strength is set to 200 G. 32
3.2 Dimensions, parameters and performances evaluated from scaling relations under low assumptions for a 20 kW thruster delivering 1 N of thrust. The magnetic field strength is fixed to 200 G. 37

4.1 Equilibrium temperature of the Al_2O_3 channel walls for the three different geometries (200 V, 220 W). 55
4.2 Energy flux to the walls q_p and power losses for the three thruster geometries (200 V, 220 W. 58
4.3 Comparison of the performances of two different Hall thrusters. 58
4.4 Operating conditions for the PPI thruster in the CORONA chamber. 60
4.5 Comparison between measured and calculated thrust for the 3 PPI configurations at 200 V and 1.0 mg/s. 65
4.6 Comparison of the thruster performances for the 3 PPI configurations operated with xenon and krypton. 66

5.1 Mean discharge current, current standard deviation and cathode potential to ground for the different operating conditions of the PPS®100-ML thruster. The abbreviation "p.m." stands for "permanent magnets". 74

6.1 Mean values of V_p, T_e and n_e on the thruster axis for 3 different distances downstream the thruster axis. 105
6.2 Mean values of I_d, CRP and V_p as a function of the modulation frequency. The values without modulation as well as the average values are also given. The plasma potential is measured by means of a heated emissive probe at 250 mm downstream the thruster exit plane on the thruster axis. 123
6.3 Mean values of V_p, T_e and n_e for the two different modulation frequencies. The measurements were taken at 250 mm downstream the thruster exit plane on the thruster axis. 125

B.1 Comparaison des performances des 3 configurations du PPI en fonctionnement avec xénon et krypton. 149

Chapter 1

General introduction

Satellites and space probes need a propulsive system to move through space. There are basically two means of space propulsion. The first and more common one is chemical propulsion, where hot gases, resulting from a chemical reaction between two substances, are ejected through a nozzle. The second technology is known as electric propulsion. Charged particles are accelerated by an electric field and ejected with velocities of up to 20 times larger than for chemical propulsion.

Electric propulsion systems offer significant advantages for commercial and scientific missions in terms of available payload mass, launch costs and mission durations thanks to propellant mass savings due to the much faster propellant ejection speed. Today's most important application of electric propulsion systems is the north-south station keeping of geosynchronous telecommunication satellites. The increase of electrical power available onboard the spacecraft will lead to new applications of electric propulsion systems in the future, like e.g. orbit raising and orbit topping maneuvers, orbit transfer maneuvers as well as end-of-life deorbiting. Many different electric propulsion technologies exist (e.g. gridded ion engines [1], Hall thrusters [1], arcjets[1], Magnetoplasmadynamic thrusters (MPD) [1], VASIMR [2], Pegases thruster [3], ...). Among all the different electric propulsion devices, two technologies, namely gridded ion engines and Hall thrusters, are today a mature technology with a long flight heritage. Gridded ion engines are characterized by the purely electrostatic acceleration of ions, extracted from a plasma source (DC electron bombardment, microwave or radio-frequency discharge), through a set of high-voltage grids. Hall thrusters provide thrust by an acceleration of ions in a low pressure cross-field discharge. Both technologies have similar efficiencies of up to 70 %. Gridded ion engines are characterized by a high specific impulse and a relatively low thrust. Hall thrusters provide a higher thrust but a lower specific impulse. However, the thrust-to-power ratio of Hall thrusters is more than 3 times larger than the one of gridded ion engines. Therefore, Hall thrusters represent today an attractive propulsion technology for most missions. Over 200 Hall thrusters have been flown on satellites since 1971.

The command of propulsion systems for satellites represents a great challenge for Europe in terms of economic and strategic aspects. Therefore, the French space agency (CNES) together with the Snecma company decided to invest in R&D activities with the support of research institutes. Hence, in 1996 a joint-research program - named *GdR Propulsion par Plasma dans l'Espace* - was started including CNRS, CNES, Snecma and several universities that work in the field of electric propulsion, especially the physics of Hall thrusters. Numerous efforts have been made to develop computational simulation tools and diagnostic tools. On an experimental point of view, various types of Hall thruster with power levels ranging from a few 100 W to more than 20 kW have been built and investigated in the ground-test facility PIVOINE-2g at ICARE, a unique test chamber in Europe. The vast ensemble of works performed within the

joint-program has allowed to better understand the physics at work in a Hall thruster.
The present dissertation work fully fits in the frame of current research activities prescribed in part by the medium-term suspected context in the aerospace domain. The motivation of this work is threefold: The first objective is to develop a semi-empirical scaling model that can be used for the extrapolation of existing Hall thrusters towards both low and high power levels. This extrapolation is necessary in order to meet the requirements for new missions. The second objective is an experimental investigation of the influence of the discharge channel width on the performances of a low power Hall thruster. The driving question here is whether it is possible to improve the performances of such a low power Hall thruster by simply changing the channel geometry. Finally, the third objective is to experimentally investigate the electron properties, such as plasma potential, electron temperature and electron density, using electrostatic probes. Experimental data is essential for the validation of numerical plume models that are necessary to find the optimized location of the thruster on the satellite. As the plasma of a Hall thruster is highly non-stationary, one needs to account for the fluctuations of the electron properties in order to obtain accurate results.

The organization of this dissertation is the following:

Chapter 2 gives a brief introduction on space propulsion. The advantages of electric propulsion compared to chemical propulsion are presented and the different types of electric propulsion techniques are introduced. Finally a more detailed description of Hall thruster physics as well as different test benches and Hall thrusters, used for the presented study, is given.

Chapter 3 is dedicated to the description of the scaling laws based on a semi-empirical model. Scaling relations are derived from the governing physical relations for a Hall thruster discharge. A vast database is used to validate the scaling relations and to determine the required proportionality coefficients. Two sets of scaling relations are established: one under high and the other under low assumptions. These two sets are then employed to design a 20 kW thruster capable of delivering 1 N of thrust.

The influence of the channel width on the thruster performances is described in **Chapter 4**. A low power, permanent magnet Hall thruster has been tested with three different channel widths while keeping the channel length and the mean diameter constant. Different values, such as ion current, ion velocity, ion energy, channel wall temperature and thrust, have been measured for the three channel configurations over a broad range of operating conditions. Furthermore the influence of the working gas (Xe and Kr) has been investigated. This study reveals that the efficiency of a low power Hall thruster can be improved by enlarging the channel width.

Time-averaged measurements of the electron properties are represented in **Chapter 5**. The plasma potential, the electron temperature as well as the electron density are measured by means of a single cylindrical Langmuir probe and a sufficiently heated emissive probe. The far-field plume of the PPS®100-ML thruster has been mapped for different operating conditions. The results obtained with the two different probes are compared. Furthermore, a fast-moving probe system based on a piezoelectric linear drive is presented. This system can be used for

near-field measurements of the electron properties.

Chapter 6 presents time-resolved measurements of the electron properties in the far-field plume of two different Hall thrusters, namely a 200 W permanent magnet Hall thruster and the 1.5 kW PPS®1350-ML.

Finally, a general conclusion and an outlook on further works is given in **Chapter 7**.

Chapter 2

Electric Propulsion

2.1 Fundamentals of space propulsion

The aim of a space propulsion device is to deliver thrust to a spacecraft in order to move it either from earth to space or directly in space. The general principle for thrust generation is based on the momentum exchange between ejected material and the spacecraft:

$$T = \frac{dm}{dt} v_{ex} = \dot{m}\, v_{ex}, \tag{2.1}$$

where T is the thrust, m the propellant mass, $\dot{m}$ the propellant mass flow rate and v_{ex} is the effective propellant exhaust velocity. The implication of the need for propellant is given by the fundamental relation between the system mass and the exhaust velocity, the so-called Tsiolkovsky rocket equation:

$$\Delta v = v_{ex} ln \frac{m_0}{m_1}, \tag{2.2}$$

where Δv is the change of speed of the spacecraft if no other external force is applied, m_0 the initial total mass of the spacecraft including propellant and m_1 the final total mass.
The performance of a propulsion device is typically reported in terms of specific impulse I_{sp}, which is related to the exhaust velocity by the following relation:

$$I_{sp} = \frac{T}{\dot{m}\, g_0} = \frac{v_{ex}}{g_0}, \tag{2.3}$$

where T is the thrust, g_0 the gravitational constant and $\dot{m}$ the propellant mass flow rate. As can be seen from Eqn. (2.2) and (2.3), the higher the I_{sp}, the less propellant is needed to provide a given thrust and to attain a certain $\Delta\, v$ necessary for a specific maneuver [4, 5].

2.2 Electric propulsion versus chemical propulsion

In general one can distinguish between two different types of propulsion. In conventional chemical propulsion, the thrust is obtained by expansion through a nozzle of a propellant previously heated by its own chemical reaction. Electric propulsion is defined by the acceleration of gases by electrical heating and/or by electric and magnetic body forces [4].
While chemical propulsion systems store their energy in the propellants, the energy required by electric propulsion systems is generated externally, e.g. by solar panels. Chemical propulsion is said to be "energy limited" because the chemical reactants have a fixed amount of energy per unit mass, which limits the achievable exhaust velocity or specific impulse. However, because the propellants are their own energy source, the rate at which energy can be supplied to the

Type	Chemical		Electric
Engine	Small monopropellant thruster	Fregat Main Engine (S5.92M)	SMART-1 Hall Hall Effect Thruster (PPS®1350)
Propellant	Hydrazin	Nitrogen tetroxide / Unsymmetrical dimethyl hydrazine	Xenon
Specific Impulse (s)	200	320	2500
Thrust (N)	1	$1.96 \cdot 10^4$	$8.8 \cdot 10^{-2}$
Thrust time (h)	46	0.24	5000
Propellant consumed (kg)	52	5350	80
Total Impulse (Ns)	$1.1 \cdot 10^5$	$1.72 \cdot 10^7$	$1.2 \cdot 10^6$

Table 2.1: Comparison between chemical and electric propulsion.

propellant is independent of the mass of propellant, so very high power and thrust levels can be achieved. Electric propulsion systems are not energy limited. Neglecting component lifetime considerations, an arbitrarily large amount of energy can be delivered (from a solar or nuclear power system) to a given mass of propellant so that the exhaust velocity (or specific impulse) can be much larger than that available from a chemical propulsion system. Electric propulsion systems are termed "power limited" because the rate at which energy from the external source is supplied to the propellant is limited by the mass available for the power system. This has the result of limiting the thrust of the electric propulsion system for a given spacecraft mass. Because of this, electric propulsion vehicles tend to be low thrust to mass ratio (and therefore low acceleration) vehicles. Although electric propulsion vehicles have low thrust to mass ratios, they can have a larger total amount of impulse (the product of specific impulse and propellant mass, equal to the total change of momentum) than a chemical propulsion system. So even though a chemical propulsion system can offer a high thrust to mass ratio, the propellant is expended in a short time at low specific impulse. By contrast, the low thrust to mass ratio electric propulsion system can be operated for periods ranging from hours to years and built up a larger total impulse. A comparison of the two different types of propulsion is available in Tab. 2.1. Fregat's main engine produces about 14 times the total impulse of SMART-1's engine, but uses nearly 70 times more propellant mass to do so. The hydrazine thruster produces less than a tenth as much total impulse while using 65 % of the propellant mass. In comparison with chemical rocket jets, electric propulsion devices offer an attractive way to save propellant mass thanks to a much faster propellant ejection speed, as can be seen in Fig. 2.1.

2.3 Methods of electric propulsion

There are three different types of electric propulsion systems, categorised according to the method used to accelerate the propellant, as electrothermal, electromagnetic, and electrostatic [4]. Electrothermal propulsion systems heat the propellant gas electrically before expanding it in a suitable nozzle. There are different subtypes: resistojets, arcjets and inductively or radiatively heated systems. Electromagnetic propulsion uses the acceleration of the ionized

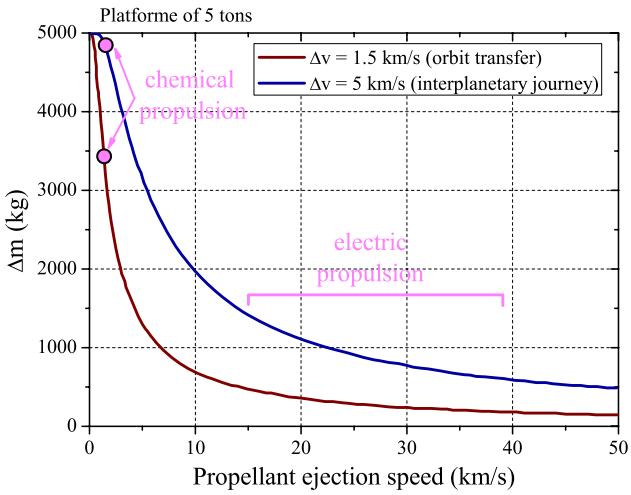

Figure 2.1: The consumed propellant mass plotted as a function of the propellant ejection speed for two types of missions in case of a 5 ton spacecraft.

propellant stream by interactions of magnetic fields with electric currents driven through the system . The electromagnetic propulsion techniques currently in use or being investigated include pulsed plasma thrusters and magnetoplasmadynamic thrusters. Electrostatic propulsion systems accelerate the ionized propellant by means of an electric field. The principal techniques are field effect electrostatic propulsion, colloidal thrusters, and gridded ion accelerators. Hall thrusters have been classed as both electrostatic and electromagnetic propulsion systems. An electrostatic field accelerates the ions in the propellant stream but that field is, to a large extent, produced by the actions of plasma electrons interacting with a magnetic field, giving both classes a claim to the technique.

2.4 Hall thrusters

Among all proposed electric propulsion devices, Hall thrusters are currently recognized as an attractive propulsion means for long duration missions and for maneuvers that require a large velocity increment. Hall thrusters, also called Stationary Plasma Thrusters or closed electron drift thrusters, are advanced propulsion devices that use an electric discharge with magnetized electrons to ionize and accelerate a propellant gas [6, 7]. Due to interesting features in terms of propellant ejection speed, efficiency, thrust-to-power ratio and lifetime, Hall thrusters are now employed for missions like geo-stationary satellite orbit correction and station keeping. Moreover, Hall thrusters appear as good candidates to be used as the primary propulsion engine for space probes during interplanetary journeys, as demonstrated by the successful solar-powered Moon mission SMART-1 of the European Space Agency [8].
A Hall thruster is a relatively simple device that consists of four major parts. The plasma is confined in a coaxial annular channel made of dielectric insulating material, e.g. BN, $BNSiO_2$,

Al_2O_3. The anode is located at the back part of the discharge channel. It often also serves as gas injector. The external cathode serves as negative electrode for the thruster and as electron source. Finally, a magnetic circuit provides a primary radial magnetic field across the channel. The magnetic flux is generated by coils or permanent magnets located on either side of the channel. A schematic of a Hall thruster is represented in Fig. 2.2.
The basic physics of a Hall thruster can be explained quite easily. A potential difference is applied between the anode and the cathode, hence an axial electric field is established. The electrons emitted by the cathode, being attracted by the positive potential applied to the anode, enter the channel. The electrons are trapped by the radial magnetic field that is maximum in the vicinity of the channel exit. The magnetic field strength has to be strong enough to efficiently trap the electrons :

$$r_{L,e} = \frac{m_e\, v_e}{e\, B} \ll L, \tag{2.4}$$

where $r_{L,e}$ is the electron Larmor radius, m_e the electron mass, v_e the electron velocity, B the magnetic field strength and L the channel length. The electrons experience joule heating in the region of maximum magnetic field. The reduced electron mobility together with the high electron temperature close to the channel exit cause the electric field also to be maximum in this region (see Fig. 2.3). The combination of the axial electric field and the radial magnetic field result in an azimuthal drift of the electrons due to the Lorentz force. This azimuthal drift of the electrons is responsible for a high induced current, the so-called Hall current. The electrons in the closed drift collide with the injected neutrals to create ions. In general Xenon is used as propellant gas because of its high mass and low ionization energy. The ionization is very efficient due to the high density of high energetic electrons. The ions are then accelerated by the axial electric field to create thrust. Therefore the magnetic field has to be weak enough not to affect ion trajectories ($r_{L,i} \ll L$). The ejected ion beam is neutralized by a fraction of the electrons emitted by the cathode. The thrust created by the ejection of the ions at high velocity is equal to the Lorentz force experienced by the electrons:

$$T = \dot{m}_i\, v_i = \int\int\int_V j_{Hall} \times B\, dV, \tag{2.5}$$

where $\dot{m}_i$ is the ion mass flow rate, v_i the ion velocity and j_{Hall} the Hall current density.
This simple description of the operating mode of a Hall thruster does not account for instabilities of the discharge, plasma-wall interactions or electron transport across the magnetic field. In fact, the number of electrons flowing through the magnetic barrier due to cross-field mobility has to be large enough to maintain the discharge (current continuity). The electron mobility exceeds classical values, i.e. the electron transport cannot be explained by diffusion due to collisions [9, 10]. There are two different possibilities to explain this phenomenon:

1. turbulent transport of the electrons due to fluctuations of the azimuthal electric field,

2. transport due to electron-wall collisions.

It might also be a combination of the two phenomena. These phenomena are refered to as anomalous transport in the literature.

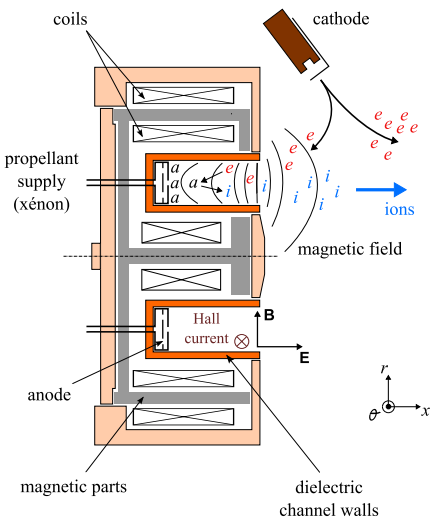

Figure 2.2: Schematic of a Hall thruster.

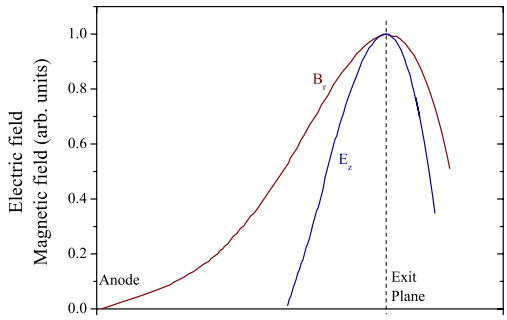

Figure 2.3: Typical Hall thruster radial magnetic field (red line) and axial electric field (blue line) along the channel length.

2.5 Description of different test benches

Different vacuum chambers have been used to obtain the experimental data presented in this work. A brief description of the main characteristics of each test bench is given in this section.

2.5.1 PIVOINE-2g

The PIVOINE-2g (Propulsion Ionique pour les Vols Orbitaux - Interprétation et Nouvelles Expérinces, 2g stands for 2nd generation) test bench is a 4 m long by 2.2 m in diameter vacuum chamber equipped with cryogenic pumps. It has a maximum pumping speed in xenon of 210 000 l/s (40 K) providing a background pressure of about 10^{-5} mbar-Xe for a broad range of operating conditions (1-50 mg/s in Xe and a power range from 100 W up to 20 kW). The multistage pumping system is composed of a primary pump, a 5000 l/s turbomolecular pump, for removal of light molecular gases like hydrogen and nitrogen that are not pumped by the cryosurfaces, as well as 2 cryogenic stages located at the back of the tank. The first stage allows a pumping speed of 70 000 l/s to be reached. The second stage adds up a 140 000 l/s pumping capacity. In addition a 16 K cryo-panel is employed for removal of nitrogen and oxygen. The cryopumps are LN2-cooled and shielded from ion beam by means of water-cooled graphite tiles. The tank pressure is measured with a cold cathode ionization gauge. The residual gas composition is continuously analyzed and monitored with a quadrupolar mass spectrometer.
Thrusters are mounted onto a pendulum-type thrust stand that can measure a thrust level between 5 mN and 5 N. Calibration is realized in situ by means of a set of balance-weights. The thrust stand is placed at the end of an arm that can be moved along the chamber axis. A lock-chamber is used when introducing the thruster in or removing it out from the test chamber in order not to modify the vacuum quality. During thruster firing, parameters like discharge current and voltage, coil current, gas flow rates, backpressure and so on are continuously measured and recorded. Several access windows and viewports allow setup of additional diagnostic

tools. A second movable arm is also available for exploration of the ion beam properties using electrostatic probes (e.g. determination of electron properties with Langmuir probes). This second arm moves perpendicular to the thruster axis. A second lock-chamber is used for the diagnostic arm.

2.5.2 NExET

A new vacuum chamber NExET (New EXperiments on Electric Thrusters) has been installed at the ICARE laboratory in 2008. The stainless-steel vacuum chamber is 1.8 m long and 0.8 m in diameter. It is equipped with a multistage pumping system. This system is composed of a large dry pump (400 m^3/h), a 200 l/s turbomolecular pump to evacuate light gases and a cryogenic pump with a typical surface temperature of 35 K (8000 l/s) to get rid of the propellant such as xenon and krypton. A background pressure of 2×10^{-5} mbar is achieved with a xenon mass flow rate of 1.0 mg/s and an input power of 250 W [11]. The back part of the chamber is water-cooled and protected with graphite tiles to absorb a part of the ion beam energy and therefore reducing the thermal load onto the cryosurface. The chamber is equipped with different observation windows, diagnostic ports as well as electrical and gas feed-throughs. The thruster can be mounted onto two moving stages to allow a displacement in both the axial (x) and radial (y) direction. The interior of the test bench is easy to access thanks to a large front door.

2.5.3 CORONA

The CORONA vacuum chamber is located in the ESA Propulsion Laboratory (EPL) at ESA-ESTEC in Noordwijk. The main chamber is 5 m long and 2 m in diameter, the hatch is 1.5 m long and 1 m in diameter. The hatch can be isolated from the main chamber by a gate valve in order to access the thruster without opening the main chamber. The test bench is equipped with a multi-stage pumping system composed of 4 oil-free rotary pumps (30 m^3/h), two turbomolecular pumps (1000 respectively 2000 l/s) as well as 4 cryogenic heads and a cryogenic pump. The total pumping speed is about 80 000 l/s of Xe and a pressure of below 1×10^{-4} mbar can be obtained with a gas flow rate of 5 mg/s [12]. Thrust measurements of low-power Hall thrusters can be carried out using the Low Thrust Balance (LTB) designed by ALTA. The thrust balance is based on an inverted pendulum with a laser displacement probe. LTB can measure thrust in the range from 2 to 40 mN with an accuracy of about 2 % [13]. CORONA is also equipped with a vertical diagnostic arm. Different probes (Faraday probe and Retarding Potential Analyzer) can be installed every 2.5 ° on this arm. The arm is moved by means of a stepper motor which transmits rotation to the arm via a gear mechanism. This allows a complete 180 ° scan of the plasma far-field plume at a distance of about 80 cm downstream the thruster exit plane [14].

2.6 Description of different types of Hall thrusters

Experimental data presented in this work has been obtained from three different Hall thrusters. A brief description of the three thrusters is given in this section.

Figure 2.4: Picture of the PPS®100-ML.

Figure 2.5: Picture of the PPS®1350.

2.6.1 PPS®100-ML

The PPS®100-ML is a 1.5 kW-class Hall thruster with a discharge chamber outer diameter of 100 mm [7]. The magnetic field is usually generated by 5 magnetic coils (4 external and 1 internal coil), but a version with permanent magnets instead of coils is also available [15]. The magnetic field topology with permanent magnets is fairly the same than the one of the original version with a coil current of 4.5 A. The thruster delivers a thrust of about 80 mN when operated at 300 V and 5 mg/s. The channel walls are made of $BNSiO_2$. A picture of the PPS®100-ML thruster is shown in Fig. 2.4.

2.6.2 PPS®1350-ML

The PPS®1350-ML is a 1.5 kW-class Hall thruster. It is a laboratory model of the PPS®1350 thruster developed by Snecma and used as primary propulsion device for the orbit transfer on ESA's SMART-1 probe [8]. The PPS®1350-ML delivers a thrust of 83 mN when operated at 350 V and 5 mg/s. A picture of the PPS®1350 is shown in Fig. 2.5. The major difference compared to the PPS®100-ML is that the PPS®1350-ML has two additional coils located at the back of the channel. These two coils can be used to modify the position of the zero magnetic field and the magnetic field gradients inside the discharge chamber.

2.6.3 PPI

The PPI thruster (french acronym for "**P**etit **P**ropulseur **I**nnovant") is a 200 W type Hall thruster able to deliver a thrust of 10 mN when operated at 250 V and 1.0 mg/s xenon mass flow rate [16]. This thruster was originally designed by the GEMaC team in Versailles [17, 18]. A picture of the PPI thruster is shown in Fig. 2.6. This thruster exhibits three interesting features that makes it highly versatile. First, the magnetic field is generated by way of small SmCo magnets brought together inside rings located on either side of the channel walls. A soft iron magnetic circuit with a back gap permits to drive the magnetic flux in order to obtain the desired topology. No magnetic screen is used. Second, the propellant gas is injected homogeneously inside the channel using a porous ceramic instead of a classical metal hollow gas injector. A stainless-steel ring placed at the back of the channel serves as anode. Third,

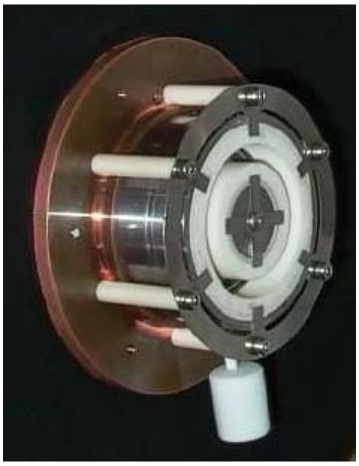

Figure 2.6: Picture of the low-power permanent magnet PPI Hall thruster.

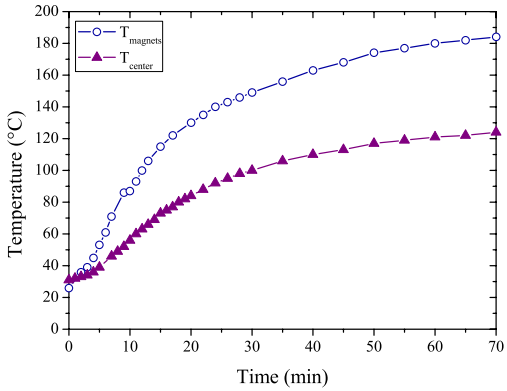

Figure 2.7: Temperatures of the 200 W-class PPI Hall thruster (S_0 configuration) operating at 200 V and 1.0 mg/s in the NExET test bench.

a central copper heat drain is employed to evacuate heat towards a radiator placed behind the thruster. The radiator, which is a thin copper disk of 25 cm in diameter, is necessary to diminish the thermal load onto dielectric walls and magnets. During operation the temperature of the thruster center T_{center} as well as the temperature of the magnets $T_{magnets}$ is measured by means of thermocouples. The time evolution of the temperatures for the thruster operating at 220 W (200 V, 1.0 mg/s) is shown in Fig. 2.7. As can be seen, the steady-state temperature of the thruster center is about 125 °C and the steady-state temperature of the magnets is about 185 °C, which is well below the SmCo magnet Curie point. The channel walls are made of alumina compound (Al_2O_3). A heated cathode with a LaB_6 insert, provided by MIREA, is used with a cathode mass flow rate of 0.2 mg/s. Xenon and krypton were used as working gases for the thruster and the cathode. Figures 2.8 and 2.9 show the 2 different configurations of the PPI thruster (see Chapter 4) operating with xenon in the NExET chamber.

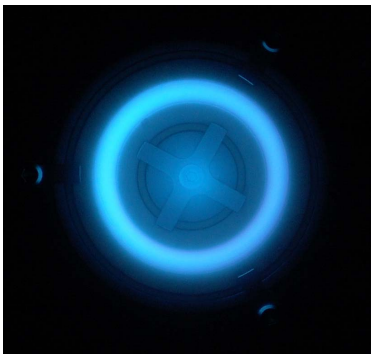

Figure 2.8: The 200 W-class PPI Hall thruster (S_0 configuration) operating at 200 V and 1.0 mg/s in the NExET test bench (front view).

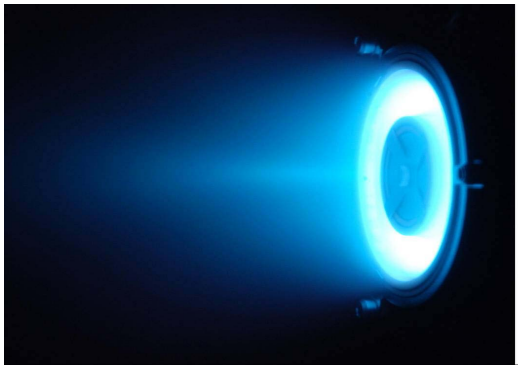

Figure 2.9: The 200 W-class PPI Hall thruster ($2S_0$ configuration) operating at 200 V and 1.0 mg/s in the NExET test bench (side view).

Chapter 3

Scaling laws[1]

3.1 Introduction

Hall thrusters are currently employed for geosynchronous satellite attitude correction and station keeping. They also appear as good candidates for the primary propulsion engine of space probes, as demonstrated by the successful SMART-1 Moon solar-powered mission [8]. Space agencies together with satellite manufacturers and users nonetheless envisage new fields of application for electric propulsion systems that require low and high power devices. Low power Hall thrusters ($\sim$100 W) are well suited for drag compensation of observation satellites that operate on a low-altitude orbit in the Earth atmosphere as well as for trajectory correction of small platforms and microsatellite constellations. The use of high power ($\sim$5 kW) Hall thrusters for orbit raising and orbit topping maneuvers of communication satellites would offer significant benefits in terms of launch mass, payload mass and operational lifetime. In addition, journeys towards far-off planets and asteroids with large and heavy robotic probes as well as Moon and Mars cargo missions necessitate to build thrusters with an input power in the range of 10 - 100 kW. In view of the projects demand, it appears necessary to expand the operating envelope of the existing technology (10 cm, 1.5 kW) to achieve the required performance level.
A non-trivial question then arises: how to extrapolate the design and architecture of currently existing Hall thrusters towards different scales and different operating conditions? In other words, what are the scaling relations that connect Hall thruster characteristic dimensions with operating parameters and performances? To date, scaling laws for magnetized plasmas, based for example on dimensionless quantities, still remain to be precisely identified even after decades of active researches conducted all around the world. The first goal of this work is to elaborate simple scaling laws for a Hall thrusters allowing to get information, at least on a qualitative order, on the relationships between dimensions, performance level and input power.
In a second step, the scaling relations and the sizing methodology previously worked out are refined by taking into account an atom density constraint inside the channel and the fact that the channel mean diameter d is proportional to the channel width h for standard Hall thrusters. Furthermore, we study the effect of reducing the number of simplifying assumptions. A new set of scaling relations is then given when considering the evolution of the electron temperature T_e, the voltage losses Δ and the fraction of doubly charged ions f_{2+} as a function of the discharge voltage U_d as well as the ion beam divergence. The two sets of scaling relations obtained under high and low assumptions are subsequently used to determine the geometry and the operating parameters of a 20 kW-class Hall thruster.

[1] Adapted from:
K. Dannenmayer, S. Mazouffre, *J. Propul. Power* **27**, 236 (2011)

3.2 Review of previous works

Scaling relations that govern the physical properties, the accelerating ability as well as propellant and energy consumption of Hall thrusters have been extensively investigated by numerous authors since the period of development of Hall thrusters in the 70's. In spite of decades of research on this subject, the assessment of scaling relations is still a topic of interest as various methodologies and results exist. Therefore, before describing the approach associated with this study as well as its outcomes, it is worth briefly reviewing works carried out on this topic during the past few years.

According to the pioneer works of the Russian physicist A. Morozov [19], in order to derive scaling relations, it is necessary to find a similarity criterion, or a set of criteria, that warrant the underlying physical processes to stay unchanged whatever the thruster. This principle states that the properties of thrusters with a different geometry are linked by way of scaling relations only if a sufficiently large number of dimensionless similarity criteria coincide. The complete set of similarity criteria has not yet been found, however, all works show that the *Melikov-Morozov criterion* has a strong impact on Hall thruster behavior and characteristics and it must always be taken into account. This criterion indicates that the ionization mean free path must be less than the channel length ($\lambda_i \ll L$). In addition to similarity criteria, the investigation of scaling laws for Hall thrusters necessitates to account for simplifying assumptions and physical constraints.

V. Zhurin and co-workers proposed a sizing method which is limited to the effects of changing either the channel width h or the channel mean diameter d [6]. The channel mean diameter being much larger than the channel width, variation of parameters in the radial direction are negligible. Furthermore, they considered a fixed discharge voltage. In order to obtain similar performances for two different thruster configurations, authors postulate that the ratio of the Larmor radius r_L, the mean free path λ and the channel length L to channel width h must stay the same for the two configurations. Using these criteria and a set of assumptions they demonstrate that the magnetic field strength is inversely proportional to the channel width, $B \propto 1/h$, whereas the discharge current and the propellant mass flow rate are proportional to the channel mean diameter, $I_d \propto d$ and $\dot{m} \propto d$.

It was demonstrated by V. Kim [20] that to reach a high level of efficiency it is not only necessary to ionize and accelerate ions but to accelerate them into the proper direction, hence the need for an optimized magnetic field topology. In short, for a Hall thruster with an optimized magnetic field map, there is a relationship between the acceleration layer length L_a and the magnetic layer characteristic size L_B and between L_a and h. The use of these similarity criteria, which include the magnetic field structure, permits to simplify the development of new Hall thruster models. V. Kim and co-workers also emphasize the fact that for a traditional Hall thruster design the Melikov-Morozov criterion must be fullfilled [21]. Moreover they give additional criteria about the geometry of thruster elements, i.e. the channel length L and mean diameter d are both proportional to the channel width h, that are equivalent to the ones given by V. Zhurin. There are two immediate consequences. First, the propellant mass flow density and the power density rise when the thruster size decreases, assuming a constant discharge voltage and a constant mass flow rate. Second, as the magnetic field strength is connected with the characteristic dimensions, notably the channel width, and with the operation mode,

the magnetic field magnitude must rise when the size reduces in order to keep comparable conditions.
The method presented by J. Ashkenazy et al. concerns low power scaling and it is based on the idea of a sufficient propellant utilization [22]. They show by means of a simplified analysis that a straightforward approach for scaling down the channel size results in a rise of power losses and a reduced overall efficiency. To avoid these effects, the acceleration region has to be scaled down along with the channel width and the magnetic field strength must be increased inversely proportional to the channel width.
M. Martinez-Sanchez et al. developed an approach for low-power thrusters that includes the use of reference points [23]. The goal is to achieve a reduction in the thruster length scale while preserving both the thrust efficiency and the specific impulse. The main result of their study is that the propellant mass flow rate and the applied power scale as the channel length, $\dot{m} \propto L$ and $P \propto L$, whereas the magnetic field strength is in inverse proportion to the latter, $B \propto 1/L$. This scaling method allows to calculate the channel size and the performances of a small thruster with a given input power provided that a well-known thruster is used as a reference.
Daren Yu and his team suggested an improvement of the existing scaling theory by introducing a scaling index variable [24]. They assume that the electron temperature and the discharge voltage are constant, that the ratio λ_i/L is constant and that the geometric similarity is given by r/R=constant and $R^{2-\xi}/L$=constant, where R and r are the channel outer respectively inner radius and ξ represents a scaling index variable. They show by way of a comparison of experimental data with numerical outcomes for different values of ξ, that results obtained from their scaling theory agree well with the experimental data for ξ=2. Therefore they deduce that the number density n is constant, whereas the mass flow rate $\dot{m}$, the input power P, the thrust T and the discharge current I_d are proportional to the square of the outer channel radius R.
Finally, the team led by M. Andrenucci advised to employ an analytical model coupled to an existing Hall thruster database [25]. This scaling methodology aims to provide design options for high power thrusters. The idea is to create a vector of fundamental parameters defining the thruster geometry and its performances. This vector is composed of three geometric parameters (L, h and d), the gas density in the injection plane and the applied discharge voltage U_d. A scaling matrix derived from the Hall thruster physical principles allows to obtain new thruster characteristics on the basis of a reference thruster.
In a recent article [26], we put forward an original way to extrapolate Hall thruster geometry (L, h and d quantities) and magnetic field strength towards both the low and high power ranges. The approach is based on the combination of a set of scaling relations that are extracted from fundamental equations along with a vast body of existing data. Strong assumptions are made to define the working frame: Among others, quantities are steady and homogeneous in the plasma, the applied potential energy is fully converted into axial kinetic energy and all xenon ions are singly-charged. Our study indicates both the input power and the thrust scale as hd/L whereas the magnetic field intensity varies as $1/hd$. Besides, realistic constraints on the performance level and on the thermal load are added in order to limit the set of possible values for the characteristic sizes.

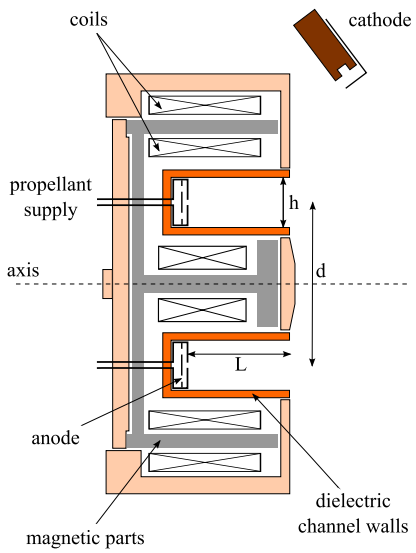

Figure 3.1: Cross-section view of a Hall thruster showing the main components. The three characteristic dimensions L, h and d are also indicated.

3.3 Set of governing relations and scaling

3.3.1 Ionization and plasma containment

The geometry of a Hall thruster is defined by three characteristic dimensions, namely: the discharge channel length L, the channel mean diameter $d = \frac{1}{2}(d_{ext} + d_{int})$ and the channel width h. For the sake of clarity, the three dimensions are shown in Fig. 3.1. As we will see, the thruster geometry depends upon a set of operating parameters such as the discharge voltage U_d and the propellant mass flow rate $\dot{m}_n$, as well as upon the magnetic field strength B.

A necessary first step in order to determine scaling relations for Hall thrusters does consist in finding some critical parameters as well as in defining similarity criteria based on the current knowledge and understanding of the physics of Hall thrusters. Therefore, processes at the origin of thrust must be considered and critically examined. In the remainder of this paragraph, all quantities are assumed to be steady in time and uniform in space in order to permit the derivation of necessary equations.

3.3.1.1 Propellant Ionization

The first relationship reflecting the impact of the thruster scale on its performance is the relationship between the discharge channel length L and the ionization mean free path λ_i. To ensure a sufficient ionization of the gas, atoms must stay long enough inside the channel. Differently said, it is necessary to satisfy the Melikov-Morozov criterion:

$$\lambda_i \ll L. \tag{3.1}$$

The ionization frequency that originates from electron-atom impacts reads:

$$\nu_i = n_n \langle \sigma_i(v_e)\, v_e \rangle \approx n_n\, \sigma_i(T_e) \sqrt{\frac{8 k_B T_e}{\pi m_e}}, \tag{3.2}$$

where σ_i is the ionization cross section, T_e the electron temperature and k_B the Boltzmann constant. The ionization length, which corresponds to the mean distance an atom can travel before being ionized, can be formulated as the ratio v_n/ν_i in a first order approximation. Therefore the Melikov-Morozov criterion can be expressed as:

$$\lambda_i = \frac{v_n(T_n)}{n_n\, \sigma_i(T_e)\, v_e(T_e)} \ll L. \tag{3.3}$$

3.3.1.2 Electron confinement

The magnetic field strength in a Hall thruster is such that electrons are magnetized and ions are not, or at least weakly, magnetized. Since ions are much heavier than electrons, the following criterion must be fulfilled [20]:

$$r_{Le} \ll L. \tag{3.4}$$

The definition of the electron Larmor radius is:

$$r_{Le} = \frac{m_e v_e(T_e)}{eB}. \tag{3.5}$$

Keeping the ratio of r_{Le} to L constant, the following relationship can be established:

$$B \propto \frac{m_e}{e} \frac{v_e(T_e)}{L}. \tag{3.6}$$

The relation (3.6) between the magnetic field strength B and the channel length L has already been mentioned by M. Martinez-Sanchez [23].
A second constraint can be established due to the fact that the electron gyroperiod τ_{ce} in the magnetic barrier must be much shorter than the time between two consecutive electron-atom collisions τ_{en} to minimize electron diffusion losses:

$$\frac{\tau_{en}}{\tau_{ce}} = \frac{\omega_{ce}}{\nu_{en}} = \frac{e\,B}{m_e n_n \sigma_{en} v_e} \gg 1, \tag{3.7}$$

where the electron cyclotron frequency is $\omega_{ce} = eB/m_e$ and the electron-atom collision frequency is $\nu_{en} = n_n \sigma_{en} v_e$ with σ_{en} being the electron-atom momentum exchange cross section [27]. This point warrants electrons are efficiently trapped inside the magnetic field of a Hall thruster, which is necessary to produce a high electric field and to favor ionization of the seeded gas. In fact, τ_{en} is so long in a Hall thruster that anomalous electron transport perpendicular to the magnetic field lines must be put forwards to correctly explain the observed properties and the magnitude of measured quantities [6, 19, 28]. Equation (3.7) implies:

$$B \propto \frac{m_e}{e} \sigma_{en}(T_n, T_e) v_e(T_e) n_n. \tag{3.8}$$

This equation indicates that B depends upon the gas density n_n in compliance with the fact that plasma confinement depends on collision events with neutrals. For a given thruster, the

higher the gas density inside the channel, i.e. the larger the propellant flow, the stronger the magnetic field must be. Aforementioned equation also shows it is necessary to increase B when the applied voltage is ramped up as the electron temperature augments with the voltage, see section 3.7.

3.3.1.3 Neutral particle density

The Melikov-Morozov criterion, see Eq. (3.3), can be used to link the propellant atom density n_n to the channel length L when keeping the ratio λ_i/L constant for all thrusters. However, two other hypothesis are necessary. The propellant speed v_n and the electron temperature T_e do not depend upon the thruster operating conditions. Whereas the first assumption is reasonable, see e.g. [29], the second one is only valid at a fixed discharge voltage as discussed in section 3.7. Thus, Eq. (3.3) leads to:

$$L \propto \frac{1}{n_n}. \tag{3.9}$$

The relation (3.9) is similar to the one developed before by e.g. V. Zhurin and M. Martinez-Sanchez [6, 23]. It tells the channel length can be decreased when the gas density rises as ionization is favored.
Another relation between n_n and Hall thruster dimensions can be established when considering the propellant mass flow rate passing through the anode $\dot{m}_n$. The mass flow rate can be decomposed into the product of several terms:

$$\dot{m}_n = n_n \cdot m_n \cdot v_n \cdot A. \tag{3.10}$$

The annular channel cross section A is given by:

$$A = \frac{\pi}{4}(d_{ext}^2 - d_{int}^2) = \frac{\pi}{4}\underbrace{(d_{ext} + d_{int})}_{2d}\underbrace{(d_{ext} - d_{int})}_{2h} = \pi h d, \tag{3.11}$$

We can therefore consider that for a constant atom temperature:

$$n_n \propto \frac{\dot{m}_n}{hd}. \tag{3.12}$$

This relationship between the atom density and the thruster dimensions h and d has never been mentioned previously, as authors never considered two sizes at the same time. In order to keep the physical processes at work in a Hall thruster unchanged, to warrant a high efficiency and to limit the thermal load as well as the channel wall wear, the number densities of electrons and atoms must stay roughly fixed inside the thruster channel whatever the input power, as we will see in a following paragraph.

3.3.2 Relationship between performances and dimensions

The definition of the thrust T, the specific impulse I_{sp}, the various currents, the thrust efficiency η_T and the anode efficiency η_a can be found in many papers and in most textbooks about electric propulsion (see e.g. [5] and [30]). Here we use common definitions in order to determine the relationships between Hall thruster functioning parameters, performances and channel characteristic dimensions.

3.3.2.1 Thrust

The thrust is the force supplied by the engine to the spacecraft. It is given by the time rate of change of the momentum since the spacecraft mass varies with time due to propellant consumption. In a Hall thruster, ions originate in the ionization of the propellant gas and they are accelerated by an electric field within the plasma. The thrust therefore results from the electrostatic acceleration of the ions:

$$T = \dot{m}_i \bar{v}_i = \alpha \, \dot{m}_n \, \bar{v}_i, \tag{3.13}$$

where the coefficient α stands for the fraction of propellant atoms that are converted into ions, whatever the electric charge. For conventional Hall thrusters, the typical value of α is around 0.9 with xenon when only singly-charged ions are accounted for. Nonetheless, the value of α depends on the discharge voltage [26]. Moreover it is known that smaller thrusters have a lower propellant conversion efficiency. Notwithstanding the fact that ions are not magnetized in a Hall thruster, the presence of a transverse magnetic field is responsible for a large azimuthal drift current, also called Hall current. Indeed, electrons in the plasma feel an $\mathbf{E} \times \mathbf{B}$ drift, hence they move perpendicular to the electric and magnetic field [6, 5]. The Lorentz force electrons experience is equal to the electrostatic force on the ions, hence:

$$T = \iiint_V \mathbf{j}_{\text{Hall}} \times \mathbf{B} \, dV \tag{3.14}$$

$$= 2\pi r \iint_S \mathbf{j}_{\text{Hall}} \times \mathbf{B} \, dS \tag{3.15}$$

$$= \pi \, d \, I_{\text{Hall}} \, B, \tag{3.16}$$

where j_{Hall} is the Hall current density and I_{Hall} the Hall current. To sum up, in a Hall thruster, the thrust is transferred from the ion flow to the thruster body through the magnetic field.
When analyzing the thrust generation in a Hall thruster, one must take into account the presence of multiply charged ion species, especially doubly-charged ions [31] of which the fraction is significant with xenon. If the beam contains the two types of ions, the ion mass flow rate is then:

$$\dot{m}_i = \frac{m_n}{e} I^+ + \frac{m_n}{2e} I^{2+}, \tag{3.17}$$

where the superscript indicates the electrical charge. The thrust can in fact be split into a finite series of elementary terms, each of them corresponding to a given ion species:

$$T = m_n \sum_{k=1}^{Z} \frac{I^{k+} \, \bar{v}^{k+}}{ke}, \tag{3.18}$$

where Z is the atomic number. Using the preceding definition for $\dot{m}_i$, the thrust corrected for the multiple species and for the ion beam divergence can then be written down in the simple form:

$$T = \gamma \, \theta_d \, \dot{m}_i \sqrt{\frac{2e}{m_n}} \sqrt{U_d - \Delta} = \alpha \, \gamma \, \theta_d \, \dot{m}_n \sqrt{\frac{2e}{m_n}} \sqrt{U_d - \Delta}, \tag{3.19}$$

where γ is the multiply charged ion correction factor, θ_d is the beam divergence correction factor and Δ represent the voltage losses. Both correction factors naturally depend on the thruster

operating conditions. If one considers solely singly and doubly-charged ions, the multiply-charged ion correction factor γ reads:

$$\gamma = \frac{1 + \frac{I^{2+}}{\sqrt{2}\,I^{+}}}{1 + \frac{I^{2+}}{2\,I^{+}}}, \quad \gamma = \frac{1 + \frac{f_{2+}}{\sqrt{2}(1-f_{2+})}}{1 + \frac{f_{2+}}{2(1-f_{2+})}}, \tag{3.20}$$

with f_{2+} being the fraction of doubly-charged ions. The θ_d factor is described in detail in reference [5]. Here, the quantity $(U_d - \Delta)$ is the potential ions really experience. The preceding equation is obtained under the assumption that all types of ions are produced at the same location and therefore undergo the same potential drop. In other words, the voltage losses for ions are independent of the charge number. In that case, the mean ion exhaust velocity can be defined as [19]:

$$\bar{v_i} = \sqrt{\frac{2e}{m_i}(U_d - \Delta)}. \tag{3.21}$$

Combining Eqs. (3.10), (3.11) and (3.19) yields an expression for the thrust as a function of the channel sizes:

$$T \propto \alpha\,\gamma\,\theta_d\,n_n\,v_n(T_n)\,\sqrt{U_d - \Delta}\,hd. \tag{3.22}$$

As we have shown previously with Eq. (3.9), varying the atom density n_n corresponds to varying the channel length the opposite way. Therefore, a general relationship between the thrust and Hall thruster characteristic sizes reads:

$$T \propto \alpha\,\gamma\,\theta_d\,v_n(T_n)\,\frac{1}{L}\,\sqrt{U_d - \Delta}\,hd. \tag{3.23}$$

3.3.2.2 Specific impulse

The specific impulse is a way to describe the efficiency of rocket and spacecraft engines. It represents the change in momentum per unit of propellant. Essentially, the higher the specific impulse, the less propellant is required to gain a given amount of momentum. In this regard a propulsion method is more propellant-efficient if the specific impulse is higher. The specific impulse is defined by the following equation:

$$I_{sp} = \frac{T}{\dot{m}\,g_0} \approx \alpha\,\gamma\,\theta_d\,\frac{\bar{v_i}}{g_0}, \tag{3.24}$$

where g_0 is the standard gravity at Earth's surface. Here, $\dot{m}$ refers to the total gas mass flow rate, that means the anode as well as the cathode gas flow rate. When solely the anode mass flow rate is used, strictly speaking the I_{sp} then corresponds to the anode I_{sp}. According to Eq. (3.19), in a first order approximation, the specific impulse is not a function of the thruster sizes [26]:

$$I_{sp} \propto \sqrt{U_d - \Delta}. \tag{3.25}$$

It is solely proportional to the square root of the discharge voltage. Note that for a parallel beam of singly-charged ion species under the condition of full ionization of the supplied propellant, the specific impulse is simply given by the ratio $\bar{v_i}/g_0$. This expression is often found in books and articles.

3.3.2.3 Electrical power

The discharge current I_d is the sum of the ion current I_i in the beam and the electron current I_e flowing across the channel outlet: $I_d = I_i + I_e$. Neglecting the electronic part, which is a small fraction of the ionic part (typically 10-20 %), one can write:

$$I_d \approx I_i = \sum_{k=1}^{Z} I^{k+}. \tag{3.26}$$

The discharge current can therefore be expressed in terms of propellant mass flow rate:

$$I_d \approx \frac{e}{m_n}\,\gamma'\,\dot{m}_i = \frac{e}{m_n}\,\gamma'\,\alpha\,\dot{m}_n \tag{3.27}$$

If again solely singly and doubly-charged ions are taken into account, the correction factor γ' is given by:

$$\gamma' = \frac{1+\frac{I^{2+}}{I^{+}}}{1+\frac{I^{2+}}{2\,I^{+}}}, \quad \gamma' = \frac{1+\frac{f_{2+}}{1-f_{2+}}}{1+\frac{f_{2+}}{2(1-f_{2+})}}. \tag{3.28}$$

Substituting Eq. (3.10) into previous equation gives:

$$I_d \approx \pi\,e\,\gamma'\,\alpha\,n_n\,v_n(T_n)\,hd. \tag{3.29}$$

Finally, from the relation between the gas density and the channel sizes, one finds:

$$I_d \propto \gamma'\,\alpha\,v_n(T_n)\,\frac{hd}{L}. \tag{3.30}$$

As a direct consequence, the input electrical discharge power is:

$$P = U_d\,I_d \tag{3.31}$$

$$\propto \gamma'\,\alpha\,v_n(T_n)\,\frac{hd}{L}\,U_d. \tag{3.32}$$

It is worth noticing that for a Hall thruster, the thrust-to-power ratio is not linked to the sizes; it solely depends upon the applied voltage. Voltage losses are always low in comparison with the applied voltage, $\Delta \ll U_d$, hence the thrust per unit input power is:

$$\frac{T}{P} \propto \frac{1}{\sqrt{U_d}} \propto \frac{1}{I_{sp}}. \tag{3.33}$$

This last equation shows that for a given input power, increasing the specific impulse reduces the thrust that can be produced.
Preceding relations between the performances and the dimensions are in agreement with those described by Daren et al. [24]. If one considers, like they do, a constant gas density n_n, a constant discharge voltage U_d and a geometric similarity such as $R \propto r$, it appears that the thrust, the electrical power and the discharge current vary as the square of the channel mean diameter.

3.3.2.4 Efficiency

The total efficiency, or thrust efficiency, of a Hall thruster is defined as the ratio of the mechanical power to the overall electrical power [5]. It reads:

$$\eta_T = \frac{T^2}{2\dot{m}P_{in}}. \tag{3.34}$$

The mass flow rate $\dot{m}$ accounts for both the anode and the cathode gas flow rate. The total power P_{in} comprises the discharge power P as well as the power dissipated into the coils and for cathode heating. As the last two quantities are much below the discharge power, the thrust efficiency is often given by:

$$\eta_T = \frac{T^2}{2\dot{m}U_d I_d}. \tag{3.35}$$

In this work, only the gas flowing through the injector is considered. The efficiency is then expressed as anode efficiency:

$$\eta_a = \frac{T^2}{2\dot{m}_n U_d I_d}. \tag{3.36}$$

Using the set of available equations for all terms, the anode efficiency appears not to be a function of the Hall thruster channel dimensions:

$$\eta_a \propto \alpha\, \theta_d^2 \frac{\gamma^2}{\gamma'} \frac{U_d - \Delta}{U_d} \neq f(h, d, L). \tag{3.37}$$

This striking result actually originates from approximations of our model. Especially, the propellant conversion efficiency α and the voltage losses Δ are said not to change with the geometry. It is well known, however, that efficiency has a strong dependence on thruster size: the efficiency is better when the thruster is larger. This fact is directly linked to the volume-to-surface ratio: plasma is produced in volume (so the thrust) and energy is lost on surfaces (i.e. channel walls) by way of particle bombardment and recombination. Neglecting losses at the channel back, the ratio $\frac{V}{S}$ is equal to $\frac{h}{2}$, which explains the gain in efficiency with the size.

3.4 Performance and geometry data

3.4.1 Description of the database

A thorough open literature search using a wide range of resources combined with data-gathering within the French research program on electric propulsion allowed us to create a large database on Hall thrusters. The database contains information about thruster geometry as well as performances, notably the thrust T, the specific impulse I_{sp} and the anode efficiency η_a for a series of 36 different single-stage Hall thrusters. The database also includes information about the magnetic field strength B, the discharge channel wall materials and the propellant gas. The entire database covers a vast range of input power that stretches from 10 W up to 50 kW and a large collection of data points in terms of applied discharge voltage and gas mass flow rate. A broad range of thrust level is covered, going from 0.4 mN with a micro Hall thruster up to

almost 3 N delivered by the high-power thruster developed at NASA. In this work, we focus on Hall thrusters equipped with BN-SiO_2 channel walls and operating with xenon as a propellant gas.
A part of the collected data in terms of performance level is displayed in Fig. 3.2 and in Fig. 3.3. For all thrusters, channel walls are made of BN-SiO_2 and the propellant gas is xenon. The thrusters used to construct the two figures are the following: a 4 mm in diameter micro-Hall thruster operating at 10-40 W [32], a laboratory model of the low power SPT20 thruster [33], a SPT50 thruster manufactured by the Kurchatov Institute [33], the 1.5 kW-class PPS®1350 Hall thruster developed and manufactured by Snecma [30], the 5 kW-class PPS®X000 thruster which is a laboratory version of the PPS®5000 technology demonstrator developed by Snecma [30], the 10 kW T220 designed and built by TRW and Space Power Inc. [34], as well as the 50 kW-class NASA-457M thruster [35]. The development of the thrust as a function of the discharge voltage is shown in Fig. 3.2 for the seven aforementioned Hall thrusters. The thrust of course increases with U_d. When operating at 0.2 mg/s and $U_d = 110$ V, the micro-thruster delivers 0.4 mN of thrust. On the opposite side of the thrust domain, the high-power NASA-457M thruster furnishes 970 mN of thrust when running at 35.2 mg/s and $U_d = 650$ V. The evolution of the specific impulse along with the applied voltage is shown in Fig. 3.3. The I_{sp} increases with U_d and all thrusters follow an identical trend but the micro-thruster. The Snecma-built PPS®1350 thruster delivers an I_{sp} above 3250 s when it is fired at 1000 V in a low gas flow regime, as can be seen in Fig. 3.3. The behavior of the anode thrust efficiency is shown in Fig. 3.3. For most thrusters, a maximum is reached around $U_d = 600$ V when the walls are made of BN-SiO_2 ceramic. This specific behavior is likely to originate from the wall material properties combined with a change of the plasma properties at high voltage [30]. The plot in Fig. 3.3 reveals that the efficiency increases with the thruster size, as discussed in the preceding section.

3.4.2 Dimensional trends in the data

It was shown in preceding studies that there is an optimum atom density n_n in order to keep the physical processes at work in a Hall thrusters unchanged, to warrant a high efficiency and to limit the thermal load as well as the wall wear [26, 36]. According to the large amount of gathered data, the critical value that turns out to guarantee a satisfying operation is $n_{n,c} = 1.2 \times 10^{19}\,\mathrm{m}^{-3}$. This is also the value that is commonly found in literature [5]. When $n_n < n_{n,c}$, the collision events between atoms and electrons are too scarce to maintain a high ionization level. This is in fact more complicated: As is shown in Chapter 4, if the channel width h is increased, a high ionization level, and therefore a high efficiency, can be maintained even if $n_n \ll n_{n,c}$. When $n_n > n_{n,c}$, the electron magnetic confinement is weakened due to the high electron-atoms collision frequency inside the channel. As the electron diffusion perpendicular to the magnetic field increases, the electric field expands and decreases in strength, the overlap between the ionization and acceleration layers stretches out and the electron back stream through the channel outlet rises. As a consequence, the thruster efficiency drops.
The existence of a critical atom density $n_{n,c}$ has one direct consequence. According to Eq. (3.10) and (3.11), the channel area is proportional to the gas flow rate: $hd \propto \dot{m}_n$. It confirms that when sizing a Hall thruster, the hd product must follow the evolution of the mass flow rate to

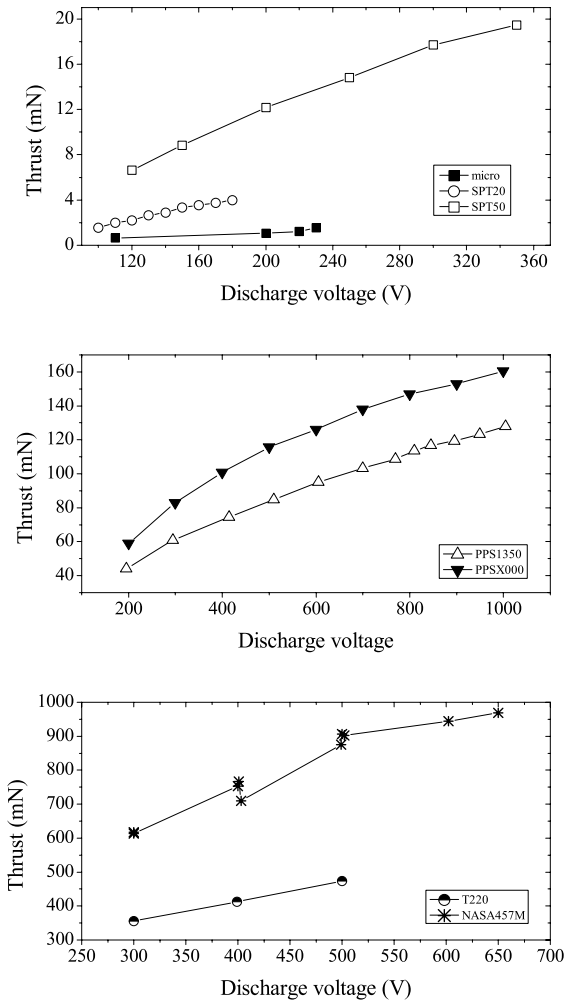

Figure 3.2: Thrust as a function of the discharge voltage for seven different Hall thrusters: micro-thruster (0.2 mg/s), SPT20 (0.472 mg/s), SPT50 (1.0 mg/s), PPS®1350 (3.5 mg/s), PPS®X000 (5.0 mg/s), T220 (19.4 mg/s) and NASA-457M (35.2 mg/s).

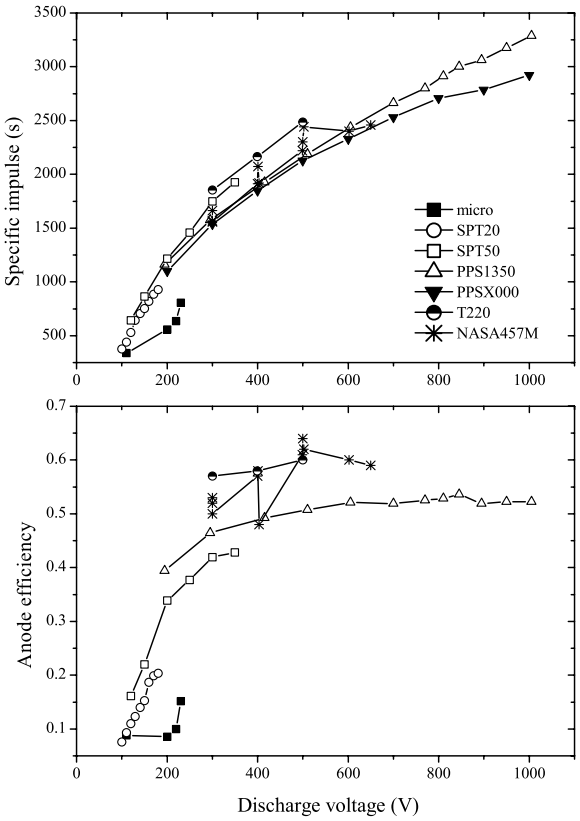

Figure 3.3: Upper graph: Specific impulse as a function of the discharge voltage for seven different Hall thrusters. Lower graph: Anode thrust efficiency as a function of discharge voltage. The xenon mass flow rate is: micro-thruster (0.2 mg/s), SPT20 (0.472 mg/s), SPT50 (1.0 mg/s), PPS®1350 (3.5 mg/s), PPS®X000 (5.0 mg/s), T220 (19.4 mg/s) and NASA-457M (35.2 mg/s).

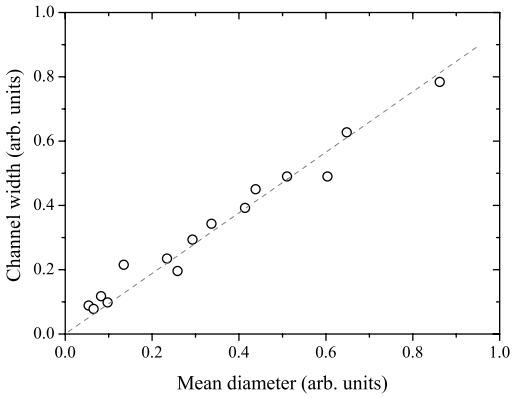

Figure 3.4: Channel width h as a function of the channel mean diameter d for a variety of Hall thrusters (sizes are in arbitrary units). The two dimensions d and h are proportional.

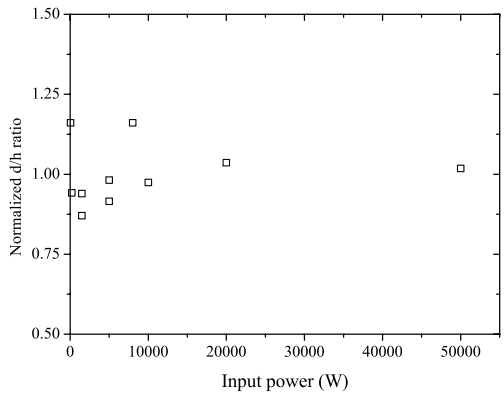

Figure 3.5: Normalized ratio of the channel mean diameter to the channel width as a function of the thruster input power.

ensure a high efficiency. In Fig. 3.4, the channel width is plotted as a function of the mean diameter for different thrusters covering a broad power range. As can be seen, the two dimensions h and d are in fact proportional. All existing Hall thrusters seem to have a similar d/h ratio whatever the input power. This surprising result could be explained by the fact that the geometry of all Hall thrusters is an extrapolation of a first Russian Hall thruster design. Fig. 3.5 shows the variation of ratio of the mean diameter to the channel width as a function of the normal input power for different thrusters. As can be seen the variation is quite low over a broad range of thruster scales.
Note that, due to $n_{n,c}$, there is also a critical electron density to ensure an efficient thruster operation. The ionization degree being roughly 10 % in a Hall thruster, the critical electron density lies around $10^{18}\,\mathrm{m}^{-3}$.

3.5 Scaling relations in the case of high assumptions

3.5.1 List of high simplifying assumptions

In order to simplify the determination of scaling relations, the following assumptions have been made first:

- All quantities are steady in time and uniform in space.
- The electron temperature is unchanging whatever the operating conditions.
- The propellant gas has a uniform and fixed temperature all over the channel, hence a constant propellant velocity.
- The potential energy is fully converted into kinetic energy and all ions experience the whole potential drop, of which the magnitude is U_d ($\Delta = 0$).

- Plasma-wall interactions are taken into account through heat load to the channel walls.
- The magnetic field is uniform; solely its value at the exit plane is considered. The channel length L is therefore the length of the region with magnetic field.
- Electron transport across the magnetic barrier is considered as classical: no anomalous transport is accounted for within the region of strong magnetic field.
- There are no multiply-charged ions in the plasma ($\gamma = \gamma' = 1$).
- A parallel monokinetic ion beam is produced, i.e. the plasma jet divergence is null (θ_d =1).

3.5.2 Set of scaling relations

The scaling relations are then obtained from equations derived in the Sec. 3.3.2 using the set of high assumptions. Therefore they read:

$$T = C_{T1}\,\dot{m}_n\,\sqrt{U_d}, \tag{3.38}$$
$$T = C_{T2}\,\sqrt{U_d}\,d^2, \tag{3.39}$$
$$I_{sp} = C_{I_{sp}}\,\sqrt{U_d}, \tag{3.40}$$
$$I_d = C_I\,d^2, \tag{3.41}$$
$$P = C_P\,U_d\,d^2, \tag{3.42}$$
$$L = C_L\,\lambda_i, \tag{3.43}$$

where C factors are proportionality coefficients. One should keep in mind that all equations are only valid when n_n is considered to be constant and equal to the critical density $n_{n,c}$. The validity of this set of relations can naturally be verified using the database. As an illustration, Fig. 3.6 displays the thrust as a function of the product $\sqrt{U_d}\,d^2$ for different thrusters. The dashed line represents a linear fit through all data points. For each thruster some values of T are chosen close to the point of normal operation.

3.5.3 Magnetic field

The magnetic field is treated separately in this work. The scaling relations for the magnetic field strength can be obtained using Eqs. (3.6), (3.8) and (3.12):

$$B \propto \dot{m}_n/h\,d \quad \text{and} \quad B \propto 1/L. \tag{3.44}$$

More general relations are obtained from the set of low assumptions, see chapter 3.7:

$$B \propto \dot{m}_n \frac{\sqrt{U_d}}{h\,d} \quad \text{and} \quad B \propto \frac{\sqrt{U_d}}{L}. \tag{3.45}$$

These relations indicate the magnetic field intensity has to be increased for a given thruster geometry when the discharge voltage rises and the propellant flow rate augments in order to keep a proper plasma confinement. Equations (3.44) and (3.45) also show that the magnetic field must be reduced when the thruster sizes increase while keeping the operating conditions

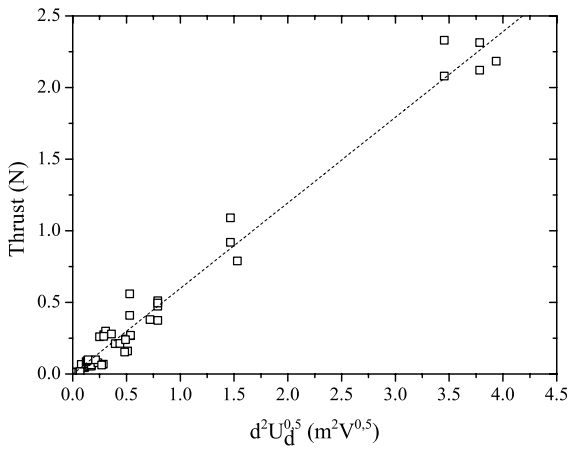

Figure 3.6: Thrust as function of $d^2U_d^{0.5}$ and the linear fit for different Hall thrusters (dashed line). For each thruster, some thrust values are chosen around the point of normal operation.

of the thruster constant. Nonetheless, according to our database, Hall thrusters operate with a magnetic field strength around typically 200 G whatever the input power. It is a consequence of the fact that most Hall thrusters operate nominally with a gas density inside the channel close to the critical atom density $n_{n,c}$. When the atom density is fixed the magnetic field does not depend anymore on the channel diameter d and width h (see Eq. (3.8)). It becomes merely a function of the channel length L. Naturally, not only the maximum of the magnetic field determines the thruster efficiency. The entire topology is of relevance. To account for gradients, curvature and position is out of the scope of this study. In the remainder of the paper, B is fixed to 200 G.

3.5.4 Assessment of proportionality coefficients

In order to assess the required thruster dimensions by way of a scaling method for an available input power or thrust level, it is thus necessary to know the proportionality coefficients C of the aforementioned equations. These coefficients can be determined either empirically, using the database, or analytically as explained in detail in a previous paper [26]. However, the empirical approach appears to be more accurate.
The empirically determined proportionality coefficients used for sizing a Hall thruster are not given in this contribution as it is sensitive information. Only the C_P and C_T coefficients can be derived from outcomes of this study. Yet, they are available in an article previously published by R. Jankovsky and co-workers [37].

3.6 Sizing of high-power Hall thrusters

3.6.1 Sizing methodology

The scaling process that consists in determining the thruster dimensions L, h and d must be carried out step by step. A detailed description of the procedure is given in another article [36]. For a fixed discharge voltage and a given thrust level, the standard procedure is the following:

1. The required mass flow rate is determined by means of Eq.(3.38).
2. The diameter d is obtained using Eq.(3.39).
3. The discharge current is given by Eq.(3.41).
4. The electric power reads: $P = I_d U_d$.
5. The size of h is found using the relationship: $h \propto d$.
6. The channel length L is assessed with Eq.(3.43).
7. At last, it should be verified that the neutral density n_n is close to $1.2\times10^{19}\,\mathrm{m}^{-3}$.

The channel length is the dimension that is the most difficult to determine as the proportionality coefficient C_L can vary over a broad range of values. As has been shown previously [26], the ratio between λ_i and L is not constant but it can vary for different thruster geometries, gas mass flow rates and discharge voltages. The Melikov-Morozov criterion can however be used to get a first estimate of the channel length by using a mean value for C_L determined from the database.
The procedure for a given input power is slightly different. The channel mean diameter can be determined from the given input power. Knowing the mean diameter d one can then determine the thrust level. The remaining thruster dimensions and operating parameters can then be calculated using the equations presented in section 3.5.

3.6.2 Thermal load

During thruster operation a certain percentage of the input power P is lost due to plasma-wall interactions. Indeed, as shown in [38], a relatively large energy flux q_p is deposited onto the discharge channel walls, mostly due to ion and electron bombardment, which results in a temperature increase of all thruster components. Naturally, there is a maximum amount of power that can be passed to the walls in order to limit the thermal load and to minimize the sputtering yield of the wall material. One can set a maximum wall temperature T_{max} above which an efficient operation of a Hall thruster is not possible. The temperature T_{max} therefore represents a thermal constraint and it must be accounted for when designing a thruster.
A semi-empirical time-dependent thermal model of a Hall thruster has been developed in order to determine the energy flux q_p from a measurement of the temporal evolution of the channel wall temperature [38]. Yet, this model can be used the other way, i.e. to determine the wall temperature from the applied power and the channel size. Here a simplified model of the thruster discharge chamber is used. The thermal enclosure is solely composed of the external

Dimensions	Parameter	Parameters	Performances
$d = 270\,mm$	$U_d = 500\,V$	$P = 17.2\,kW$	$T = 1\,N$
$L = 70\,mm$	$\dot{m} = 41.5\,mg/s$	$n_n = 1.3 \times 10^{19}\,m^{-3}$	$I_{sp} = 2456\,s$
	$I_d = 34.3\,A$	$T_{wall} = 670\,K$	$\eta = 70\,\%$

Table 3.1: Computed dimensions, parameters and performances evaluated from scaling relations for a 20 kW thruster delivering 1 N of thrust in the case of high hypothesis. The magnetic field strength is set to 200 G.

and the internal cylindrical walls, meaning that the anode and the rear part of the channel are not taken into account. A more detailed description of the thermal model geometry is given in a previous article [26].
In order to assess the channel wall temperature, only the steady-state wall temperature, i.e. the equilibrium temperature, is of relevance, meaning that the transient regime is ignored. The temperature gradient through the walls being weak, thermal exchanges can be modelled considering radiation as the dominant heat transfer mechanism [38]. Knowing the thruster dimensions L, h and d, the wall temperatures T_{int} and T_{ext} can be computed as a function of the power transferred to the channel walls by the plasma wall interactions P_{wall}. As was shown in a previous work [38], the ratio $\frac{P_{wall}}{P_{input}}$ is a function of the thruster size and it decreases when the size rises. The process of calculating the wall temperatures can be iterative: in case that the wall temperature is above T_{max}, the dimensions must be changed until the thermal constraint is satisfied. In this work the maximum temperature for the BN-SiO_2 walls is set to: $T_{max} = 900\,K$ in compliance with outcomes of a study on the thermal behavior of a Hall thruster performed a few years ago [39].

3.6.3 Design of a 20 kW Hall thruster

High power Hall thrusters in the range of 10 - 30 kW and able to deliver a thrust level around 1 N with a specific impulse of about 2500 s, are thought to be used as primary propulsion system for robotic space probes during interplanetary journeys [40, 41]. Such high-power Hall thrusters may also be of interest for orbit transfer maneuvers of large satellites. Only a few high-power prototypes have been developed in the world so far and a significant research effort on this specific technology is now appearing within Europe. For this reason, the sizing method based on the aforementioned widely applicable scaling relations in combination with our large database is employed to design a 20 kW-class thruster with a thrust level of 1 N.
The discharge voltage is fixed to $U_d = 500\,V$ in order to limit the thermal load and the secondary electron emission. Xenon is used as propellant gas. The thruster channel walls are assumed to be made of BN-SiO_2 ceramics. The wall losses for the thermal constraint are fixed to 4 % of the applied power.
The dimensions, the parameters and the estimated performances of a 20 kW-class Hall thruster are given in Table 3.1. The external wall temperature is $T_{ext} = 640\,K$ and the internal wall temperature is $T_{int} = 700\,K$.

3.7 Scaling relations with low assumptions

3.7.1 List of low assumptions

In order to investigate the influence of the different assumptions on the scaling model it is worth reducing the list of high assumptions given in paragraph 3.5. It has to be checked if the accuracy of the scaling relations can be improved by using less restrictive assumptions. In the remainder of the work the following assumptions are changed compared to the assumptions presented previously:

- The electron temperature is no longer considered to be constant but it is assumed to increase linearly with the discharge voltage
- The potential energy is not fully converted into kinetic energy, hence the voltage loss is assumed to be constant and equal 50 V
- Multiply-charged ions are taken into account (γ and $\gamma' \neq 1$), the fraction of doubly-charged ions is assumed to increase linearly with the voltage
- The ion beam is no longer considered to be parallel, the beam divergence angle is assumed to be constant and equal to 30 °

3.7.2 Available data and scaling relations

Former studies showed that the electron temperature is a function of the applied discharge voltage U_d [42]. Although experimental data about the electron temperature is rare in the literature, we tried to deduce a law on the evolution of T_e as a function of U_d. The electron temperature was measured by a floating movable probe [42] in hot and cold regimes in the plasma plume of different Hall thrusters. The different thrusters are: a 2 kW laboratory model with two different configurations, a narrow (Raitses narrow) and a wide (Raitses wide) one [42] and the NASA-173Mv1 with (NASA-173Mv1[1]) and without trim coil (NASA-173Mv1[2]) [43]. The maximum electron temperature, that is measured in the ionization region, for the different voltages and thrusters is shown in Fig. 3.7. The evolution of the electron temperature can be assumed to be linear for the different thrusters. A linear fit through all datapoints gives the following law for the evolution of T_e:

$$T_e = 0.12 \times U_d. \tag{3.46}$$

As can be seen, this linear fit is not quite precise but it is anyhow in good agreement with the common rule-of-thumb for Hall thrusters that the electron temperature is about one-tenth of the discharge voltage [5]. Therefore it will be used for the determination of the scaling relations. Note that here one assumes a single electron temperature whereas due to the peculiar properties of the crossed-field discharge of a Hall thruster one should take into account two electron temperature components: T_e along the magnetic field lines and T_e perpendicular to the field lines.

The voltage losses in a Hall thruster can be calculated from ion velocity measurements by Laser-Induced Fluorescence or by means of a retarding potential analyzer. Fig.3.8 shows the

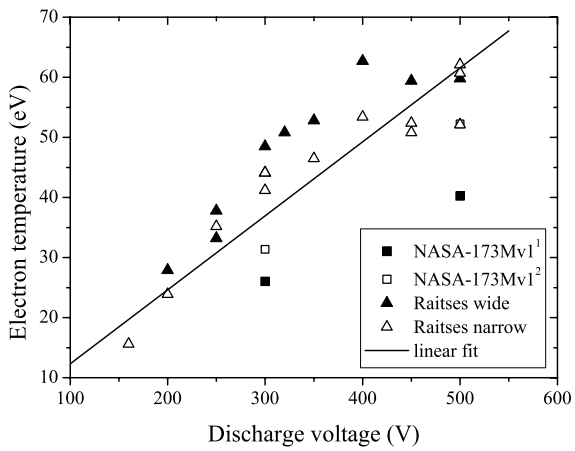

Figure 3.7: The maximum electron temperature T_e as a function of the discharge voltage for different Hall thrusters. The equation for the linear fit is: $T_e = 0.12\,U_d$.

evolution of of the loss term Δ as a function of the input power. The analyzed thrusters are a SPT100 at a mass flow rate of 2.5 mg/s and the PPS®X000-ML on the one hand for a voltage series at a constant mass flow rate of 6 mg/s and on the other hand for a mass flow series at a constant discharge voltage of 300 V. As can be seen in Fig. 3.8, voltage losses Δ are more or less fixed for a given thruster geometry and magnetic field map. There is no obvious relation between Δ and thruster size. For the determination of the scaling relations in this work, a constant value of $\Delta = 50\,V$ is used. The plasma plume of a Hall thruster contains a nontrivial amount of energetic, multiply-charged ions. These multiply-charged ions have a higher velocity than singly-charged ions when they are accelerated through the same potential drop, which results in a higher erosion rate. The production of multiply-charged ions is a loss mechanism for thrust, efficiency and mass flow utilization.
Fig. 3.9 shows the evolution of the fraction of doubly-charged ions Xe^{2+} as a function of the discharge voltage. The ion species fractions were measured in the NASA-173Mv2 plume far-field by means of an E×B probe [44]. The measurements were taken with the thruster operating at an anode mass flow rate of 10.0 mg/s. As can be seen in Fig. 3.9, the Xe^{2+} species fraction f_{2+} increased from 0.04 to 0.12. The evolution of the Xe^{2+} fraction as a function of the discharge voltage can be approximated by the following linear relation:

$$f_{Xe^{2+}} = 1.325 \times 10^{-4}\,U_d. \tag{3.47}$$

The beam divergence angle is set to 30°. Considering an ion beam that diverges uniformly upon the exit of the discharge channel, the beam divergence correction factor is: $\theta_d = cos(30°) = \frac{\sqrt{3}}{2}$. The scaling relations in the case of low assumptions can then be obtained from the equations in Sec. 3.3.2 in combination with the list of low assumptions mentioned above and the relations

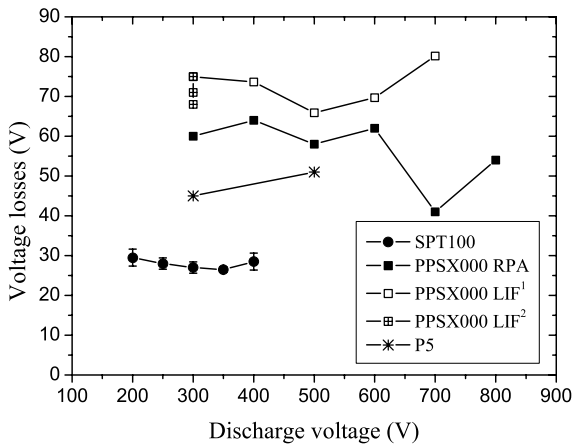

Figure 3.8: Voltage losses for the SPT100 and the PPS®X000-ML measured by RPA and LIF as a function of the discharge voltage. PPS®X000-ML LIF^1 operates at a constant mass flow rate ($\dot{m} = 6\,mg/s$), whereas PPS®X000-ML LIF^2 operates at a constant discharge voltage ($U_d = 300\,V$).

between T_e, Δ and f_{2+} and the discharge voltage U_d.

$$T = C^*_{T1}\,\gamma\,\theta_d\,\dot{m}_n\,\sqrt{U_d - \Delta}, \tag{3.48}$$

$$T = C^*_{T2}\,\gamma\,\theta_d\,\frac{1}{\sqrt{U_d}}\sqrt{U_d - \Delta}\,\frac{d^2}{L}, \tag{3.49}$$

$$I_{sp} = C^*_{I_{sp}}\gamma\,\theta_d\,\sqrt{U_d - \Delta}, \tag{3.50}$$

$$I_d = C^*_I\,\gamma'\,\frac{1}{\sqrt{U_d}}\frac{d^2}{L}, \tag{3.51}$$

$$P = C^*_P\gamma'\,\sqrt{U_d}\,\frac{d^2}{L}, \tag{3.52}$$

$$L = \frac{C^*_L}{\sqrt{U_d}}, \tag{3.53}$$

Again the validity of these relations can be verified using the database. Fig. 3.10 shows the thrust as a function of the product $\gamma\,\theta_d\,\frac{1}{\sqrt{U_d}}\sqrt{U_d - \Delta}\frac{d^2}{L}$ for different thrusters. The dashed line represents a linear fit through all datapoints. As can be seen in Fig. 3.10 the datapoints for the NASA-457M thruster are slightly above the datapoints for the other thrusters. The NASA-457M was in fact designed to be used either with xenon or with krypton. Krypton has a lower mass and a higher ionization energy than xenon, thus the discharge channel must be longer. The channel length of the NASA-457M is probably a trade-off for the two propellants.

3.7.3 Sizing of a 20 kW Hall thruster

The scaling relations developed using the low assumptions are used for the design of a 20 kW-class Hall thrusters in order to be able to compare the outcomes from the two sizing methods

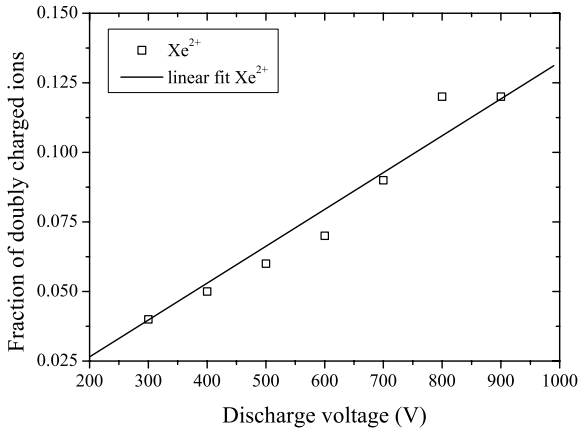

Figure 3.9: Fraction of doubly charged ions as a function of the discharge voltage for the NASA-173Mv2 at a mass flow rate of 10 mg/s

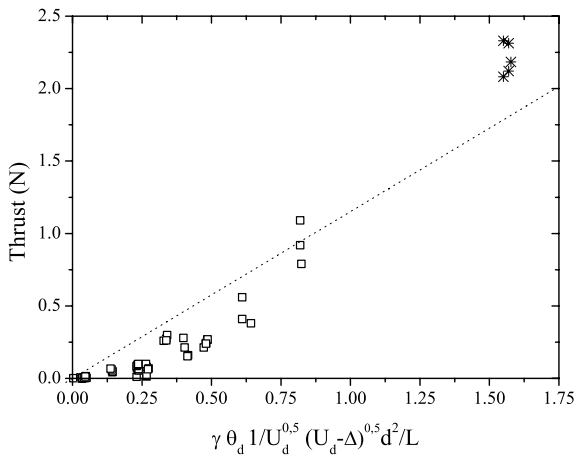

Figure 3.10: Thrust as function of $\gamma\,\theta_d\,1/\mathrm{U}_d^{0.5}\,(\mathrm{U}_d\text{-}\Delta)^{0.5}\,\mathrm{d}^2/\mathrm{L}$ and the linear fit for different Hall thrusters (dashed line). For each thruster, some thrust values are chosen around the point of normal operation. The NASA-457M thruster is represented by the asterisk-symbol.

Dimensions	Parameter	Parameters	Performances
$d = 324\,mm$	$U_d = 500\,V$	$P = 16.8\,kW$	$T = 1\,N$
$L = 101\,mm$	$\dot{m} = 49.19\,mg/s$	$n_n = 1.2 \times 10^{19}\,m^{-3}$	$I_{sp} = 2072\,s$
	$I_d = 33.65\,A$	$T_{wall} = 707.5\,K$	$\eta = 61\,\%$

Table 3.2: Dimensions, parameters and performances evaluated from scaling relations under low assumptions for a 20 kW thruster delivering 1 N of thrust. The magnetic field strength is fixed to 200 G.

and to estimate the impact of the simplifying assumptions. The design-procedure under low assumptions is slightly different. For a fixed discharge voltage of $U_d = 500\,V$ and a given thrust level, the product $\frac{d^2}{L}$ can be determined using Eq.(3.49). The mass flow rate, the specific impulse and the discharge current can be determined using the equations given above (3.48, 3.50, 3.51). Assuming an atom density of $n_n = 1.2 \times 10^{19}\,m^{-3}$ the channel mean diameter can then be calculated from the mass flow rate.
The dimensions, the operating parameters and the performances of the 20 kW thruster with a thrust of 1 N are listed in Table 3.2. The external wall temperature is $T_{ext} = 670\,K$ and the internal wall temperature is $T_{int} = 745\,K$.

3.7.4 Comparison between the two approaches

When comparing the results for the two sets of scaling relations (see Table 3.1 and Table 3.2), one can see there are differences for the operating conditions as well as for the characteristic dimensions of a 20 kW Hall thruster. Solely the value for the discharge current I_d stays almost unchanged. As voltage losses and the divergence angle are taken into account in the case of low assumptions, the required mass flow rate is larger whereas the specific impulse is lower. The characteristic dimensions are bigger in the case of low assumptions. However, the two scaling approaches are in fact in reasonable agreement as these scaling relations are solely supposed to give a first estimation of the required thruster dimensions and operating conditions. As can be seen in Fig. 3.6 and 3.10 both set of scaling relations are able to reproduce experimental data over a broad range of power. The accuracy of the scaling relations in the case of low assumptions is however lower. One reason for this is the error introduced due to the lack of a sufficiently large number of experimental data; this is especially true for the relation between the electron temperature and the discharge voltage. The last approach also suffers from other sources of inaccuracy. The evolution of voltage losses with sizes is disregarded whereas Δ is less for larger thrusters. Changes in the ion beam divergence with operating conditions and geometry are not considered. In summary, to get a first estimation of the characteristic dimensions and operating conditions for a given input power or a given thrust level, the scaling relations developed in the case of high assumptions are likely sufficient.

Figure 3.11: Picture of the 20 kW-class PPS-20k ML Hall thruster with the cathode mounted in the center of the thruster.

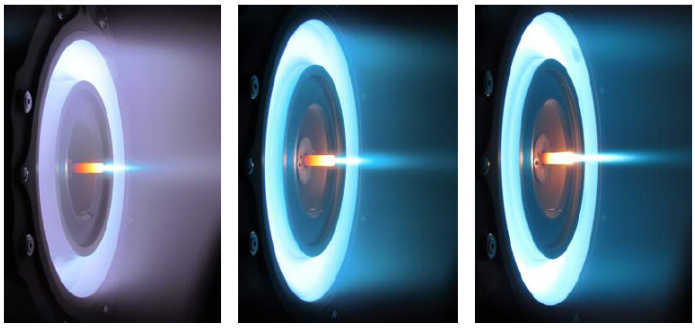

Figure 3.12: Photograph of the 20 kW-class PPS-20k ML Hall thruster operating with xenon in the PIVOINE-2g test bench. From left to right: low power, 15 kW and 23.5 kW.

3.8 Comparison with the 20 kW-class thruster PPS-20k ML

The 20 kW-class PPS-20k ML Hall thruster was designed, fabricated and tested in the frame of the HiPER project (High Power Electric propulsion: a Roadmap for the future) funded by the European Union under the 7th Framework Program [45].
A picture of the PPS-20k ML thruster is shown in Fig. 3.11. As can be seen, the cathode is placed at the center of the thruster. Details about design and construction can be found in reference [46]. The PPS-20k ML thruster is a large size device of which the geometry was partly defined from studies on scaling relations presented in this chapter. The thruster delivers a thrust of 1 N for a discharge voltage of 400 V and an anode mass flow rate of 43 mg/s (19.3 kW) [46, 47]. These values are very close to those predicted by the scaling laws in the case of high assumptions ($U_d = 500$ V, $\dot{m}_a = 41.5$ mg/s).

3.9 Conclusion

It is nowadays necessary to expand the operating envelope of existing Hall thruster technology in order to be able to respond to the demand for either high or low power electric propulsion devices for manifold applications such as drag compensation with low power thrusters or orbit topping maneuvers with high power thrusters. Therefore one must find a possibility to extrapolate the design and architecture of currently existing Hall thrusters towards the required scales and operating conditions. Sizing methods can be used to do so. The aim of this work was hence to find simple scaling laws that connect Hall thruster characteristic dimensions with the operating parameters and the performances of such propulsion devices. A possible approach is based on the combinations of a set of scaling laws with a vast body of existing data. Simplifying assumptions and realistic constraints on the performance level and the thermal load allow the refinement of the set of possible characteristic scale lengths found for a given thruster input power.
The Hall thruster sizing method described in this work considers the three characteristic

thruster dimensions L, d and h, as well as the magnetic field strength B. The method relies on analytical laws that are established from the fundamental principles that govern the physics of a Hall thruster in the frame of simplifying assumptions such as a constant and homogenous electron temperature, a uniform gas temperature all over the channel, any voltage losses due to the ionization process as well as the anode and cathode potential drop are neglected. One considers a uniform magnetic field, multiply charged ions in the plasma are neglected and the ion beam is considered to be monokinetic and parallel. Besides, the thruster geometry must fulfill criteria about the maximum channel wall temperature in order to limit the thermal load and to minimize the sputtering yield of the wall material. A second constraint has been made on the atom density to warrant an efficient functioning of the Hall thruster. A vast database that incorporates 36 single-stage Hall thrusters covering a power range between 10 W and 50 kW allows to check the validity of scaling laws and to find the value of corresponding coefficients necessary to proportion a thruster. The sizing approach was then employed to obtain a proper estimate of characteristic dimensions and magnetic field strength for a 20 kW Hall thruster capable of providing a thrust level of 1 N. The calculated dimensions and operating conditions are in good agreement with the 20 kW PPS20k Hall thruster developed in the frame of the European project HiPER.

Scaling laws developed here solely represent a first order approach due to the numerous simplifying assumptions on the physics at work in a Hall thruster. Nevertheless, for a given set of operating conditions they furnish a first estimate of the geometry and the magnetic field strength of a thruster, which permits time saving during the design and optimization stages.

One way to improve the accuracy of the scaling method is to reduce the number of assumptions. A second order approach was therefore developed including the evolution of the electron and the gas temperature as a function of the discharge voltage and accounting for the voltages losses. The relations between the different parameters and the discharge voltage are found empirically. However, available data on these parameters are scarce which limits the gain in improvement of the scaling method. The second order approach was employed to design again a 20 kW Hall thruster providing a thrust of 1 N. A comparison between the dimensions found with the first and the second order approach, revealed no significant differences. Due to the fact that the relations, found with the second order approach, are more complex, without leading to a real improvement of the scaling model, the first order approach is sufficient to get a initial estimate of the dimensions and operating parameters.

The described scaling model can still be improved by eliminating further assumptions, for example by taking into account the fraction of multiply-charged ions (and not only doubly-charged ions) or the divergence of the plasma beam. More experimental data about the evolution of the gas temperature, the electron temperature, the propellant conversion efficiency as a function of the discharge voltage could improve accuracy of the second order approach. Finally, an attempt to incorporate the magnetic field topology into scaling laws would represent a tremendous progress as the latter is the most fundamental feature to ensure a successful operation.

Chapter 4

Influence of discharge channel width on performances[1]

4.1 Introduction

The scaling laws presented in chapter 3 revealed a linear relationship between the channel width h and the channel mean diameter d for the majority of existing Hall thrusters. In other words, the h to d ratio is independent of the thruster size, input power and thrust level. That means that the normal anode mass flow rate for optimized Hall thrusters is chosen in such a way that they operate at the same neutral gas density. The ion current density, however, tends to increase with an increasing thruster size due to a better mass utilization [48]. The origin of a constant h to d ratio is still unclear. This fact might be the direct consequence of extrapolation of the original Russian design. It might also arise from technological constraints like the use of coils along with an iron circuit to produce the magnetic field.

In 1998, Raitses et al. investigated the impact of the channel length and profile upon the performances of a 500 W-class Hall thruster with glass walls [49]. The channel cross-section was solely modified in the near-anode region by means of glass spacers to tailor the electron temperature owing to a pinch effect. Authors found a narrow channel solely improves propellant utilization and thrust efficiency at low mass flow rates, i. e. when ionization is weak.

In this contribution, we study the influence of the channel width on ionization and acceleration processes in a low-power Hall thruster. The goal is to verify if the performances of a low-power Hall thruster, that are generally relatively low, can be improved by a modification of the channel geometry. The influence of the channel width on the thruster performances is investigated for two different working gases (Xe and Kr). In order to investigate the impact of the h to d ratio on discharge properties, three sets of ceramic rings were used to modify the channel width without modifying the channel mean diameter and the channel length. Several quantities have been measured over a broad range of propellant mass flow rates and applied voltages for the three channel configurations, namely: the discharge current, the ion current density in the plume, the Xe^+ ion axial velocity profile, the ion energy in the plume far-field and the channel wall temperature. The thrust and the anode efficiency are calculated for Xe and measured for Kr. As we shall see throughout the next sections, analysis of the complete data set reveals the channel cross-section area has a noticeable impact on Hall thruster discharge properties and performance.

[1] Adapted from:
S. Mazouffre et al, *J. Phys. D: Appl. Phys* **45**, 185203 (2012)

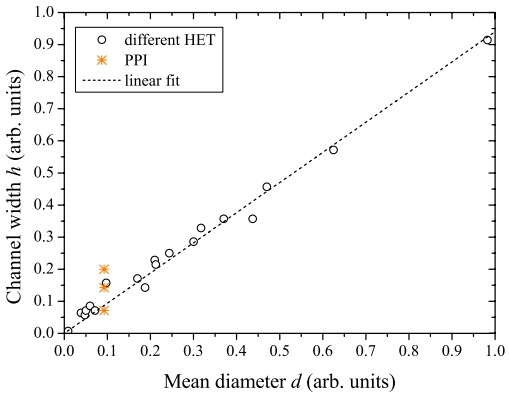

Figure 4.1: Channel width h against mean diameter d for different Hall thrusters [48]. Star symbols show the three different PPI configurations.

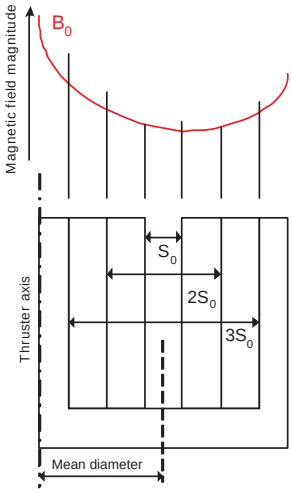

Figure 4.2: Schematic of the thruster acceleration channel showing the three geometries. A sketch of the magnetic field strength along the channel radius is also shown.

4.2 PPI thruster with variable channel width

A special version of the PPI thruster (described in Sec. 2.6) was used to investigate the influence of the channel width on the discharge properties and thruster performances. With this special version the channel width h can easily be modified while keeping the channel mean diameter d and the channel length L constant. Three different channel width can be achieved by inserting different sets of alumina rings, such that the channel cross-section is either S_0, 2 times S_0 or almost 3 times S_0. The S_0 configuration is very close to the configuration of standard Hall thrusters, as can be seen in Fig 4.1. The three geometries are labeled S_0, $2S_0$ and $3S_0$. A broad outline of the three channel configurations and the magnetic field amplitude along the channel radius is depicted in Fig. 4.2. Although the magnetic field map was unchanged during all experiments, i.e. the maximum on-axis magnetic field strength at the channel exit plane is constant, Fig. 4.2 shows the magnetic field gradient and strength at the channel walls depend on the channel configuration. The fact that the channel is made of Al_2O_3 instead of $BNSiO_2$ is not decisive for the purpose of the work, as a qualitative comparison does not depend on the wall material. Furthermore, the thruster is solely operated at low voltages ($U_d \leq 300\,V$) so that the influence of the wall material is limited [7].

4.3 PPI thruster operating with xenon

The three different geometrical configurations of the thruster were successfully operated with xenon as propellant gas in the NExET test bench [11]. An external hollow cathode with a LaB_6 insert, provided by MIREA, was used as neutralizer with a constant xenon mass flow rate of 0.2 mg/s. This cathode mass flow rate is relatively high because the cathode was originally

designed to be used with a 1.5 kW Hall thruster. The normal mass flow rate is 0.4 mg/s, but it was tested previous to the PPI tests, that a cathode mass flow rate of 0.2 mg/s is sufficient for correct operation of the thruster. The cathode orifice was placed 10 cm below the thruster axis and 3 cm away from the channel exit plane. When moving the cathode away from the thruster, the discharge current decreases by about 10 % (e.g. 0.9 A instead of 1 A at 1 mg/s and 200 V). The cathode gas flow therefore influences the performance, yet the observed qualitative behavior does not change. One can therefore assume that the described cathode operating conditions are suitable for the investigation of the channel width on the thruster performance. In the following sections different key parameters are investigated for the 3 different PPI configurations in order to investigate the influence of the channel width h.

4.3.1 Discharge current waveform

The discharge current waveform of the PPI thruster was recorded by means of DC coupled current probe (Tektronix TCP202) that offers a bandwidth up to 50 MHz. The current signal was sampled at 1.25 MHz. The length of each time series was typically 6 ms, which corresponds to about 100 breathing oscillations[2] of the discharge. Five waveforms of the anode discharge current are displayed in Fig. 4.3 in the case of the PPI thruster with the S_0 configuration. The current level as well as the shape of the I_d waveform depend critically on the thruster operating parameters, which is common for Hall thrusters. The current oscillations can be almost periodical with high (top waveform) or low (second waveform) amplitudes. As shown by the top waveform of Fig. 4.3, the discharge is almost extinguished during each oscillation cycle. On the contrary, discharge waveforms can be highly non stationary with many elementary frequencies which leads to a broad Fourier spectrum (third waveform). At the extreme, oscillations can be so random that no specific frequency is visible (fourth waveform). Finally, in a few cases, two current oscillation regimes with different amplitudes coexist (fifth waveform). The current waveforms displayed in Fig. 4.3 have been recorded with the S_0 configuration, but similar results are obtained for the two other geometries.

4.3.2 Operating envelope

The three PPI configurations have been operated over a broad range of anode mass flow rates and discharge voltages. The question was: Is it possible to broaden the operating envelope with a larger discharge channel?
Figure 4.4 illustrates the operating parameter envelope, i.e. the voltage-flow rate curve, covered with each channel geometry. As can be seen, the thruster was operated over a broad range of xenon anode mass flow rates [0.4-3.1] mg/s and applied discharge voltages [50-400] V [11]. The corresponding background pressure range was [1.5-5] $\times 10^{-3}$ Pa-Xe. The pressure was measured with an ionization gauge. In terms of input power, the thruster was operated between 25 W and 460 W. Values above 350 W were only maintained for a short duration to limit the thermal load. We first noticed the thruster is easier to ignite with the $3S_0$ configuration, i.e. with the widest channel, at lower discharge voltages whatever the anode mass flow rate. Second, the parameter

[2]The discharge of a Hall thruster is highly non stationary and the frequency spectrum of the instabilities is dominated by low frequency oscilations in the kHz range, the so-called breathing-type oscillations [50].

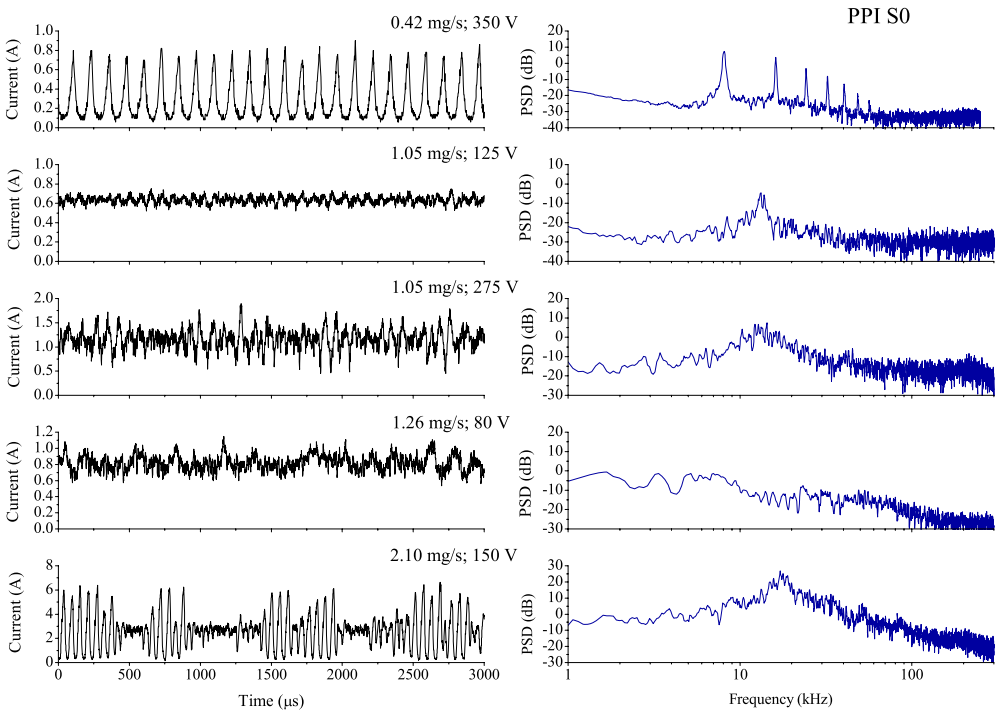

Figure 4.3: Waveform of the anode current and the associated power spectrum density for various operating conditions in the case of the S_0 configuration of the PPI thruster.

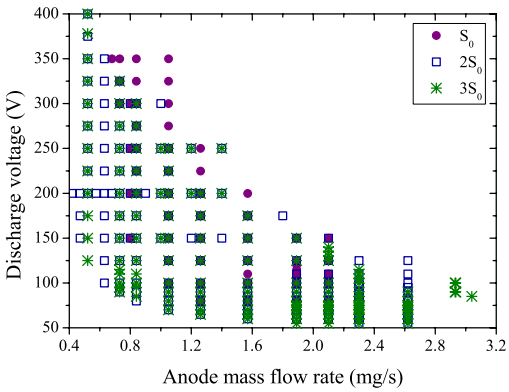

Figure 4.4: Influence of the channel geometry upon the mass flow rate-voltage envelope.

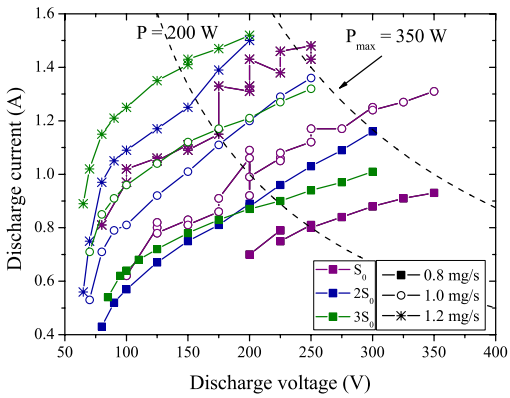

Figure 4.5: Discharge current as a function of the discharge voltage for 3 anode mass flow rates and the 3 PPI configurations

envelope is broader with the $2S_0$ and $3S_0$ configurations, as exemplified in Fig. 4.4. With a wide channel, the thruster can operate at low voltage with low gas flow rates as well as at power well above the normal one. The extended operation envelope and easy ignition support the idea that losses diminish when the channel width h increases. Operation at relatively high power is possible without trouble since the atom density that warrants a great ionization degree corresponds to a large porpellant flow for a wide channel [48].
Figure 4.5 shows the discharge current as a function of the discharge voltage for the 3 PPI configurations. The normal thruster power of 200 W as well as the maximum tolerated power of 350 W are also represented in the figure (dashed lines). As can be seen, the discharge current is higher for a larger channel at a fixed anode mass flow rate. The discharge current is defined by the sum of ion and electron current ($I_d = I_i + I_e$). The fact that I_d is bigger for a larger channel means that either the ion or the electron current increase when h increases. A bigger ion current would stand for a better ionization with a larger channel, whereas a bigger electron current would mean that the electron transport towards the anode depends on the channel width.

4.3.3 Ionization efficiency

In order to investigate the influence of h on the ionization process, measurements of the ion current in the plasma plume are necessary.

4.3.3.1 Ion current density profile

The ion current density profile in the plasma plume of a Hall thruster is generally measured by means of a Faraday probe. A Faraday probe is an electrostatic probe that is polarized negatively to act as ion collector. There are several types of Faraday probes including nude,

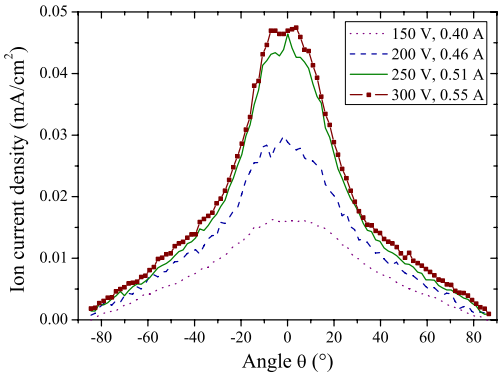

Figure 4.6: Plume ion current density angular profile for the PPI Hall thruster in the S_0 configuration for several discharge voltages (0.8 mg/s). The 0° angle corresponds to the thruster axis.

cupped, collimated, gridded and magnetically filtered probes. Nude Faraday probes are often equipped with a guard ring that is polarized to the same negative potential as the collector in order to minimize edge effects around the collector by creating a flat and uniform sheath over the collection area.

In the present study, the ion current was measured in the far-field plume by means of a planar Faraday probe equipped with a guard ring. The probe was made of graphite in order to withstand ion bombardment. Note that graphite also exhibits a low secondary-electron emission yield. The probe active area is 1 cm^2. The gap between the collector and the guard ring is 1 mm. The probe was negatively biased at -50 V to act as ion collector. This bias voltage has been found in a previous test, where the probe bias has been changed in order to obtain saturation of the measured ion current. The resulting probe current was measured over a 10 Ω load in order to minimize disturbance of the plasma sheath. A low-pass (35 kHz) amplifier with a gain of 10 dB delivers the output signal. The probe was located 40 cm downstream of the channel exit plane and rotated over almost 180 °. The measured current density is typically below 0.1 mA/cm^2. Figure 4.6 shows the ion current density angular profile acquired in the (x,z) plane with the S_0 geometry for several discharge voltages ($\dot{m}_a = 0.8$ mg/s). The tails observed at large angle with respect to the thruster axis originate in charge exchange collision events between fast Xe^+ ions of the beam and slow background gas Xe atoms as well as in ion scattering due to elastic collisions. As can be seen in Fig. 4.6, tails are strong despite a low residual xenon gas pressure. Charge exchange collisions are certainly favored here as the cathode delivers a non negligible amount of neutrals in the near-field plume.

4.3.3.2 Total ion current

The total ion current in the beam $I_{i,t}$ can be computed from the experimentally measured ion current profile. It is equal to the integral of the current density $j_i(r, \theta, \phi)$ over the elementary surface dS at the measurement location. In case the Faraday probe is located at a fixed distance

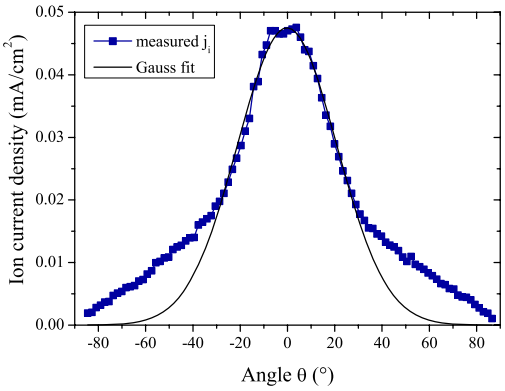

Figure 4.7: Plume ion current density profile of the PPI thruster (S_0 geometry, 300 V, 0.8 mg/s) and associated Gaussian fit (line). Corrected data removes the tails for angles larger than 30°.

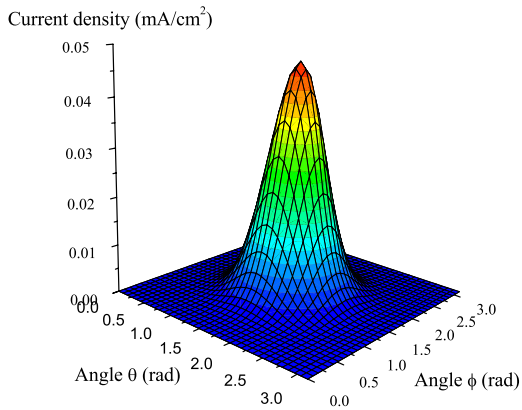

Figure 4.8: Reconstructed 3D ion current density distribution in the plume of the PPI thruster (S_0 geometry, 300 V, 0.8 mg/s).

R, the ion current is defined in spherical coordinates as:

$$I_{i,t} = \int\int_S j_i dS = R^2 \int_{-\pi/2}^{\pi/2} \int_{-\pi/2}^{\pi/2} j_i(\theta, \phi)\, sin(\theta) d\theta\, d\phi. \tag{4.1}$$

The quantity $j_i(r, \theta, \phi)$ is not measured directly. Instead one measures $j_i(R, \theta, 0)$, see Fig. 4.6. The 3D ion current density distribution can however be obtained assuming a cylindrical symmetry with respect to the thruster axis and a probe apparatus function with no dependence on the angle. Before computing the total ion current, the current flux distribution must be corrected to suppress the effect of charge exchange collisions. In this study, the lateral spread of the ion beam profile is strongly reduced by fitting the central part of the ion distribution to a Gaussian function. An example is shown in Fig 4.7. Note that tails are clearly removed and that the ion current density is forced to be zero at θ = -$\pi/2$ and $\pi/2$. Our correction method is disputable as there are several ways to correct for the tails of the ion current density profile [51, 52]. Yet, the correction method will not modify the ordering of the ion current for the three different geometries. Figure 4.8 represents a reconstructed 3D ion current density profile from which one can compute the total ion current. According to our correction method, $j_i(\theta, \phi)$ reads:

$$j_i(\theta, \phi) = j_{i,0} exp\left(-\frac{\theta^2}{w^2}\right) \cdot exp\left(-\frac{\phi^2}{w^2}\right), \tag{4.2}$$

where $j_{i,0} = j_i(0, 0)$ in A/m^2 and w denotes the width of the fitted Gaussian function centered at 0 °.

The total ion current as a function of the discharge voltage for the three PPI configurations is represented in Fig. 4.9. The total ion current is almost independent of the discharge voltage but it increases with the anode mass flow rate. As can be seen in Fig. 4.9, the total ion current

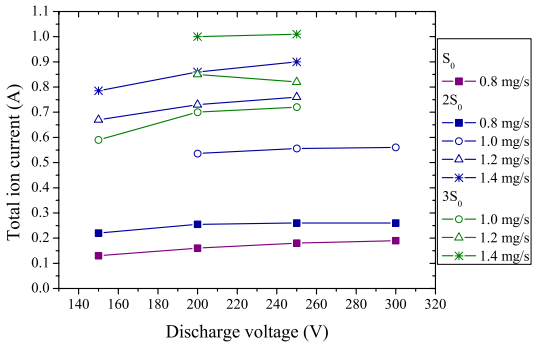

Figure 4.9: Total ion current as a function of the discharge voltage for the three different channel geometries.

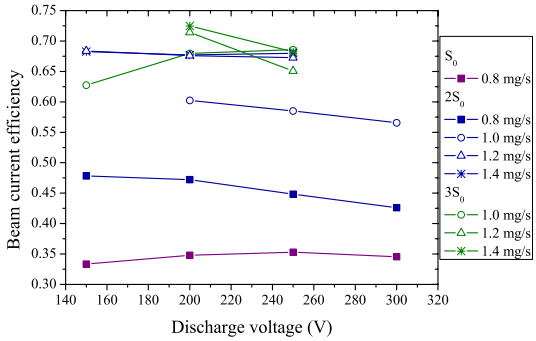

Figure 4.10: Beam current efficiency as a function of the discharge voltage for the three different channel geometries.

is the lowest for the S_0 configuration and the highest for the $3S_0$ configuration. However, the difference between the $2S_0$ and the $3S_0$ configuration is relatively small. The electron current, that can be obtained from the difference between the discharge current and the ion current is almost the same for the different geometries. The higher discharge current observed for a wider channel (see Fig. 4.5) is therefore mostly due to a more efficient ionization in the case of a wider channel. Figure 4.10 shows the beam current efficiency, i.e. the total ion current divided by the discharge current, as a function of the discharge voltage U_d. As can be seen, the beam current efficiency increases with an increasing channel width, which means that the ionization is more efficient with a larger channel.

4.3.3.3 Propellant utilization

The ion mass flow rate generated by the thruster reads:

$$\dot{m}_i = \frac{M}{e} I_{i,t}, \tag{4.3}$$

where M and e denote the ion mass and the elementary charge respectively. The ionization efficiency α, also called anode propellant utilization, corresponds to the fraction of propellant gas flow rate injected through the anode that is converted into ion flow. It is given by the ratio of $\dot{m}_i$ to $\dot{m}_a$. The uncertainty in the calculation of α is large due to the necessary correction of the ion current density profile by a Gaussian fit. A statistical analysis indicates an error bar of about 20 %. The anode propellant utilization does not account for the amount of gas flowing through the cathode. The quantity α is plotted as a function of the discharge voltage in Fig. 4.11 for the three channel geometries. First, α increases with the applied voltage U_d for all geometries. This increase has two main origins: the gain in ionization probability and the growth of the multiply charged ion species fraction, especially Xe^{2+}. The ionization rate and the production yield of multiply-charged ions increase with the electron temperature. The latter increases with the discharge voltage [48]. Therefore the ion density increases with U_d, which explains

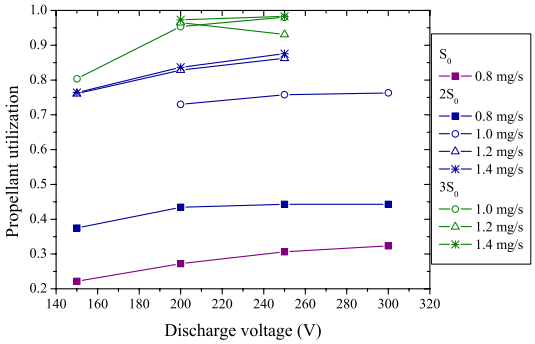

Figure 4.11: Anode propellant utilization as a function of the discharge voltage for the three channel configurations.

the larger propellant utilization. Second, for a given mass flow rate the ionization efficiency increases drastically with the channel width h, like the beam current efficiency. With the $3S_0$ configuration, α is above 0.9 for $U_d > 200\,\mathrm{V}$, a value commonly reached for large thrusters. It is preferable to examine the impact of h on the propellant utilization for a fixed atom density in the channel. According to our dataset, data from the S_0 configuration operated at 0.8 mg/s can be compared to the data set of the $2S_0$ configuration operated at 1.4 mg/s and data from the $2S_0$ configuration operated at 1.0 mg/s can be compared to the $3S_0$ configuration operated at 1.4 mg/s. It is important to note that the absolute value of α is certainly overestimated due to the uncertainty of the correction method of the ion current density profile. However, the relative ordering is correct.

4.3.4 Ion velocity

In order to investigate the relationship between channel geometry and ion acceleration, the Xe^+ ion velocity was measured along the channel axis by means of Laser-induced fluorescence spectroscopy (LIF). The optical bench used to probe the metastable $5d^2F_{7/2}$ Xe^+ state is extensively described in Ref. [53]. A high-power tunable single-mode laser diode is used to excite xenon ions at 834.723 nm. A high-precision wavemeter monitors the laser wavelength. Laser stability is real-time checked by a 2 GHz confocal Fabry-Pérot interferometer. The laser beam passes through several optics until it reaches the thruster through a window located at the back of the NExET vacuum chamber. The laser beam is shined along the thruster channel axis. The 541.915 nm fluorescence light is collected at 90° with respect to the laser beam direction. A 10 nm bandwidth filter is used to isolate the fluorescence line. A photomultiplier tube serves as a radiation source. Lock-in detection permits to improve the signal-to-noise ratio. The Hall thruster is mounted onto a translation stage to enable measurements at several axial positions. With the 834.723 nm optical transition, the fluorescence profile images to a large extent the Xe^+ ion velocity distribution function (IVDF) [53, 54]. In this study we solely consider the most probable velocity of each VDF. Assessment of the maximum of the VDF leads to a random error of $\pm\,150\,\mathrm{m/s}$.

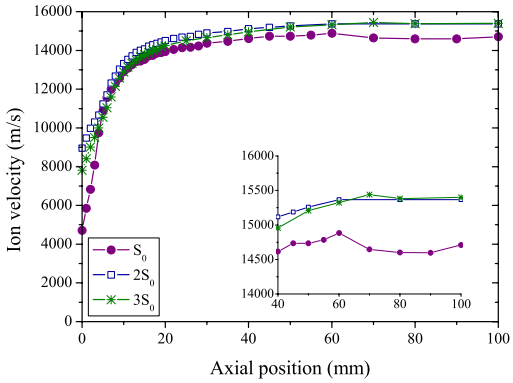

Figure 4.12: Influence of the channel width on Xe^+ ion axial velocity. The PPI thruster is operated at 200 V and 1 mg/s for the 3 configurations. The position $x = 0$ mm refers to the channel exit plane.

The on-axis profile of the Xe^+ axial velocity component is displayed in Fig. 4.12 for the 3 channel configurations. For all three configurations, the PPI thruster was operated with a discharge voltage of 200 V and an anode mass flow rate of 1.0 mg/s. The position $x = 0$ mm refers to the channel exit plane. The three velocity profiles exhibit the same trend. The Xe^+ ion velocity increases quickly over the first 20 mm. Ions still accelerate a little until $x = 60$ mm. Beyond this distance they travel at constant axial velocity whatever the geometry. As can be seen in Fig. 4.12, the axial velocity is the lowest for the S_0 configuration, there is almost no difference between the $2S_0$ and the $3S_0$ configuration.

4.3.5 Ion energy

The ion energy is measured by means of a Retarding Potential Analyzer (RPA) for the three different PPI configurations. Before presenting the results, the theory of RPA measurements is briefly introduced.
A RPA is a gridded probe that uses electric fields to act as energy filter for charged particles [55, 56]. A typical RPA contains four grids and a collector as shown in Fig. 4.13.

- The first grid at the entrance serves to shield the plasma from the field inside the probe in order to minimize plasma disturbance. The grid is either at floating potential or grounded.
- The second grid is biased negatively in order to repel electrons so that only ions can reach the collector.
- The third grid acts as ion repeller. A variable positive potential is applied to this grid. By changing the grid polarization, one can scan the ion energy distribution. Ions with energies below the grid bias are repelled and prevented from being detected.
- A fourth grid may be added behind the ion repeller. It is biased negatively to prevent secondary electrons emitted by the collector from escaping. Note that the potential of

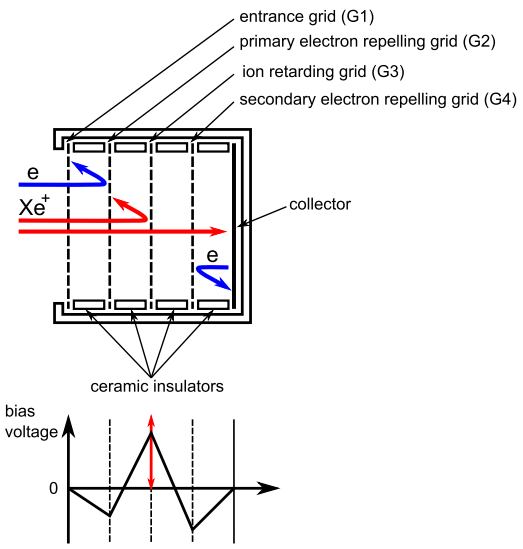

Figure 4.13: Schematic view of a RPA. Also shown in the polarization of the grids, where 0 corresponds to the ground.

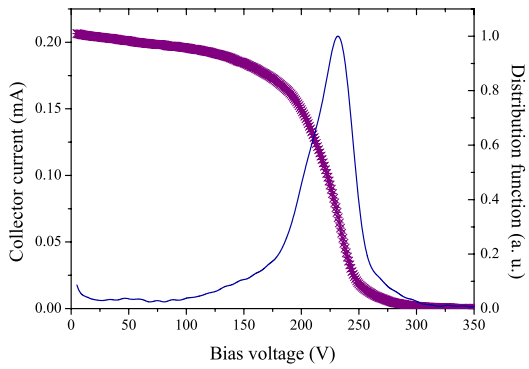

Figure 4.14: RPA current trace (circle) and corresponding ion energy distribution function (blue line). Measurements were performed in the plume at $x = 70\,\mathrm{cm}$ ($3S_0$, 250 V, 1.2 mg/s).

G4 should be below the potential of G2 not to trap electrons inside the device (hence to limit ionization of the residual gas).

- The ion collector can be negatively biased (useful when the ion energy is very low) or grounded. Note that if the collector is grounded, the RPA measures the ion energy with respect to ground.

The grids as well as the ion collector are usually made of low SEE yield material such as tungsten or molybdenum.
A RPA is typically used to measure the ion energy distribution function (IEDF) [57, 58]. The probe acts as high-pass filter: only ions with voltages, that is energy-to-charge ratio, greater than the repeller grid voltage can pass and reach the collector. The potential of the ion retarding grid is then varied while monitoring the ion current on the collector. As a result, one obtains a I versus V curve, the so called RPA characteristic. As a RPA is an electrostatic device, it cannot distinguish between singly charged and multiply charged ions. The current measurement of a RPA does not dependent on the ion energy, but rather on the energy per unit charge of the ion. Thus a singly charged ion with 300 eV of energy and a doubly charged ion of 300 eV will be filtered identically by the probe.
The ion energy distribution function IEDF is obtained from the first derivative of the I-V trace [56]. An example of a typical RPA trace, recorded with a 4-grid RPA in the far-field plume of the PPI thruster, and the corresponding IEDF is shown in Fig. 4.14.
A MatLab program is used to determine the IEDF and the associated macroscopic quantities. Prior to the derivative calculation, data points of the I-V curve are interpolated with a cubic spline function and subsequently smoothed with a 4th-order Savitzky-Golay filter. Outcomes of the MatLab program were validated for several series using the Origin software for calculations.

The following macroscopic quantities can be extracted from the IEDF:

- the most probable energy E_{max}, i.e. the maximum of the EDF,
- the mean energy E_{mean}, i.e. the 1st-order moment:

$$E_{mean} = \frac{\int_0^\infty E\, f(E)\, dE}{\int_0^\infty f(E)\, dE}, \tag{4.4}$$

- the standard deviation SD, i.e. the 2nd-order moment:

$$SD = \frac{\int_0^\infty (E - E_{mean})^2\, f(E)\, dE}{\int_0^\infty f(E)\, dE}, \tag{4.5}$$

- the full width at half maximum $FWHM$.

The ion EDF can be converted into an ion velocity distribution function (IVDF) using the energy conservation principle:

$$\frac{1}{2} m\, v^2 = q\, e\, E, \tag{4.6}$$

where q is the electric charge number. In our case only singly-charged ions ($q = 1$) are considered when converting an EDF into a VDF and vice-versa.
For the RPA trace represented in Fig. 4.14, the macroscopic quantities are:

- $E_{max} = 233\,\mathrm{V}$ ($v_{max} = 18505\,\mathrm{m/s}$),
- $E_{mean} = 214\,\mathrm{V}$ ($v_{mean} = 17734\,\mathrm{m/s}$),
- $SD = 42\,\mathrm{V}$,
- $FWHM = 44\,\mathrm{V}$.

The broadening of the IEDF has four main origins in the case of a Hall thruster:

- the ion thermal speed (Doppler broadening $\approx 0.5\,\mathrm{eV}$ at $1000\,\mathrm{K}$),
- the overlap between the ionization and acceleration layers [54, 53],
- the presence of multiply-charged ion species, especially Xe^{2+},
- the apparatus profile of the RPA probe.

For the measurements in the NExET test bench, the 4-grid RPA was placed 70 cm downstream the thruster exit plane on the thruster axis. The voltage resolution was set to 1 V. Figure 4.15 shows the most probable ion energy E_{max} as well as the mean ion energy E_{mean} as a function of the discharge voltage for the 3 PPI configurations. The S_0 configuration is operated at 0.8 mg/s, the $2S_0$ and the $3S_0$ configuration at 1.0 mg/s. However, it has been verified that the anode mass flow rate has almost no influence on the ion energy. As can be seen, E_{max} and E_{mean} increase with the discharge voltage and E_{max} is bigger than E_{mean}. Furthermore, one can observe that E_{max} and E_{mean} are the lowest for the S_0 configuration and the highest for

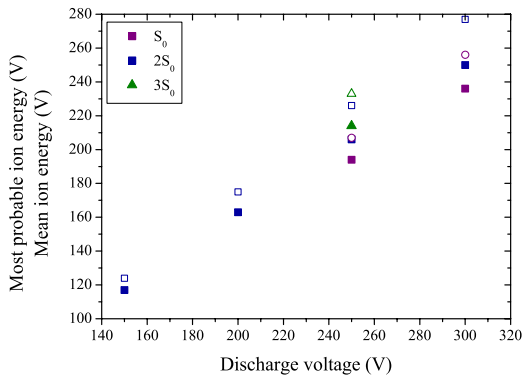

Figure 4.15: Most probable (open symbols) and mean ion energy (full symbols) measured with the RPA as a function of the discharge voltage for the three PPI thruster channel configurations.

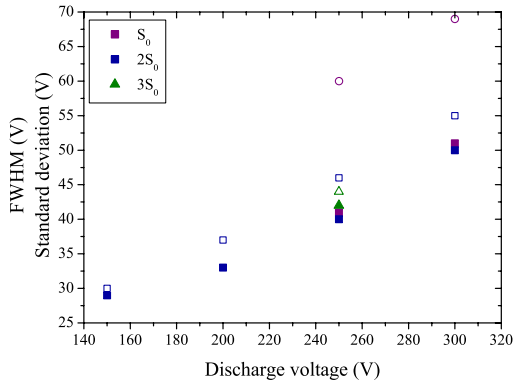

Figure 4.16: Full width at half maximum (open symbols) and standard deviation (full symbols) of the IEDF as a function of the discharge voltage for the three PPI thruster channel configurations.

the $3S_0$ configuration. As for the total ion current and the propellant utilization, the difference between the $2S_0$ and the $3S_0$ configuration is relatively small. Similar results have also been obtained by means of LIF measurements presented in the previous section and in Ref. [59]. The full width at half maximum as well as the standard deviation of the IEDF are represented in Fig. 4.16 as a function of the discharge voltage. $FWHM$ and SD increase with the discharge voltage. There is almost no influence of the channel width on SD, whereas the influence of h is clearly visible on $FWHM$. It is the lowest for the widest channel ($3S_0$) and the highest for the narrowest channel (S_0).

4.3.6 Thrust

The thrust of the PPI operating with Xe has not yet been measured with a thrust stand for the three different channel geometries. The thrust can nevertheless be inferred from ion current and ion velocity measurements. The thrust reads:

$$T = \dot{m}_i \times v_i, \tag{4.7}$$

where $\dot{m}_i$ is the ion mass flow rate in mg/s and v_i is the mean ion velocity in m/s. The latter is assumed to be given by the maximum ion axial velocity measured by laser spectroscopy on the channel centerline in the plume far-field. The calculated thrust is overestimated, as the ion velocity is not uniform but it decreases with an increasing distance from the thruster axis [60]. Note that multiply-charged ion species are not accounted for. Thrust values computed with Eq. 4.7 are represented in Fig. 4.17 for the three channel geometries. As can be seen, the thrust increases with the input power as expected. The largest thrust level is produced with the $3S_0$ configuration as it can tolerate large mass flow rates and high input power.

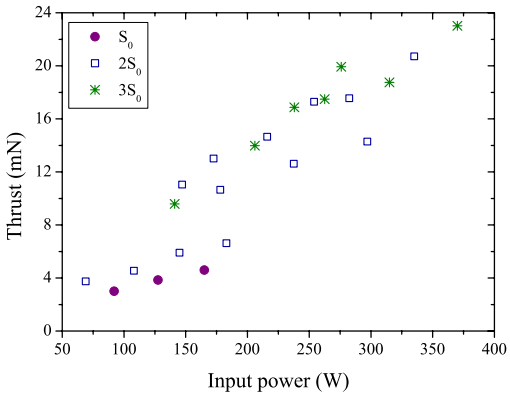

Figure 4.17: Computed thrust level as a function of the input power for the three PPI thruster channel configurations.

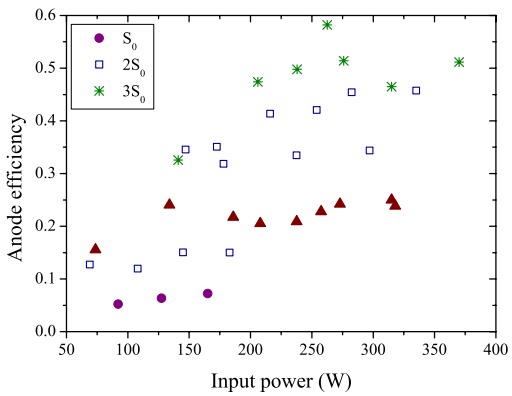

Figure 4.18: Anode efficiency η_a as a function of the input power for the three channel geometries. The triangle symbols correspond to thrust measurements carried out in 2008 in the PIVOINE test bench with a different version of the PPI thruster in the S_0 configuration [16].

4.3.7 Anode efficiency

The anode efficiency can be determined from thrust data. It corresponds to the ratio of mechanical power to the applied electrical power. The anode efficieny η_a therefore reads:

$$\eta_a = \frac{T^2}{2\,\dot{m}_a U_d I_d}. \tag{4.8}$$

This quantity does not account for the gas flow rate supplied through the cathode. Figure 4.18 represents the evolution of the anode efficiency as a function of the input power for the three channel configurations. The efficiency drastically increases with the channel width h from about 10 % with the S_0 configuration to about 50 % with the $3S_0$ configuration. Note that in Fig. 4.18, triangle symbols correspond to thrust measurements carried out in the PIVOINE vacuum chamber in 2008 with the S_0 configuration and $BNSiO_2$ as wall material [16]. The overall value of η_a is certainly overestimated due to uncertainties in total ion current measurements and the fact that the ion velocity is assumed to be homogenous, but the relative ordering of the three channel geometries is correct. This study therefore clearly shows that the performance of a low-power Hall thruster can be increased by simply increasing the discharge channel width.

4.3.8 Plasma wall interactions

After a critical examination of ionization and acceleration processes as a function of the thruster channel width, it is worth studying the influence of the geometry on plasma-surface interac-

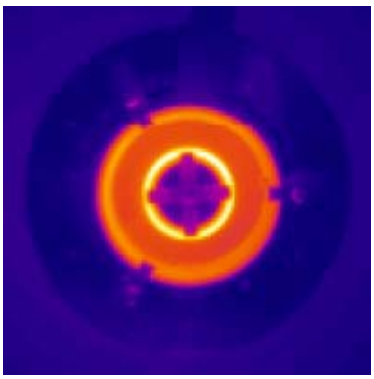

Figure 4.19: Calibrated infrared image of the low-power permanent magnet PPI Hall thruster operating at 200 V and 1.1 A (front view, $3S_0$ configuration)).

Table 4.1: Equilibrium temperature of the Al_2O_3 channel walls for the three different geometries (200 V, 220 W).

Geometry	Inner wall temperature (K)	Outer wall temperature (K)
S_0	860	722
$2S_0$	796	666
$3S_0$	770	605

tion inside the channel. Two quantities are therefore of prime interest: the steady-state wall temperature and the energy flux to the walls.

4.3.8.1 Steady-state wall temperature

The equilibrium temperature of both internal and external Al_2O_3 channel walls was determined by means of calibrated thermal imaging. The discharge voltage was set to 200 V and the anode mass flow rate was adjusted around 1.0 mg/s to keep the discharge current constant at 1.1 A. Experiments were therefore performed at a fixed input power of 220 W. Hall thruster infrared image acquisition was accomplished with a calibrated infrared camera suited for measurements in the 8 - 9 μm domain [39]. The camera covers a temperature range from -20° C to 1500 ° C. Experiments were conducted in the NExET test bench with the infrared camera located in front of the PPI thruster at 1.5 m. Observation was carried out through a CaF_2 window. An example of calibrated infrared image of the PPI thruster is represented in Fig. 4.19. In order to enable absolute temperature determination for the thruster channel walls the normal spectral emissivity of the Al_2O_3 ceramic was measured in air as a function of temperature. The mean emissivity is about 1. The steady-state temperature of the inner and outer walls is given in Tab. 4.1 for the three channel configurations. The temperature of the internal wall T_{int} is always higher than the one of the external wall T_{ext} as it is more difficult for the former to evacuate heat [39]. The temperature of the two walls decreases with the channel width. A lower temperature means less thermal constraint on the thruster components. Besides, a low chamber wall temperature may lead to an increase in the thruster lifetime. The drop of the wall temperature with the increasing channel width is first a direct consequence of a geometrical effect as can be shown by a very simple thermal model of the PPI thruster. This simple model only takes radiative heat exchanges into account. The PPI thruster is described as a thermal enclosure that consists of the internal, the external and the back ceramic, see Fig. 4.20. All surfaces are supposed to be isothermal. The energy is assumed to be emitted diffusely

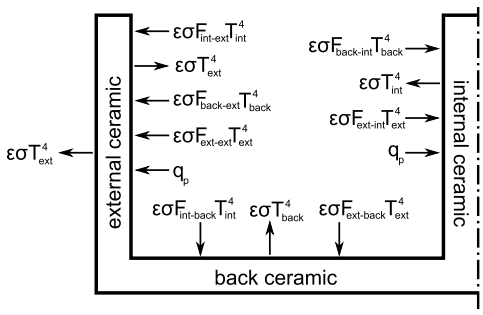

Figure 4.20: Simplified thermal enclosure with radiative heat exchanges of the PPI thruster. Plasma-wall interactions are characterized by the energy flux q_p.

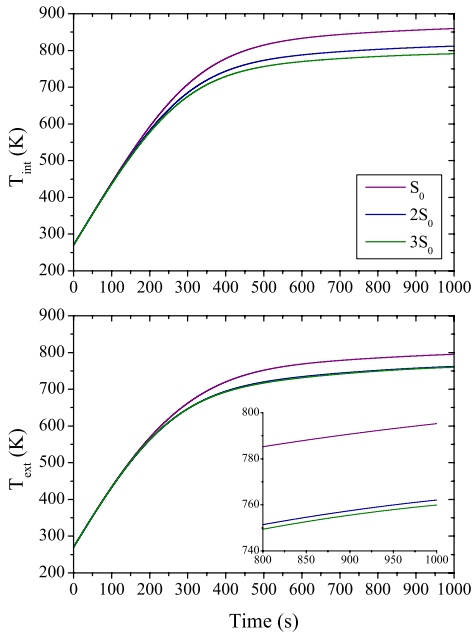

Figure 4.21: Calulated channel wall temperatures assuming a constant loss term q_p for the three geometries

within the enclosure and the incident energy flux is assumed to be uniform over each individual area. Radiative heat exchanges are calculated using geometrical configuration or view factors F [38]. These factors define the fraction of heat exchanged between each individual surface of the thermal enclosure [61]. For a simple geometry such as the thruster discharge channel, the geometrical configuration factors can be found in the literature [62]. The radiative heat flux for an enclosure element k can be written as:

$$\phi_{rad}(z) \approx \sigma \left(\varepsilon_k T_k^4 - \sum_i \varepsilon_i F_{ik} T_i^4 \right), \tag{4.9}$$

where σ is the Stefan-Boltzmann constant, ε is the normal spectral emissivity [39], T_k is the element surface temperature, T_i is the temperature of the ith surface facing the considered element, and F_{ik} the black body configuration factor between the element k and the environment element i [61]. The first term corresponds to the heat flux evacuated by the element whereas the second term represents the heat flux received from the surrounding surfaces. All the different heat fluxes are represented in Fig. 4.20. Plasma-surface interactions are characterized on a macroscopic level by the energy flux deposited onto the thruster channel walls q_p. Simulation results with this simple thermal model of the PPI thruster are displayed in Fig. 4.21 for the

three different channel geometries. A constant value of q_p was used for all three geometries. As can be seen, the temperature of the inner channel wall is higher than the temperature of the outer channel wall. This is in agreement with the measurements. The simulations also show that the temperature gap between the $2S_0$ and the $3S_0$ configuration is smaller than the gap between the S_0 and the $2S_0$ configuration. Furthermore, simulation results indicate that the wall temperature decreases with an increasing channel width due to geometrical effects, as already observed by the measurements. However, this geometrical effect cannot fully explain the measured temperature difference between the three geometries, see Tab. 4.1. The possible link between the observed drop in wall temperature with the channel size and a decrease in the energy flux deposited by the plasma onto the walls is therefore still a remaining question.

4.3.8.2 Wall losses

It has been shown previously by our team that the energy flux deposited by the plasma onto the channel walls q_p can be assessed by combining temperature measurements of the channel walls with a thermal model of the thruster [38, 63]. The time-dependent thermal model of the thruster relies on the energy conservation equation and a set of simplifying assumptions [38]. Instead of performing a full calculation of energy transfers an option consist in treating the problem of radiation exchanges in a thermal enclosure. The latter is the same as described in Sec. 4.3.8.1. The thermal model then reduces to the well-known unsteady heat-conduction equation without sources or sinks [38]:

$$\frac{\partial T(r,t)}{\partial t} = \kappa \frac{\partial^2 T(r,t)}{\partial r^2}, \tag{4.10}$$

where κ is the thermal diffusivity. The energy rates to take into account are: a conductive heat flux through the channel walls, a radiative flux for all surfaces ϕ_{rad} of the thermal enclosure, the energy flux to the channel walls resulting from plasma-wall interactions q_p, which is the unknown variable. The temperatures of the adjacent thruster elements measured with thermocouples are used as boundary conditions. To compute the temperature of a given channel element implies knowing at each time step of all other parts as well as the value of the energy flux q_p. Therefore, measured temperature fields of the surrounding channel elements are used as input data and the value of q_p is adapted in an iterative manner so that the calculated temperature matches the measured temperature of the given channel element. Advantages of this semi-empirical approach are twofold: it allows drastic reduction of the number of parameters and it brings the simulation closer to the real thermal behavior of the thruster.
For a fixed input power, the energy flux deposited by the plasma onto the channel walls q_p decreases with an increasing channel width h for both, the inner and the outer ceramic as can be seen in Tab. 4.2.

Note that the absolute values of q_p are certainly underestimated due to the fact that the influence of the radiator is not correctly accounted for by this simple model. In order to get a more precise value of q_p, a complete 3D thermal model would be necessary. However, the qualitative ordering is correct and these results therefore demonstrate that the observed decrease in wall temperature is not solely due to a geometrical effect but also due to a change in the energy flux deposited onto the channel walls by the plasma.

Table 4.2: Energy flux to the walls q_p and power losses for the three thruster geometries (200 V, 220 W.

Geometry	q_p (W/cm^2) inner wall	q_p (W/cm^2) outer wall
S_0	1.98	0.7
$2S_0$	1.80	0.6
$3S_0$	1.65	0.57

Table 4.3: Comparison of the performances of two different Hall thrusters.

Thruster	Anode mass flow rate (mg/s)	Atom density (m^{-3})	Thrust (mN)	Anode efficiency
PPS®1350	4.8	2.6×10^{19}	82.4	0.55
PPS®X000-ML	5	1.2×10^{19}	82.8	0.50
	7	1.7×10^{19}	124.6	0.55
	11	2.7×10^{19}	211.2	0.59

4.4 Discussion

It was shown in the previous section that the channel width clearly influences the performance of the low-power PPI Hall thruster. Two mechanisms can be put forward to explain the improvement of the performances of the thruster with a wider channel.
First, it is related to a purely geometrical effect. In a low-pressure discharge, the charged particles are produced in the bulk and lost onto the channel walls, hence a surface. The production of mechanic energy in a Hall thruster is thus linked to the surface-to-volume ratio S/V which is $2/h$ [48]. Increasing the channel width h leads to a favored ion production and a reduction of wall losses due to plasma-wall interactions, with the direct consequence that the discharge can be maintained at low power and that the thruster can endure high power operation. Finally, a larger fraction of energy supplied to the device can be converted into axial ion motion, and therefore a higher thrust, when h is increased. The surface-to-volume ratio can therefore partly explain why bigger Hall thrusters have globally a bigger efficiency than smaller Hall thrusters. It seems to be interesting to compare two Hall thrusters of different size in order to validate this statement. Table 4.3 shows the performances of the 1.5 kW-class PPS®1350 and the 5 kW-class PPS®X000-ML. Both thrusters were operated at a discharge voltage of 300 V for the presented performance data. The PPS®X000-ML has been operated at a fixed magnetic field, i.e. no optimization of B was done. As can be seen in Tab. 4.3, at 5 mg/s the PPS®1350 has a higher anode efficiency than the bigger PPS®X000-ML. This can be explained by the fact the atom density for the PPS®X000-ML at 5 mg/s is too low for a optimized ionization of the supplied gas. If the assumption that the S/V-ratio influences the performance of a Hall thruster would be wrong, the two thrusters should have about the same anode efficiency at a similar atom density, i.e. at 11 mg/s for the PPS®X000-ML and 5 mg/s for the PPS®1350 respectively. However, as can be seen in Tab. 4.3, this is not the case.

At 7 mg/s the PPS®X000-ML has already a similar anode efficiency than the PPS®1350 at 5 mg/s. The anode efficiency at 11 mg/s is higher. This is a direct consequence of the reduction of wall losses with a wider channel.
This reduction of wall losses can also explain the fact the the 20 kW-class PPS20k-ML thruster can be operated a 5 mg/s and 350 V with an anode efficiency of about 23 % although the atom density is only $2\times10^{18}\,\mathrm{m}^{-3}$ (this would correspond to a mass flow rate of 0.4 mg/s for the PPS®1350) [47].
The second mechanism is linked to the magnetized area the plasma is exposed to. As shown in Fig. 4.2, stretching the channel in the radial direction leads to a stronger magnetic field in the vicinity of the channel walls. The magnetic field gradient in radial direction is thus stronger, which enhances the magnetic mirror effect [64]. The magnetic mirror ratio, i.e. the ratio of the magnetic field intensity near the wall to the magnetic field intensity on the channel axis, increases with h. For the internal wall at the channel exit plane it equals 1.2, 1.9 and 3.2 for the S_0, $2S_0$ and $3S_0$ configuration, respectively. Values are similar for the external wall. An increased magnetic mirror effect leads to an improved magnetic confinement of charged particles inside the channel. This has several consequences. First, the electron, and respectively ion, flux towards the wall is limited. Second, the radial electric field in the sheath is reduced and therefore more energy is available for an acceleration of the ions in the axial direction. Third, a bigger electron density as well as a slightly higher temperature, due to a reduced injection of secondary electrons, leads to an improved ionization of the gas. The improved magnetic confinement of the charged particles is thus also responsible for a higher propellant utilization and reduced plasma-wall interactions [65].

4.5 PPI thruster operating with krypton

The PPI thruster was operated with krypton in the CORONA test bench of the ESA Propulsion Laboratory at ESTEC in Noordwijk. Two series of experiments have been performed. First, the discharge voltage has been changed from 150 to 300 V at a constant anode mass flow rate of 1.0 mg/s (Kr). Second, the anode mass flow rate has been varied from 0.8 to 1.4 mg/s at a constant discharge voltage of 250 V. The cathode mass flow rate was set to 0.2 mg/s and the cathode-to-ground potential was maintained at about - 19 V for all experiments. The discharge current for the different operating conditions is given in Tab. 4.4.

4.5.1 Ionisation efficiency

4.5.1.1 Total ion current

The ion current density angular profile was measured in the CORONA chamber by means of eleven Faraday cups. Contrary to a planar probe, edge effects do not exist with a Faraday cup. Furthermore, with a cup design, ions crossing the well-defined entrance area are likely to be detected, hence a good accuracy on the local current density can be obtained. The eleven Faraday cups were mounted on the CORONA diagnostics arm at different angular positions from -55.4 to 52.9 °, where 0 ° corresponds to the thruster axis. In normal case, the diagnostics arm can be moved by means of a stepper motor, which allows a complete 180° scan of the

Table 4.4: Operating conditions for the PPI thruster in the CORONA chamber.

U_d (A)	$\dot{m}_a$ (mg/s)	S_0 I_d (A)	$2S_0$ I_d (A)	$3S_0$ I_d (A)
150	1.0	-	0.67	0.72
170	1.0	0.51	-	-
200	1.0	0.66	0.84	0.9
250	1.0	0.69	0.96	0.97
300	1.0	0.7	1.04	1.02
250	0.8	0.55	-	0.72
250	1.2	1.01	1.25	1.28
250	1.4	1.37	1.62	1.68

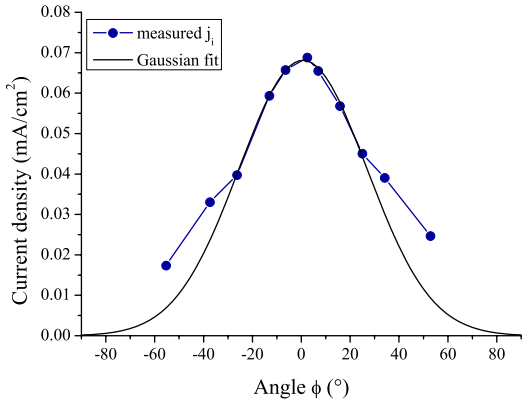

Figure 4.22: Plume ion current density angular profile of the $3S_0$ configuration of the PPI thruster operated at 250 V and 1.0 mg/s. The associated Gaussian fit (solid line) removes the tails at angles larger than 30°.

far-field plume. The combination of the 11 Faraday cups together with the rotation of the diagnostics arm enables the measurement of the three-dimensional ion current density profile in the far-field plume of the PPI thruster. Unfortunately, the rotation of the diagnostics arm wasn't working properly during the test. The arm was therefore positioned manually on the thruster axis, so that the vertical ion current density profile could be recorded by the 11 Faraday cups. The collector of these probes was made of molybdenum in order to reduce secondary electron emission. The collecting surface of the probe was 0.785 cm^2. The collector was polarized to -20 V and the shield polarization was set to 10 V. An example of a measured ion current density profile for the PPI thruster in the $3S_0$ configuration operating at 250 V and 1.0 mg/s (Kr) is shown in Fig. 4.22. The associated Gaussian fit that is used to correct for the influence of charge exchange collisions is also shown in the figure (solid line).

The total ion current $I_{i,t}$ is obtained by integrating the corrected ion current density profile

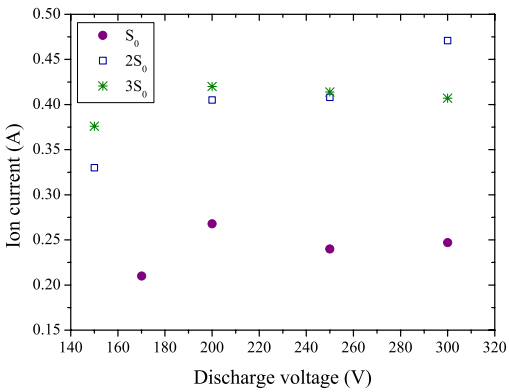

Figure 4.23: Total ion current as a function of the discharge voltage at a constant anode mass flow rate of 1.0 mg/s (Kr) for the 3 PPI configurations.

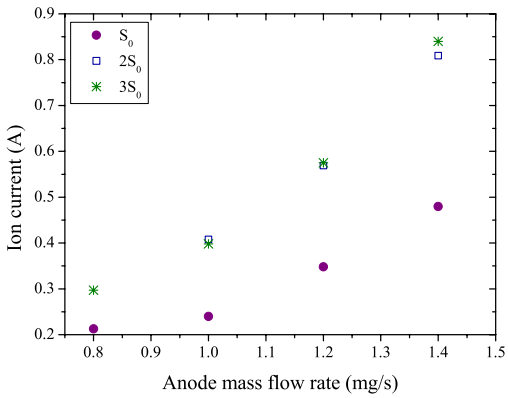

Figure 4.24: Total ion current as a function of the anode mass flow rate at a constant discharge voltage of 250 V for the 3 PPI configurations.

as explained in Sec. 4.3.3.2. The total ion current is shown in Fig 4.23 as a function of the discharge voltage and in Fig. 4.24 as a function of the anode mass flow rate. As can be seen in Fig. 4.23, the ion current is only slightly influenced by the discharge voltage: $I_{i,t}$ increases slightly from 150 V to 200 V and is almost constant for voltages above 200 V except for the $2S_0$ configuration, where it increases slightly between 250 V and 300 V. The ion current is the lowest for the S_0 configuration and there is almost no difference between the $2S_0$ and the $3S_0$ configuration. The ion current increases for the 3 configurations with the anode mass flow rate, as shown in Fig. 4.24. Again, $I_{i,t}$ is the lowest for the S_0 configuration and there is almost no difference between the $2S_0$ and the $3S_0$ configuration.

The beam current efficiency ($I_{i,t}/I_d$) is represented in Fig. 4.25 as a function of the input power for the 3 PPI configurations. The beam current efficiency is comprised between 0.35 and 0.5. For the S_0 configuration it decreases from 90 to 170 W and is almost constant at higher power. The beam current efficiency decreases for the $2S_0$ and the $3S_0$ configuration from 100 to about 250 W and increases slightly at higher power. As can be seen in Fig. 4.25, the lowest value is achieved for the S_0 configuration and there is almost no difference between the $2S_0$ and the $3S_0$ geometry.

4.5.1.2 Propellant utilization

The propellant utilization α can be calculated from the total ion current as explained in Sec. 4.3.3.3. Figure 4.26 shows the evolution of α as a function of the input power for the 3 channel widths. The value of α is comprised between 0.2 and 0.5. As can be seen, α is almost constant up to about 250 W and increases for higher values of the input power. Like the beam current efficiency, α is the lowest for the narrowest channel and there is almost no difference for the two wider channels.

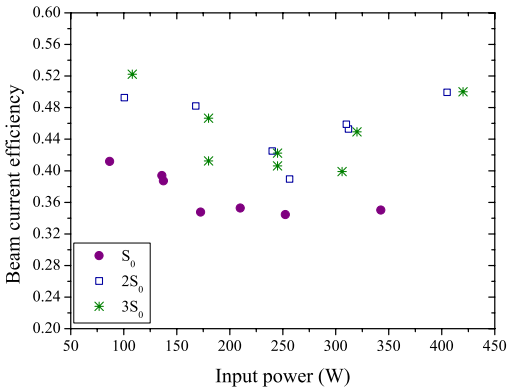

Figure 4.25: Beam current efficiency as a function of the input power for the 3 PPI configurations.

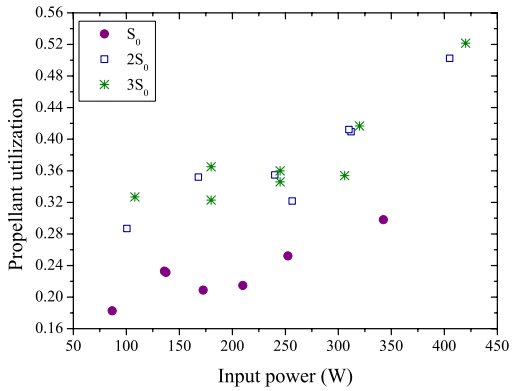

Figure 4.26: Anode propellant utilization as a function of the input power for the 3 PPI configurations.

4.5.2 Ion energy

The ion energy distribution function was measured using a 4-grid RPA placed at 83 cm downstream the thruster exit plane in the CORONA chamber. The voltage resolution was set to 5 V. The I-V trace was smoothed and interpolated with a cubic spline function before computing the first derivative. The analysis of the resulting IEDF is carried out as described in Sec. 4.3.5. The most probable ion energy E_{max} is shown in Fig. 4.27 as a function of the discharge voltage and in Fig 4.28 as a function of the anode mass flow rate. The 3 PPI configurations are operated at a constant mass flow rate of 1.0 mg/s to investigate the influence of the discharge voltage and a constant discharge voltage of 250 V to investigate the influence of the anode mass flow rate. As can be seen in Fig. 4.27, E_{max} increases with the discharge voltage for all 3 geometries. The lowest value of E_{max} is achieved for the S_0 configuration and the values for the $2S_0$ and the $3S_0$ configuration are almost the same. Figure 4.28 shows that for the two wider channel configurations, the anode mass flow rate has almost no influence on E_{max}. This was already observed with xenon as working gas. On the contrary, E_{max} decreases with an increasing anode mass flow rate for the S_0 configurations. As for all the previously investigated parameters, E_{max} is the lowest for the narrowest channel and the difference between the two wider channel configurations is insignificant. Similar results are obtained for the mean ion energy E_{mean}. Like with xenon, the measured E_{mean} values are smaller than the E_{max} values.

The efficiency ξ of the thruster discharge for converting the input electrical energy into kinetic energy can be inferred from the RPA measurements. The efficiency ξ is in fact defined by the following equation:

$$\xi = \frac{E_{max}}{(U_d - CRP)}. \tag{4.11}$$

The cathode-to-ground potential (CRP) is negative and therefore not accessible for the ion acceleration, i.e. this electrical energy can never be converted into kinetic energy. Note that one

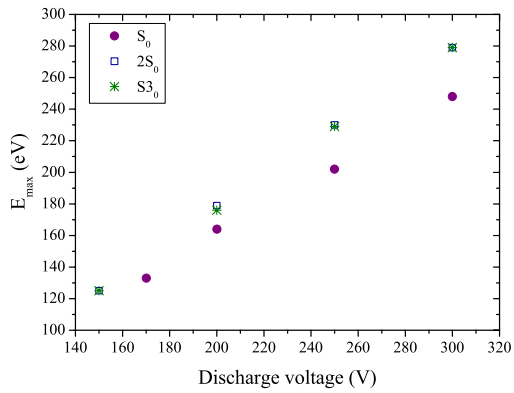

Figure 4.27: Most probable ion energy as a function of the discharge voltage for the 3 PPI configurations.

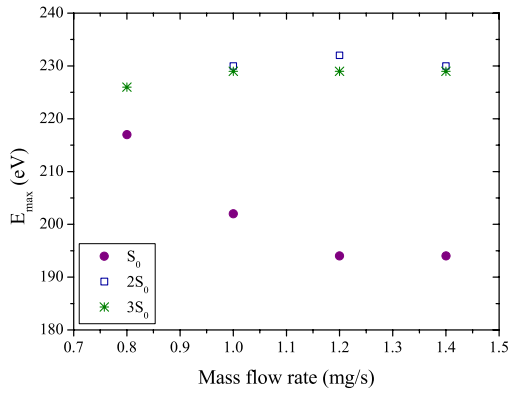

Figure 4.28: Most probable ion energy as a function of the anode mass flow rate for the 3 PPI configurations.

can also use the mean ion energy E_{mean} instead of E_{max}. The energy conversion efficiency ξ, calculated with E_{max}, is shown in Fig. 4.29 as a function of the discharge voltage and in Fig. 4.30 as a function of the anode mass flow rate. As can be seen in Fig. 4.29, ξ increases with the discharge voltage for the 3 PPI configurations. Again, ξ is the lowest for the S_0 configuration and there is almost no difference between the two other configurations. The energy conversion efficiency is almost independent of the anode mass flow rate for the two wider channel configurations and decreases with an increasing anode mass flow rate, as shown in Fig. 4.30. At high voltage, the energy conversion efficiency ξ can exceed 90 %.

The full width at half maximum of the IEDF is represented in Fig. 4.31 and Fig. 4.32 as a function of the discharge voltage and the anode mass, respectively. It increases with the discharge voltage for all 3 geometries. On the contrary, the FWHM decreasess with the anode mass flow rate for the $2S_0$ and the $3S_0$ configuration whereas is slightly increases with $\dot{m}_a$ for the S_0 configuration. The highest values of FWHM are achieved for the S_0 configuration and the lowest values are obtained with the $2S_0$ configuration. However, the difference between the two wider channel configurations is very small. That fact that the ion energy decreases and the FWHM increases with an increasing anode mass flow rate for the S_0 configuration indicates that the overlap of the ionization and the acceleration region is more important for this geometry than for the two other configurations.

4.5.3 Performances: thrust and anode efficiency

The PPI thruster was installed on the Low Thrust Balance (LTB) in the CORONA chamber. The thrust for the 3 PPI configurations is shown in Fig. 4.33 as a function of the input power. As can be seen, the thrust increases with the input power. The anode efficiency η_a is calculated using Eqn. 4.8. The results for the 3 geometries are represented in Fig. 4.34 as a function of the input power. Like the thrust, η_a increases with the input power. Contrary to the previously

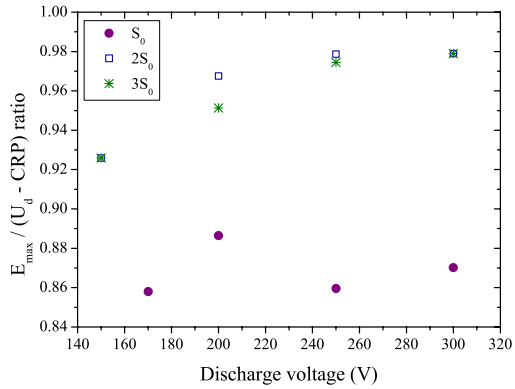

Figure 4.29: Energy conversion efficiency ξ as a function of the discharge voltage for the 3 PPI configurations.

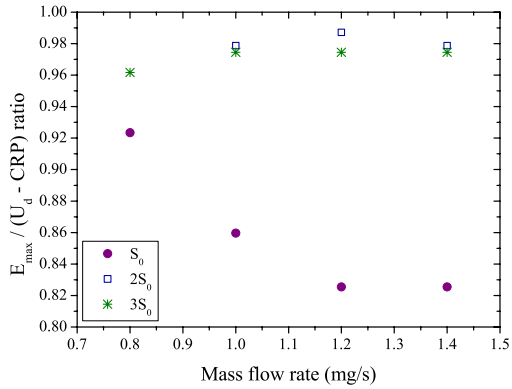

Figure 4.30: Energy conversion efficiency ξ as a function of the anode mass flow rate for the 3 PPI configurations.

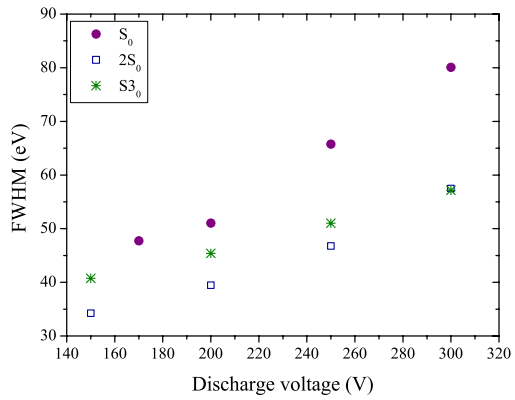

Figure 4.31: Full width at half maximum as a function of the discharge voltage for the 3 PPI configurations.

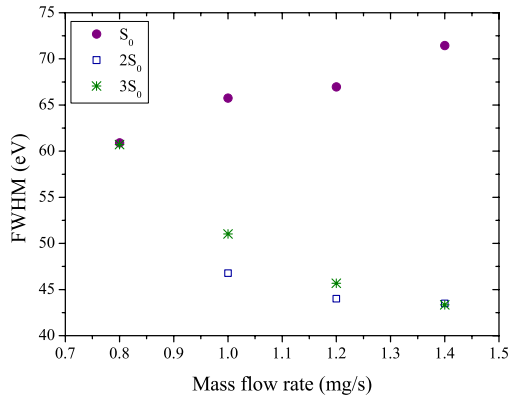

Figure 4.32: Full width at half maximum as a function of the anode mass flow rate for the 3 PPI configurations.

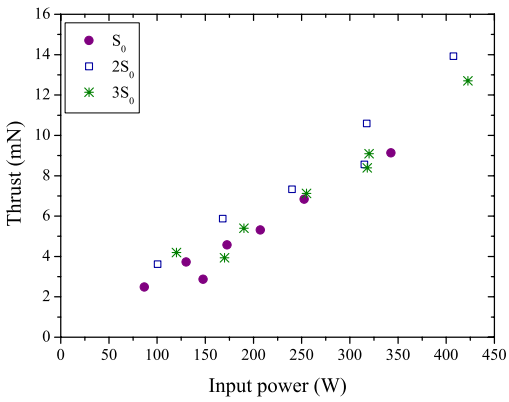

Figure 4.33: Thrust as a function of the input power for the 3 PPI configurations.

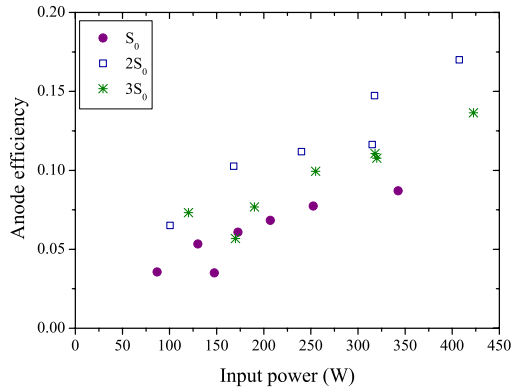

Figure 4.34: Anode efficiency as a function of the input power for the 3 PPI configurations.

Table 4.5: Comparison between measured and calculated thrust for the 3 PPI configurations at 200 V and 1.0 mg/s.

geometry	T_{mes}	T_{cal}
S_0	3.7 mN	4.1 mN
$2S_0$	5.9 mN	6.6 mN
$3S_0$	5.4 mN	6.3 mN

presented parameters, one cannot distinguish a clear influence of the channel width on the thrust. The anode efficiency is the lowest for the S_0 configuration and the highest for the $2S_0$ configuration. However, the difference is rather small. This might be due to the fact, that the discharge current, and therefore the input power, is much smaller for the S_0 configuration than for the two other geometries for the same operating conditions (U_d and $\dot{m}_a$), as can be seen in Tab. 4.4. Figure 4.35 and Figure 4.36 show the thrust and the anode efficiency for the 3 geometries as a function of the discharge voltage. In this case, the influence of the channel width is more pronounced. One can clearly distinguish that the lowest thrust, and hence the lowest anode efficiency, are delivered by the S_0 configuration whatever the operating conditions. It is also shown that the thrust and the anode efficiency increase with the mass flow rate and the discharge voltage for all three configurations. As explained in Sec. 4.3.6, the thrust can be calculated using Eq. 4.7 if one knows the total ion current as well as the ion velocity. For the PPI thruster operating with krypton, the ion velocity has been measured by LIF for the three geometries operating at 200 V and 1.0 mg/s. A comparison of the measured and calculated thrust for the 3 PPI configurations is given in Tab. 4.5. As can be seen, the calculated thrust is overestimated compared to the measured one, but the observed trends are the same: the lowest thrust is mesured with the S_0 configuration and the highest thrust is measured with the $2S_0$ configuration.

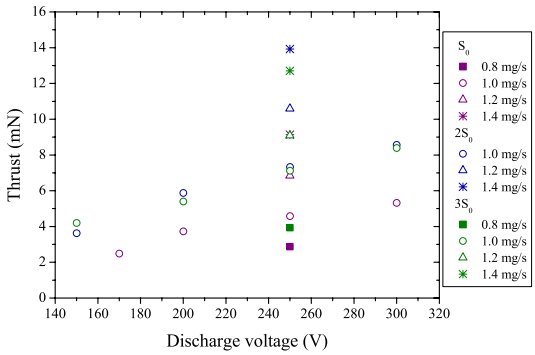

Figure 4.35: Thrust as a function of the input power for the 3 PPI configurations.

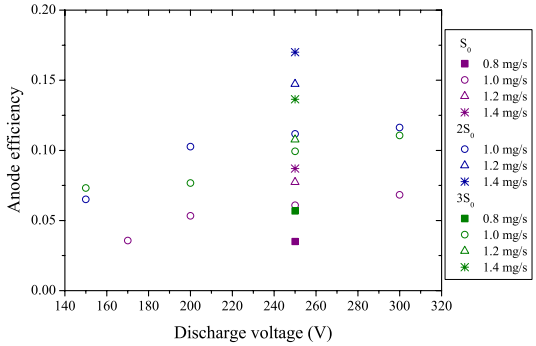

Figure 4.36: Anode efficiency as a function of the input power for the 3 PPI configurations.

Table 4.6: Comparison of the thruster performances for the 3 PPI configurations operated with xenon and krypton.

working gas	geometry	beam current efficiency	propellant utilization	energy conversion efficiency	anode efficiency
Xe	S_0	≈ 0.35	0.2 - 0.3	0.88 - 0.9	0.05 - 0.07
	$2S_0$	0.4 - 0.7	0.4 - 0.98	0.91 - 0.97	0.1 - 0.45
	$3S_0$	0.6 - 0.7	0.4 - 0.98	0.95 - 0.98	0.3 - 0.6
Kr	S_0	0.35 - 0.4	0.2 - 0.3	0.82 - 0.92	0.03 - 0.09
	$2S_0$	0.4 - 0.5	0.3 - 0.5	0.92 - 0.98	0.07 - 0.17
	$3S_0$	0.4 - 0.5	0.3 - 0.5	0.92 - 0.98	0.06 - 0.14

4.6 Comparison between xenon and krypton

As has been shown in Sec. 4.3 and Sec. 4.5, the channel width h influences the the ionization and acceleration processes as well as the performances of a low-power Hall thruster for both investigated working gases, namely xenon and krypton. The thruster performances in terms of beam current efficiency, propellant utilization, energy conversion efficiency as well as anode efficiency are summarized in Tab. 4.6.

As can be seen in Tab. 4.6, the performances of the S_0 configuration are almost the same for the two different gases. In both cases, they are well below the performances of the $2S_0$ and the $3S_0$ configuration. On the contrary, for the two larger channel geometries, the performances are cleary better for xenon than for krypton. This can be explained by the fact that the PPI thruster is optimized for a operation with xenon. In order to obtain better performances with krypton, the whole discharge channel geometry as well as the magnetic field topology would have to be modified. The influence of the working gas is not explicit for the narrowest channel, as the performance level is very low whatever the working gas. It can also be noticed that the energy conversion efficiency is almost similar for the two different working gases. The lower

anode efficiency with Kr is therefore due to a less efficient ionization.

4.7 Conclusion

A thorough analysis of existing Hall thruster has revealed a linear relationship between the channel width h and the channel mean diameter d whatever the thrust and power level. The aim of the present study was to investigate the influence of h on the ionization and acceleration processes as well as the performances of a low-power Hall thruster.
The low-power permanent magnet PPI thruster with a variable channel geometry was used. In fact, the channel width could easily be modified while keeping channel mean diameter and channel length constant. The PPI thruster was operated with xenon and krypton.
For both gases it has been shown that enlarging the channel of a low-power Hall thruster enhances ionization and acceleration processes, broadens the operating envelope and improves the thruster performances. Two mechanisms are proposed to explain experimental facts. First, the surface-to-volume ratio decreases with h, which reduces wall-losses. Second, the magnetic field strength near the walls increases with h, which leads to a better plasma confinement.
Note that so far the thrust has only been measured for krypton. One of the next experiments shall therefore consist in accurately measuring the thrust of the PPI Hall thruster for the three configurations operating with xenon.
The present study was performed with a low-power Hall thruster. It shows that the linear scaling of h with d should be modified for small thrusters in order to obtain a higher efficiency. However, it does not warrant the method can be successfully applied to large size devices. The surface-to-volume ratio is already great for high power thrusters. Moreover, technological constraints could appear due to the use of coils along with an iron circuit to produce the magnetic field.
However, the study is of great interest: It shows that the efficiency of low-power Hall thrusters, that is in general relatively low, can be increased by simply changing the channel width.

Chapter 5

Time-averaged measurements of electron properties [1]

5.1 Introduction

The plasma plume of a Hall thruster exhibits a relatively large divergence angle of about 45° [52]. A concern in the use of these devices is therefore the possible damage their plume may cause to the host spacecraft [66]. Although the plume is quasineutral, it still consists of charged particles, which can lead to electrical and mechanical interactions with the spacecraft. The impact of the plume on the solar arrays may lead to a thrust loss and a torque affection of the spacecraft attitude and therefore cause a propellant overconsumtion. The sputtering yield of xenon ions is significant. The spacecraft surfaces close to the exhaust beam, e.g. solar arrays, will be degraded due to erosion. Furthermore, onboard optical devices can be contaminated by the sputtered material. The re-deposition of the charged particles leads to a charging of the spacecraft and may cause short circuit and arcs which are potentially hazardous for the onboard electronic devices. The transient behavior of the plume may also be responsible for radio-electric noise. It is thus important to develop and improve numerical models of the plume in order to help assessing the spacecraft integration issues. The numerical models of the thruster plume need to be validated by comparison with experimental data. Therefore the entire plasma plume needs to be mapped to obtain ion, electron and neutral properties.

So far most of the experimental plasma plume investigations for the comparison with numerical plume models have been focused on ion properties [67, 68, 69]. However, the global dynamic of the discharge is controlled by the electrons. Hence, in the presented work, electron properties in the far-field plume of a Hall thruster are extensively investigated using electrostatic probes, in order to provide new experimental data for the validation of numerical plume models taking into account the electron properties. Electrostatic probes can be used to measure the electron properties. The plasma potential V_p, the electron temperature T_e and the electron density n_e can be measured by means of a cylindrical Langmuir probe. The plasma potential can also be measured with a heated emissive probe.

The time-averaged values of V_p, T_e and n_e have been measured with a Langmuir and an emissive probe for different operating conditions of the 1.5 kW-class PPS®100-ML thruster. The far-field plume is mapped between 300 and 660 mm downstream the thruster exit plane and between 0 and 60 °, where 0 ° corresponds to the thruster axis. The influence of the discharge voltage U_d, the anode mass flow rate $\dot{m}_a$, the cathode mass flow rate $\dot{m}_c$ as well as the magnetic field strength are investigated. Plasma potential and electron temperature values obtained with

[1] Adapted from:
K. Dannenmayer et al., *Plasma Sources Sci. Technol.* **20**, 065012 (2011)

both types of probes are compared.
In the last part of this chapter a new fast-moving probe system is introduced. This system is based on a ultrasonic piezo linear drive that allows the insertion and removal of an electrostatic probe into the plasma plume with a speed of up to 350 mm/s. Given the very short residence time of the probe in the plasma plume with this system, measurements of the plasma parameters in the near-field plume are possible. A first validation of the system was performed in the near-field plume of the low power PPI Hall thruster.

5.2 Probes

Electrostatic probes are a simple and versatile diagnostic tools for the experimental investigation of plasma properties. In the present work, a Langmuir and an emissive probe were used to investigate the electron properties in the far-field plume of a Hall thruster. The two different probes are briefly described in this section before presenting the experimental results.

5.2.1 Langmuir probe

A single cylindrical Langmuir probe was used to characterize the far-field plume of the PPS® 100-ML. The Langmuir probe was made of a 0.38 mm in diameter tungsten wire. The non-collecting part of the wire was insulated from the plasma by a 100 mm long and 2 mm in diameter alumina tube. The length of the collecting part was 5 mm. The probe axis was oriented parallel to the thruster axis. Since the Debye length was small compared to the probe radius no irregularities in ion collection as described e.g. in [70] are expected. The voltage sweep and the resulting probe current measurement were performed using the ALP System^{TM} manufactured by Impedans. The measured electron energy distribution function was in its lower-energetic part close to Maxwellian. Consequently, the parameters V_p, T_e and n_e were derived from the probe characteristics using the standard Langmuir probe theory assuming a Maxwellian electron distribution function [71, 72]. The plasma potential is obtained from the maximum of the first derivative of the probe characteristic ($V_p = (dI/dV)_{max}$). It can also be obtained from the intersection of linear fits in the transition and electron saturation region. The electron temperature is determined from the slope of the logarithm of the electron current in the transition region ($T_e = (\frac{d \ln I_e}{dV})^{-1}$). The electron density is calculated using the Orbit Motion Limited (OML) assumption. In the OML regime the slope of I_e^2 vs V plot is proportional to n_e^2. An example of a current-voltage characteristic and the resulting analysis is given in Fig. 5.1.

5.2.2 Emissive probe

The plasma potential can also be measured by means of an emissive probe. Different techniques exist to determine V_p from an emissive probe, e.g. the separation technique, the floating point with large emission technique, as well as the inflection point method [73]. In the present work, the floating point method was used, as it provides a direct measurement of V_p, if one does not account for the influence of the electron temperature.
The emitting part of the probe consisted of a 8 mm long loop of 150 μm in diameter thoriated

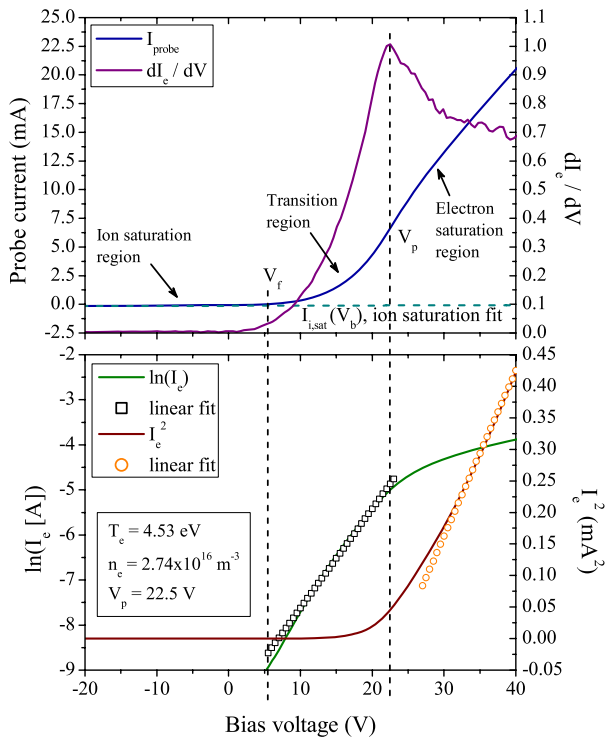

Figure 5.1: Example of a current-voltage characteristic recorded at a discharge voltage of 200 V and a mass flow rate of 4.0 mg/s. The probe was located at 300 mm downstream the thruster exit plane on the thruster axis.

tungsten wire. The ends of the wire were mechanically crimped to copper wires and inserted into two parallel holes of a 100 mm long and 4 mm in diameter alumina tube. A picture of the emissive probe and all components necessary to built the probe are shown in Fig. 5.2. The filament was heated with a DC power supply up to the regime of electron emission. In the ideal case the floating potential of a sufficiently emitting probe is equal to the plasma potential. In this case the electron current is completely compensated by the emission current from the probe, therefore no net current flows through the probe and there is no sheath around the probe [74]. However the electrons emitted by the probe are usually colder than the electrons in the plasma. The space charge of the cold emitted electrons causes a saturation of the sheath around the hot filament and therefore the measured probe potential is not exactly equal to the plasma potential [75]. If the temperature of the plasma electrons is large compared to the temperature of the emitted electrons, the plasma potential measured with the emissive probe is underestimated. If the emitted electrons and the plasma electrons have approximately the same temperature, the value of the plasma potential measured by the emissive probe is overestimated. The electron temperature can also be determined from the emissive probe mea-

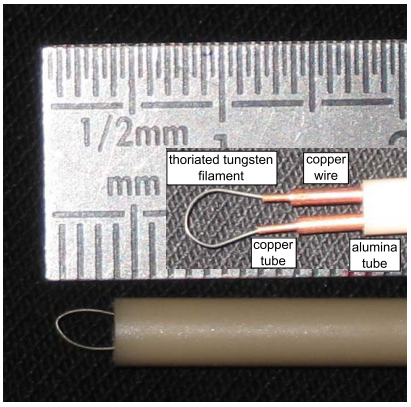

Figure 5.2: Picture of the emissive probe. Also shown are all the different elements necessary to built the probe.

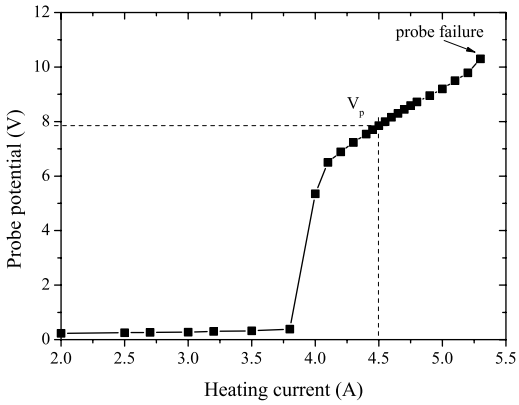

Figure 5.3: Emissive probe potential against the heating current in the far-field plume of the PPS®100-ML thruster.

surements. Therefore the probe floating potential has to be recorded for the cold probe as well as for the sufficiently heated probe. The electron temperature can then be determined using an adequate model of the collected electron and ion current [76, 77].
Before measuring the plasma potential, one needs to determine the necessary heating current of the probe to be in the saturation region of the probe floating potential. The heating current is increased step by step and the resulting floating potential is recorded. A typical measurement of the probe potential as a function of the heating current is depicted in Fig. 5.3. As can be seen in Fig. 5.3, the probe potential never really saturates but the slope clearly levels off if the current is increased above 4 A. This has already been observed in other thrusters and plasma sources [75, 78]. For the measurement of the plasma potential in the far-field, the heating current was fixed to 4.5 A. The lifetime of the emissive probe in the far-field plume was in the order of several hours allowing a complete mapping of the far-field with one probe.

5.3 Time-averaged measurements in the far-field plume of the PPS®100-ML

The experimental work was carried out in the plume of PPS®100-ML Hall thruster, operating in the PIVOINE-2g test chamber. Two different versions of the PPS®100-ML thruster were used: the magnetic field was either provided by coils or permanent magnets [15]. The magnetic field is approximately the same for the two thruster versions. The thruster was mounted on a moveable arm, that allows a displacement of the thruster along the thruster axis (x-direction). The diagnostics were mounted on a second arm that moves perpendicular to the thruster axis (y-direction). A rotation stage at the end of the diagnostics arm allowed a displacement of the probes in the θ-direction, so that the probes always pointed towards the thruster center, see

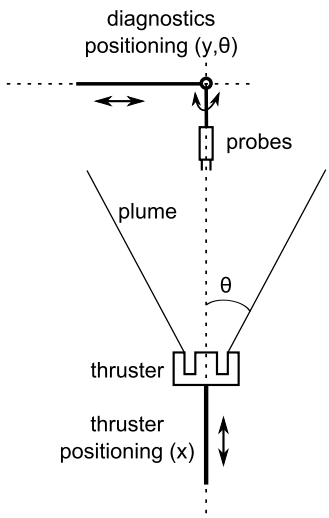

Figure 5.4: Schematic view of the Hall thruster and probe positioning system.

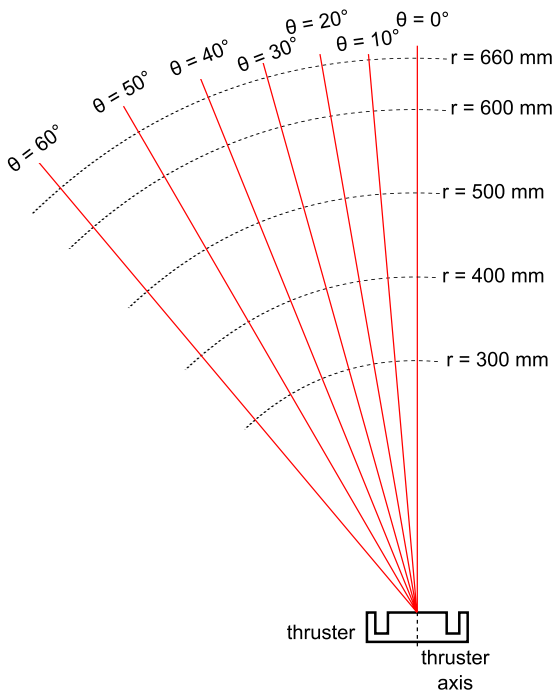

Figure 5.5: Schematic view of the different measurement positions in the far-field plume of the PPS®100-ML thruster.

Fig. 5.4. The combination of the displacement of the probes in the y and θ-direction together with the possibility to move the thruster along its axis allowed to map the complete far-field plume. For the present study the far-field plume was mapped from 300 to 660 mm downstream the thruster exit plane and from 0 to 60 °, where 0 ° corresponds to the thruster axis (see Fig. 5.5).

Both probes were mounted next to each other in the far-field plume. The probes were oriented parallel to the thruster axis. An examination of the discharge current time evolution with and without the probes revealed that the probes do not influence the discharge behavior whatever the probe position. The measurements with the Langmuir probe and the emissive probe were carried out simultaneously after verification that the two measurements do not influence each other. The measurement of the plasma parameters in the far-field plume of the PPS®100-ML are presented for different operating conditions of the thruster. The discharge voltage, the anode and cathode mass flow rate and the coil current are varied in order to check their influence on V_p, T_e and n_e. For every operating condition the discharge current oscillations and the cathode potential towards ground are recorded. The discharge parameters for the different operating conditions are represented in Tab. 5.1.

Table 5.1: Mean discharge current, current standard deviation and cathode potential to ground for the different operating conditions of the PPS®100-ML thruster. The abbreviation "p.m." stands for "permanent magnets".

Dischage voltage U_d (V)	Anode mass flow rate $\dot{m}_a$ (mg/s)	Cathode mass flow rate $\dot{m}_c$ (mg/s)	Coil current I_b (A)	Mean discharge current $\bar{I}_d$ (A)	Current standard deviation (A)	Cathode potential to ground (V)
150	4.0	0.42	p. m.	3.46	0.23	-13.2
200	4.0	0.42	p. m.	3.47	0.12	-14.4
200	2.5	0.42	p. m.	1.89	0.35	-14.4
300	4.0	0.42	p. m.	3.65	0.35	-15.1
300	4.0	0.3	p. m.	3.58	0.26	-19.2
300	4.0	0.5	p. m.	3.67	0.34	-14.6
200	2.5	0.42	2.5	2.09	0.46	-12.2
200	2.5	0.42	4.5	1.9	0.17	-14.7
200	2.5	0.42	5.5	1.93	0.43	-14.5

5.3.1 Complete map of the far-field plume

An example for a complete map of the plasma parameters (V_p, T_e and n_e) in the far-field plume between 300 and 660 mm and from 0 to 60 ° measured with a Langmuir probe is shown in Fig. 5.6. The full contour plot of the electron properties is interpolated from values measured at 35 different positions in the plume. The PPS®100-ML is fired at a discharge voltage of $U_d = 300\,\mathrm{V}$, an anode mass flow rate of $\dot{m}_a = 4.0\,\mathrm{mg/s}$ and a cathode mass flow rate of $\dot{m}_c = 0.42\,\mathrm{mg/s}$. The magnetic field is provided by permanent magnets. As can be seen in Fig. 5.6, V_p, T_e and n_e decrease with an increasing distance from the thruster exit plane and from the thruster axis. This can be explained by the fact that the plume of a Hall thruster is an expanding plasma jet.

5.3.1.1 Electron flow properties in the far-field plume

The data from this complete far-field map can be used for a more detailed analysis of the electron flow properties in the far-field plume of a Hall thruster.
The expansion of a plasma into a vacuum can often be considered as a steady expansion. The flow which is initially in thermodynamic equilibrium can be assumed to be adiabatic and if the flow is laminar, the expansion is isentropic. For a steady isentropic flow, the energy conservation can be replaced by the Poisson adiabatic law:

$$\left(\frac{n_e}{n_0}\right)^{\gamma-1} = \frac{T_e}{T_{e,0}}, \tag{5.1}$$

where γ is the specific heat ratio or isentropic exponent and $T_{e,0}$ the average, or a reference, electron temperature [80]. Figure 5.7 represents the normalized electron temperature as a func-

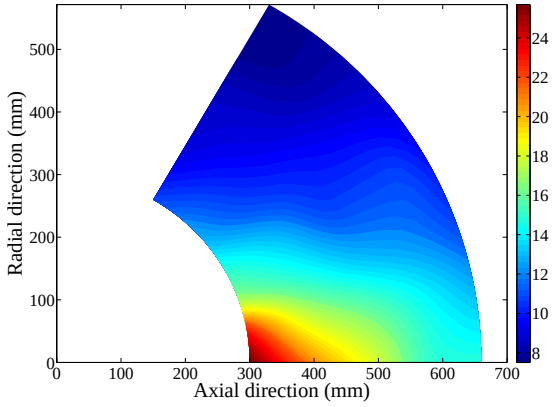

(a) Plasma potential (V)

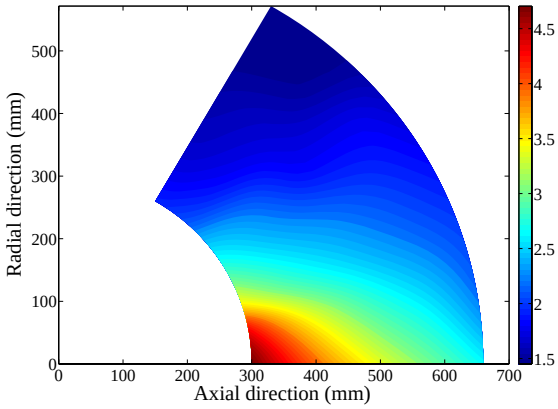

(b) Electron temperature (eV)

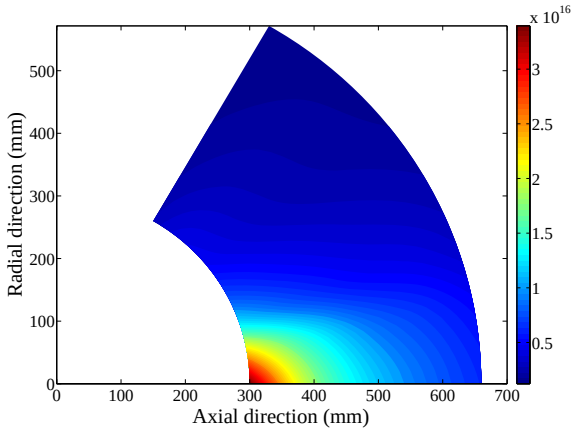

(c) Electron density (m^{-3})

Figure 5.6: Complete map of the plasma parameters (V_p, T_e and n_e) in the far-field plume for $U_d = 300\,\mathrm{V}$, $\dot{m}_a = 4.0\,\mathrm{mg/s}$.

tion of the normalized electron density for the 35 different measurement positions in the far-field plume of the PPS®100-ML thruster operating at 300 V and 4.0 mg/s. The isentropic fit is also represented (dashed line). As can be seen, the plasma plume of a Hall thruster is an isentropic expansion. The isentropic exponent γ is 1.373 for the presented fit. The theoretical isentropic exponent for xenon is: $\gamma = 5/3$ (atomic gas). However, in a plasma the value of γ is lower than the theoretical value for the gas as an additional degree of freedom is caused by ionization [81]. The fact that the plasma plume is an isentropic expansion is in agreement with the isentropic model of the electron transport presented by Knoll [82].
The electron flow properties can also be analyzed with respect to the momentum conservation equation. Assuming that the electron flow is in steady state $\left(\frac{D}{Dt} = 0\right)$ and that there is no magnetic field, the stationary electron momentum conservation equations can be written as the balance between the electron pressure and the electric field [79]:

$$0 = -\nabla p_e - e\, n_e \mathbf{E}. \tag{5.2}$$

The electric field $\mathbf{E}$ can be represented as the gradient of the plasma potential ($\mathbf{E} = -\nabla V_p$). For a constant electron temperature, Eq. 5.2 leads to the well-known *Boltzmann law* which relates the stationary electron density to the plasma potential:

$$n_e = n_0\, exp\left(\frac{V_p}{\hat{T}_e}\right), \tag{5.3}$$

where n_0 is the average electron density and $\hat{T}_e$ is in eV [79]. Figure 5.8 shows n_e as a function of $V_p\,/\,T_e$ for the 35 different measurement positions in the far-field plume of the PPS®100-ML thruster operating at 300 V and 4.0 mg/s. As can be seen, the Boltzmann law is not valid in the far-field plume of a Hall thruster. This is in fact logical, as the electron temperature in the plasma plume is not constant. For the non-isothermal case, Eq. 5.2 leads to the following relationships between the electron density and the plasma potential and between the plasma potential and the electron temperature:

$$V_p \propto n_e^{\gamma-1} \qquad \text{and} \qquad V_p \propto T_e, \tag{5.4}$$

where γ is the isentropic exponent. Figure 5.9 shows the plasma potential as a function of the electron density for the 35 different measurement positions in the far-field plume of the PPS®100-ML. As can be seen, the stationary electron momentum conservation equation is valid in the plasma plume of a Hall thruster. The value of γ obtained from Eq. 5.4 is 1.371. This value is in good agreement with the one obtained from Eq. 5.1.

Figure 5.10 shows the electron temperature as a function of the plasma potential for the 35 different measurement positions in the far-field plume of the PPS®100-ML. As can be seen, T_e is proportional to V_p as expected from the momentum conservation equation.

5.3.2 Influence of the discharge voltage

The influence of the discharge voltage on the plasma parameters is investigated at constant anode and cathode mass flow rates ($\dot{m}_a = 4.0$ mg/s and $\dot{m}_c = 0.42$ mg/s). The magnetic field is again provided by permanent magnets. Figure 5.11 shows the variation of V_p, T_e and n_e measured with a Langmuir probe as a function of the angle θ for three different discharge voltages.

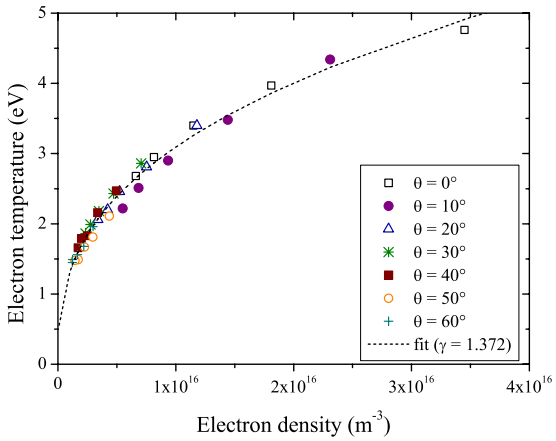

Figure 5.7: Electron temperature as a function of the electron density in the far-field plume of the PPS®100-ML operating at 300 V and 4.0 mg. The isentropic fit is also shown (dashed line).

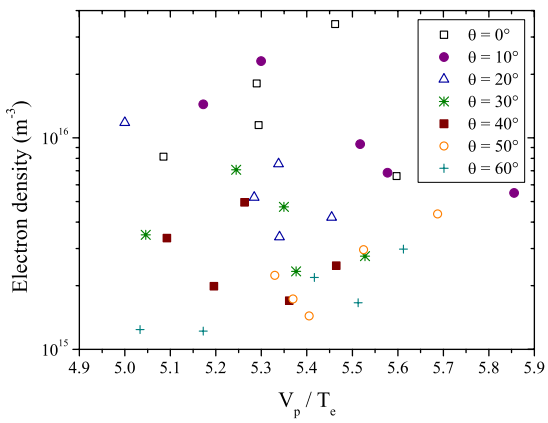

Figure 5.8: Electron density (log scale) as a function of the V_p / T_e ratio in the far-field plume of the PPS®100-ML operating at 300 V and 4.0 mg.

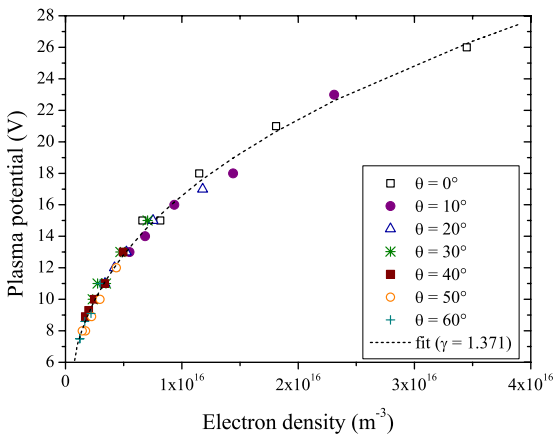

Figure 5.9: Plasma potential as a function of the electron density in the far-field plume of the PPS®100-ML operating at 300 V and 4.0 mg. The corresponding fit is also shown (dashed line).

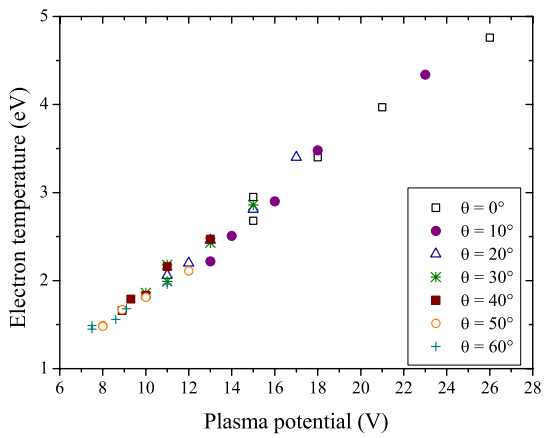

Figure 5.10: Electron temperature as a function of the plasma potential in the far-field plume of the PPS®100-ML operating at 300 V and 4.0 mg.

For clarity reasons the results are solely presented for two different distances from the thruster exit plane, 300 and 500 mm respectively.

The cathode potential to ground is very similar for the three operating conditions: $CRP = -14 \pm 1$ V, see Tab. 5.1. As can be seen in Tab. 5.1, the mean discharge current is almost the same for a discharge voltage of 150 V and 200 V, the current standard deviation is higher for $U_d = 150$ V. For $U_d = 300$ V the mean discharge current as well as the current standard deviation are the highest.

As can be seen in Fig. 5.11(a), the plasma potential V_p decreases with the angle θ. For angles smaller than 20 ° the plasma potential is higher for a higher discharge voltage. For $\theta > 20°$, there is no clear difference for the 3 different operating conditions. The electron temperature T_e also decreases with the angle θ, as shown in Fig. 5.11(b). For $\theta < 30°$, the electron temperature is higher for a higher discharge voltage, whereas for $\theta > 30°$, there is almost no difference for the 3 different discharge voltages. Figure 5.11(c) shows that the electron density n_e decreases with the angle θ. The electron density drops by a factor of 3 for $U_d = 300$ V, respectively by a factor of 2 for $U_d = 200$ V and by a factor of 1.5 for $U_d = 150$ V. Similar results for a SPT100 have been observed by Myers et al. [83].

5.3.3 Influence of the anode mass flow rate

The influence of the anode mass flow rate on V_p, T_e and n_e was investigated at a discharge voltage of 200 V and a constant cathode mass flow rate of 0.42 mg/s. The magnetic field was provided by permanent magnets. Fig. 5.12 shows V_p, T_e and n_e as a function of the angle θ at 300 and 500 mm downstream the thruster axis for the two different anode mass flow rates ($\dot{m}_a = 2.5$ and 4.0 mg/s).

The cathode potential is the same for the two different anode mass flow rates. As can be seen in Tab. 5.1, the mean discharge current is of course higher for 4.0 mg/s than for 2.5 mg/s, whereas the current standard deviation is higher for the lower anode mass flow rate.

The plasma potential, the electron temperature as well as the electron density measured with the Langmuir probe decrease with an increasing distance from the thruster exit plane and the thruster axis, as can be seen in Fig. 5.12. All three parameters are higher for the higher anode mass flow rate.

5.3.4 Influence of the cathode mass flow rate

The far-field plume of the PPS®100-ML with permanent magnets has been mapped for 3 different cathode mass flow rates ($\dot{m}_c = 0.3$, 0.42 and 0.5 mg/s) at a discharge voltage of $U_d = 300$ V and a constant anode mass flow rate of $\dot{m}_a = 4.0$ mg/s. Results of the Langmuir probe measurements are shown in Fig. 5.13 for two different distances from the thruster exit plane.

The cathode potential to ground is almost the same for $\dot{m}_c = 0.42$ and 0.5 mg/s, whereas it is significantly higher for $\dot{m}_c = 0.3$ mg/s, as can be seen in Tab. 5.1. As shown in Tab. 5.1, the mean discharge current and the current standard deviation are slightly lower for the lowest cathode mass flow rate and almost identical for the two higher cathode mass flow rates.

Figure 5.13(a) shows the evolution of the plasma potential V_p. As can be seen, the values of

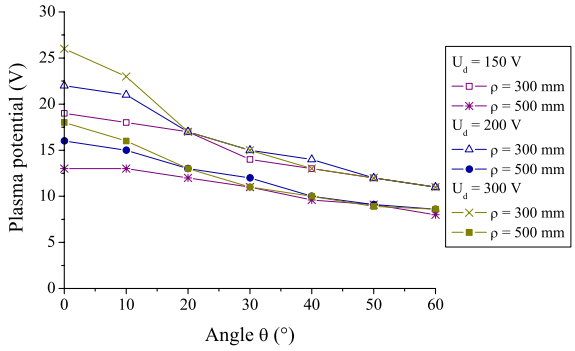

(a) Plasma potential

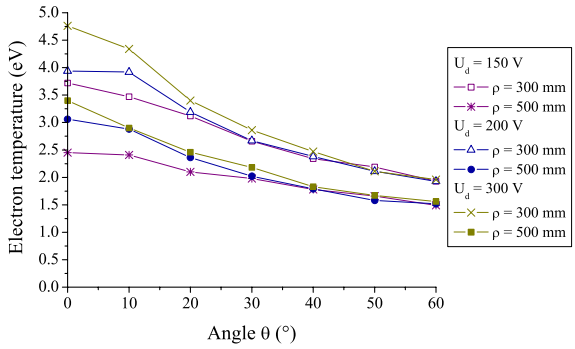

(b) Electron temperature

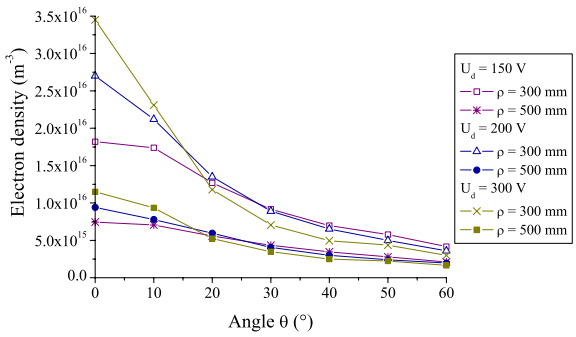

(c) Electron density

Figure 5.11: Influence of the discharge voltage on the plasma parameters for $\dot{m}_a = 4.0\,\mathrm{mg/s}$ and $\dot{m}_c = 0.42\,\mathrm{mg/s}$.

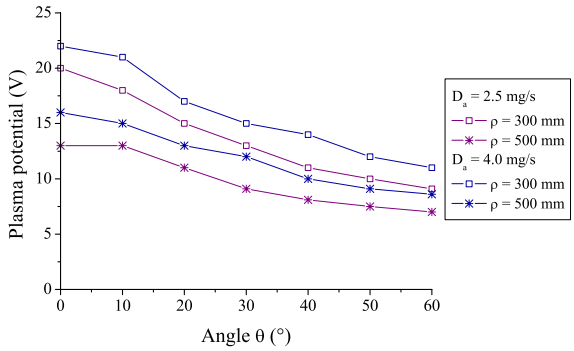

(a) Plasma potential

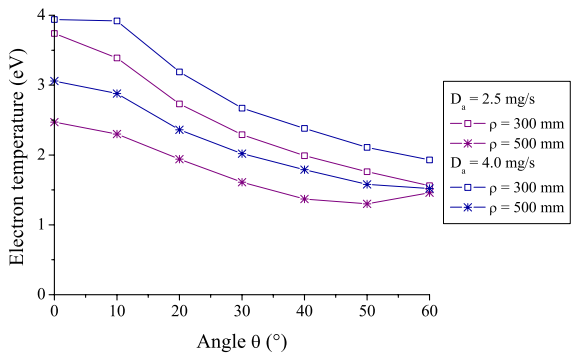

(b) Electron temperature

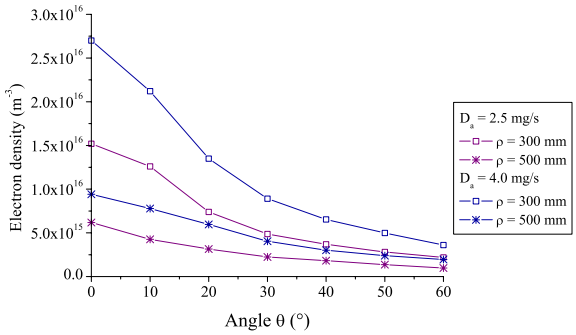

(c) Electron density

Figure 5.12: Influence of the anode mass flow rate on the plasma parameters for $U_d = 200\,\mathrm{V}$, $\dot{m}_c = 0.42\,\mathrm{mg/s}$.

V_p are almost the same for $\dot{m}_c = 0.42\,\mathrm{mg/s}$ and $\dot{m}_c = 0.5\,\mathrm{mg/s}$. For $\dot{m}_c = 0.3\,\mathrm{mg/s}$, the values of V_p are higher than for the 2 other cathode mass flow rates. The electron temperature T_e is represented in Fig. 5.13(b). The highest values of T_e can be observed for $\dot{m}_c = 0.3\,\mathrm{mg/s}$ and the lowest values of T_e are measured for $\dot{m}_c = 0.5\,\mathrm{mg/s}$. However, the difference for the two higher cathode mass flow rates is very small. As can be seen in Fig. 5.13(c), there is almost no difference for the electron density n_e for the 3 different cathode mass flow rates.

For the 3 different cathode mass flow rates, the cathode-to-ground potential is different as can be seen in Tab. 5.1. In order to clearly distinguish between the influence of the cathode-to-ground potential and the cathode mass flow rate, further experiments are necessary.

The influence of the cathode-to-ground potential CRP and the cathode mass flow rate on the plasma potential, the electron temperature as well as the electron density has been investigated using the low-power PPI Hall thruster in the $2S_0$ configuration. The thruster has been operated with three different cathode mass flow rates and different CRPs, in order to investigate the influence of these two parameters. The CRP can be varied by changing the heating current of the hollow cathode used with the PPI. A higher heating current facilitates the emission of electrons and the CRP is thus less negative. A Langmuir probe was used to measure V_p, T_e and n_e. The probe was positioned 165 mm downstream the thruster exit plane on the thruster axis. An emissive probe was placed next to the Langmuir probe to obtain a direct measurement of the plasma potential. The results obtained by both probes are in good agreement. The PPI thruster was operated in the NExET test bench at two different operating conditions: first with a discharge voltage of 200 V and an anode mass flow rate of 1.0 mg/s and second at 250 V and 0.8 mg/s. The cathode mass flow rate was set to 0.1, 0.2 and 0.3 mg/s and the CRP was changed by changing the cathode heating current from 12.7 to 15 A. The discharge current is slightly influenced by both the cathode mass flow rate and the cathode-to-ground potential: it increases with the mass flow rate and decreases with an increasing CRP (i.e. a less negative CRP). Fig. 5.14 shows the influence of the cathode mass flow rate as well as the cathode-to-ground potential on V_p, T_e and n_e. As can be seen, the plasma potential and the electron temperature increase with an increasing CRP for all 3 cathode mass flow rates for the 2 different operating conditions as the electrons acquire more energy, whereas the electron density decreases with an increasing CRP. Furthermore one can observe that V_p and T_e decrease with an increasing cathode mass flow rate due to an increasing number of collisions, which lead to cooling. On the contrary, the electron density increases with an increasing cathode mass flow rate. A higher cathode mass flow rate leads to an increased ion bombardment of the emitting material and hence a higher n_e. This is in agreement with what was observed for the PPS®100-ML. This study reveals that both the cathode mass flow rate $\dot{m}_c$ as well as the cathode-to-ground potential CRP influence the plasma parameters. However, the influence of $\dot{m}_c$ is more pronounced than the influence of CRP.

5.3.5 Influence of the magnetic field strength

The far-field plume of the standard version of PPS®100-ML (with coils) has been mapped for 3 different currents through the coils at a discharge voltage $U_d = 200\,\mathrm{V}$, a constant anode mass flow rate $\dot{m}_a = 2.5\,\mathrm{mg/s}$ as well as a constant cathode mass flow rate $\dot{m}_c = 0.42\,\mathrm{mg/s}$. The

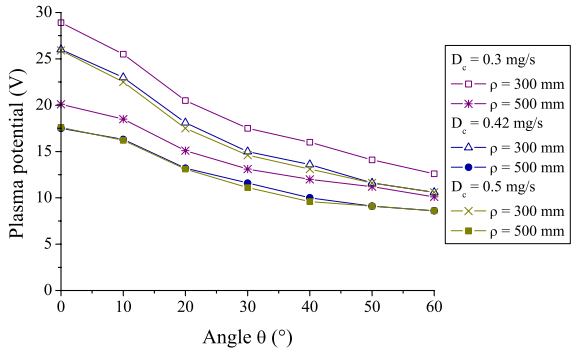

(a) Plasma potential

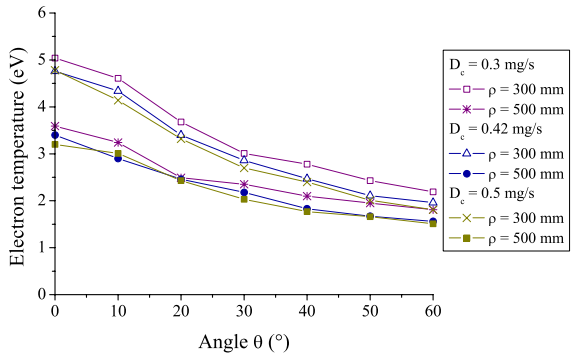

(b) Electron temperature

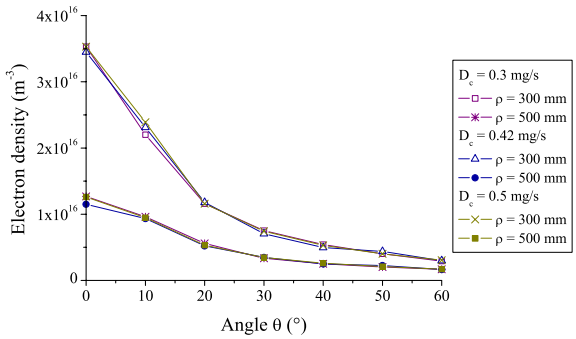

(c) Electron density

Figure 5.13: Influence of the cathode mass flow rate on V_p, T_e and n_e for $U_d = 300\,\mathrm{V}$, $\dot{m}_a = 4.0\,\mathrm{mg/s}$.

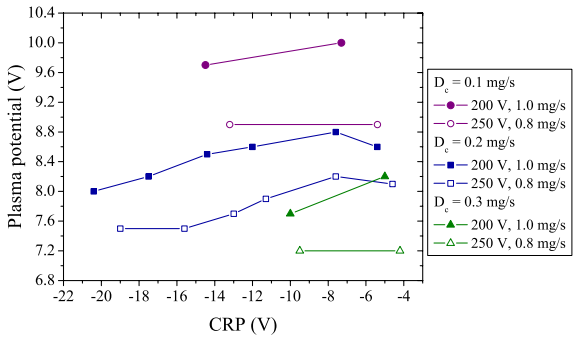

(a) Plasma potential

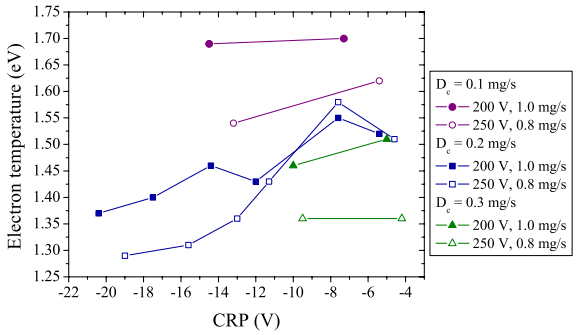

(b) Electron temperature

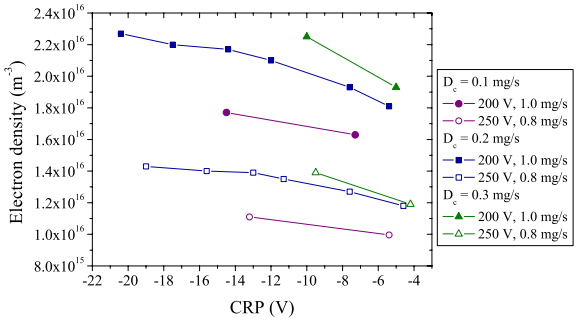

(c) Electron density

Figure 5.14: Influence of CRP and cathode mass flow rate on V_p, T_e and n_e. The PPI thruster is operated at 200 V and 1.0 mg/s (full symbols) as well as at 250 V and 0.8 mg/s (open symbols).

coil current was varied between 2.5 and 5.5 A which corresponds to a change of the maximum magnetic field strength from about 100 to 200 G. The optimized magnetic field topologie of the PPS®100-ML is obtained for a coil current of 4.5 A. The evolution of V_p, T_e and n_e measured with a Langmuir probe is depicted in Fig. 5.15 for two different distances from the thruster exit plane.

Table 5.1 shows that the cathode potential to ground is almost the same for $I_b = 4.5$ A and $I_b = 5.5$ A, whereas it is lower for $I_b = 2.5$ A. The mean discharge current is very similar for the two higher coil currents and slightly higher for the lowest coil current. The discharge currrent standard deviation is almost the same for $I_b = 2.5$ A and $I_b = 5.5$ A, but significantly lower for $I_b = 4.5$ A. This is in agreement with the fact the magnetic field topologie is optimized for 4.5 A.

The plasma potential V_p is represented in Fig. 5.15(a), it decreases with the angle θ. The highest values for V_p can be observed for $I_b = 5.5$ A. At the distance of 500 mm from the thruster exit plane, the values of V_p are almost the same for $I_b = 4.5$ A and $I_b = 5.5$ A. The values for $I_b = 2.5$ A are significantly lower. The evolution of the electron temperature T_e is represented in Fig. 5.15(b). The values for $I_b = 4.5$ A and $I_b = 5.5$ A are very close, especially at a distance of 500 mm from the thruster exit. At 300 mm, T_e is decreasing up to an angle of about 50 ° whereas for $\theta > 50°$, T_e is almost constant. At 500 mm, T_e decreases up to an angle of 20 ° and is almost constant for higher angles. The values for $I_b = 2.5$ A are significantly lower than for the two other coil currents I_b. For this configuration T_e decreases up to an angle of 40 ° and for higher angles T_e is almost constant. The evolution of the electron density n_e is represented in Fig. 5.15(c). The values for n_e are almost the same for the three different currents I_b, solely for $I_b = 2.5$ A n_e is slightly higher at $\theta = 0°$.

5.3.6 Comparison between Langmuir and emissive probe

For all the different operating conditions, the plasma potential V_p was measured with a Langmuir and an emissive probe. The plasma potential is assumed to be determined by the floating potential of the emissive probe heated with a current of 4.5 A. An example for the plasma potential measured with the emissive probe is given in Fig. 5.16. The PPS®100-ML with permanent magnets was operated at discharge voltage of $U_d = 200$ V with an anode mass flow rate of $\dot{m}_a = 4.0$ mg/s and a cathode mass flow rate of $\dot{m}_c = 0.42$ mg/s. The profiles of V_p for the map have been interpolated from the values measured at the 35 different positions in the far-field. As can be seen, the far-field map of V_p looks similar to the one measured by the Langmuir probe (see Fig. 5.6(a)). The plasma potential decreases with the distance from the thruster exit plane and from the thruster axis.

Figure 5.17 shows the fractional difference D_{V_p} between the values measured with the Langmuir and the emissive probe, where $D_{V_p} = (V_{p,EP} - V_{p,LP})/V_{p,mean}$. As can be seen in Fig. 5.17, values of the plasma potential obtained with a Langmuir and an emissive probe are in relatively good agreement. The difference between the results obtained by both types of probes is in the order of 5 to 10 %, except for angles above 50 ° and more than 500 mm downstream the thruster exit plane. In this region the value of V_p is relatively small, which leads to a larger fractional difference. As can be seen in Fig. 5.17, in the region of higher electron temperature, i.e. close

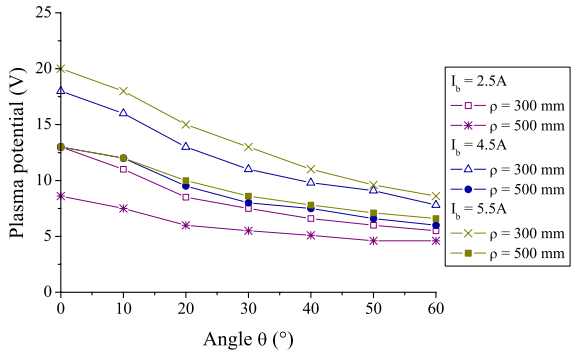

(a) Plasma potential

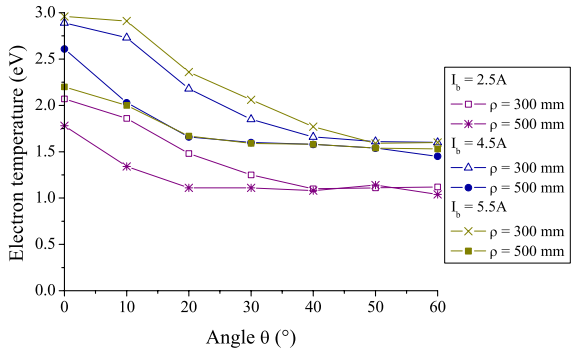

(b) Electron temperature

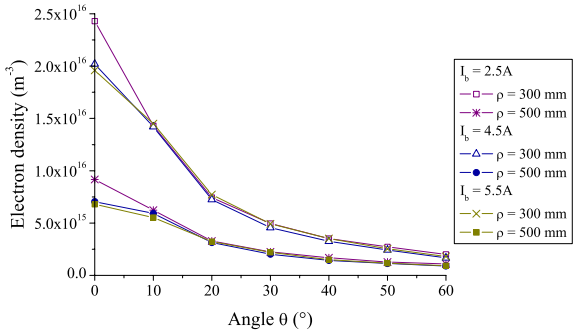

(c) Electron density

Figure 5.15: Influence of the coil current on the plasma parameters for $U_d = 200\,\mathrm{V}$, $\dot{m}_a = 2.5\,\mathrm{mg/s}$ and $\dot{m}_c = 0.42\,\mathrm{mg/s}$.

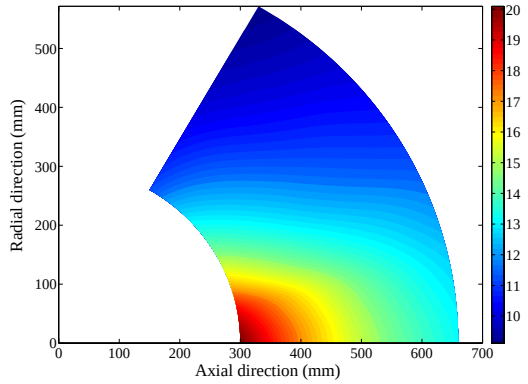

Figure 5.16: Plasma potential measured with an emissive probe in the far-field plume of the PPS®100-ML with permanent magnets at $U_d = 200\,\mathrm{V}$ and $\dot{m}_a = 4.0\,\mathrm{mg/s}$.

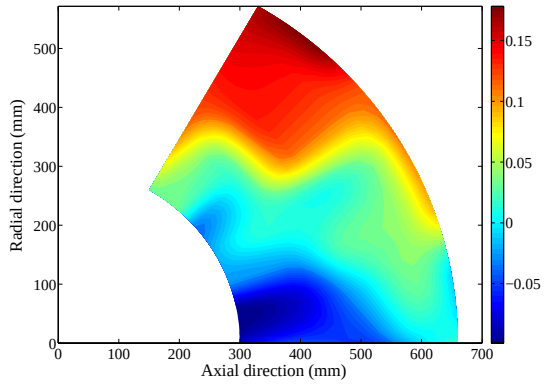

Figure 5.17: Fractional difference of plasma potential D_{V_p} measured with an emissive probe (EP) and a Langmuir probe (LP) for the PPS®100-ML operating at $U_d = 200\,\mathrm{V}$ and $\dot{m}_a = 4.0\,\mathrm{mg/s}$.

to the thruster axis, the emissive probe gives slightly lower values for the plasma potential than the Langmuir probe. In the region with a lower electron temperature, the plasma potential measured with the emissive probe is higher than the one measured with the Langmuir probe. This qualitatively agrees with considerations described in Section 5.2.2 and in [84]. Similar trends have also been observed by Marek et al. in a low temperature Argon plasma [75].
The electron temperature can be determined from emissive probe measurements using the floating potential of the cold (ϕ_{fl}^{cold}) and the heated probe, which is assumed to be the plasma potential ($\phi_{fl}^{hot} = V_p$). In the far-field plume value of the Debye length λ_d is between 90 and $180\,\mu\mathrm{m}$, the probe radius is thus smaller than the Debye length. In this case the orbital motion limited (OML) regime is valid and the electron temperature in eV can be obtained by the following equation [77]:

$$T_e = \frac{V_p - \phi_{fl}^{cold}}{5.24}. \tag{5.5}$$

The value of 5.24 naturally depends on the gas. It relies on the knowledge of the electron and ion current drawn by the probe at a given potential.
A map of the electron temperature measured with the emissive probe is displayed in Fig. 5.18 for the PPS®100-ML with permanent magnets operated at a discharge voltage of $U_d = 200\,\mathrm{V}$, with an anode mass flow rate of $\dot{m}_a = 4.0\,\mathrm{mg/s}$ and a cathode mass flow rate of $\dot{m}_c = 0.42\,\mathrm{mg/s}$. The fractional difference $D_{T_e} = (T_{e,EP} - T_{e,LP})/T_{e,mean}$ of the electron temperature measured with the Langmuir probe and with the emissive probe is shown in Fig. 5.19. As can be seen the difference for the values obtained with the two different probes is 10 to 20 % except for the near-axis area. The Debye length in the near-axis area is smaller than further off-axis. The OML-regime assumption is therefore less accurate in the near-axis area, which can explain the bigger difference between the two values. Figure 5.19 also shows that the electron temperature

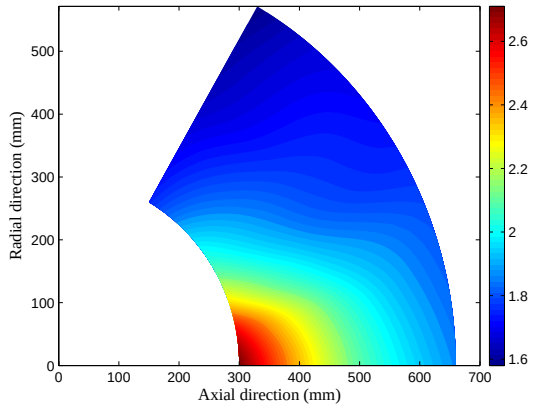

Figure 5.18: Electron temperature measured with an emissive probe (EP) for the PPS®100-ML operating at $U_d = 200\,\mathrm{V}$ and $\dot{m}_a = 4.0\,\mathrm{mg/s}$.

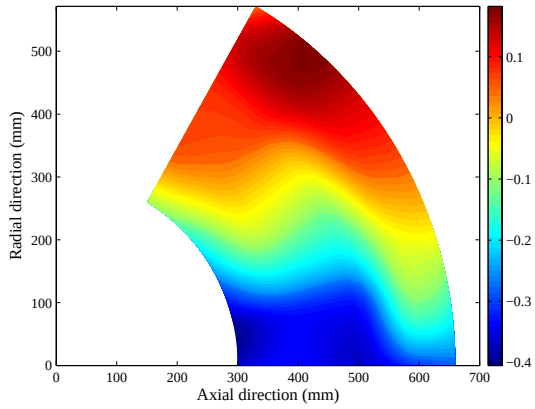

Figure 5.19: Fractional difference of electron temperature D_{T_e} measured with an emissive probe (EP) and a Langmuir probe (LP) for the PPS®100-ML operating at $U_d = 200\,\mathrm{V}$ and $\dot{m}_a = 4.0\,\mathrm{mg/s}$.

obtained by the emissive probe measurements is underestimated in the near-axis area and overestimated in the off-axis area. This can be explained by the under-, respectively overestimation of the plasma potential by the emissive probe.
Although the absolute values of V_p and T_e are not exactly the same, both types of probes provide the same evolution of the plasma potential and the electron temperature in the far-field and the difference between the values is relatively small. Emissive probes are therefore a very interesting diagnostic tool as they provide a direct and instantaneous measurement of the plasma potential. No voltage sweep or analysis of the current-voltage characteristic is needed as for a Langmuir probe. The emissive probe allows also one to obtain a rough estimate of the electron temperature. Even if the value of T_e is not determined as precisely as by a Langmuir probe, the emissive probe can nonetheless be used to validate the Langmuir probe measurements.

5.4 Fast-moving probe system

5.4.1 Introduction

So far only far-field plume measurements of the electron properties have been presented. However, in order to improve the performance level of Hall thrusters it is necessary to better understand the ionization and acceleration processes and therefore accurate measurements of the electron parameters in the near-field plume[2] and even inside the discharge channel are essential.
The plasma density inside the discharge channel and in the near-field plume is quite high and the plasma is composed of highly energetic charged particles. This leads to sputtering and/or

[2]typically the region between the thruster exit plane and the cathode plane

Figure 5.20: Picture of the ultrasonic piezo PILine® Linear Motor Stage M664K018.

ablation of probe material by the direct particle flux. The local plasma parameters (temperature and density) around the probe are then modified by the sputtered or ablated cold probe material. These modifications may remain localized near the probe, but they might also propagate further into the plasma and therefore influence the macroscopic plasma parameters, e.g. the discharge current and the cathode-to-ground potential [85]. The probe lifetime may also become an issue if it is inserted too long into the plasma. Considering all this, a high-speed, reciprocating probe system is necessary to perform proper probe measurements inside the discharge channel or in the near-field plume of a Hall thruster.
Fast reciprocating probe systems have been extensively used to investigate edge effects in Tokamaks [86, 87]. These systems are based on external, pneumatic cylinders which provide drive speeds of several m/s. On the contrary, to investigate Hall thrusters, the high-speed actuator has to be placed inside the vacuum chamber as the thruster needs to be positioned as far as possible from the chamber walls in order to minimize interactions between the plasma beam and the chamber walls. Therefore, pneumatic systems cannot be used.
A fast reciprocating system based on a linear electromagnetic motor assembly has been developed to study the plasma of a Hall thruster [85]. This linear drive can achieve a speed up to 3 m/s over a travel range of about 200 mm with a positioning resolution of 5 μm. The problem of such a linear drive is its size, it is too bulky to be used in our test chambers.

5.4.2 Description of the system

In order to overcome the above mentioned problems, a compact but nonetheless fast-moving stage is necessary. The selected linear drive is an PILine® Linear Motor Stage M664K018. It is an ultrasonic piezo linear drive that does not use leadscrews or gearheads. It is backlash-free and does not create nor is it influenced by magnetic fields. The linear stage is very compact: the external dimensions are $140 \times 63 \times 14$ mm. A picture of the piezo linear drive is shown in Fig. 5.20. The drive is composed of a stator that contains the piezoceramic oscillator and a slider (friction bar) that is attached to the moving part of the stage. The linear stage has a travel range of 90 mm with a speed of up to 350 mm/s and a resolution of 0.1 μm. Furthermore

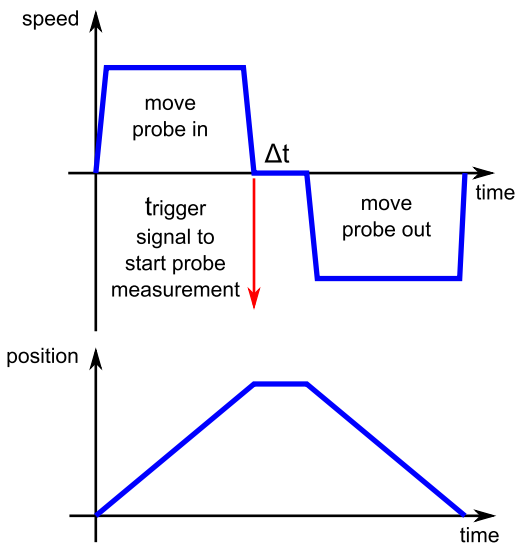

Figure 5.21: Motion profile of the fast reciprocating probe for the measurement of the plasma parameters in the near-field plume.

it is vacuum compatible down to 10^{-6} mbar and has a lifetime of up to 20 000 hours. The linear stage is controlled by a C-867 PILine® Controller. This controller is a highly specialized PID servo-controller that is designed for closed-loop positioning systems equipped with PILine® piezo linear motion drives.
For the measurements of the electron parameters in the plume near-field, an electrostatic probe (Langmuir or emissive probe) is mounted onto the piezo linear drive that is placed outside the thruster plume. The linear drive is placed under a graphite cover in order to protect it against direct ion bombardment and to prevent the motor from beein extensively heated which would lead to a performance degradation. The probe is quickly moved to the measurement position. The controler of the piezo linear drive sends a trigger signal when the desired position is attained to start the probe measurement. After the measurement the probe is rapidly moved out of the near-field plume. In order to minimize the perturbation of the plasma due to the sputtered probe material, the residence time of the probe in the near-field plume should be as short as possible. A typical motion profile for a near-field measurement is shown in Fig. 5.21.

5.4.3 First results

A first validation of the fast-moving probe system has been performed in the near-field plume of the PPI thruster inside the NExET test bench. The thruster was operated at a discharge voltage of 200 V and an anode mass flow rate of 1.0 mg/s. An emissive probe was used as it provides a instantaneous measurement of the plasma potential (see Sec. 5.2.2). The probe was heated with a current of 4.3 A. The fast-moving system is positioned next to the thruster so that the emissive probe can be moved into the near-field plume perpendicular to the thruster axis. The thruster is placed on a linear motion table so that measurements can be taken at different axial positions downstream the thruster exit plane. A schematic view of the setup is

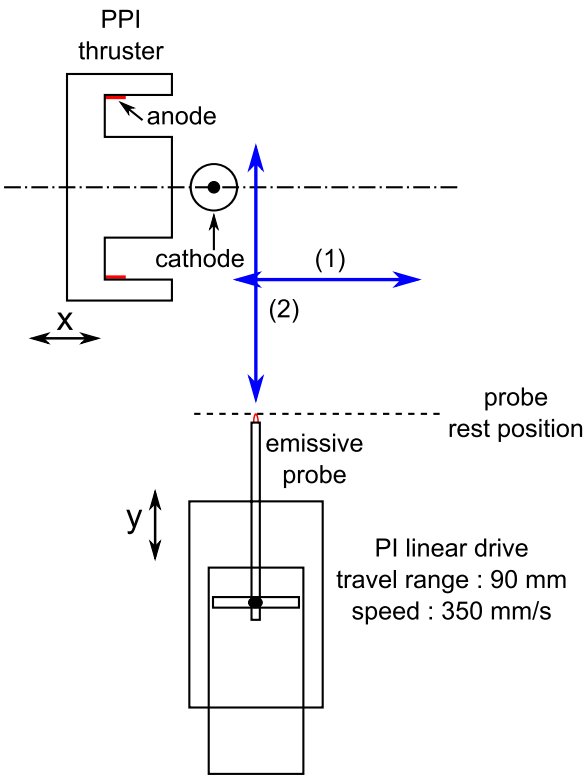

Figure 5.22: Schematic view of the setup (not at scale). The blue arrows show the implementations of the first and second measurement series.

shown in Fig. 5.22. Figure. 5.23 and Fig. 5.24 show two pictures of the setup together with the PPI thruster inside the NExET test bench. The linear drive is placed under a graphite shelter in order to protect it from direct ion bombardment and to minimize the heat load.

As a first step of the system validation it was checked that the probe does not perturb the discharge behavior. Therefore, the discharge current was recorded while moving the probe into the near-field plasma plume and out at a distance of 20 mm downstream the thruster exit plane. The probe was moved up to 5 mm ahead the channel centerline (this radial position actually corresponds to the outer channel wall), stopped there for 10 ms and then moved back to the rest position. The plasma potential measured by the emissive probe was recorded simultaneously to the discharge current and the cathode-to-ground potential. The time evolution of I_d, CRP and V_p during the probe sweep is shown in Fig. 5.25 and Fig. 5.26. As can be seen, V_p increases when moving the probe in and decreases when moving the probe out. Moreover, the profile of V_p is perfectly symmetric, as expected if the probe has no impact on the plasma parameters. Furthermore, no influence of the probe position on the discharge current and the cathode-to-gound potential is visible. One can therefore assume that the discharge behavior as well as the plasma parameters are not perturbated by the fast-moving probe system during near-field plume measurements. Various stop periods up to 1 s have been tested and no influence of the probe insertion on the discharge current as well as on the plasma potential was noticed.

The next step of the system validation consisted in measuring the plasma potential at different

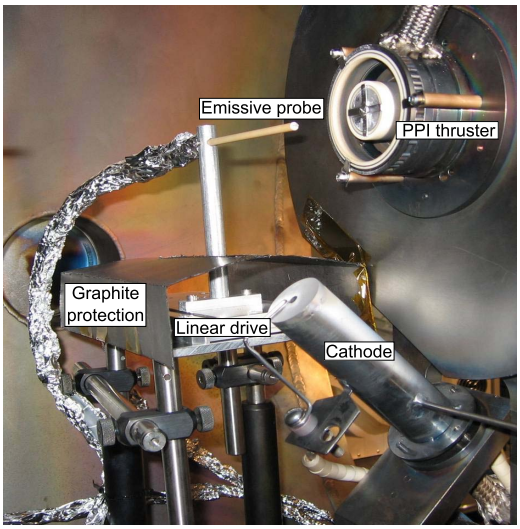

Figure 5.23: Picture of the PPI thruster and the high-speed reciprocating probe system (sideview).

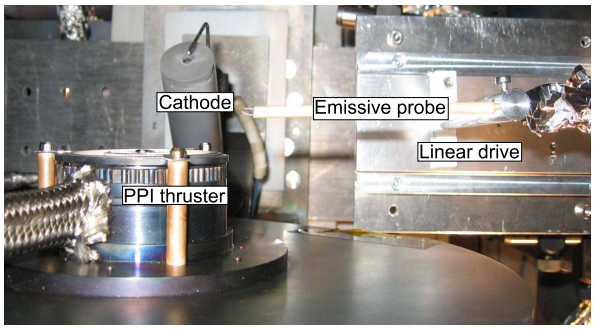

Figure 5.24: Picture of the PPI thruster and the high-speed reciprocating probe system (topview).

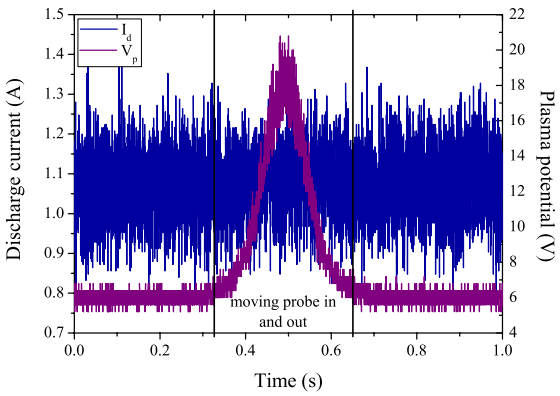

Figure 5.25: Discharge current and plasma potential time series measured by means of a current probe and a heated emissive probe during probe sweep.

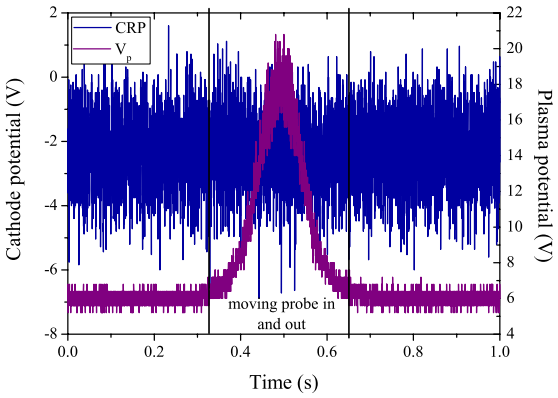

Figure 5.26: Cathode-to-ground potential and plasma potential time series measured by means of a voltage probe and a heated emissive probe during probe sweep.

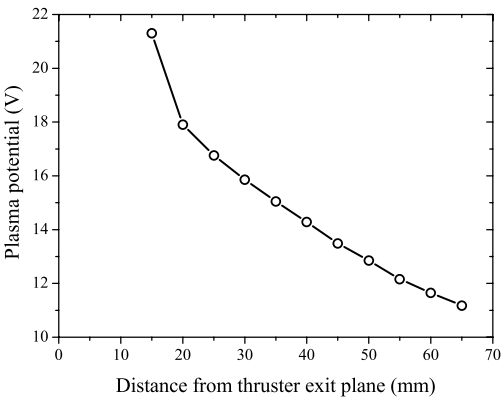

Figure 5.27: Axial profile of V_p measured with the emissive probe in the near-field plume along axial direction 5 mm away from the channel centerline of the PPI thruster operating at 200 V and 1.0 mg/s.

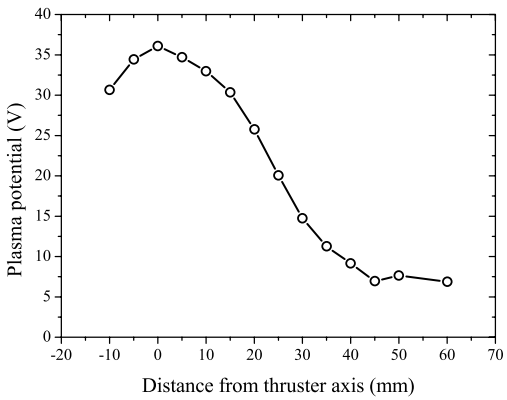

Figure 5.28: Radial profile of V_p measured with the emissive probe in the near-field plume 20 mm downstream the channel exit plane of the PPI thruster operating at 200 V and 1.0 mg/s.

positions in the near-field plume of the PPI thruster. Therefore the emissive probe was moved into the near-field plume and the measurement of the plasma potential with the oscilloscope was initiated by the trigger signal of the piezo linear controler once the probe has attained its position. Two series of measurements have been carried out: First, V_p was measured as a function of the distance from the thruster exit plane d_x 5 mm away from the channel centerline from 15 to 65 mm downstream the thruster exit plane by steps of 5 mm. The results are shown in Fig. 5.27. As can be seen, V_p decreases with an increasing d_x.
Second, V_p was measured as a function of the distance from the thruster axis d_y at a distance of 20 mm downstream the thruster exit plane. Measurements were performed every 5 mm from -10 to 60 mm away from the thruster axis. The evolution of V_p as a function of d_y is represented in Fig. 5.28. As can be seen, the plasma potential is maximum on the thruster axis and it decreases with an increasing d_y.

Note that the plasma potential measured by the emissive probe is certainly underestimated as the electron temperature in the plasma near-field plume is much higher than the temperature of the electrons emitted by the emissive probe (see Sec. 5.2.2). In order to get a more accurate estimation of V_p, a Langmuir probe should be used. A Langmuir probe would also provide a measurement of the electron temperature and the electron density. However, using a Langmuir probe in the near-field plume has different drawbacks. First, a voltage sweep of the probe is necessary in order to obtain the current-voltage characteristic. Second, in this area the magnetic field is not negligible and one needs therefore to account for it for the Langmuir probe I-V curve analysis. An emissive probe is less sensitive to magnetic fields.
It is also interesting to notice that as the probe residence time in the high density plasma region is only very short, the probe lifetime is not an issue. Several hours of measurements have been

performed with the same probe during the testing.

5.5 Conclusion

Experimental data for the plasma properties in the plume of a Hall thruster are essential for the validation of numerical plume models. These models are necessary to find the optimized position of the thruster on the satellite in order to minimize hazardous plasma-spacecraft interactions. So far, most of the experimental investigations were focused on ion properties. However, the global dynamic of the discharge is controlled by the electrons. Time-averaged measurements of the plasma potential, the electron temperature as well as the electron density have therefore been performed in the far-field plume of the PPS®100-ML thruster using a Langmuir and an emissive probe. The parameters were measured between 300 and 660 mm downstream the thruster exit plane and between 0 and 60 °. The influence of the discharge voltage, the anode and the cathode mass flow rate as well as the magnetic field strength on the plasma parameters was investigated.

The results show that the plume is an expanding plasma jet in a subsonic regime with cooling and recombination of electrons and ions [88]. A comparison of the experimental data with the Boltzmann law and the law for an isentropic expansion show that the plasma plume of a Hall thruster is in fact a steady isentropic expansion. The determined isentropic exponent is lower than the theoretical value for gases as in a plasma an additional degree of freedom is caused by ionization.

The emissive probe as well as the Langmuir probe give similar results for the plasma potential and the electron temperature. Hence emissive probes can be used for a direct measurement of these two parameters.

The presented data set is of great relevance for the validation and refinement of plume models. Yet time-averaged measurements of the plasma parameters can only give a first estimate of the plasma plume properties. Time-resolved measurements are necessary to correctly measure the time-correlated plasma properties, as the plasma of a Hall thruster is proved to be highly non-stationary.

The measurement of the plasma parameters in the far-field plume is insufficient for a better understanding of ionization and acceleration processes. Measurements in the near-field plume and even inside the discharge chamber are therefore essential for an improvement of thruster performances.

A fast-moving probe system has been developed in order to measure the plasma parameters in the thruster near-field plume and even inside the discharge chamber where the ion density is so high that sputtering and ablation of the probes becomes an issue. A compact piezoelectric linear drive is used to move the probe in and out of the measurement region with a speed of up to 350 mm/s. A first validation of the new fast-moving probe system has been performed in the near-field plume of the PPI thruster. The plasma potential has been measured at different positions by means of an emissive probe.

Chapter 6

Time-resolved measurements of electron properties [1]

6.1 Introduction

The plasma in a Hall thruster has been shown to be strongly non-stationary with many types of oscillations. Plasma and discharge instabilities in the 1 kHz to 60 MHz frequency range have been observed during operation of Hall thrusters [50, 19]. It is important to notice that in this context "instability" does not mean "unstable operation". In fact not all oscillations are disadvantageous. Natural discharge and plasma instabilities play major roles in ionisation, particle diffusion and acceleration processes. However, if these plasma oscillations become uncontrolled, they can cause a decrease of the thruster performance, they can damage electric power supplies and they can even provoke the extinction of the discharge [50]. The power spectrum of discharge and plasma instabilities in a Hall thruster is dominated by low-frequency oscillations in the kHz range, the so-called breathing mode oscillations [89, 90]. Two major interests exist for time-resolved measurements of the plasma parameters: First, anomalous transport is often attributed to turbulent plasma oscillations and low-frequency oscillations [9, 91, 92, 93]. Second, time-averaged measurements of plasma parameters using Langmuir probes do not account for transient fluctuations of these parameters. However, strong plasma oscillations are known to distort electrostatic probe measurements, hence rendering their accuracy questionable [94, 95]. The use of DC diagnostics may be responsible for differences between experimental data and numerical simulations in terms of anomalous transport, performances and erosion. Furthermore, accurate measurements of the plasma parameters are necessary for the validation of numerical plume models that are essential for the integration of plasma thrusters on the spacecraft.
Breathing mode oscillations are mainly investigated by observing the temporal behavior of the discharge current. Some experiments indicate that these oscillations can also be observed on the plasma parameters inside the discharge chamber or in the plume expansion near-field [96, 90, 97]. More recently Lobbia et al. have shown that the transient fluctuations travel almost undamped throughout the entire far-field plume [98]. The aim of the present study is thus to provide time-resolved measurements of the plasma potential V_p, the electron temperature T_e and the electron density n_e in the far-field plume of a Hall thruster. The main feature here is that the thruster discharge is maintained in a periodic quasi-harmonic, low-frequency oscillation regime by applying a sinusoidal modulation on a floating electrode in the vicinity of the cathode. With the thruster operating in a periodic quasi-harmonic regime, proper time-resolved measurements using Langmuir and emissive probes can be carried out,

[1] Adapted from:
K. Dannenmayer et al., *Plasma Sources Sci. Technol.*, (2012), submitted

as the discharge current frequency content does not change in time. The plasma potential is measured with a cylindrical Langmuir probe and a heated emissive probe. The electron temperature and the electron density are measured with a cylindrical Langmuir probe. The influence of the working gas as well as the channel geometry on V_p, T_e and n_e is investigated. Furthermore, the technique is validated with two different Hall thrusters, namely the 200 W PPI thruster and the 1.5 kW PPS®1350-ML.

6.2 Review of previous works

Before describing our method to perform time-resolved measurements in a periodic quasi-harmonic, low-frequency oscillation regime, it is worth briefly reviewing works carried out on this topic during the past few years.

Albarède et al. carried out time-resolved measurements in the near-field plume of a SPT-100 thruster using a single, cylindrical Langmuir probe based on a coaxial cable architecture [97]. The discharge current oscillations were acquired with a 50 MHz bandwidth current probe and the Langmuir probe current was measured over a 1 kΩ resistor. The time evolution of the Langmuir probe current was recorded for different bias voltages to reconstruct the time-dependent current-voltage characteristic with a time resolution of 1 μs. The discharge current signal was used as trigger to synchronize the probe current waveform acquisition. The total acquisition duration to obtain the time-dependent current-voltage characteristic exceeded several minutes. The thruster discharge had to be identical for every single measurement in order to obtain a coherent dataset. The low-frequency oscillations in a Hall thruster are however non-stationary. Therefore identical events had to be selected for the triggering. Furthermore, these events had to represent the average behavior of the thruster. The trigger level was thus set 10 % higher than the mean discharge current. The recorded probe signal was averaged over 128 samples. By analyzing the I-V characteristic at every time step using the classical theory of electrostatic probes, the time evolution of the plasma parameters (V_f, V_p, T_e and n_e) was obtained. The drawback of this method is that even if the trigger level is set to 10 % above the mean discharge current, the frequency content of selected events is not necessarily identical and hence the discharge behavior may be different for the different measurement points.

A different method of measuring transient plume properties was presented by Lobbia and Gallimore [98]. They used a high-speed Langmuir probe system to measure time series of current-voltage characteristics at different positions in the plume. The sweep frequency was 100 kHz and the time resolution 10 μs. A null probe was used to correct for leakage currents due to the fast voltage sweep. The discharge current signal was sampled simultaneously with the probe characteristics. The time evolution of the plasma parameters (V_f, V_p, T_e and n_e) was obtained by means of the standard thin sheath theory. The thruster-plume system is modeled by transfer functions obtained from the measured plasma properties and discharge current signals. Time-coherent signals of the plasma parameters at every measured position were finally obtained by means of Fourier synthesis of the transfer functions. This approach has several disadvantages: First, the system is very complex, especially the electronic devices have to be designed to operate with such a high frequency. Second, only a low number of voltage steps is used to construct the current-voltage characteristic, which introduces an uncertainty in the

measurement of the floating and the plasma potential [99]. Third, the model is solely correct if the frequency response and the power spectral density of the discharge current signal, used for the determination of the time-coherent plasma parameter signals, is similar to the initial signal, used to construct the transfer function.

Smith and Capelli presented a method to measure time and space-correlated plasma properties in the near-field plume using an emissive probe [78]. The discharge current and the probe potential, for the cold as well as for the heated probe, were recorded simultaneously to reconstruct the time correlated plasma properties (V_f, V_p and T_e) by synchronizing the temporal data to the dominant low-frequency discharge current oscillations. The electron temperature was obtained by an adequate model of the collected ion and electron currents. One of the drawbacks of this approach is that only an emissive probe is used. Hence, the electron density cannot be determined and the plasma potential as well as the electron temperature may be underestimated due to the high plasma electron temperature compared to the temperature of the emitted electrons [75]. Furthermore, this method does not provide an absolute determination of the temporal behavior for two reasons: First, the discharge properties are not identical from one low-frequency oscillation period to the next. Second, the determination of the dominant low-frequency oscillation is not absolute given the many higher frequency oscillations present in the signal.

6.3 Time-resolved measurement technique

In the present work, the Langmuir probe I V-characteristic was reconstructed from the time evolution of the probe current recorded for different probe bias voltages [97]. The idea of this method is based on the fact that the studied periodic plasma phenomenon changes in a slow way compared to the temporal response of the Langmuir probe at particular plasma conditions. The method consists of recording the temporal evolution of the probe current at a particular probe voltage. By repeating such measurements at many different probe voltages one obtains a 2D matrix of probe currents with time and voltage as independent variables. The time dependent probe characteristics can easily be extracted from this matrix. This technique is mainly used for pulsed plasmas as the plasma behavior is stationary which warrants repeatable measurement conditions [100, 101].

In order to use this technique for a Hall thruster, the discharge needs to be maintained in a periodic quasi-harmonic oscillation regime. This has two main advantages: First, the harmonic signal can be used as trigger signal, hence there is no need for a fast power switch that perturbs the thruster behaviour like in time-resolved LIF measurements [102]. Second, the frequency content is fairly the same at any time, which warrants reproducible measurement conditions. Furthermore time series can be added up without propagating noise and error and therefore the signal-to-noise ratio can be improved. The fact that the thruster is maintained in a periodic quasi-harmonic oscillation regime is the main difference to the work described by Albarède.

To achieve a synchronized quasi-harmonic operating regime of the thruster, a sinusoidal potential with a tunable frequency is applied between a floating electrode, here the keeper electrode, and the negative pole of the cathode heating circuit. A schematic view of the electrical set-up is represented in Fig. 6.1. The modulation frequency cannot be chosen randomly. It has to be

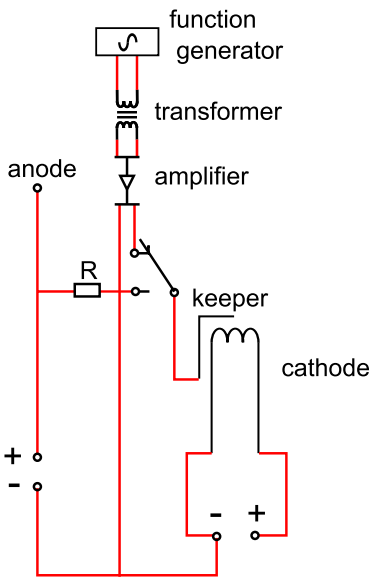

Figure 6.1: Schematic view of the electrical set-up of the keeper electrode modulation.

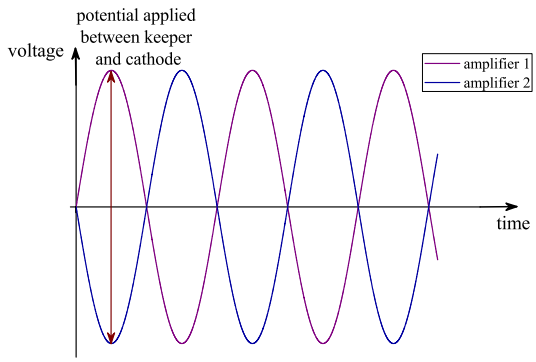

Figure 6.2: Modulation signal applied between the keeper and the negative pole of the cathode heating circuit.

one of the resonance frequencies of the discharge. The modulation signal was provided by a function generator and amplified to achieve an amplitude of about 100 V. A home-made amplifier was used to amplify the modulation signal. The amplifier system was built up of two amplifiers that operate in opposite phase. A schematic view of the modulation signal applied between the keeper and the negative pole of the cathode heating circuit is shown in Fig. 6.2. The amplifier has to be adapted for each thruster in order to provide the necessary current. The modulation signal was applied by way of an isolation transformer to keep the keeper and the cathode insulated from ground. The square wave output of the function generator was used as trigger signal for the ALP system in time-resolved mode. The current driven to the keeper was below 10 % of the discharge current and therefore it did not represent a significant perturbation.

The ALP system provides a time-resolved option. In this mode the probe current is recorded over one period of the modulation signal for a fixed bias voltage of the probe. This procedure is repeated for all the necessary voltage steps in order to reconstruct the current-voltage characteristic for every time step.

The time evolution of the potential of the heated emissive probe was recorded simultaneously to the discharge current oscillations. The power supply for the probe heating was powered via a battery or an isolation transformer in order to reduce the capacity against ground. If this capacity is too high, the oscillations of the probe potential cannot be observed as the capacity together with the inner resistance of probe form a low-pass filter. The bandwith of our configuration was about 60 kHz.

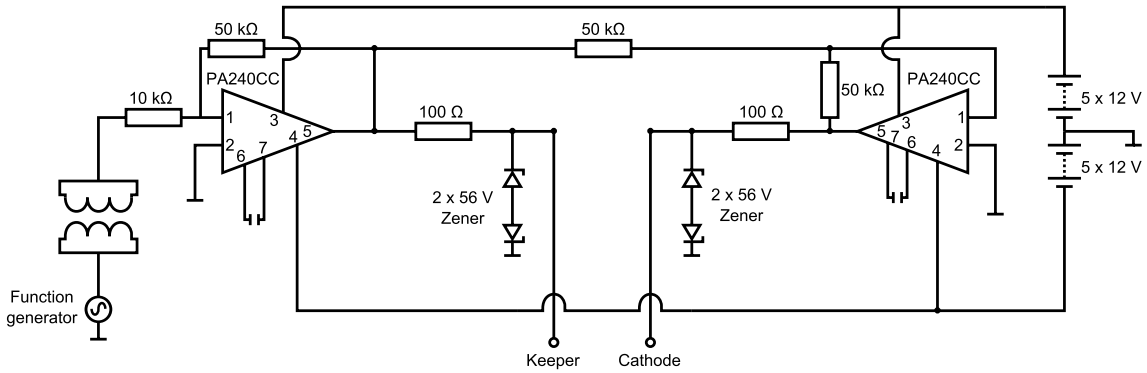

Figure 6.3: Schematic view of the amplifier of the keeper electrode modulation.

6.4 Time-resolved measurements in the far-field plume of the PPI thruster

The aforementioned time-resolved measurement technique was first tested with the low-power PPI thruster. The aim of this study was to validate the technique and to investigate the influence of the working gas and the thruster geometry on the electron properties. Therefore the PPI thruster was operated with xenon and krypton and with the $2S_0$ and the $3S_0$ configuration. The amplifier for the PPI thruster is built using two high voltage power operational amplifiers (PA240CC). A schematic view of the amplifier is shown in Fig. 6.3. In this work, the time resolution was set to $1\,\mu$s, the acquisition was averaged over 1000 records and the Langmuir probe bias voltage was increased by steps of 0.2 V.

6.4.1 PPI thruster operated with xenon

The PPI thruster was operated at a discharge voltage of $U_d = 200$ V and an anode mass flow rate of $\dot{m}_a = 1.0$ mg/s (Xe) resulting in a mean discharge current of $I_d = 0.93$ A for Xe . The background pressure in the vacuum chamber during thruster operation was about 3×10^{-5} mbar. The thruster was mounted onto two linear moving stages in order to displace it along and perpendicular to the thruster axis so that measurements could be taken at different positions in the far-field plume. The measurements of the electron properties were performed at three different axial positions (x = 100, 150 and 200 mm) and four different radial positions (y = 0, 18.5, 25 and 50 mm), where x = 0 mm corresponds to the thruster exit plane and y = 0 mm corresponds to the thruster axis. A schematic view of the different measurement positions is shown in Fig. 6.4.

6.4.1.1 Influence of the keeper modulation

As has been mentioned before, in order to perform proper time-resolved measurements, the thruster discharge needs to be in a periodic quasi-harmonic regime. Fig. 6.5 represents the time evolution of the discharge current I_d, the cathode-to-ground potential CRP and the plasma potential V_p as a function of the modulation frequency for the PPI thruster operating at 200 V

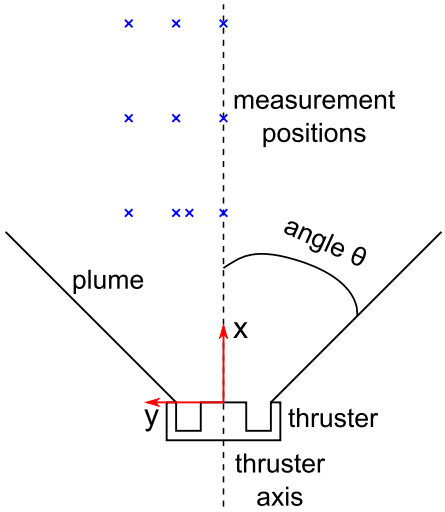

Figure 6.4: Schematic view of the different measurement positions in the far-field plume of the PPI thruster.

and 1.0 mg/s (Xe). The corresponding power spectrum of the discharge current and the plasma potential is shown in Fig. 6.6. The plasma potential was measured with a heated emissive probe. The time evolution of V_p was recorded at 100 mm downstream the thruster exit plane (x = 100 mm) on the thruster axis (y = 0 mm). As can be seen in Fig. 6.5 and Fig. 6.6, without a modulation signal, the discharge current is non-stationary and one cannot distinguish a dominant frequency in the discharge current time series, whereas for a modulation frequency of 13 kHz the discharge current is fairly well synchronized to the modulation waveform. The oscillation amplitude is not completely constant, but the oscillation frequency is constant. At a modulation frequency of 3 kHz, one can distinguish a slight synchronization of I_d to the modulation signal, but higher frequencies are superimposed to the modulation frequency. In any case, the influence of the modulation on the mean discharge current is very weak ($\overline{I_d} = 0.93 \pm 0.004$ A). The time evolution of the cathode potential to ground is represented in the second row of Fig. 6.5. The CRP is fairly well synchronized for both modulation frequencies. Contrary to the discharge current the mean value of the cathode potential is slightly different for the three operating conditions ($\overline{CRP} = -18.79 \pm 1.25$ V). Without modulation the plasma potential V_p is non-stationary and no dominant frequency can be distinguished. For a modulation frequency of 13 kHz, the time evolution of V_p is influenced by the modulation but no dominant frequency can be distinguished. Contrary to the discharge current, the plasma potential can be stabilized if the modulation frequency is set to 3 kHz. Again the influence of the modulation on the mean value of the plasma potential is very weak ($\overline{V_p} = 13.85 \pm 0.18$ V). This is also valid for the plasma potential measured at other positions in the far-field plume.

As the mean values of I_d and V_p are almost independent, one can assume that the modulation does not influence the global thruster behavior. This can also be shown by the ion velocity distribution function (IVDF) measured by means of LIF. The IVDF is represented in Fig. 6.7 for two different positions, namely at the thruster exit plane and 30 mm downstream the thruster exit plane on the channel axis. As can be seen, the modulation has almost no influence on the

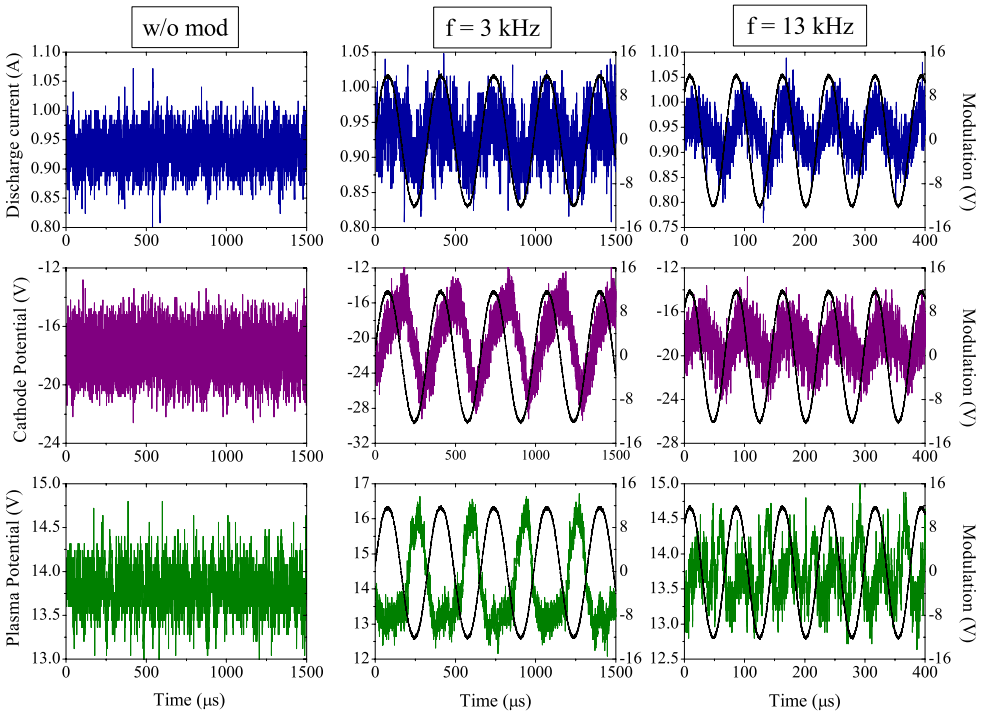

Figure 6.5: Influence of the keeper modulation on I_d, CRP and V_p for the PPI thruster operating at $U_d = 200\,\mathrm{V}$, $\dot{m}_a = 1.0\,\mathrm{mg/s}$ (Xe). The solid black line represents the modulation signal.

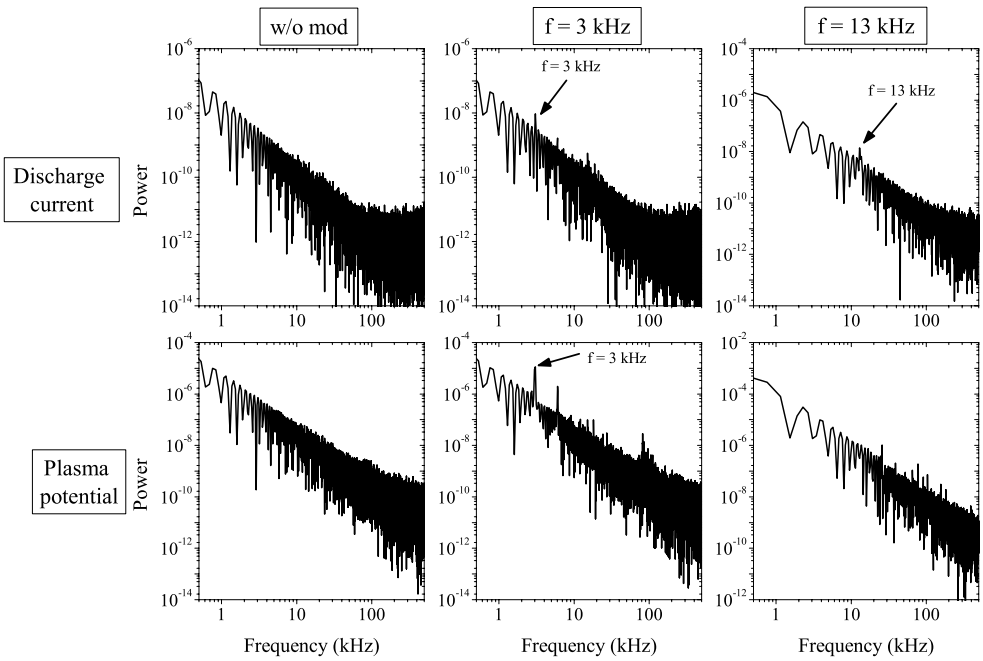

Figure 6.6: Power spectrum of the discharge current and the plasma potential without modulation and for the 2 modulation frequencies.

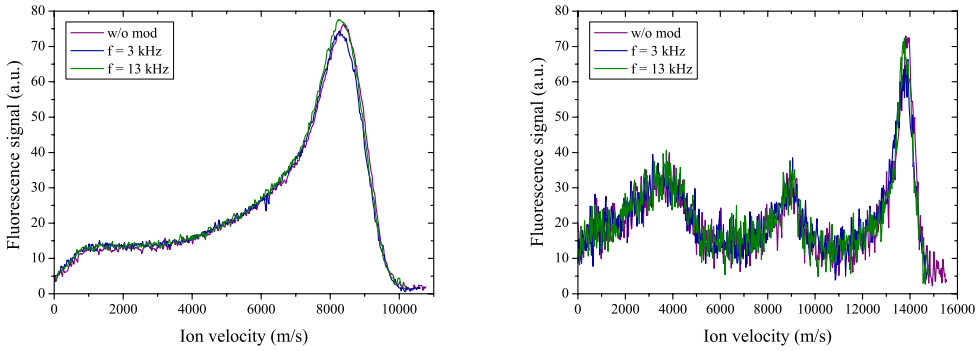

(a) x = 0 mm (b) x = 30 mm

Figure 6.7: Influence of the modulation on the Xe^+ ion velocity distribution measured by means of LIF at two different positions along the channel centerline.

IVDF.

As the modulation has only a very little influence on the global thruster behavior, the time-resolved measurements of the electron properties were performed with a modulation frequency of 3 kHz and 13 kHz respectively. The modulation frequency has been scanned from 0 up to 60 kHz and no other frequency with a special thruster behavior could be found. The modulation frequency of 13 kHz corresponds in fact to the breathing mode frequency. The lower frequency of 3 kHz might correspond to the frequency of the spoke instability. However, further investigation on the origin of this lower frequency is necessary. A test with a CCD camera at the modulation frequency of 3 kHz did not show a spoke instability.

6.4.1.2 Time evolution of plasma parameters

The time evolution of V_p, T_e and n_e in Xe for the two different modulation frequencies is displayed in Fig. 6.8 over one oscillation period. The first row represents the evolution over one period at 3 kHz, the second row the one for 13 kHz. The measurements were taken at 100 mm downstream the thruster exit plane and on the thruster axis. The time evolution of the discharge current is also represented (black line).

As can be seen in Fig. 6.8, the time evolution of V_p, T_e and n_e is different for the two modulation frequencies. The time evolution of the electron density at f = 13 kHz is almost sinusoidal, whereas the time evolution for f = 3 kHz is almost rectangular. Nevertheless, one can distinguish a high frequency oscillation superimposed to the basic rectangular n_e waveform. The frequency of these superimposed oscillations is about 13 kHz. However for both frequencies changes are very weak, i.e. approximately 7 % of the mean value. For both frequencies n_e follows almost exactly the time evolution of I_d. The phase delay between I_d and n_e is about 20 μs for the modulation at 13 kHz. At 3 kHz, there is no clear phase delay between I_d and n_e. The fact that n_e follows the time evolution of I_d with a slight phase delay has already been observed by Lobbia et al. [99]. For 3 kHz, the time evolution of V_p and T_e is almost the same

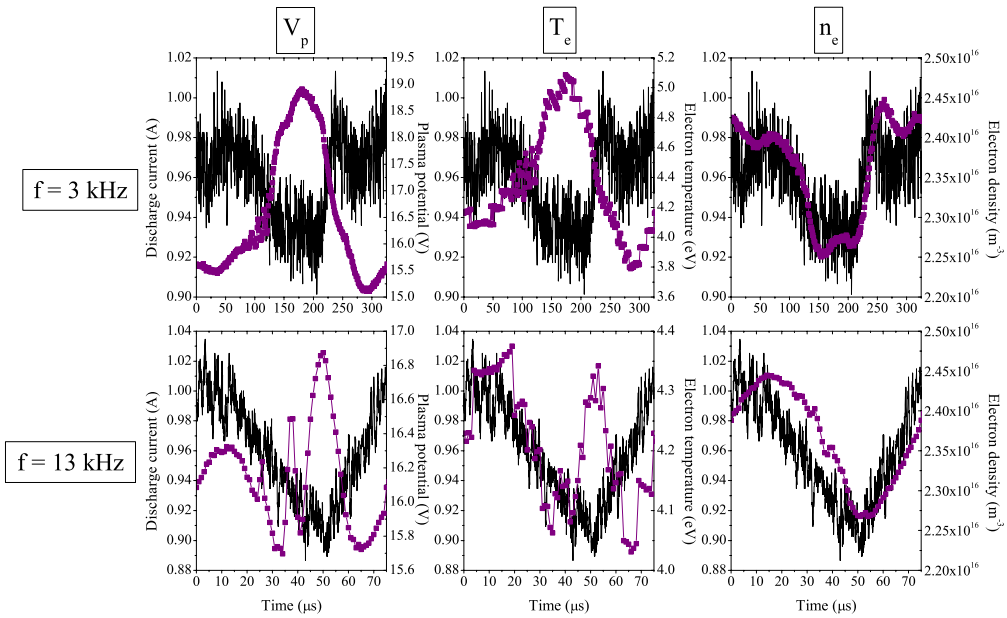

Figure 6.8: Time evolution of the plasma potential V_p, the electron temperature T_e and the electron density n_e measured by means of a Langmuir probe at x = 100 mm and y = 0 mm in the plasma plume of the PPI operating at $U_d = 200$ V, $\dot{m}_a = 1.0$ mg/s (Xe). The discharge current I_d time series is shown in solid line

Table 6.1: Mean values of V_p, T_e and n_e on the thruster axis for 3 different distances downstream the thruster axis.

axial position [mm]	V_p 3 kHz [V]	T_e 3 kHz [eV]	n_e 3 kHz [m^{-3}]	V_p 13 kHz [V]	T_e 13 kHz [eV]	n_e 13 kHz [m^{-3}]
100	16.5	4.4	2.4×10^{16}	16.2	4.2	2.4×10^{16}
150	11.4	2.2	1.2×10^{16}	11.3	2.2	1.2×10^{16}
200	9.1	1.7	7.7×10^{15}	8.9	1.7	7.7×10^{16}

and in antiphase with the discharge current. At the modulation frequency of 13 kHz, the time evolution of V_p and T_e show some similarities, the location of the different peaks is the same but the peak amplitude is different. The time evolution of V_p and T_e is more complex than the one of I_d with a multi-peak structure. The fluctuations of V_p and T_e are significantly higher for 3 kHz than for 13 kHz, i.e. 23 % against 7 % for the plasma potential and 30 % against 8 % for the electron temperature.
It should be noticed that the multipeak structure for V_p and T_e at 13 kHz is real and stable, otherwise it would vanish due to the averaging over 1000 cycles.
Like the mean values of the thruster operating parameters (I_d and CRP), the mean values of V_p, T_e and n_e calculated from the time-resolved data over one period do not depend much on the two modulation frequencies, in contrast to their different time evolution as can be seen in Tab. 6.1. This is again a proof that the modulation has almost no influence on the global thruster behavior and the plasma parameters.

6.4.1.3 Time and space evolution of plasma parameters

The evolution in time (over one modulation period) and space (radial direction) of the plasma potential, the electron temperature and the electron density at 100 mm downstream the thruster exit plane is exemplified in Fig. 6.9 for the two different modulation frequencies. The radial profile is interpolated from the four recorded radial positions. The plotted data is unsmoothed. The structure of the fluctuations that can be observed in the example trace in Fig. 6.8 can also be seen in the different maps represented in Fig. 6.9. The profile of the fluctuations is similar for all radial positions. As has already been shown in chapter 5, V_p, T_e and n_e decrease with an increasing distance from the thruster axis (radial direction), as the plume is an expanding plasma jet.
The fluctuation magnitude, which corresponds to the ratio peak-to-peak value over mean value was calulated for V_p, T_e and n_e, i.e. $V_{p,peak-peak} / \overline{V_p}$, $T_{e,peak-peak} / \overline{T_e}$ and $n_{e,peak-peak} / \overline{n_e}$. The fluctuation magnitude for each parameter is approximately the same at all the different measurement positions. This implies that the fluctuations of the plasma parameters propagate almost undamped throughout the complete far-field plume. This has already been shown previously by time-resolved measurements of n_e in the far-field plume of BHT-600 Hall thruster [98].

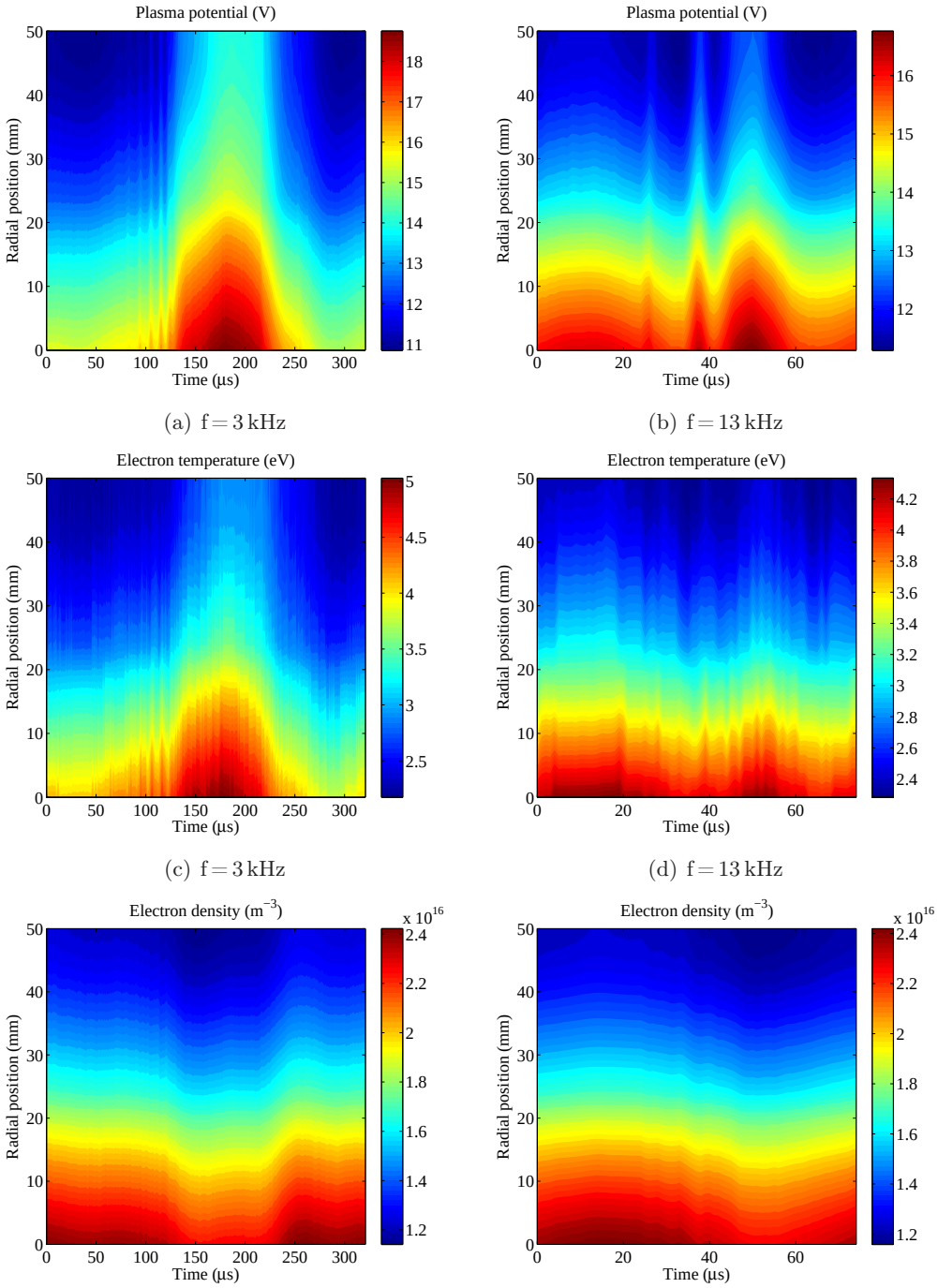

(a) f = 3 kHz (b) f = 13 kHz

(c) f = 3 kHz (d) f = 13 kHz

(e) f = 3 kHz (f) f = 13 kHz

Figure 6.9: Evolution in time and space (radial direction) of V_p, T_e and n_e for the two different frequencies at 100 mm downstream thruster exit plane. The thruster is operated at $U_d = 200$ V, $\dot{m}_a = 1.0$ mg/s (Xe).

6.4.1.4 Comparison between time-averaged and time-resolved measurements

The plasma in a Hall thruster is proved to be highly non-stationary. Hence, a time-averaged measurement of the plasma parameters with a Langmuir probe is expected not to give correct values. In order to evaluate the difference between time-averaged and time-resolved measurements, the mean value of the time-dependent plasma parameters (V_p, T_e and n_e) is compared to the value obtained from time-averaged Langmuir probe measurements. The time-averaged measurements are performed for the same operating conditions and at the same positions in the plume as the time-resolved measurements. The floating electrode close to the cathode is again modulated at 3 kHz and 13 kHz. Time-averaged measurements were also performed without modulation. As has been shown previously, the modulation frequency has almost no influence on the mean value obtained from time-resolved measurements. A comparison of the plasma parameters obtained from time-averaged with and without modulation, shows that the modulation frequency has almost no influence on the values of V_p, T_e and n_e. Hence, Fig. 6.10 shows a comparison of the values of the plasma parameters obtained from time-averaged and time-resolved measurements in the far-field plume of the PPI thruster with a modulation frequency of 3 kHz. As can be seen, the value of the plasma potential and the electron temperature obtained from time-averaged measurements is smaller than the value obtained from time-resolved measurements. However, the difference for T_e is very small. On the contrary, the value of the electron density is bigger for time-averaged measurements.
The difference between time-averaged and time-resolved measurements may be explainded by the fact that the current-voltage characteristic of a Langmuir probe is non linear. Fluctuations of the plasma parameters may lead to a distortion of the time-averaged probe characteristic. Hence, time-resolved measurements of the plasma parameters are necessary in order to get accurate measurements.

6.4.1.5 Comparison between Langmuir and emissive probe measurements

The time evolution of the plasma potential was also measured using an emissive probe. The plasma potential is assumed to be the floating potential of the emissive probe heated with a current of 4.3 A. The time evolution of the plasma potential was recorded simultaneously to the discharge current for the two different modulation frequencies. A comparison of V_p measured either with a Langmuir or an emissive probe is represented in Fig. 6.11 for the two modulation frequencies and at two different positions in the far-field plume. The time evolution of V_p over one period measured by the emissive probe is averaged over 25 consecutive periods. On the contrary, the time-resolved I-V characteristic obtained with the Langmuir probe is averaged over 1000 cycles.

The first column of Fig. 6.11 shows the time evolution of V_p on the thruster axis 100 mm downstream the thruster exit plane (position 1). As can be seen V_p measured with the emissive probe is lower than V_p measured with the Langmuir probe. The second column shows the time evolution of V_p 25 mm off thruster axis and 150 mm downstream the thruster exit plane (position 2). The two time series of V_p coincide almost perfectly although the absolute values are different for position 1. It has already been shown before that the temperature of the electrons has an influence on the difference between the real plasma potential and the plasma potential measured by the emissive probe as the floating potential of the sufficiently heated

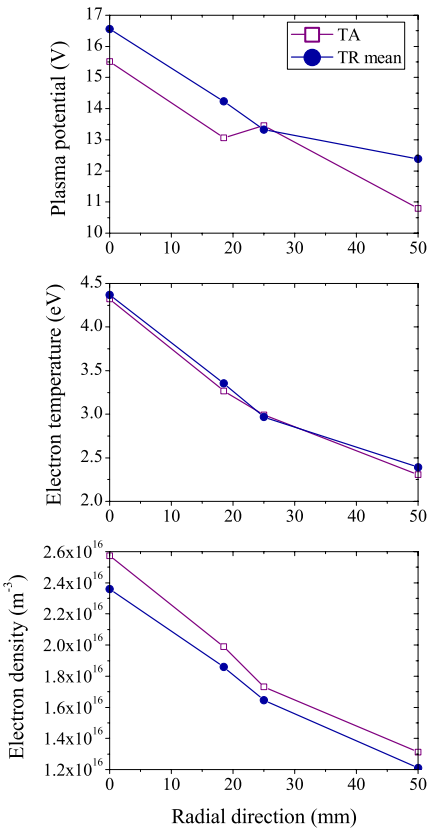

Figure 6.10: Comparison of V_p, T_e and n_e obtained from time-resolved and time-averaged measurements with a Langmuir probe at 100 mm downstream the thruster exit plane in the far-field plume of the PPI thruster ($3S_0$ configuration) operating with Xe at $U_d = 200$ V, $\dot{m}_a = 1.0$ mg/s.

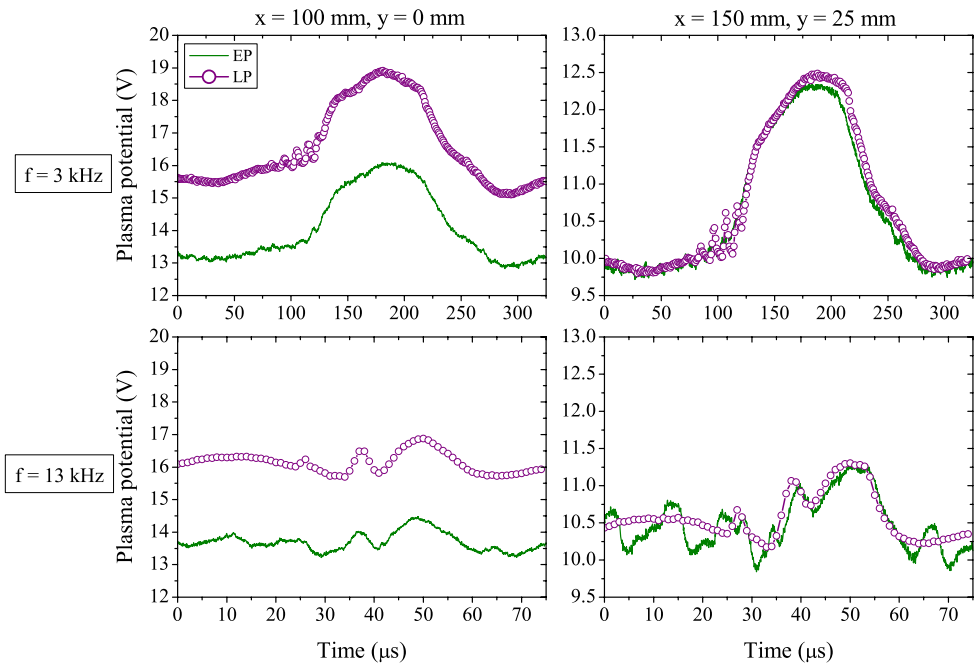

Figure 6.11: Comparison of the plasma potential measured with an emissive (green line) and a Langmuir (purple symbols) probe in the far-field plume of the PPI thruster operating at $U_d = 200\,\mathrm{V}$, $\dot{m}_a = 1.0\,\mathrm{mg/s}$ (Xe).

probe [75, 103]. Due to space-charge effects, the accuracy of the plasma potential determined by the floating potential of an emissive probe is in the order of T_e/e, where T_e is the temperature of the plasma electrons [104, 84]. The accuracy is thus better at position 2, where the temperature of the plasma electrons is about 2 eV than at position 1, where T_e is about 4.4 eV.
The results for a modulation frequency of 3 kHz are shown in the first row of Fig. 6.11. As can be seen, the time evolution of V_p measured with both probes is almost identical. In contrast, for a modulation frequency of 13 kHz, the time evolution measured with the emissive probe is slightly different than the one measured with the Langmuir probe, as can be seen in the second row of Fig. 6.11. For 3 kHz, V_p is well synchronized and therefore an average over 25 periods is enough to obtain the global temporal behavior of V_p as measured by the Langmuir probe with an average of 1000 cycles. Since for a frequency of 13 kHz, synchronization of V_p is not completly achieved, an average over 25 periods for the emissive probe will not give the same temporal behavior of V_p than the average over 1000 samples for the Langmuir probe. Averaging over a higher number of samples may lead to a smoother curve in the case that no complete stabilization of the signal to one frequency is achieved. This has to be checked by changing the number of samples for the averaging procedure.
However, as for the Langmuir probe, the mean values, obtained from the time series of V_p measured by the emissive probe, are almost identical for the two modulation frequencies.
Despite the differences for the values of V_p obtained by means of emissive and Langmuir probe, the results are still in fairly good agreement. Both probes show a similar time evolution of V_p. Even if the value of V_p may be slightly underestimated, emissive probes can be used to get a direct and instantaneous measurement of V_p. No voltage sweep or analysis of the current-voltage characteristic are needed as for a Langmuir probe. This makes emissive probes a very interesting diagnostic tool especially for time-resolved measurements.

6.4.1.6 Influence of the averaging (Langmuir probe)

In order to evaluate the influence of averaging on the plasma parameters measured with the Langmuir probe, measurements for different numbers of samples per voltage step have been performed in the far-field plume of the PPI thruster. The thruster was operated at 200 V and 1.0 mg/s (Xe) as well as at 175 V and 0.8 mg/s. The influence of the modulation on the discharge current as well as the plasma potential, measured with the emissive probe, are shown in Fig. 6.12. The probes were positioned at 165 mm downstream the thruster exit plane on the thruster axis.
As can be seen in Fig. 6.12, the modulation frequencies necessary to achieve a synchronization of I_d and V_p are the same for the two operating conditions. The discharge current is maintained in a periodic quasi-harmonic oscillation regime for a modulation frequency of 13 kHz. In this case, the synchronizations of V_p is rather poor. The plasma potential can be maintained in a periodic quasi-harmonic oscillation regime for a modulation frequency of 3 kHz. In this case, the synchronizations of I_d is rather poor.
Time-resolved measurements using the Langmuir probe have been performed with 50, 100 and 1000 samples per voltage step. Figure 6.13 shows the time evolution of V_p, T_e and n_e for the two different operating conditions as a function of the number of samples per voltage step. As can be seen, increasing the number of samples per voltage steps leads to smoother curves and

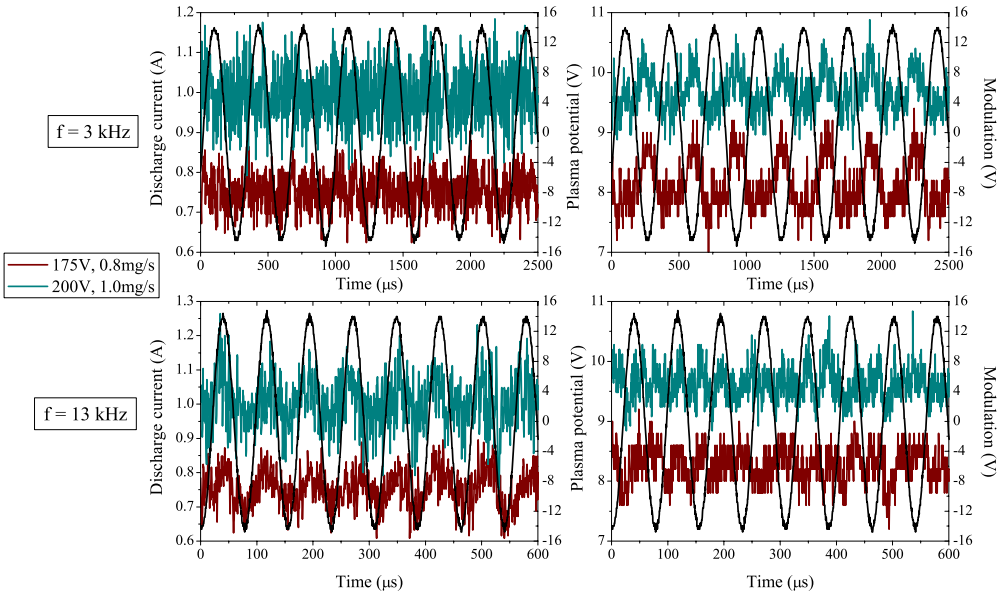

Figure 6.12: Operating conditions of the PPI thruster for the investigation of the influence of the average on plasma parameters.

the curve is shifted to lower values. These effects are especially visible for the plasma potential.

The described effect of the number of samples for the averaging process is probably due to the fact that the fluctuations are not perfectly harmonic. A little stochastic component remains for both the amplitude and the frequency of the fluctuations. Therefore increasing the number of samples for the averaging process leads to a decrease of the measured values as the probability to come across fluctuations with a higher amplitude, that lead to a stronger decrease of the measured value, increases with the number of samples [105].

6.4.1.7 Comparison between different thruster geometries

The influence of the channel width on the time evolution of the plasma parameters has been investigated with the $2S_0$ and the $3S_0$ configuration of the PPI thruster. Both thruster configurations were operated at a discharge voltage of 200 V and an anode mass flow rate of 1.0 mg/s. The mean discharge current is slightly different for the two configurations: $I_d = 0.88$ A for the $2S_0$ configuration and $I_d = 0.93$ A for the $3S_0$ configuration. As already decribed before, two different modulation frequencies are necessary to maintain the discharge current, respectively the plasma potential in a periodic quasi-harmonic oscillation regime. The influence of the modulation on the discharge current and the plasma potential for the two channel geometries is shown in Fig. 6.14. As can be seen, the two modulation frequencies are independent of the thruster configuation. A frequency of 13 kHz is necessary to stabilize the discharge current, whereas the plasma potential can be stabilized by a frequency of 3 kHz. As can be seen in

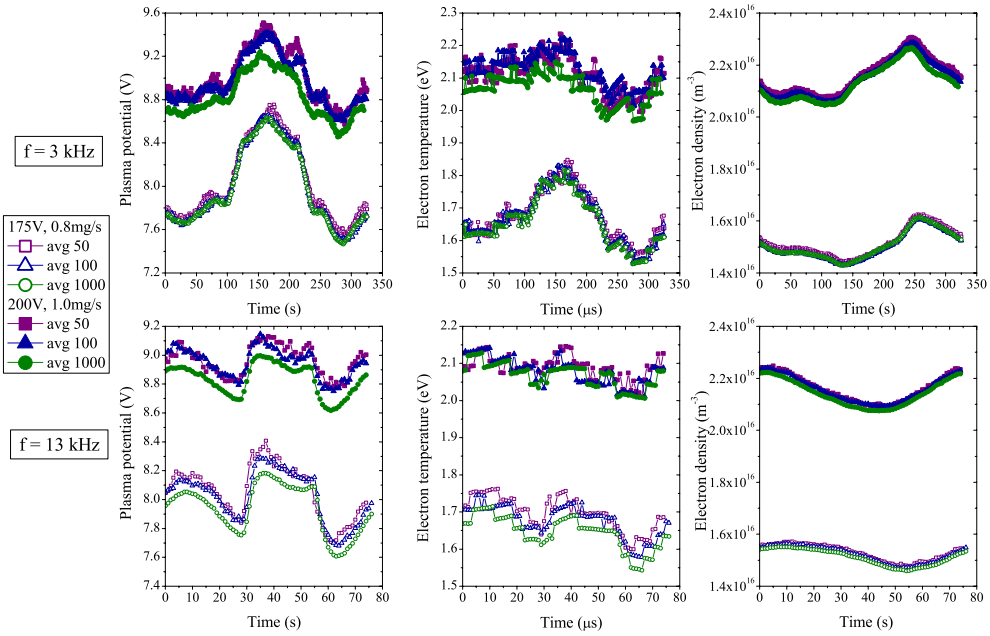

Figure 6.13: Influence average on the plasma parameters for two different operating conditions of the PPI thruster.

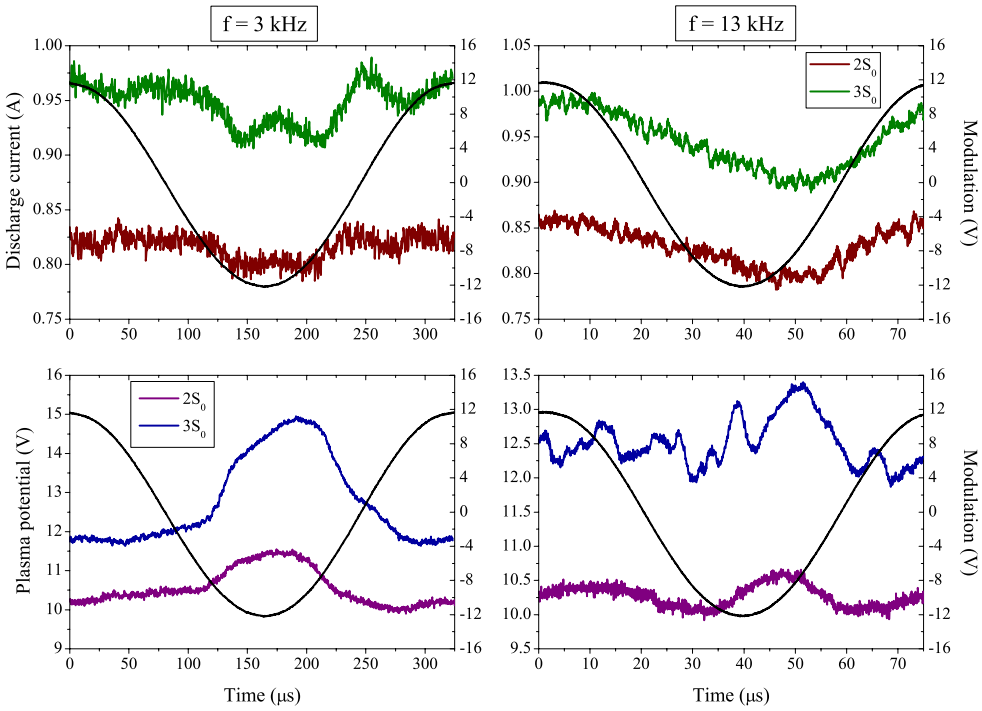

Figure 6.14: Comparison operating conditions (I_d and V_p) of the PPI thruster operating at $U_d = 200\,\mathrm{V}$, $\dot{m}_a = 1.0\,\mathrm{mg/s}$ for two different channel widths ($2S_0$ and $3S_0$). The plasma potential is measured with an emissive probe 100 mm downstream the thruster exit plane on the thruster axis.

Fig. 6.14, the time evolution of I_d is almost the same for the two geometries. However, the discharge current and the fluctuation amplitude are higher for the larger channel ($3S_0$). At 3 kHz, the time evolution of V_p is similar for both geometries with one peak. At 13 kHz, the time evolution of V_p shows two peaks for the $2S_0$ configuration whereas for the $3S_0$ configuration the time evolution is more complexe with a multipeak structure. Like for I_d, the plasma potential as well as the fluctuation amplitude are higher for the larger channel for both modulation frequencies.

The plasma potential, the electron temperature and the electron density were measured by means of the Langmuir probe for the two modulation frequencies at different positions in the far-field plume. In the following, the time evolution of V_p, T_e and n_e is represented for 3 distances downstream the thruster exit plane on the thruster axis.

The time evolution of V_p is shown in Fig. 6.15 for the two modulation frequencies. As was already shown by the emissive probe measurements, the time evolution of V_p is in fairly good agreement for a modulation frequency of 3 kHz. On the contrary, at 13 kHz the time evolution of V_p is different for the two thruster configurations. One can observe a two-peak structure for

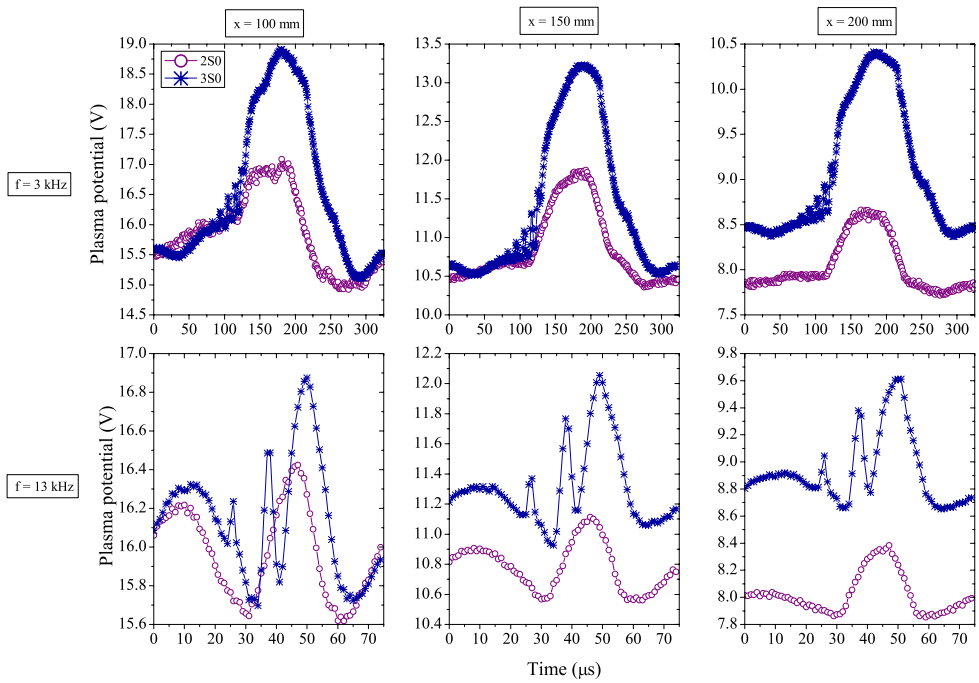

Figure 6.15: Influence of the channel width on the time evolution of V_p measured with a Langmuir probe at three different axial positions on the axis of PPI thruster operating at $U_d = 200\,\mathrm{V}$, $\dot{m}_a = 1.0\,\mathrm{mg/s}$ (Xe). The $2S_0$ and the $3S_0$ configuration are compared.

the $2S_0$ configuration and a multipeak structure for the $3S_0$ configuration. It should also be mentioned that V_p as well as the fluctuation amplitude is higher for the $3S_0$ configuration for both modulation frequencies. Furthermore, one can see in Fig. 6.15 that the difference between the two geometries increases with the distance from the thruster axis.

The time evolution of T_e is shown in Fig. 6.16. Contrary to V_p, T_e shows a similar time evolution for the two geometries for both modulation frequencies. It is also interesting to notice that at 100 mm downstream the thruster axis, T_e is higher for the $2S_0$ configuration, whereas at 200 mm, T_e is higher for the $3S_0$ configuration. As explained previously (Sec. 6.4.1.2), the multipeak structure for V_p and T_e is real and stable.

The time evolution of n_e is shown in Fig. 6.17. As can be seen, the electron density is higher for the $2S_0$ configuration. A comparison with the time evolution of the discharge current depicted in Fig. 6.14 shows that the electron density and the discharge current have the same temporal behavior for both geometries.

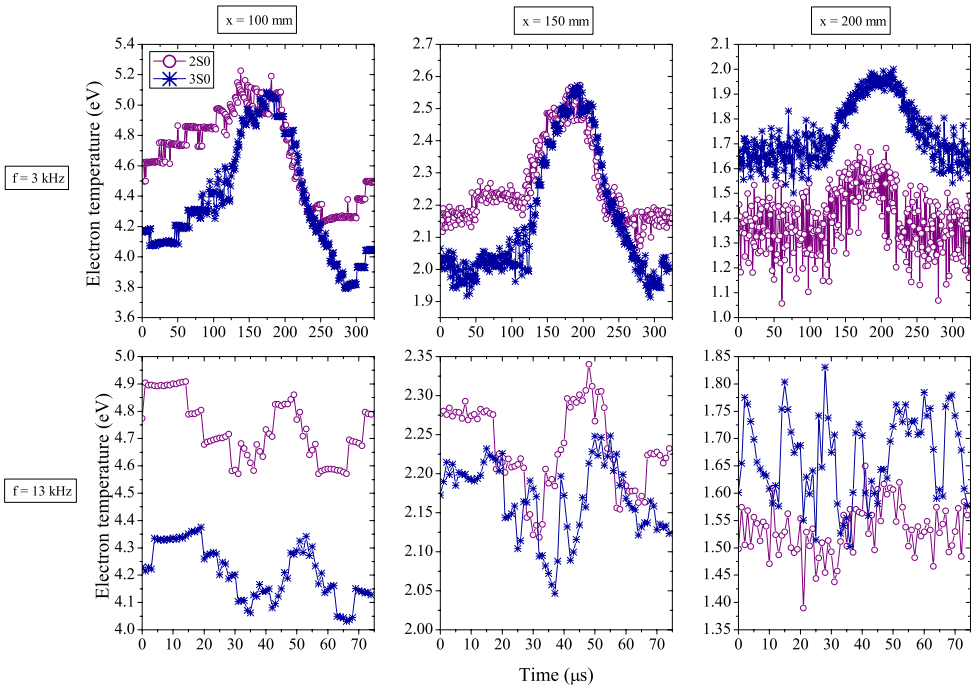

Figure 6.16: Influence of the channel width on the time evolution of T_e measured with a Langmuir probe at three different axial positions on the axis of PPI thruster operating at $U_d = 200\,\mathrm{V}$, $\dot{m}_a = 1.0\,\mathrm{mg/s}$ (Xe). The $2S_0$ and the $3S_0$ configuration are compared.

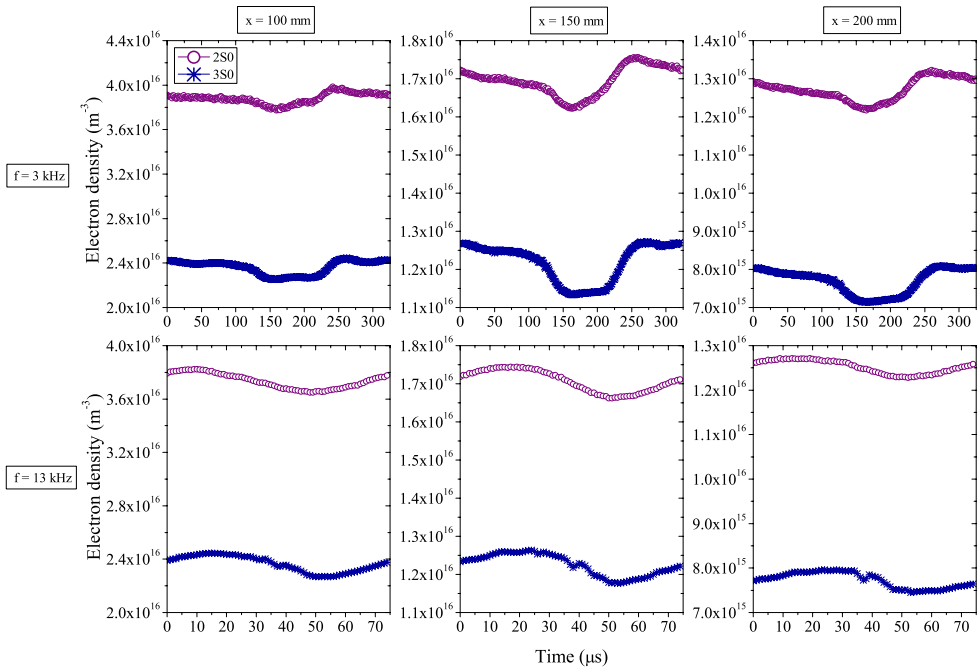

Figure 6.17: Influence of the channel width on the time evolution of n_e measured with a Langmuir probe at three different axial positions on the axis of PPI thruster operating at $U_d = 200\,\mathrm{V}$, $\dot{m}_a = 1.0\,\mathrm{mg/s}$ (Xe). The $2S_0$ and the $3S_0$ configuration are compared.

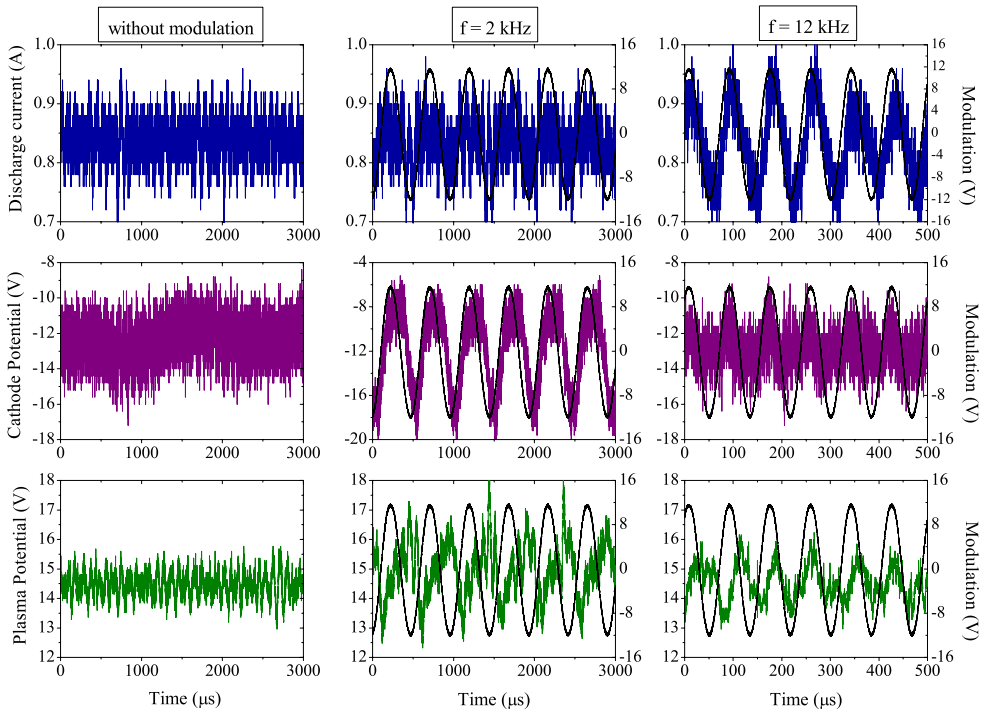

Figure 6.18: Influence of the keeper modulation on I_d, CRP and V_p for the PPI thruster operating at $U_d = 200\,\mathrm{V}$, $\dot{m}_a = 1.0\,\mathrm{mg/s}$ (Kr). The solid black line represents the modulation signal.

6.4.2 Comparison between xenon and krypton

In order to evaluate the influence of the working gas on the plasma parameters, the PPI thruster was operated at 200 V with xenon and krypton. In both cases, an anode mass flow rate of 1.0 mg/s was used. The resulting mean discharge current was $I_d = 0.93\,\mathrm{A}$ for Xe and $I_d = 0.84\,\mathrm{A}$ for Kr.

The influence of the keeper modulation on the discharge current, the cathode-to-ground potential as well as the plasma potential for the PPI thruster operating with krypton is shown in Fig. 6.18. As can be seen in Fig. 6.5 and Fig. 6.18, the modulation of the keeper electrode to maintain the thruster in a periodic quasi-harmonic oscillation regime works for both gases. The modulation frequencies for the two gases are slightly different: in order to obtain a periodic quasi-harmonic oscillation of I_d, the frequency is 13 kHz for Xe and 12 kHz for Kr, the plasma potential V_p can be maintained in a periodic quasi-harmonic regime with a frequency of 3 kHz for Xe and 2 kHz with Kr. The time evolution of V_p, T_e and n_e over one period of the oscillation for Xe and Kr is represented in Fig. 6.19. As the modulation frequencies are different, the time evolution is represented over one normalized period. The time evolution of the discharge current is also represented. The measurements were performed on the thruster

axis 100 mm downstream the thruster exit plane.
As can be seen in Fig. 6.19, the time evolution of I_d and n_e is very similar for Xe and Kr. The time evolution of V_p and T_e is not exactly the same, but the global trend is similar. The values for all quantities are lower with Kr than with Xe. Even if the modulation frequencies are slightly different, the time evolution of the plasma parameters over one oscillation period is almost the same for the two gases meaning that the observed phenomena are independent of the propellant gas.

The measurements of the plasma parameters were performed at 4 different radial positions for Xe (y = 0, 18.5, 25 and 50 mm) and 3 radial positions for Kr (y = 0, 18.5 and 25 mm). The mean values of the plasma parameters for the two different gases obtained from the time resolved measurements are represented in Fig. 6.20. Note that also for Kr, the modulation has almost no influence on the mean values of I_d, V_p, T_e and n_e. As can be seen, the mean values for Kr are lower than the mean values for Xe. However, the values decrease slower with an increasing distance from the thruster axis for Kr than for Xe.

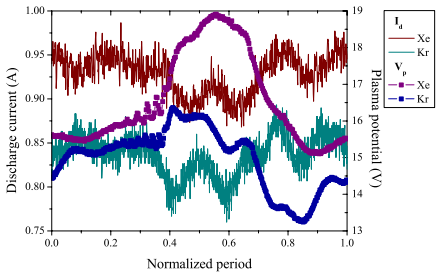

(a) Xe: f = 3 kHz, Kr: f = 2 kHz

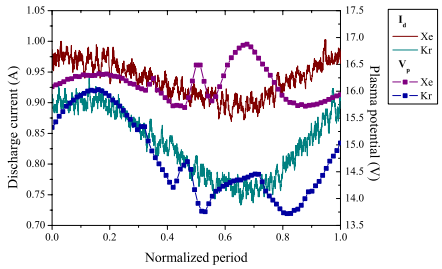

(b) Xe: f = 13 kHz, Kr: f = 12 kHz

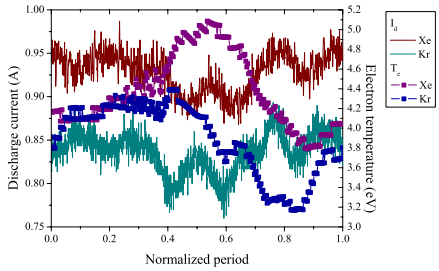

(c) Xe: f = 3 kHz, Kr: f = 2 kHz

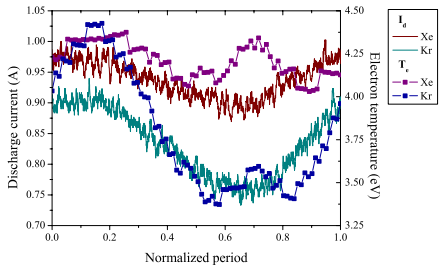

(d) Xe: f = 13 kHz, Kr: f = 12 kHz

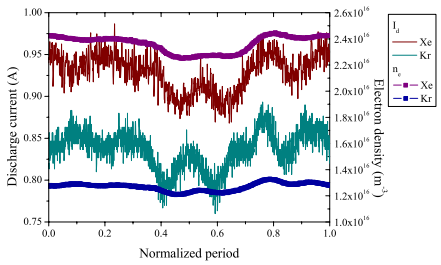

(e) Xe: f = 3 kHz, Kr: f = 2 kHz

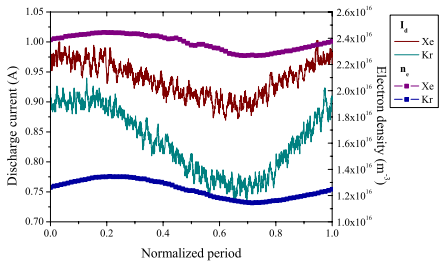

(f) Xe: f = 13 kHz, Kr: f = 12 kHz

Figure 6.19: Comparison of the time evolution over one period of V_p, T_e and n_e for Xe and Kr for the two different frequencies at 100 mm downstream thruster exit plane on the thruster axis.

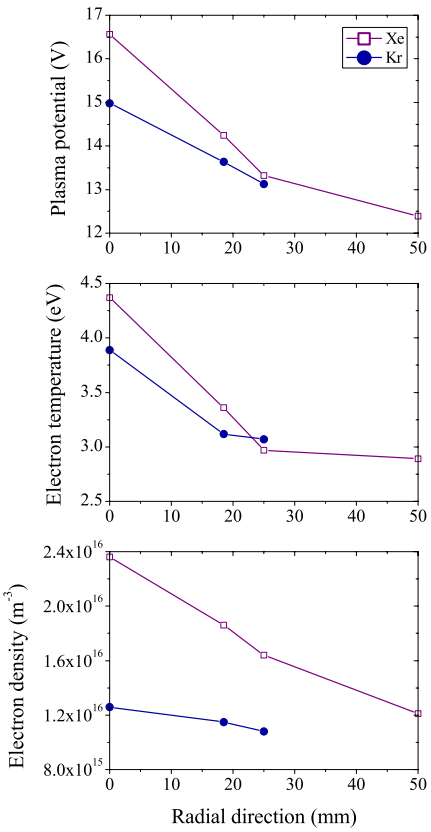

Figure 6.20: Comparison of the mean values of V_p, T_e and n_e measured with a Langmuir probe in the far-field plume of the PPI thruster operating with Xe (purple symbol) and Kr (blue symbol) at $U_d = 200\,\mathrm{V}$, $\dot{m}_a = 1.0\,\mathrm{mg/s}$.

6.5 Time-resolved measurements in the far-field plume of the PPS®1350-ML

In order to validate the modulation technique, the latter was used to measure the time dependent electron properties in the far-field plume of the PPS®1350-ML. For this purpose, the amplifier had to be modified. In fact, the PA240CC amplifiers can only deliver 60 mA, which is enough for the low-power PPI thruster, but not enough for the PPS®1350-ML. The first idea was thus to replace the PA240CC amplifiers by two PA92 amplifiers. These amplifiers are able to deliver up to 4 A. This was impossible due to availability issues of the components. Therefore, the amplifier for the PPS®1350-ML keeper modulation was built using PA240CC high voltage operational amplifiers complemeted by current booster stages. The current booster is constructed from two bipolar transistors (MJE 15032 and MJE15033). The amplifier is hence capable of delivering a current of 400 mA which is sufficient for the PPS®1350-ML thruster. The amplifier was powered by a home-made power supply able to deliver a voltage of ± 80 V. This power supply is equipped with a transformer with a relatively low capacity (less than 100 pF) in order to keep the whole system well isolated from ground.
The PPS®1350-ML thruster was operated in the PIVOINE-2g test bench at 250 V and 3.0 mg/s resulting in a mean discharge current of 2.32 A. This is not the normal operating point of the thruster. However, for the validation of the new amplifier, it was advisable to choose an operating point of the thruster with a relatively low discharge current in order the guarantee a save operation of the amplifier. The background pressure in the vacuum chamber during thruster operation was about 1.5×10^{-5} mbar (Xe).

6.5.1 Influence of the keeper modulation on the discharge behavior

As has already been shown in Sec. 6.4.1.1, the frequency has to be adapted to obtain a periodic quasi-harmonic oscillation regime of the thruster. AZs for the PPI thruster, two different frequencies have been found for the PPS®1350-ML thruster. The amplitude of the modulation was adapted in order to maintain the keeper current at about 10 % of the discharge current. The influence of the keeper modulation on the discharge current, the cathode-to-ground potential and the plasma potential measured with a heated emissive probe is shown in Fig. 6.21. The corresponding power spectrum of the discharge current and the plasma potential is shown in Fig. 6.22. The emissive probe was positioned at 250 mm downstream the thruster exit plane on the thruster axis. As can be seen in Fig. 6.21 and Fig. 6.22, without modulation the discharge current and the plasma potential are non-stationary and no dominant frequency can be observed. A broad peak centered around 13 kHz is visible. This broad peak shows that many elementary frequencies are present in the discharge current and plasma potential signal. For a modulation frequency of 13.8 kHz, one can achieve a periodic quasi-harmonic oscillation regime of both the discharge current and the plasma potential (clear peak at 13.8 kHz in the power spectrum). This is in contrast to what was observed with the PPI thruster, where one could obtain a periodic, quasi-harmonic oscillation regime of either I_d or V_p. The second modulation frequency that was used for the further investigations is 2.2 kHz. At this frequency one obtains also a periodic, quasi-harmonic oscillation regime of V_p but no clear influence of the modulation on I_d is visible. The time evolution of V_p has an almost rectangular shape in this case. In the

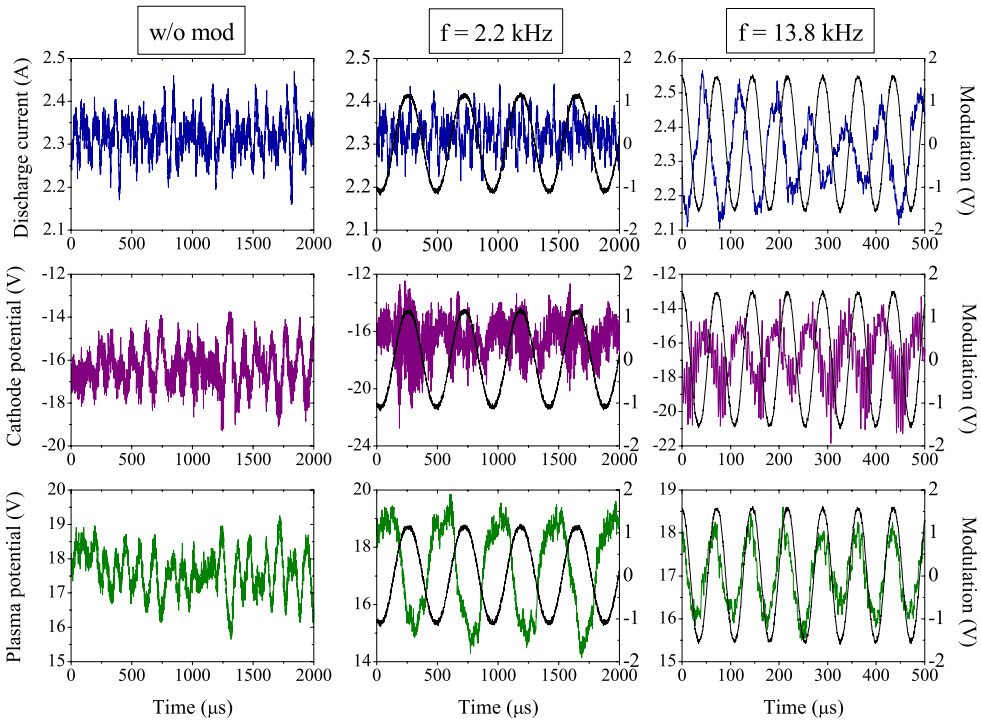

Figure 6.21: Influence of the keeper modulation on I_d, CRP and V_p for the PPS®1350-ML thruster operating at $U_d = 250\,\mathrm{V}$, $\dot{m}_a = 3.0\,\mathrm{mg/s}$ (Xe). The solid black line represents the modulation signal.

power spectrum of the discharge current one can actually observe a small peak at 2.2 kHz, but the same broad peak than without modulation is dominant. The power spectrum of the plasma potential represents clearly a peak at 2.2 kHz. Furthermore the second and third harmonics of this frequency are also visible.

As for the PPI thruster, the mean discharge behavior of the thruster is almost not influenced by the keeper modulation, as can be seen in Tab. 6.2.

6.5.2 Time evolution of the plasma parameters

The time evolution of V_p, T_e and n_e in Xe for the two different modulation frequencies is displayed in Fig. 6.8 over one oscillation period. The first row represents the evolution over one period at 2.2 kHz, the second row the one for 13.8 kHz. The measurements are taken at 250 mm downstream the thruster exit plane and on the thruster axis.

As can be seen in Fig. 6.23, the time evolution of V_p, T_e and n_e is different for the two modulation frequencies. At 2.2 kHz, the time evolution of V_p, T_e and n_e is almost rectangular, whereas it is almost perfectly sinuoidal at 13.8 kHz. A second fact that can be noticed is that

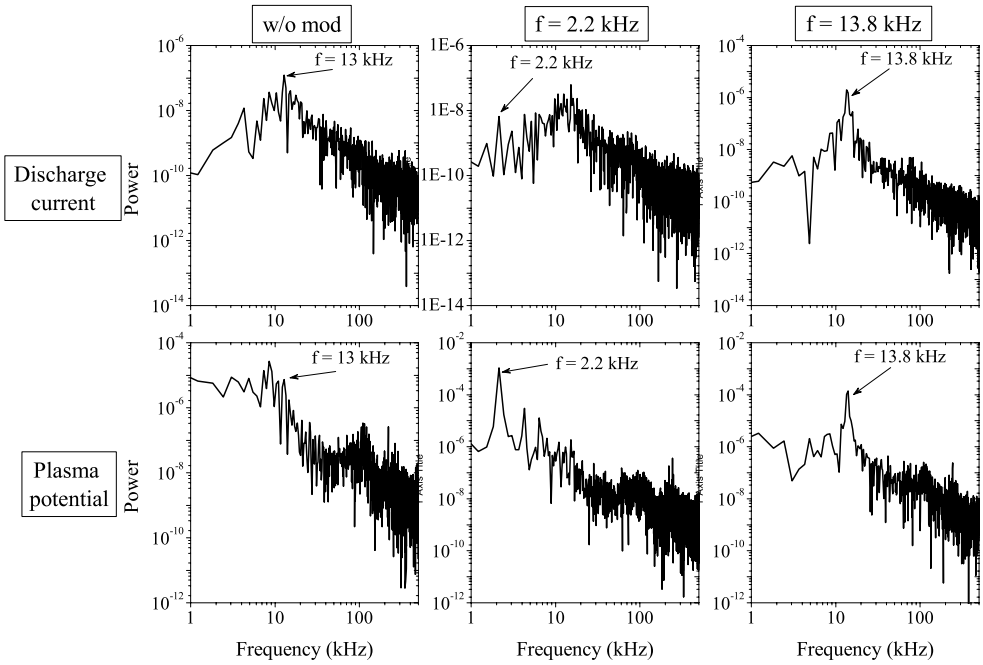

Figure 6.22: Power spectrum of the discharge current and the plasma potential without modulation and for the 2 modulation frequencies.

Table 6.2: Mean values of I_d, CRP and V_p as a function of the modulation frequency. The values without modulation as well as the average values are also given. The plasma potential is measured by means of a heated emissive probe at 250 mm downstream the thruster exit plane on the thruster axis.

frequency	I_d	CRP	V_p
[kHz]	[A]	[V]	[V]
w/o mod	2.32	-16.34	17.6
2.2	2.32	-16.49	17.18
13.8	2.32	-16.8	16.98
average value	2.32	-16.54 ±0.23	17.25 ±0.31

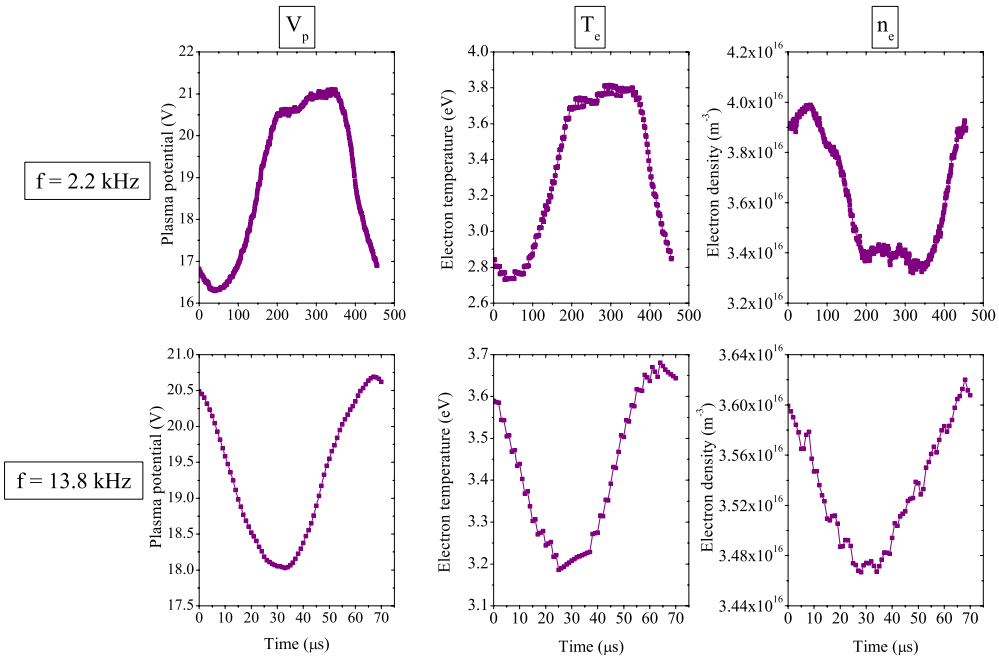

Figure 6.23: Time evolution of the plasma potential V_p, the electron temperature T_e and the electron density n_e measured by means of a Langmuir probe at 250 mm downstream the thruster exit plane on the thruster axis in the plasma plume of the PPS®1350-ML operating at $U_d = 250\,\mathrm{V}$, $\dot{m}_a = 3.0\,\mathrm{mg/s}$ (Xe).

Table 6.3: Mean values of V_p, T_e and n_e for the two different modulation frequencies. The measurements were taken at 250 mm downstream the thruster exit plane on the thruster axis.

frequency	V_p	T_e	n_e
[kHz]	[V]	[eV]	[m^{-3}]
2.2	18.96	3.34	3.61×10^{16}
13.8	19.3	3.42	3.53×10^{16}
average value	19.13 ± 0.24	3.38 ± 0.06	$3.57 \times 10^{16} \pm 5.66 \times 10^{14}$

for 2.2 kHz, V_p and T_e are in phase and n_e is in antiphase with V_p and T_e. On the contrary, for 13.8 kHz V_p, T_e and n_e are in phase. Finally, Fig. 6.23 also shows that the amplitude of the fluctuations is bigger for the lower modulation frequency, i.e. 26 % against 13 % for the plasma potential, 33 % against 15 % for the electron temperature and 19 % against 4.5 % for the electron density.
It has been shown for the PPI thruster that the modulation has almost no influence on the mean values of the electron properties. This is also valid for the PPS®1350-ML, as can be seen in Tab. 6.3.

6.6 Conclusion

In this chapter, time-resolved measurements of the plasma potential, the electron temperature and the electron density in the far-field plume of two different Hall thrusters, namely the 200 W PPI thruster and the 1.5 kW PPS®1350-ML, are presented. A cylindrical Langmuir probe is used to measure V_p, T_e and n_e. The time evolution of the plasma potential is also directly measured with a sufficiently heated emissive probe. In order to perform proper time-resolved measurements, the thruster is forced to a periodic quasi-harmonic regime by applying a sinusoidal modulation to a floating electrode in the vicinity of the cathode. The frequency of this modulation is adjusted to obtain a stable operating regime of the thruster synchronized to the modulation. The frequency required for thruster synchronization is different whether the discharge current is observed or if one observes the plasma potential measured with a sufficiently heated emissive probe. The time evolution of V_p, T_e and n_e over one period is different for the two modulation frequencies. However, the mean values remain almost uninfluenced by the modulations. It has been shown by a comparison of the plasma potential measured by means of a Langmuir and an emissive probe, that the latter can be used to get an instantaneous and direct measurement of V_p. Furthermore, it has been demonstrated that the presented measurement technique works for different gases (Xe and Kr) and for different thrusters (PPI and PPS®1350-ML). The required modulation frequencies depend on the propellant gas but the time evolution over one oscillation period is almost the same for both gases.
Although the thruster is forced to a specific operating regime (periodic quasi-harmonic oscillation), neither the global thruster behavior nor the plasma parameters are significantly altered by the modulation. This has also been verified by measuring the ion velocity distribution by means of LIF with and without modulation at different positions in the far-field plume of

the PPI thruster. The presented method is thus a powerful technique for performing proper time-resolved measurements of the plasma parameters in an instationary cross-field discharge.

Chapter 7

General conclusion and perspectives

Hall thrusters are nowadays a mature space technology with a long flight heritage. However, extensive research works are still going on in order to achieve a better understanding of the complex physical processes, to improve the efficiency and to increase the thruster lifetime as well as to reduce hazardous thruster-spacecraft interactions.

The presented work fully fits in the frame of current research activities. The objectives of this work were to develop a semi-empirical scaling model for Hall thrusters, to investigate the influence of the channel width on the performances of a low power Hall thruster and to perform an experimental investigation of the electron properties in the plume of a Hall thruster.

A semi-empirical scaling model for Hall thrusters has been developed. This scaling model considers the three characteristic dimensions, namely the channel length L, the channel mean diameter d and the channel width h. It relies on analytical laws that are obtained from the fundamental physical principles of Hall thrusters. A set of simplifying assumptions naturally specifies the validity domain of the scaling relations. Besides, the approach considers rigorous rules about atom density and channel wall temperature. A vast database with 36 different Hall thrusters, that cover a power range from 10 W to 50 kW and a thrust range from 0.4 mN to more than 3 N, is used to validate the developed scaling relations and to assess the necessary proportionality coefficients. The scaling method was used to determine the geometry and the operating conditions of a 20 kW Hall thruster capable of delivering a thrust of 1 N. Results obtained with two different series of simplifying assumptions are compared. The first set forms a very restrictive frame. The second set offers a more realistic description of the physics at work as the electron temperature, the energy losses and multiply charged ion species are taken into account. However, a comparison of the two series shows that using a more realistic description of the physics does not lead to an improvement of the accuracy. Scaling relations with quite restrictive assumptions are therefore satisfactory to get a first estimate of the geometry and the operating conditions of a new Hall thruster. The use of scaling relations permits time savings during the design and optimization phase.
The calculated dimensions and operating conditions are in good agreement with the 20 kW PPS20k Hall thruster developed and tested in the frame of the European project HiPER.

The influence of the channel width on the ionization and acceleration processes and hence the performance level of a Hall thruster have been investigated. The idea for this study arose from the linear relationship between the channel width and the channel mean diameter pointed out in the work on scaling laws. The goal of the study was to verify if the performance level of a low power Hall thruster could be increased by a modification of the channel geometry.

A low power, permanent magnet Hall thruster with a variable channel width h was used to investigate the influence of h for two different working gases (Xe and Kr). The channel width could be modified by means of different sets of ceramic rings while keeping the channel mean diameter, the channel length as well as the magnetic field map constant. Several quantities, such as discharge current, ion current density, Xe^+ ion axial velocity, ion energy, channel wall temperature and thrust, have been measured over a broad range of propellant mass flow rates and applied voltages. These measurements have shown for both gases that enlarging the channel width enhances the ionization and acceleration processes, broadens the operating envelope, reduced the channel wall temperature and the losses due to plasma-wall interactions and improves the thruster performance level. Two mechanisms can be in fact put forward to explain the experimental outcomes: First, the surface-to-volume ratio decreases with h, which reduces the wall-losses. Second, the magnetic field strength near the wall increases with h, which leads to a better plasma confinement.
This study is of great interest, as is shows that the efficiency of low power Hall thrusters, that is in general relatively low, can be increased by simply changing the channel width.

The plasma plume of a Hall thruster exhibits a relatively large divergence angle which leads to electrical and mechanical interactions between the charged particles in the plasma plume and the spacecraft. Numerical models of the plume are necessary to find the optimized position of the thruster on the satellite so that hazardous plasma-spacecraft interactions can be minimized. Experimental data for the electron properties in the far-field plume are essential for the validation of these numerical plume models. Time-averaged measurements of the plasma potential, the electron temperature and the electron density have been performed in the far-field plume of the PPS®100-ML thruster by means of a single, cylindrical Langmuir probe and a heated emissive probe. The far-field plume has been mapped from 300 to 660 mm downstream the thruster exit plane and from 0 to 60 °, where 0 ° corresponds to the thruster axis. The influence of different operating parameters, such as discharge voltage, anode and cathode mass flow rate as well as magnetic field strength, on the electron properties was investigated. The results show that the plume is an isentropic expansion. The values of V_p and T_e obtained with the two different probes are in good agreement. Hence, an emissive probe can be used to get a direct measurement of these parameters without sweeping the probe voltage.
The measurement of the plasma parameters in the far-field plume is insufficient for a better understanding of ionization and acceleration processes. A fast moving probe system has therefore been developed in order to measure the plasma parameters in the thruster near-field plume and even inside the discharge chamber where the ion density is so high that sputtering and ablation of the probes becomes an issue. This new system is composed of a compact piezo linear drive that can achieve a speed of up to 350 mm/s with a travel range of 90 mm. With the new system, the profile of the plasma potential has been measured in the near-field plume of the PPI thruster by means of an emissive probe.

Finally, time-resolved measurements of the electron properties have been performed. These measurements are necessary in order to account for transient fluctuations of the plasma parameters due to the highly non-stationary behaviour of the thruster discharge. In order to perform proper time-resolved measurements, the thruster was maintained in a periodic, quasi-harmonic

oscillation regime by applying a sinusoidal modulation to a floating electrode in the vicinity of the cathode. The frequency of the modulation was adjusted to obtain a stable operating regime of the thruster synchronized to the modulation. The time evolution of V_p, T_e and n_e has been measured for two different thrusters, namely the 200 W PPI thruster and the 1.5 kW PPS®1350-ML as well as for two different working gases, xenon and krypton, respectively. The time evolutions of V_p measured with the two different probes are in good agreement. An emissive probe can therefore be used to get an instantaneous measurement of $V_p(t)$. Although the thruster is forced to a specific operating regime, neither the global thruster behavior nor the plasma parameters are significantly altered by the applied modulation. The presented method is thus a powerful technique for performing time-resolved measurements of the electron properties in an instationary cross-field discharge.

Perspectives

Based on the results presented in this work, the following future investigations are advisable:

1. **Scaling laws:** The described scaling method could still be improved by eliminating further assumptions. It would be interesting to account for the beam divergence or the fraction of multiply-charged ions and not only singly- and doubly-charged ions. The accuracy of the second order approach could be significantly improved by more experimental data about the evolution of the gas and electron temperature as well as the propellant conversion efficiency as a function of the discharge voltage. Attempting to include the magnetic field topology would represent a powerful progress as the latter is the most fundamental feature to ensure a successful operation. More experimental data on the influence of the magnetic field amplitude as well as the magnetic field gradient on the thruster performances (thrust and efficiency) shall soon be available. A new Hall thruster PPS-Flex has recently been designed in order to investigate the influence of divers parameters of the magnetic field topology on the thruster performances [106]. The magnetic circuit of the PPS-Flex has been modified so that each component of the magnetic field topology can be modified individually. Another improvement of the scaling method would be to extend it to other working gases. So far, the scaling relations are solely valid for xenon. The recent development of a low power Hall thruster optimized for krypton by our team should provide necessary experimental data for this extension.

2. **Influence of the channel width:** It has been shown that the performance level of small Hall thrusters could be improved by increasing the channel width. However, the approach should be tested on a larger thruster, e.g. the 1.5 kW PPS®1350-ML, in order to check if the method can be successfully applied to large size device. The surface-to-volume ratio is already more favorable for high power thrusters, so the gain in efficiency would certainly be lower than for low power thrusters.

3. **Electron properties:** The large amount of experimental data obtained from far-field measurements should now be compared to numerical plume models. Currently, in cooperation with M. Merino from the *Universidad Politécnica* in Madrid, the experimental far-field plume data is used to fit a set of semi-analytical fluid models that rely on quasi-

selfsimilarity exhibited by hypersonic plasma plumes. A first comparison between model outcomes and experimental data show a good agreement. A simple characterization of plasma density and flux in the each thruster can therefore be provided by the models. Hence, the validated models can be used as a tool for preliminary thruster optimization. In additions, further measurements of the electron properties at larger angles off the thruster axis would be of great interest for the validation of the SPIS software (**S**pacecraft **P**lasma **I**nteraction **S**ystem) [107, 108].

The new fast-moving probe system could now be used to map the plasma parameters in the complete thruster near-field plume and even inside the discharge chamber. A Langmuir probe should be used, as it provides a measurement of V_p, T_e, n_e and even the electron energy distribution function.

Different additional works concerning the time-resolved measurement technique are certainly conceivable. It would be interesting to investigate the temporal behavior of the electron properties in the high frequency domain. Two different frequency ranges appear to be of great interest, namely the frequency range between 100 and 500 kHz that corresponds to the ion transit time oscillations and the range of frequencies above 1 MHz corresponding to the electron azimuthal fluctuations (ExB drift). This necessitates a modification of the amplifier system and the emissive probe system. The emissive probe system is so far limited to a upper frequency of about 60 kHz. Furthermore it would be interesting to better understand the different structures that can be observed for the time evolution of V_p and T_e. A possible idea to get further insights on these structures could be to use a different waveform for the modulation signal. One could for example use a dirac instead of the sinusoidal waveform. Nevertheless, numerical simulations of the transient fluctuations are vital for a more detailed understanding of the observed phenomena.

One of the next steps is to extract the time-resolved electron energy distribution function (EEDF) from the measured data. A first attempt has already shown that the signal-to-noise ratio of the experimental data is suitable for the determination of the EEDF from the second derivative of the Langmuir probe characteristic. Two examples of EEDFs measured in the far-field plume of the PPS®1350-ML and the PPI thruster are represented in Fig. 7.1. The EEDFs were obtained from the time-resolved I-V characteristics.

The modulation of the keeper electrode could also be used for time-resolved LIF measurements. So far, this measurements have been performed using a fast power switch that perturbates the thruster behavior. With the thruster operating in a periodic, quasi-harmonic oscillation regime, the fast power switch would no longer be necessary for the synchronization of the measurements.

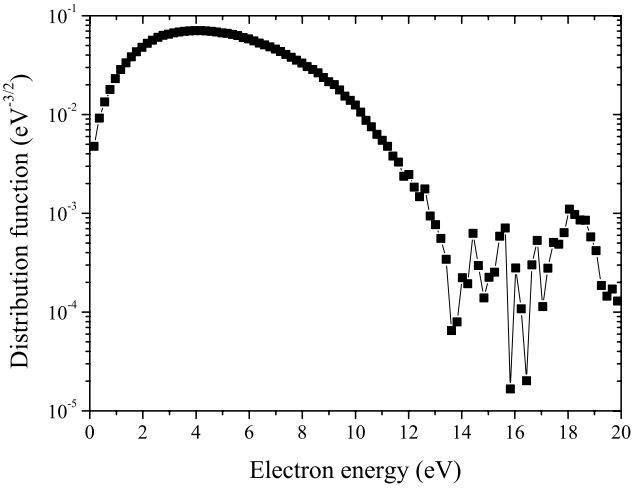

(a) EEDF in the far-field plume of the PPS®1350-ML thruster at 300 mm downstream the thruster exit plane on the thruster axis.

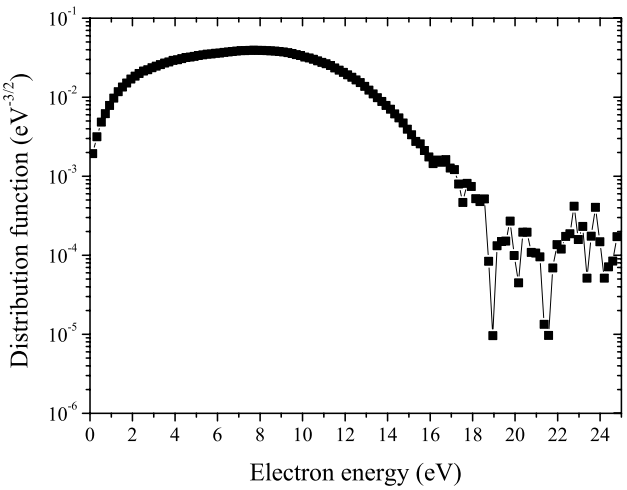

(b) EEDF in the far-field plume of the PPI thruster at 100 mm downstream the thruster exit plane on the thruster axis.

Figure 7.1: Electron energy distribution function (EEDF) measured with a single cylindrical Langmuir probe in the far-field plume of two different Hall thrusters (PPS®1350-ML and PPI).

Bibliography

[1] R.G. Jahn, Y. Choueiri, Electric Propulsion, Encyclopedia of Physical Science and Technology 3rd Edition, Vol. 5 (Academic Press, San Diego), 125-141 (2002).

[2] F.R. Chang Díaz et al, The VASIMR engine: project status and recent accomplishments, Proceedings of the 42nd AIAA Aerospace Science Meeting (Reno), AIAA-2004-0149 (2004).

[3] A. Aanesland, S. Mazouffre, P. Chabert, PEGASES - A new promising electric propulsion concept, EuroPhysics News **42**, 28-31 (2011).

[4] R. G. Jahn, Physics of electric propulsion, Dover Publications, Mineola, New York, 1996.

[5] D. M. Goebel, I. Katz, Fundamentals of Electric Propulsion, Wiley, Hoboken, NJ, 2008.

[6] V.V. Zhurin, H.R. Kaufmann, R.S. Robinson, Physics of closed drift thrusters, Plasma Sources Sci. Technol. **8**, R1-R20 (1999).

[7] N. Gascon, M. Dudeck, S. Barral, Wall material effects in stationary plasma thrusters I. Parametric studies of an SPT-100, Phys. Plasmas **10**, 4123-4136 (2003).

[8] C.R. Koppel, F. Marchandise, M. Prioul, D. Estublier, F. Darnon, The SMART-1 electric propulsion subsystem around the Moon: In flight experience, Proceedings of the 41th Joint Propulsion Conference (Tucson), AIAA paper 05-3671 (2005).

[9] G.S. Janes, R.S. Lowder, Anomalous electron diffusion and ion acceleration in a low density plasma, Physics of Fluids **9**, 1115-1123 (1966).

[10] N.B. Meezan, W.A. Hargus, M.A. Cappelli, Anomalous electron mobility in a coaxial Hall discharge plasma, Physical Review E **63**, 026410 (2001).

[11] A. Lejeune et al., Impact of the channel width on Hall thruster discharge properties and performances, Proceedings of the 32nd International Electric Propulsion Conference (Wiesbaden), IEPC-2011-019 (2011).

[12] TEC-MP-EPL-WI006, CORONA operational manual, Manufacturer reference ALTA CUP TN-06 1.3-01, ESA document

[13] TEC-MP-EPL-D046, LTB Operational Manual v1.0, ESA document

[14] TEC-MP-EPL-D045, CORONA Diagnostics Arm UM v1.0, ESA document

[15] F. Renaudin, V. Cagan, M. Guyot, A. Cadiou, V. Vial, P. Dumazert, Magnetic Circuits for Hall thrusters: Use of permanent magnets, Proceedings of the 28th International Electric Propulsion Conference (Toulouse), IEPC 03-284 (2003).

[16] A. Leufroy, T. Gibert, A. Bouchoule, Characteristics of a permanent magnet low-power Hall thruster, Proceedings of the 31th International Electric Propulsion Conference (Ann Arbor), IEPC-2009-083 (2009).

[17] M. Guyot, P. Renaudin, V. Cagan, C. Boniface, patent FR 07 05658 (2007).

[18] M. Guyot et al., New Concepts for Magnetic Field Generation in Hall Effect Thrusters, *Proceedings of the 5th International Spacecraft Propulsion Conference*, Heraklion, Greece, 2008.

[19] A.I. Morozov and V.V. Savelyev, Fundamentals of Stationary Plasma Thruster Theory, Reviews of Plasma Physics **21** (edited by B.B. Kadomtsev and V.D. Shafranov) Consultant Bureau, New York (2000).

[20] V. Kim, Main Physical Features and Processes Determining the Performance of Stationary Plasma Thrusters, Journal of Propulsion and Power, **14**, 736-743 (1998).

[21] V. Kim, V. Kozlov, A. Skrylnikov et al., Development and Investigation of the SPT-20 and SPT-25 Laboratory Models, Proceedings of the 1st Annual International Conference and Exhibition. Small Satellites: New technologies, achievements, problems and prospects for the International co-operation in the new millenium, section YIII "Jet Propulion" (Moscow), 2000.

[22] J. Ashkenazy, Y. Raitses, G. Appelbaum, Low Power Scaling of Hall Thrusters, Proceedings of the 2nd European Spacecraft Propulsion Conference (Noordwijk), ESA Publications Division (1997).

[23] V. Khayms, M. Martinez-Sanchez, Design of Miniaturized Hall Thruster for Microsatellites, Proceedings of the 32nd Joint Propulsion Conference (Lake Buena Vista), AIAA paper 96-3291 (1996).

[24] Y. Daren, D. Yongjie, Z. Zhi, Improvement on the Scaling Theory of the Stationary Plasma Thruster, Journal of Propulsion and Power **21**, 139-143 (2005).

[25] T. Misuri, F. Battista, C. Barbieri, E.A. De Marco, M. Andrenucci, High Power Hall Thruster Design Options, Proceedings of the 30th International Electric Propulsion Conference (Florence), IEPC 07-311 (2007).

[26] K. Dannenmayer, S. Mazouffre, Sizing of Hall Effect Thrusters with Input Power and Thrust Level: An Empirical Approach, Journal of Technical Physics **49**, 231-254 (2008).

[27] M. A. Lieberman, A. J. Lichtenberg, Principles of Plasma Discharges and Materials Processing, John Wiley & Sons, Inc., New York (1994).

[28] J.W. Koo, I.D. Boyd, Modelling of Anomalous Electron Mobility in Hall Thrusters, Physics of Plasmas **13**, 033501 (2006).

[29] W.A. Hargus, Jr., M.A. Cappelli, Laser-induced fluorescence measurements of velocity within a Hall discharge, Appl. Phys. B **72**, 961-969 (2001).

[30] S. Mazouffre, A. Lazurenko, P. Lasgorceix, M. Dudeck, S. d'Escrivan, O. Duchemin, Expanding Frontiers: Towards High Power Hall Effect Thrusters for Interplanetary Jouneys, Proceedings of the 7th International Symposium on Launcher Technologies, Paper O-25 (2007).

[31] A. Gallimore, Near- and Far-Field Characterization of Stationary Plasma Thruster plumes, J. Spacecraft Rockets **38**, 441-453 (2001).

[32] T. Ito, N. Gascon, W.S. Crawford, M.A. Cappelli, Experimental Characterization of a Micro-Hall Thruster, J. Propul. Power **23**, 1068-1074 (2007).

[33] G.Guerrini, C.Michaut, M. Dudeck, M. Bacal, Parameter Analysis of Three Small Ion Thrusters, Proceedings of the 2nd European Spacecraft Propulsion Conference, (1997).

[34] R.S. Jankovsky, C. McLean, J. McVey, Preliminary Evaluation of a 10kW Hall Thruster, Proceedings of the 37th AIAA Aerospace Science Meeting and Exhibit (Reno), AIAA-99-0456 (1999).

[35] D.H. Manzella, R.S. Jankovsky, R.R. Hofer, *Laboratory Model 50kW Hall Thruster*, Proceedings of the 39th AIAA/ASMA/SAE/ASEE Joint Propulsion Conference (Indianapolis), AIAA-02-3676 (2002).

[36] K. Dannenmayer, S. Mazouffre, Elementary scaling laws for sizing up and down Hall effect thrusters: Impact of simplifying assumptions, Proceedings of the 31st International Electric Propulsion Conference (Ann Arbor), IEPC 09-077 (2009).

[37] R.S. Jankovsky, S. Tverdokhlebov, D. Manzella, High Power Hall Thruster, Proceedings of the 35th Joint Propulsion Conference (Los Angeles), AIAA-99-2949 (1999).

[38] S. Mazouffre, K. Dannenmayer, J. Pérez-Luna, Examination of Plasma-Wall Interactions in Hall Effect Thrusters by Means of Calibrated Thermal Imaging, J. Appl. Phys. **102**2, 023304 (2007).

[39] S. Mazouffre, P. Echegut, M. Dudeck, A Calibrated Infrared Imaging Study on the Steady State Thermal Behavior of Hall Effect Thrusters, Plasma Sources Sci. Technol. **15**, 13-22 (2006).

[40] K.E. Witzberger, D. Manzella, Performances of Solar Electric Powered Deep Space Missions Using Hall Thruster Propulsion, Proceedings of the 41st Joint Propulsion Conference (Tucson), AIAA paper 05-4268 (2005).

[41] L. Johnson, R. A. Meyer, K. Frame, In-Space Propulsion Technologies for Robotic Exploration of the Solar System, Proceedings of the 42nd Joint Propulsion Conference (Sacramento), AIAA paper 06-4687 (2006).

[42] Y. Raitses, D. Staack, M. Keidar, N.J. Fisch, Electron-Wall Interaction in Hall Thrusters, Phys. Plasmas **12**, 057104 (2005).

[43] J.A. Linnel, A.D. Gallimore, Internal Plasma Potential Measurement of a Hall Thruster Using Plasma Lens Focusing, Physics of Plasma **13**, 103504 (2006).

[44] R.R. Hofer, A.D. Gallimore, Ion Species Fractions in the Far-Field Plume of a High-Specific Impulse Hall Thruster, Proceedings of the 39th Joint Propulsion Conference (Hundsville), AIAA paper 03-5001 (2003).

[45] C. Casaregola, G. Cesaretti, M. Andrenucci, HiPER: A roadmap for future space exploration with innovative electric propulsion technologies, Proceedings of the 31st International Electric Propulsion Conference (Ann Arbor), IEPC-2009-066 (2009).

[46] S. Zurbach, N. Cornu, P. Lasgorceix, Performance evaluation of a 20 kW Hall effect thruster, Proceedings of the 32nd International Electric Propulsion Conference (Wiesbaden), IEPC-2011-020 (2011).

[47] S. Mazouffre, A. Lejeune, High power electric propulsion for robotic exploration of our solar system, Proceedings of the Space Access International Conference (Paris), Paper 2011-051 (2001).

[48] K. Dannenmayer, S. Mazouffre, Elementary scaling relations for Hall effect thrusters, J. Propul. Power **27**, 236-245 (2011).

[49] Y. Raitses, J. Ashkenazy, M. Guelmann, Propellant Utilization in Hall thrusters, J. Propul. Power **14**, 247-253 (1998).

[50] E. Y. Choueri, Plasma oscillations in Hall thrusters, Phys. Plasmas **8**, 1411-1426 (2001).

[51] D.L. Brown, C.W. Larson, B.E. Beal, A.D. Gallimore, Methodology and historical perspective of a Hall thruster efficiency analysis, J. Propul. Power **25**, 1163-1177 (2009).

[52] R.R. Hofer, R.S. Jankovsky, A.D. Gallimore, High-specific impluse Hall thrusters, Part 1: Influence of current density and magnetic field, J. Propul. Power **22**, 721-731 (2006).

[53] S. Mazouffre, V. Kulaev, J. Pérez-Luna, Ion diagnostics of a discharge in crossed electric and magnetic fields for electric propulsion, Plasma Sources Sci. Technol. **18**, 034022 (2009).

[54] D. Gawron, S. Mazouffre, N. Sadeghi, A. Héron, Influence of magnetic field and discharge voltage on the acceleration layer features in a Hall effect thruster, Plasma Sources Sci. Technol. **17**, 025001 (2008).

[55] S.D. Johnson, M.M. El-Gomati, L. Enloe, High-resolution retarding field analyzer, J. Vac. Sci. Technol. B **21**, 350-353 (2003).

[56] C. Böhm, J. Perrin, Retarding field analyzer for measurements of ion energy distributions and secondary electron emission coefficients in low-pressure radiofrequency discharges, Rev. Sci. Instrum. **64**, 31-44 (1993).

[57] L.B. King, A.D. Gallimore, C.M. Marrese, Transport-property measurements in the plume of a SPT-100 Hall thruster, J. Propul. Power **14**, 327-335 (1998).

[58] B.E. Beal, A.D. Gallimore, Energy analysis of a Hall thruster cluster, Proceedings of the 29th International Electric Propulsion Conference (Toulouse), IEPC-2003-035 (2003).

[59] S. Mazouffre, G. Bourgeois, K. Dannenmayer, A. Lejeune, Ionization and acceleration processes in a small, variable channel width, permanent-magnet Hall thruster, J. Phys. D: Appl. Phys. **45**, 185203 (2012)

[60] W.A. Hargus Jr., C.S. Charles, Near plume laser induced fluorescence velocity measurementes of a 600 W Hall thruster, Proceedings of the 44th Joint Propulsion Conference (Hartford), AIAA 2008-5004 (2008).

[61] R. Siegel, J.R. Howell, Thermal radiation heat transfer, McGraw-Hill, New York, 1972.

[62] J.R. Howell, A catalog of radiation heat transfer configuration factors (http://www.me.utexas.edu/ howell/).

[63] S. Mazouffre, K. Dannenmayer, C. Blank, Impact of discharge voltage on wall-loses in a Hall thruster, Physics of Plasmas **18**, 064501 (2011).

[64] M. Keidar, I.D. Boyd, On the magnetic mirror effect in Hall thrusters, Appl. Phys. Lett. **87**, 064501 (2005).

[65] L.B. King, A (re-) examination of electron motion in Hall thruster fields, Proceedings of the 29th International Electric Propulsion Conference (Princeton), IEPC-2005-258 (2005).

[66] F. Darnon, Plume effects in plasma propulsion, An overview of CNES activities, Proceedings of the 3rd International Conference on Spacecraft Propulsion (Cannes), ESA SP-465 (2000).

[67] I.G. Mikellides, G.A. Jongeward, I. Katz, D.H. Manzella, Plume modeling of stationary plasma thrusters and interactions with the Express-A spacecraft, Journal of Spacecraft and Rockets **39**, 894-903 (2002).

[68] I.D. Boyd, R.A. Dressler, Far field modeling of the plasma plume of a Hall thruster, J. Appl. Phys. **92**, 1764-1774 (2002).

[69] A. Passaro, A. Vicini. F. Nania, L. Biagioni, Numerical Rebuilding of SMART-1 Hall effect thruster plasma plume, J. Propul. Power **26**, 149-158 (2010).

[70] S.D. Hester, A.A. Sonin, Ion temperature sensitice end effect in cylindrical Langmuir probe response at ionosphere satellite conditions, Phys. Fluids **13**, 1265-1274 (1970).

[71] P.M. Chung, L. Talbot, K.J. Touryan, Electric Probes in Stationary and Flowing Plasmas: Theory and Application, Springer-Verlag New York Inc. (1975).

[72] F.F. Chen, Electric Probes in Plasma Diagnostic Techniques (edited by: R.H. Huddlestone and S.L. Leonard), Academic Press New York, 113-200 (1965).

[73] J.P. Sheehan, N. Hershkowitz, Emissive probes, Plasma Sources Sci. Technol. **20**, 063001 (2011).

[74] C. Ionita C et al., The use of emissive probes in laboratory and Tokamak plasmas, Contrib. Plasma Phys. **51**, 264-270 (2011).

[75] A. Marek et al., Emissive probe diagnostics in low temperature plasma - Effect of space charge and variations of electron saturation current, Contrib. Plasma Phys. **48**, 491-496 (2008).

[76] A. Smirnov, Y. Raitses, N.J. Fisch, Plasma measurements in a 100 W cylindrical Hall thruster, J. Appl. Phys. **95**, 2283-2292 (2004).

[77] Y. Raitses, D. Staack, A. Smirnov, N.J. Fisch, Space charge saturated sheath regime and electron temperature saturation in Hall thrusters, Phys. Plasmas **12**, 073507 (2005).

[78] A. W. Smith, and M. A. Cappelli, Time and space-correlated plasma potential measurements of a coaxial Hall thruster discharge, Phys. Plasmas **16**, 073504 (2009).

[79] W. Baumjohann, R.A. Traumann, Basic space plasma physics, Imperial College Press London, 146-147 (1997).

[80] S. Mazouffre, Transport phenomena in plasma expansions containing hydrogen, PhD thesis University of Eindhoven, 21 (2001).

[81] K.T.A.L. Burm, W.J. Goedheer, D.C. Schram, The isentropic exponent in plasmas, Phys. Plasmas **6**, 2622-2627 (1999).

[82] A.K. Knoll, M.A. Capelli, A simple isentropic model of the electron transport in Hall thrusters, J. Phys. D: Appl. Phys **41**, 162003 (2008).

[83] R.M. Myers, D.H. Manzella, Stationary plasma thruster plume characteristics, Proceedings of the 23rd International Electric Propulsion Conference (Seattle), IEPC 93-096 (1993).

[84] S. Takamura, N. Ohno, M.Y. Ye, T. Kuwabara, Space-charge limited current from plasma-facing material surface, Contrib. Plasma Phys **44**, 126-137 (2004).

[85] J.M. Haas, A.D. Gallimore, K. McFall, G. Spanjers, Developement of a high-speed reciprocating electrostatic probe system for Hall thruster interrogation, Rev. Sci. Instrum. **71**, 4131-4138 (2000).

[86] J. Boedo, D. Gray, L. Chousal, R. Conn, Fast scanning probe for tokamak plasmas, Rev. Sci. Instrum. **69**, 2663-2670 (1998).

[87] L. Yan, W. Hong, J. Qian, C. Luo, L. Pan, Fast reciprocating probe system on the HL-2A Tokamak, Rev. Sci. Instrum. **76**, 093506 (2005).

[88] M.C.M. van de Sanden, J.M de Regt, D.C. Schram, Recombination of argon in an expanding plasma jet, Phys. Rev. E **47**, 2792-2797 (1993).

[89] J. P. Boeuf, and L. Garrigues, Low frequency oscillations in a stationary plasma thruster, J. Appl. Phys. **84**, 3541-3554 (1998).

[90] J. Kurzyna et al., Spectral analysis of Hall effect thruster plasma oscillations based on empirical mode decomposition, Phys. Plasmas **12**, 123506 (2005).

[91] C. Boniface et al., Anomalous cross field electron transport in a Hall effect thruster , Appl. Phys. Lett. **89**, 161503 (2006).

[92] J.W. Connor, The 13th EU-US Transport Task Force on transport in fusion plasmas, Nucl. Fusion **49**, 047001 (2009).

[93] A.V. Nedospasov, On the estimation by Kadomtsev of coefficients of turbulent transport in magnetized plasmas, Phys. Plasmas **16**, 060501 (2009).

[94] K. Matsumoto, M. Sato, Langmuir probe characteristic modulated with random fluctuations, J. Appl. Phys. **54**, 1781-1786 (1983).

[95] L. Oksuz, F. Soberón, A.R. Ellingboe, Analysis of uncompensated Langmuir probe characteristics in radio-frequency discharges revisited, J. Appl. Phys. **99**, 013304 (2006).

[96] E. Chesta, A characterization of plasma fluctuations within a Hall discharge, IEEE Transactions on Plasma Science **29**, 582-591 (2001).

[97] L. Albarède, S. Mazouffre, A. Bouchoule, and M. Dudeck, Low-frequency electron dynamics in the near-field of a Hall effect thruster, Phys. Plasmas, **13**, 063505 (2006).

[98] R. B. Lobbia, and A. D. Gallimore, A method of measuring transient plume properties, Proceedings of the 44th Joint Propulsion Conference, Hartford, USA, AIAA 2008-4650 (2008).

[99] R. B. Lobbia, and A. D. Gallimore, High-speed dual Langmuir probe, Rev. Sci. Instrum. **81**, 073503 (2010).

[100] A.G. Dean, D. Smith, I.C. Plumb, A technique for recording Langmuir probe characteristics in afterglow plasmas, J. Phys. E: Sci. Instrum. **5**, 776-778 (1972).

[101] A.D. Pajdarová, J. Vlček, P. Kudláček, J. Lukàš, Electron energy distribution and plasma parameters in high-power pulsed magnetron sputtering discharges, Plasma Sources Sci. Technol. **18**, 025008 (2009).

[102] S. Mazouffre, and G. Bourgeois, Spatio-temporal characteristics of ion velocity in a Hall thruster discharge, Plasma Sources Sci. Technol., **19**, 065018 (2010).

[103] K. Dannenmayer, P. Kudrna, M. Tichý, S. Mazouffre, Measurements of plasma parameters in the far-field plume of a Hall effect thruster, Plasma Sources Sci. Technol. **20**, 065012 (2011).

[104] M.Y. Ye, S. Takamura, Effect of space-charge limited emission on measurements of plasma potential using emissive probes, Phys. Plasmas **7**, 3457-3463 (2000).

[105] S. Klagge, M. Maass, The influence of the fluctuation amplitude on the probe characteristic, Contrib. Plasma Phys. **23**, 355-368 (1983).

[106] R. Vilamot, Optimisation de la configuration magnétique d'un propulseur à effet Hall, PhD thesis Université de Toulouse (in french), (2012).

[107] SPIS website: http://dev.spis.org/projects/spine/home/spis.

[108] J.-F. Roussel et al., SPIS open-source code: methods, capabilities, achievements and prospects, IEEE Trans. Plasma Sci. **36**, 2360-2368 (2008).

Appendix A

List of publications

Peer reviewed internationl journal papers

- *Examination of plasma-wall interactions in Hall effect thrusters by means of calibrated thermal imaging.*
  S. Mazouffre, J. Pérez Luna and K. Dannenmayer
  J. Appl. Phys. **102**, 023304 (2007).
- *Sizing of Hall effect thrusters with input power and thrust level: An empirical approach.*
  K. Dannenmayer and S. Mazouffre
  J. Tech. Phys. **49**, 167-190 (2008).
- *Elementary scaling relations for Hall effect thrusters.*
  K. Dannenmayer and S. Mazouffre,
  J. Propul. Power **27**, 236-245 (2011).
- *Elementary scaling laws for the design of low and high power Hall effect thrusters.*
  K. Dannenmayer and S. Mazouffre
  Progress in Propulsion Physics, Ed. L. Deluca, EUCASS book, 19 (2011).
- *Impact of discharge voltage on wall-losses in a Hall thruster.*
  S. Mazouffre, K. Dannenmayer and C. Blank
  Phys. Plasmas **18**, 064501 (2011).
- *Measurement of plasma parameters in the far-field plume of a Hall effect thruster.*
  K. Dannenmayer, P. Kudrna, M. Tichý and S. Mazouffre
  Plasma Sources Sci. Technol. **20**, 065012 (2011).
- *Ionization and acceleration processes in a small, variable channel width, permanent-magnet Hall thrusters.*
  S. Mazouffre, G. Bourgeois, K. Dannenmayer and A. Lejeune
  J. Phys. D : Appl. Phys. **45**, 185203 (2012).
- *Time resolved measurement of plasma parameters in the far-field plume of a low-power Hall effect thruster.*
  K. Dannenmayer, P. Kudrna, M. Tichý and S. Mazouffre
  Plasma Sources Sci. Technol. **21**, 055020 (2012).

- *Time-resolved measurements of plasma properties using electrostatic probes in the cross-field discharge of a Hall effect thrusters.*
  K. Dannenmayer, P. Kudrna, M. Tichý and S. Mazouffre
  Contrib. Plasma Phys. **53**, No. X, 1-6 (2013).

- *Compact high-speed reciprocating probe system for measurements in a Hall effecht thruster discharge and plume.*
  K. Dannenmayer and S. Mazouffre
  accepted for publication in Rev. Sci. Instrum.

Conference proceedings

- *Elementary scaling laws for the design of low and high power Hall effect thrusters.*
  S. Mazouffre and K. Dannenmayer,
  3rd European Conference for Aerospace Sciences, Versailles, France, paper 53, 2009.

- *Elementary scaling laws for sizing up and down Hall effect thrusters: Impact of symplifying assumptions*
  K. Dannenmayer and S. Mazouffre,
  31st International Electric Propulsion Conference, Ann Arbor, USA, paper 09-077, 2009.

- *Measurement of plasma properties in the far-field plume of a Hall effect thruster using Langmuir and emissive probes.*
  K. Dannenmayer, S. Mazouffre, P. Kudrna, M. Tichý,
  International Conference on Plasma Diagnostics, Pont-à-Mousson, France, 2010.

- *Effect of channel geometry on discharge properties and performances of a low-power Hall effect thruster.* S. Mazouffre, K. Dannenmayer, G. Bourgeois, M. Guyot, S. Denise, P. Renaudin, V. Cagan and M. Dudeck,
  Space Propulsion Conference, San Sebastian, Spain, 2010.

- *Impact of discharge chamber geometry on characteristics of a low-power Hall thruster.*
  S. Mazouffre, K. Dannenmayer, G. Bourgeois, A. Lejeune, M. Guyot, S. Denise, P. Renaudin and V. Cagan,
  5th International Conference on Recent Advances in Space Technologies (RAST), Istanbul, Turkey, 2011.

- *Impact of the channel width on Hall thruster discharge properties and performances.*
  A. Lejeune, K. Dannenmayer, G. Bourgeois, S. Mazouffre, M. Guyot and S. Denise,
  32nd International Electric Propulsion Conference, Wiesbaden, Germany, IEPC-2011-019, 2011.

- *Time-resolved measurements of plasma properties in the far-field plume of a low-power Hall Effect thruster.*
  K. Dannenmayer, S. Mazouffre, P. Kudrna and M. Tichý,

32nd International Electric Propulsion Conference, Wiesbaden, Germany, IEPC-2011-219, 2011.

- *Measurement of plasma parameters in the plume of a Hall effect thrusters.*
  K. Dannenmayer, P. Kudrna, M. Tichý and S. Mazouffre,
  Space Propulsion Conference, Bordeaux, France, 2012.

- *Performances of a variable channel width Hall effect thruster using xenon and krypton.*
  G. Bourgeois, A. Lejeune, K. Dannenmayer, S. Mazouffre and M. Guyot,
  Space Propulsion Conference, Bordeaux, France, 2012.

- *Hall effect thruster plasma plume characterization with probe measurements and self-similar fluid models.*
  K. Dannenmayer, S. Mazouffre, M. Merino and E. Ahedo
  48th AIAA/ASME/SAE/ASEE Joint Propulsion Conference, Atlanta, USA, AIAA-2012-2491, 2012.

Appendix B

Version française

B.1 Introduction

Un satellite ou une sonde spatiale nécessite un système de propulsion pour se déplacer dans l'espace. Il y a deux systèmes de propulsion différents. Le premier, plus répandu, est la propulsion chimique où des gaz chauds, issus d'une réaction chimique entre deux substances, sont éjectés à travers une tuyère. La deuxième technologie est connue sous le nom de propulsion électrique. Des particules chargées sont accélérées par un champ électrique et éjectées avec des vitesses jusqu'à 20 fois supérieures à celles obtenues en propulsion chimique.
Les systèmes de propulsion électrique offrent des avantages significatifs pour des missions commerciales et scientifiques sur le plan de la charge utile, du coût de lancement et de la durée des missions grâce à une économie en masse carburant due à la vitesse d'éjection élevée. A l'heure actuelle, la plus importante application des systèmes de propulsion électrique est la correction de trajectoire nord-sud des satellites de télécommunication géostationaire. L'augmentation de puissance électrique disponible à bord des véhicules spatiaux va ouvrir la voie à de nouvelles applications dans le futur comme p.ex. le transfert d'orbite (partiel ou complet) et la désorbitation en fin de vie. De nombreuses technologies de propulsion électrique coexistent. On peut citer les moteurs à grilles [1], propulseurs de Hall [1], propulseurs magnétohydrodynamiques [1], VASIMR [2] et le propulseur Pegases [3]. Parmi les différents types de propulseurs électriques, deux technologies, moteurs à grilles et propulseurs de Hall, sont aujourd'hui matures et bénéficient d'un long héritage en vol. Les moteurs à grilles sont caractérisés par une accélérations purement électrostatique des ions qui sont extraits d'une source plasma (DC bombardement électronique, décharge micro-onde ou radiofréquence) par des grilles à haute tension. Les propulseurs de Hall fournissent la poussée par une accélération d'ions dans une décharge en champs-croisés à basse pression. Les deux technologies ont un rendement similaire, jusqu'à 70 %. Les moteurs à grilles se caractérisent par une impulsion spécifique (I_{sp}) élevée et une poussée relativement faible. Les propulseurs de Hall délivrent une poussée plus élevée mais une I_{sp} moyenne. Néanmoins, le rapport poussée-sur-puissance des propulseurs de Hall est jusqu'à trois fois supérieur à celui des moteurs à grilles. C'est pourquoi les propulseurs de Hall représentent aujourd'hui une technologie attractive pour la plupart des missions. Plus que 200 propulseurs de Hall ont été embarqués sur des satellites depuis 1971.
La maîtrise des systèmes propulsifs des satellites représente un grand défi pour l'Europe en ce qui concerne les aspects économiques et stratégiques. Ainsi, l'agence spatiale francaise (CNES) a décidé, avec l'industriel Snecma, d'investir dans des activités de R&D avec le soutien des instituts de recherche. De ce fait, en 1996 un groupement de recherche - nommé GdR "propulsion par plasma dans l'espace" - a été formé par le CNRS, le CNES, la Snecma et diverses universités qui travaillent dans le domaine de la physique des propulseurs de Hall. De nombreux efforts

ont été fait pour développer des outils de simulation numérique et des diagnostics. D'un point de vue expérimental, plusieurs types de propulseurs de Hall dans une gamme de puissance de 100 W à 20 kW ont été construits et testés dans la chambre PIVOINE-2g à ICARE, une chambre à vide unique en Europe. Le vaste ensemble de travaux menés dans le GdR a permit de mieux comprendre la physique des propulseurs de Hall.
La présente thèse s'insère parfaitement dans le cadre des recherches acutelles définies en partie par les prévisions à moyen terme des activités dans le secteur spatial. L'objectif de ce travail est triple: Premièrement il s'agit d'établir un modèle de lois d'échelle semi-empirique qui peut être utilisé pour une extrapolation des propulseurs de Hall existants vers des niveaux de puissance plus bas et plus hauts. Cette extrapolation est nécessaire afin de répondre aux exigences pour les nouvelles missions. Le deuxième but est d'étudier l'influence de la largeur du canal de décharge sur les performances d'un propulseur à faible puissance. La question est de savoir si on peut améliorer le rendement d'un propulseur à faible puissance en modifiant simplement la géométrie du canal. Finalement, il est impératif d'étudier expérimentalement les propriétés électroniques, telles que le potentiel plasma, la température électronique et la densité électronique, par sondes électrostatiques. Des données expérimentales sont indispensables pour la validation des modèles numériques de la plume employés pour de trouver la position optimale du propulseur sur le satellite. Comme le plasma d'un propulseur de Hall est fortement instationnaire, on doit prendre en compte les fluctuations temporelles des propriétés électroniques afin d'obtenir des résultats précis.

L'organisation de ce manuscrit est la suivante:

Le **chapitre 2** donne une courte introduction à la propulsion spatiale. Les avantages de la propulsion électrique sont comparés à ceux de la propulsion chimique et les différents types de propulsion électriques sont introduits. Finallement, une description détaillée de la physique des propulseurs de Hall ainsi que des différentes installations expérimentales et propulseurs de Hall utilisés est donnée.

Le **chapitre 3** est dédié à la description des lois d'échelle basé sur un modèle semi-empirique. Les relations de dimensionnement sont déterminées en partant des équations de la physique fondamentale d'un propulseur de Hall. Une vaste base de données est utilisée pour valider les lois d'échelle et déterminer les coefficients de proportionalités nécessaires. Deux series de lois sont ensuite utilisées pour le dimensionnement d'un propulseur de Hall de 20 kW capable de fournir une poussée de 1 N.

L'influence de la largeur du canal sur les performances d'un propulseur est décrit dans le **chapitre 4**. Un propulseur de Hall de faible puissance équipé d'aimants permanents a été testé avec 3 largeurs de canal différentes tout en gardant la longueur et le diamètre moyen constants. Divers paramètres, comme p.ex. le courant ionique, la vitesse des ions, l'énergie des ions, la température des parois et la poussée, ont été mesurés pour les trois configurations sur une large gamme de points de fonctionnement. De plus, l'influence du gaz (Xe et Kr) a été étudié. Cette étude a révélé que le rendement d'un propulseur de Hall de faible puissance peut être amélioré en augmentant la largeur du canal.

Des mesures moyennées en temps des propriétés électroniques sont présentées dans le **chapitre 5**. Le potentiel plasma, la température électronique ainsi que la densité électronique sont mesurés à l'aide d'une sonde de Langmuir cylindrique et d'une sonde émissive suffisamment chauffée. La plume du propulseur PPS®100-ML a été cartographiée pour différents points de fonctionnement. Les résultats obtenus avec les deux types de sondes sont comparés. De plus, un système de déplacement rapide de sonde basé sur un moteur linéaire piézoélectrique est présenté. Ce système peut être utilisé pour des mesures des propriétés électroniques au voisinage du propulseur.

Le **chapitre 6** présente des mesures résolues en temps des propriétés électroniques dans la plume de deux propulseurs de Hall différents, un propulseur de 200 W avec des aimants permanents et le PPS®1350-ML opérant autour de 1.5 kW.

Finalement, une conclusion générale ainsi qu'une perspective pour des travaux futurs sont données dans le **chapitre 7**.

B.2 Chapitre 2: Propulsion électrique

Chaque véhicule spatial est équipé d'un système de propulsion. Le but de ce système propulsif est de délivrer une poussée afin que le véhicule puisse se déplacer dans l'espace. Le principe de génération de poussée est basé sur l'échange de quantité de mouvement entre la matière éjectée par le propulseur et le véhicule spatial. La poussée T est définie comme:

$$T = \frac{dm}{dt} v_{ex} = \dot{m}\, v_{ex}, \tag{B.1}$$

où m est la masse d'ergol, $\dot{m}$ le débit de l'ergol et v_{ex} la vitesse d'éjection d'ergol. Il y a deux technologies de propulsion spatiale différentes: la propulsion chimique et la propulsion électrique, aussi connue sous le nom de propulsion par plasma. La vitesse d'éjection en propulsion chimique est limité à 3-4 km/s. En propulsion électrique, on peut atteindre des vitesse d'éjection aussi élevées que 100 km/s. Il est donc évident que le gain en masse d'ergol consommée pour un système de propulsion électrique est considérable. Ce gain en consommation se traduit par une réduction du coût de lancement ou une augmentation de la durée de mission avec la même quantité d'ergol. Les propulseurs électriques sont aujourd'hui surtout utilisés pour des corrections d'orbite des satellites de télécommunication.
En propulsion électrique on distingue trois technologies différentes: électrothermique, électrostatique et électromagnétique. Ces trois technologies sont caractérisées par leur mode d'accélération du gaz propulsif.
Les travaux de cette thèse concernent un type de propulsion électrique spécifique: la propulsion par effet Hall. Dans un propulseur de Hall les ions sont créés et accélérés par un champ électrique dans une décharge plasma à basse pression dans un champ magnétique. Ces propulseurs peuvent donc être classés aussi bien dans les propulseurs électrostatiques que dans les propulseur électromangétiques.
Le travail expérimental de cette thèse a été conduit dans différents installations à vide:

1. **PIVOINE-2g:** Cette chambre à vide de 4 m de long et 2.2 m de diamètre est localisé au laboratoire ICARE à Orléans. La vitesse de pompage est environ 210 000 l/s ce qui permet de tester des propulseurs jusqu'à 20 kW qui produissent une poussée d'environ 1 N.

2. **NExET:** Cette chambre à vide de 1.8 m de long et 0.8 m de diamètre se trouve également au laboratoire ICARE à Orléans. Avec une vitesse de pompage de l'ordre de 8 000 l/s, elle est déstinée aux essais de propulseurs de Hall de faible puissance.

3. **CORONA:** Cette chambre à vide de 5 m de long et 2 m de diamètre fait partie des installations expérimentales du laboratoire de propulsion de l'ESA (EPL) à l'ESTEC aux Pays-Bas. La vitesse de pompage est de l'orde de 80 000 l/s ce qui permet de tester des moteurs jusqu'à une puissance d'environ 1 kW.

Les mesures expérimentales ont été conduit avec trois propulseurs de Hall différents:

1. **PPS®100-ML:** C'est un propulseur de 1.5 kW qui délivre une poussée de 80 mN à 300 V et 5.0 mg/s de xénon.

2. **PPS®1350-ML:** Ce propulseur de 1.5 kW est le modèle de laboratoire du PPS®100-ML développé par la Snecma. Il produit une poussée de 83 mN à 350 V et 5.0 mg/s de xénon.

3. **PPI:** C'est un propulseur de faible puissance (200 W) qui délivre une poussée de 10 mN à 250 V et 1.0 mg/s de xénon.

B.3 Chapitre 3: Lois d'échelle

Il est aujourd'hui nécessaire d'élargir le domaine de fonctionnement des propulseur de Hall existant afin de répondre aux exigences de nouvelles missions spatiales. Il est donc indispensable de trouver des lois d'échelle qui permettent un extrapolation de la technologie actuelle. L'approche présentée dans ce chapitre est basée sur une combinaison d'une série de lois d'échelle avec une vaste base de données. Des hypothèses simplificatrices et des contraintes réalistes sur la charge thermique et la densité d'atomes permettent de trouver une série de relations entre les dimensions caractéristiques du propulseur et ses performances.
Les lois d'échelle présentées prennent en compte les trois dimensions caractéristiques d'un propulseur de Hall, à savoir la longueur du canal L, la largeur du canal h et le diamètre moyen d, ainsi que l'intensité du champ magnétique. Des lois analytiques sont déterminées à partir des principes physiques fondamentaux sur le fonctionnment des propulseur de Hall dans le cadre d'hypothèses simplificatrices comme p.ex. une température électronique constante et homogène, une température de gaz uniforme, la non prise en compte du terme de pertes dû à l'ionisation. De plus les ions multi-chargés ainsi que la divergence du jet sont négligés. Deux contraintes doivent être respéctées: la température des parois ne doit pas dépasser une certaine valeur afin de limiter la charge thermique; une densité d'atomes suffisante doit être maintenue afin de garantir une ionisation efficace. Une base de données (36 propulseur de 10 W à 50 kW avec une poussée de 0.4 mN jusqu'à 3 N) est utilisée pour valider les lois d'échelle et déterminer

Table B.1: Comparaison des performances des 3 configurations du PPI en fonctionnement avec xénon et krypton.

gaz	géométrie	efficacité de courant	efficacité d' utilisation d'ergol	efficacité de conversion d'énergie	rendement anodique
Xe	S_0	≈ 0.35	0.2 - 0.3	0.88 - 0.9	0.05 - 0.07
	$2S_0$	0.4 - 0.7	0.4 - 0.98	0.91 - 0.97	0.1 - 0.45
	$3S_0$	0.6 - 0.7	0.4 - 0.98	0.95 - 0.98	0.3 - 0.6
Kr	S_0	0.35 - 0.4	0.2 - 0.3	0.82 - 0.92	0.03 - 0.09
	$2S_0$	0.4 - 0.5	0.3 - 0.5	0.92 - 0.98	0.07 - 0.17
	$3S_0$	0.4 - 0.5	0.3 - 0.5	0.92 - 0.98	0.06 - 0.14

les coefficients de proportionalité. Dans une deuxième étape, la liste d'hypothèses simplificatrices est réduite. La température du gaz et des électrons, la fractions d'ions multi-chargés et les pertes sont pris en compte en fonction de la tension appliquée.
Les deux séries de lois d'échelle sont ensuite utilisées pour déterminer les dimensions et les conditions de fonctionnement d'un propulseur de 20 kW capable de fournir une poussée de 1 N. Les résultats sont en très bon accord avec les dimensions et conditions de fonctionnement du propulseur PPS20k développé et testé dans le cadre du projet européen HiPER.

B.4 Chapitre 4: Influence de la géométrie

Une analyse détaillée des propulseurs existants a montré l'existance d'une relation linéaire entre la largeur du canal h et le diamètre moyen d, indépendamment de la gamme de poussée et de puissance. Le but de la présente étude est donc d'étudier l'influence de h sur les processus d'ionisation et d'accélération et donc sur les performances d'un propulseur de Hall.
Un propulseur de faible puissance équipé d'aimants permanents avec une géométrie du canal variable est utilisé. En fait, h peut facilement être modifiée tout en gardeant L et d constant. Le propulseur est utilisé avec du xénon et du krypton comme gaz propulsif. Divers paramètres, comme p.ex. le courant de décharge, le courant ionique, la vitesse des ions, l'énergie des ions, la température des parois ainsi que la poussée, sont mesurés pour les trois différentes configurations du PPI.
Comme on peut le voir pour le deux gaz dans le Tab. B.1, le fait d'élargir le canal améliore les processus d'ionisation et d'accélération et augmente les performances. De plus, l'enveloppe de fonctionnement est plus grande pour un canal plus large. Deux mécanismes peuvent être proposés pour expliquer ces résultats: Premièrement, le rapport surface-sur-volume decroît avec h ce qui réduit les pertes aux parois. Deuxièmement, l'intensité du champ magnétique proche des parois augmente avec h ce qui se traduit par un meilleure confinement du plasma.

Cette étude montre donc clairement qu'on peut augmenter le rendement d'un propulseur de Hall de faible puissance, qui est en général relativement bas, simplement en modifiant la géométrie du canal.

B.5 Chapitre 5: Propriétés électronique moyennées dans le temps

Des données expérimentales concernant les propriétés du plasma dans la plume d'un propulseur de Hall sont essentielles pour la validation des modèles numériques de la plume. Ces modèles sont nécessaires pour trouver le meilleure emplacement du propulseur sur le satellite afin de limiter les interactions néfastes entre le plasma et le satellite. Pour l'instant, la plupart des études expérimentales étaient concentrées sur les propriétés des ions. Mais la dynamique globale de la décharge est contrôlée par les électrons. Il faut donc des mesures des propriétés électroniques (potentiel plasma V_p, température électronique T_e et densité électronique n_e). Des sondes électrostatiques peuvent être utilisées pour des mesures dans le plasma. Des mesures moyennées en temps ont été réalisées dans la plume du PPS®100-ML avec une sonde de Langmuir cylindrique et une sonde émissive. La plume du propulseur a été cartographié de 300 à 660 mm en aval du plan de sortie et de 0 à 60 °, où 0 ° correspond à l'axe du propulseur. Nous avons étudié l'influence de la tension de décharge, du débit d'anode et cathode ainsi que l'intensité du champ magnétique sur V_p, T_e et n_e.
Ces mesures montrent que la plume est en fait une détente isentropique. L'exposant isentropique déterminé est inférieure à la valeur théorique du gaz ce qui peut s'expliquer par le degré de liberté supplémentaire dû à l'ionisation dans le cas d'un plasma.
La sonde émissive et la sonde de Langmuir donnent des résultats similaires pour V_p et T_e. Une sonde émissive peut donc être utilisée pour une mesure directe de ces paramètres.
Un nouveau système de déplacement rapide pour sondes a été développé. Ce système permet de mesurer les propriétés du plasma au voisinage du plan de sortie du propulseur et même à l'intérieur du canal de décharge où la densité ionique est tellement élevée que la pulvérisation de la sonde devient critique. Ces mesures sont indispensables pour une meilleure compréhension des processus d'ionisation et d'accélération. Le nouveau système est basé sur un moteur linéaire piézoélectrique très compact qui se déplace avec une vitesse de 350 mm/s sur une course de 90 mm. La sonde est insérée et retirée rapidement avec la platine afin de minimiser la perturbation du plasma et préserver la sonde. Une première validations du nouveau système de déplacement rapide a été conduit proche du plan de sortie du propuleur PPI. Le potentiel plasma a été mesuré à différents endroits à l'aide d'une sonde émissive.

B.6 Chapitre 6: Propriétés électronique résolues en temps

Le plasma d'un propulseur de Hall est fortement instationnaire. Des mesures résolues en temps sont donc indispensables afin de prendre en compte les fluctuations des propriétés électroniques et d'obtenir des résultats exacts. L'évolution temporelle de V_p, T_e et n_e a été mesurée dans la plume de deux propulseur différents (PPS®1350-ML et PPI) avec une sonde de Langmuir et une sonde émissive. Afin de réaliser des mesures propres avec résolution temporelle, le propulseur est forcé dans un régime périodique, quasi-harmonique en applicant une modulation sinusoïdale sur une électrode flottante proche de la cathode (il s'agit en fait du keeper). La fréquence de cette modulation doit être ajustée afin d'obtenir un régime stable du propulseur synchronisé avec la modulation. La fréquence nécessaire à la synchronisation est différente si l'on considère le courant de décharge ou le potentiel plasma mesurée par sonde émissive. Même si la modulation influence le comportement temporelle du moteur, elle n'a presque pas

d'influence sur le comportement global; c'est-à-dire que la valeure moyenne de I_d et du potentiel de la cathode ne change pas avec et sans modulation. L'évolution temporelle de V_p, T_e et n_e sur une periode est différente pour les deux fréquences de modulation. Mais comme pour le comportement global du propulseur, la modulation n'influence pas la valeur moyenne des propriétés électroniques. Les deux types de sondes mesurent une évolution temporelle de V_p similaire. Une sonde émissive peut donc être utilisée afin d'obtenir une mesure directe de V_p qui est plus facile et plus rapide qu'une mesure par sonde de Langmuir.
La technique de mesure présentée a été utilisée pour deux propulseurs et deux gaz différents. La fréquence de modulation dépend légèrement du gaz et de la taille du propulseur mais les phénomènes observés sont similaires.
Même si le propulseur est maintenu dans un régime de fonctionnement spécifique (périodique, quasi-harmonique), ni le comportement global du propulseur ni les propriétés électroniques sont significativement modifiés par la modulation. Cela a également été vérifié par des mesures de la fonction distribution de la vitesse des ions par LIF avec et sans modulation. La technique présentée est donc un outil puissant pour la mesure des propriétés électroniques avec résolution temporelle dans une décharge en champs-croisés instationnaire.

B.7 Conclusion

Les propulseurs de Hall sont aujourd'hui une technologie spatiale mature avec une longue expérience en vol. Néanmoins, de nombreux travaux de recherche sont toujours menés afin de mieux comprendre les processus physiques complexes, d'améliorer le rendement, d'augmenter la durée de vie des propulseurs et de reduire les interactions plasma-satellite.

Le travail présenté s'insère parfaitement dans le cadre des activités de recherche actuelles. Les objectifs de ce travail étaient d'établir un modèle de lois d'échelle semi-empirique pour les propulseurs de Hall, d'étudier l'influence de la largeur du canal sur les performances d'un propulseur de Hall de faible puissance et de mesurer les propriétés électroniques dans la plume d'un propulseur de Hall.

Un modèle de lois d'échelle semi-empirique pour les propulseurs de Hall a été développé. Ce modèle prend en compte les trois dimensions caractéristiques, à savoir la longueur du canal L, le diamètre moyen du canal d et la largeur du canal h. Les lois découlent de lois analytiques qui ont été obtenues à partir des principes physiques fondamentaux des propulseurs de Hall. Une serie d'hypothèses simplificatrices décrit évidemment le domaine de validité des lois d'échelle. Par ailleurs, l'approche respecte des contraintes strictes sur la densité d'atome et la température des parois. Une vaste base de données avec 36 différents propulseurs de Hall, qui couvre un domaine de puissance de 10 W à 50 kW et une plage de poussées de 0.4 mN à plus que 3 N, est utilisée pour valider les lois d'échelle et déterminer les coefficients de proportionalités nécessaires. Les lois d'échelle ont été utilisées pour déterminer la géométrie et les conditions de fonctionnement d'un propulseur de 20 kW capable de délivrer une poussée de 1 N. Les résultats obtenus avec deux séries d'hypothèses simplificatrices ont été comparés. La première série forme un cadre très restrictif. La deuxième série offre une description plus réaliste de la physique d'un

propulseur puisqu'elle prend en compte la température électronique, les pertes d'énergie et les ions multi-chargés. Néanmoins, une comparaison des deux approches montre que l'utilisation d'une description physique plus réaliste n'améliore pas significativement la précision. Les lois d'échelle basées sur des hypothèses assez restrictives sont en conséquence satisfaisantes pour obtenir une première estimation de la géométrie et des conditions de fonctionnement pour un nouveau propulseur de Hall. L'application de ces lois d'échelle permet de gagner du temps lors de phase de dimensionnement et d'optimisation.
Les dimensions et les paramètres de fonctionnement calculés sont en bon accord avec ceux du propulseur de 20 kW PPS20k développé et testé dans le cadre du projet européen HiPER.

L'influence de la largeur du canal sur les processus d'ionisation et d'accélération et en conséquence sur le niveau de performance d'un propulseur de Hall a été étudiée. L'idée d'une telle étude résulte de la relation linéaire entre la largeur et le diamètre moyen du canal mise en évidence lors des travaux sur les lois d'échelle. Le but de l'étude était de vérifier si les performances d'un propulseur de Hall de faible puissance pourraient être améliorées par une modification de la géométrie du canal. Un propulseur de Hall de faible puissance équipé d'aimants permanents avec une largeur de canal h variable a été utilisé pour étudier l'influence de h pour deux gaz différents (Xe et Kr). La largeur du canal pouvait être modifiée à l'aide de différents cylindres en céramique tout en gardant le diamètre moyen, la longueur du canal et la topologie magnétique constants. Divers paramètres, comme p.ex. le courant de décharge, la densité du courant ionique, la vitesse des ions (Xe^+, Kr^+), l'énergie des ions, la température des parois et la poussée, ont été mesurés sur une large gamme de débits de gaz et de tensions appliquées. Ces mesures ont montré pour les deux gaz, qu'élargir le canal améliore l'ionisation et l'accélération, agrandit la plage de fonctionnement, réduit la température des parois ainsi que les pertes dues aux interactions plasma-surface et améliore les performances du propulseur. Deux mécanismes peuvent en fait expliquer ses résultats expérimentaux: Premièrement, le rapport surface-sur-volume décroit avec h ce qui réduit les pertes aux parois. Deuxièmement, l'intensité du champ magnétique proche des parois augmente avec h ce qui conduit à un meilleure confinement du plasma.
Cette étude est très intéressante, parce qu'elle montre que le rendement d'un propulseur de Hall de faible puissance, qui est en général relativement faible, peut être augmenté simplement en changeant la largeur du canal.

La plume d'un propulseur de Hall présente un angle de divergence assez important ce qui mène à des interactions électriques et mécaniques entre les particules chargées dans la plume plasma et le satellite. Des modèles numériques de la plume sont donc indispensables pour trouver l'emplacement optimal du propulseur sur le satellite afin de minimiser les interactions plasma-satellite. Des données expérimentales sur les propriétés électroniques dans la plume sont indispensables pour la validation de ces modèles numériques de la plume. Des mesures moyennées en temps du potentiel plasma, de la température électronique et de la densité électronique ont été réalisées dans la plume du PPS®100-ML à l'aide d'une sonde de Langmuir cylindrique et d'une sonde émissive chauffée. La plume a été cartographiée de 300 à 660 mm en aval du plan de sortie et de 0 à 60 °, où 0 ° correspond à l'axe du propulseur. L'influence des différentes conditions de fonctionnement, comme p.ex. la tension de décharge, le débit anodique

et cathodique ainsi que l'intensité du champ magnétique, sur les propriétés électroniques a été étudiée. Les résultats montrent que la plume est une détente isentropique. Les valeurs de V_p, et T_e mesurées par les deux sondes sont en bon accord. En conséquence, une sonde émissive peut être utilisée pour obtenir une mesure directe de ces paramètres sans balayage de la tension de la sonde. La mesure des paramètres du plasma dans la plume est insuffisante pour une bonne compréhension des processus d'ionisation et d'accélération. C'est pourquoi un système de déplacement rapide de sonde a été développé. Ce système permet la mesure des propriétés du plasma proche du plan de sortie du propulseur et même à l'intérieur du canal ou la densité ionique est tellement élevée que la pulverisation des sondes pose un problème. Ce nouveau système consiste en un moteur linéaire piézoélectrique très compact qui peut atteindre une vitesse de 350 mm/s avec une course de 90 mm. Avec ce nouveau système, le profil du potentiel plasma a été mesuré au voisinage du propulseur avec une sonde émissive.

Finallement, des mesures résolues en temps des propriétés électroniques ont été réalisées. Ces mesures sont nécessaires afin de prendre en compte les fluctuations temporelles des propriétés du plasma qui sont dues aux comportement fortement instationnaire de la décharge. Afin de faire des mesures résolues en temps propres, il faut maintenir le propulseur dans un régime périodique, quasi-harmonique en applicant une modulation sinusoïdale sur une électrode flottante proche de la cathode. La fréquence de cette modulation était ajustée afin d'avoir un régime de fonctionnement stable du propulseur synchronisé avec la modulation. L'évolution temporelle de V_p, T_e et n_e a été mesurée pour deux propulseurs différents, à savoir le propulseur de 200 W PPI et le propulseur de 1.5 kW PPS®1350-ML, et pour deux gaz différents (Xe et Kr). Les évolutions temporelles de V_p mesurées avec les deux types de sondes (sonde de Langmuir et sonde émissive) sont en bon accord. Une sonde émissive peut donc être utilisée pour des mesures instantanées de $V_p(t)$. Bien que le propulseur soit forcé dans un régime de fonctionnement spécifique, ni le comportement global du propulseur ni les paramètres du plasma ne sont modifiés par la modulation appliquée. La méthode présentée est donc une technique puissante pour des mesures avec résolution temporelle des propriétés électroniques dans une décharge en champs-croisés instationnaire.

Perspectives

Sur la base des résultats présentés dans ce manuscrit, les études ultérieures suivantes sont recommendable:

1. **Lois d'échelle:** Les lois d'échelle décrites peuvent encore être améliorées en éliminant des hypothèses supplémentaires. Il serait intéressant de prendre en compte la divergence du jet ou les fractions d'ions multi-chargés et non pas seulement les ions chargés une ou deux fois. La précisison de l'approche du second ordre pourrait être significativement améliorée avec plus de données expérimentales concernant l'évolution de la température du gaz et des électrons ainsi que celle de l'efficacité de conversion d'ergol en fonction de la tension de décharge. Une prise en compte la topologie magnétique représenterait un progrès puissant, comme c'est elle qui garantit un fonctionnement correct. Un plus grand nombre de données expérimentales concernant l'influence de l'amplitude du champ

magnétique et de la topologie magnétique sur les performances d'un propulseur (poussée et rendement) devraient prochainement être disponibles. Un nouveau propulseur de Hall PPS-Flex a récemment été construit afin d'étudier l'influence de divers paramètres de la topologie magnétique sur les performances [106]. Le circuit magnétique du PPS-Flex a été modifié de telle sorte que chaque composante de la topologie magnétique peut être modifiée indépendamment. Une autre amélioration des lois d'échelle serait de les élargir à d'autres gaz. Pour l'instant, les lois d'échelle sont seulement valables pour du xénon. Le développement récent d'un propulseur de Hall de faible puissance optimisé pour le krypton par notre équipe devrait apporter de nouvelles données expérimentales.

2. **Influence de la géométrie:** Il a été montré que les performances d'un petit propulseur de Hall peuvent être améliorées en augmentant la largeur du canal. Néanmoins, l'approche devrait être testée sur un propulseur plus grand, p.ex. le 1.5 kW PPS®1350-ML, afin de vérifier si la méthode peut être appliqué avec succès sur des propulseur plus grand. Le rapport surface-sur-volume est déjà plus favorable pour un propulseur de plus forte puissance et le gain en rendement serait donc certainement plus faible que pour un propulseur de faible puissance.

3. **Propriétés électroniques:** La grande quantité de données expérimentales obtenues par des mesures dans la plume devrait maintenant être comparée aux modèles numériques de la plume. Actuellement, en collaboration avec M. Merino de *Universidad Politécnica* à Madrid, les données expérimentales sont utilisées pour ajuster un modèle fluide semi-empirique qui est basé sur les lois d'une détente plasma hypersonique. Une première comparaison entre le modèle et les données expérimentales montre un bon accord. Une simple caractérisation de la densité du plasma et du flux dans chaque propulseur peut donc être fournie par ce modèle. C'est pourquoi le modèle validé peut être utilisé comme outil pour une otpimisation préliminaire d'un propulseur. De plus, des mesures des propriétés électroniques supplémentaire à grand angle serait intéressant pour la validation du logiciel SPIS (**S**pacecraft **P**lasma **I**nteraction **S**ystem) [107, 108].
   Le nouveau système de déplacement rapide pour sondes pourrait maintenant être utilisé pour cartographier les paramètres du plasma dans toute la zone proche du propulseur et même à l'intérieur du canal. Une sonde de Langmuir devrait être utilisée afin d'obtenir des mesures de V_p, T_e, n_e et même la fonction de distribution en énergie des électrons.
   Divers travaux supplémentaires concernant la technique de mesure avec résolution temporelle sont certainement envisageables. Il serait intéressant d'étudier le comportement temporelle des propriétés électroniques à haute fréquence. Deux domaines de fréquence différents semblent être intéressants, à savoir le domaine entre 100 et 500 kHz qui correspond aux oscillations du temps de transit des ions et le domaine de fréquence supérieur à 1 MHz qui correspond aux fluctuations azimutales des électrons (dérive ExB). Cela nécessite une modification du système d'amplification et du système de sonde émissive. Le système de sonde émissive est jusqu'à présent limité par une fréquence maximale de 60 kHz. De plus, il serait intéressant de mieux comprendre les différentes structures qui peuvent être observées pour l'évolution temporelle de V_p et T_e. Une idée pour obtenir plus d'informations sur ces structures serait d'utiliser une autre forme d'onde pour la modulation. On pourrait p.ex. utiliser un dirac au lieu de la modulation sinusoïale. Néanmoins,

des simulations numériques des fluctuations instationnaires sont cruciales pour une compréhension détaillée des phénomènes observés.
Une des prochaines étapes est d'extraire la fonction de distribution en énergie des électrons (FDEE) résolues en temps des données expérimentales. Un premier essai a déjà montré que le rapport signal-sur-bruit des données expérimentales est approprié pour la détermination de la FDEE à partir de la deuxième dérivée de la caractéristique de la sonde de Langmuir. Deux exemples de FDEE mesurées dans la plume du PPS®1350-ML et du PPI sont montrés en Fig. B.1. Les FDEE ont été obtenues à partir des caractéristiques résolues en temps.

La modulation du keeper pourrait aussi être utilisée pour des mesures de LIF résolues en temps. Jusqu'à présent ces mesures ont été conduit en utilisant un interrupteur rapide qui perturbe la décharge du propulseur. Si le propulseur fonctionne dans un régime periodique, quasi-harmonique, l'interrupteur ne serait plus nécessaire pour la synchronisation des mesures.

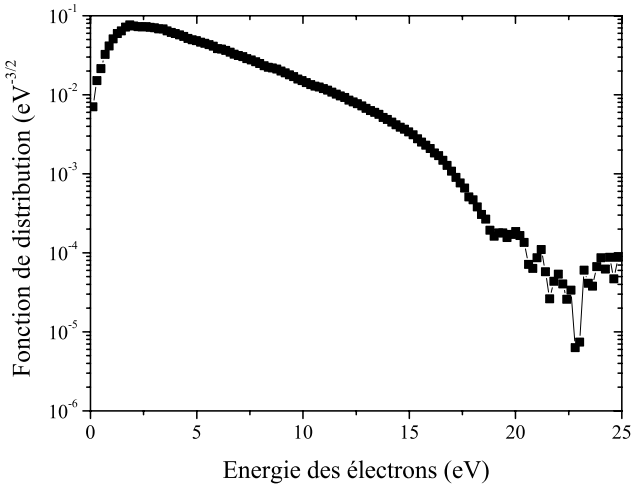

(a) FDEE dans la plume du PPS®1350-ML à 300 mm en aval du plan de sortie sur l'axe du propulseur.

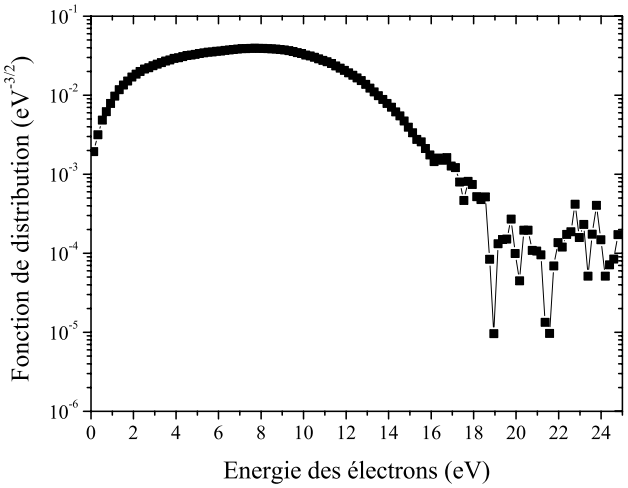

(b) FDEE dans la plume du PPI à 100 mm en aval du plan de sortie sur l'axe du propulseur.

Figure B.1: Fonction de distribution en énergie des électrons (FDEE) meaurée avec une sonde de Langmuir dans la plume de deux propulseurs de Hall différents (PPS®1350-ML et PPI).

Käthe DANNENMAYER

Lois d'échelle et propriétés électroniques dans les propulseurs à effet Hall

Chaque satellite nécessite un système de propulsion pour des corrections d'orbite. Les propulseurs électriques à effet de Hall sont une technologie intéressante pour des applications spatiales. Le grand avantage par rapport à la propulsion chimique est une impulsion spécifique Isp plus élevée, une vitesse d'éjection plus élevée et donc un gain substantiel en terme de consommation de carburant. Dans un propulseur à effet Hall les ions sont créés et accélérés dans une décharge plasma à basse pression dans un champ magnétique.

La première partie de ce travail concerne les lois d'échelle pour les propulseurs à effet Hall. Un modèle de dimensionnement semi-empirique basé sur des lois analytiques et reposant sur des hypothèses simplificatrices a été développé. Ce modèle de dimensionnement peut être utilisé pour une extrapolation des propulseurs existants afin de répondre aux exigences pour de nouvelles missions.

Dans une deuxième étape, l'influence de la largeur du canal sur les performances d'un propulseur est étudiée. Il a été démontré qu'augmenter la largeur du canal conduit à une amélioration de l'efficacité du propulseur.

Finalement, les propriétés électroniques ont été mesurées à l'aide de sondes électrostatiques dans la plume de différents propulseurs à effet Hall. Des données expérimentales concernant les propriétés électroniques sont très intéressantes pour la validation des modèles numériques de la plume indispensables pour l'intégration du propulseur sur le satellite. Des mesures moyennées et résolues en temps des propriétés électroniques ont été réalisées pour différents points de fonctionnement du propulseur. Un système de déplacement rapide pour les sondes a été développé afin de pouvoir faire des mesures des propriétés électroniques dans la zone proche du plan de sortie du propulseur.

Mots clés : propulsion spatiale électrique, propulseur à effet hall, lois d'échelle, influence géométrie, propriétés électroniques, sonde électrostatiques

Scaling laws and electron properties in Hall effect thrusters

All satellites need a propulsion system for orbit correction maneuvers. Electric Hall effect thrusters are an interesting technology for space applications. The big advantage compared to chemical propulsion devices is the higher specific impulse Isp, a higher ejection speed and thus a substantial gain in terms of propellant consumption. In a Hall effect thruster the ions are created and accelerated in a low pressure discharge plasma in a magnetic field.

The first part of the work concerns scaling laws for Hall effect thrusters. A semi-empirical scaling model based on analytical laws and relying on simplifying assumptions is developed. This scaling model can be used to extrapolate existing thruster technologies in order to meet new mission requirements.

In a second part, the influence of the channel width on the thruster performance level is investigated. It has been demonstrated that enlarging the channel width of a low power Hall effect thruster leads to an increase in thruster efficiency.

Finally, electron properties are measured by means of electrostatic probes in the plume of different Hall effect thrusters. Experimental data on electron properties is of great interest for the validation of numerical plume models that are essential for the integration of the thruster on the satellite. Time-averaged and time-resolved measurements of the electron properties have been carried out for different operating conditions of the thruster. A fast-moving probe system has been developed in order to perform measurements of the electron properties close to the thruster exit plane.

Keywords : electric space propulsion, Hall effect thruster, scaling laws, influence of the geometry, electron properties, electrostatic probes

ICARE
1c avenue de la recherche scientifique,
45071 Orléans cedex 2, France